

Faculty of Science & Engineering
WASM: Minerals, Energy and Chemical Engineering

Implications of Wettability Alteration of Sandstone Rocks Using
Non-fluorinated scCO₂-based Silylation

Eghan Arjomand

This thesis is presented for the Degree of
Doctor of Philosophy
of
Curtin University

July 2020

DECLARATION

To the best of my knowledge and belief, this thesis contains no material previously published by any other person except where due acknowledgment has been made.

This thesis contains no material which has been accepted for the award of any other degree or diploma in any university.

Signature:..... (Eghan Arjomand)

Date: 6th of July 2020

*With a loving dedication to my Mum,
without your love and constant prayers, I would not have been able to
accomplish anything.*

ACKNOWLEDGMENT

A journey of a thousand miles begins with a single step, and there will be an end to every journey. Now, at the conclusion of my PhD's journey, I look back at the intensive research works and restless days and nights, and I am filled with the ecstatic feelings of satisfaction and content. This amazing journey would not have been completed without the support of many great people, and it's my sincere pleasure to thank you all.

Firstly, I would like to acknowledge and express my deepest gratitude to my supervisors, Assoc. Prof. Ali Saeedi and Dr. Colin D. Wood for being such incredible mentors during the past five years of my research. It has indeed been a privilege for me to be completing my PhD under your supervision. Your continuous and never-ending support and guidance have from the very beginning helped me to achieve the objectives of this work. Despite yourselves being on a tight time schedule, you never hesitated to provide me with technical and emotional support, whenever I found myself in a hard situation. I would also like to acknowledge my co-supervisor, Dr. Matthew Myers, with whom I had many profound and thoughtful conversations on numerous interesting topics.

I would like to thank Dr. Christopher D. Easton and Dr. Wendy Tian (from CSIRO – Melbourne) for their help on XPS data acquisition, and in helping me to interpret and analyse all the XPS data presented in this work. Also, I would like to thank Dr. Lionel Esteban (CSIRO – Perth), who provided me with NMR training and gave me unrestricted access to use the instrument during these past years. Many thanks to our former technical officer Mr. Bob Webb for his continuous technical support, and his efforts for providing a safe laboratory environment for everyone. I would also like to thank Dr. Matthew A. Flett (Chevron – Perth), who was a great mentor and provided me with valuable industrial insights. I am deeply grateful to my Mathematical Methods teacher, Mrs. Diana Willshire (Box Hill High School – Melbourne). If it wasn't for your kindness, support and thoughtful advice back then (VCE studies), I would not have been where I am right now. Special thanks to the Commonwealth Scientific and Industrial Research Organisation for providing the financial support (approved by Energy Flagship) during the development of this study.

During this work, I had the honour to meet and work with many amazing colleagues. Much gratitude goes to Ahmad Sari and Mohsen Ghasemi, who were always there to support me through the hardships. This work would not have been accomplished without your help in setting up instruments and conducting experiments. I would also like to extend my gratitude to the following people: Omar, Ezy, Felany, Jeffery, Ruby, Nichole, Jamiu, Nasser and Nasser. Special thanks to Nadia and auntie Mila, who were always there to reassure me that everything

will be fine. I want to thank Bella, Lollie, and specially Jimo, who made the last few months of thesis writing more enjoyable. To my friends back home in Melbourne, Amir, Niaz, Arash, Ghasem, Fahad and Yuting, thank you very much for your friendship, well-wishes and support over the past few years.

To my uncles and auntie Behnam, Bahereh and Behdad, I don't think I can ever express the depth of my gratitude to you for all that you have done for my family and me during the past 20 years. Without your support, this work would have been much harder for me to complete.

To my dear brothers and their families, Amir (and Annery), Arash (and Mariana), and Iman (Khatereh and Iliya), you have always been there for me for the past 35 years and counting. Thank you very much for your unconditional support. To my beloved baby sister Anisa (Memol), like your name states, you are our life companion. From your earliest age until now and forever, you have supported us, and I cannot thank you enough. I sincerely and wholeheartedly appreciate your love and support.

Lastly, but most importantly, to my dear parents, my mum Rohanieh Darougheh, and my dad Mohammad Mehdi Arjmand, to whom I will eternally be grateful. Words cannot express how grateful and blessed I am to have your unconditional love, support, and encouragement throughout my life. To my mum, you have always been there to support me and get me back up on my feet every time that I fell. You have sacrificed your life so we could achieve and fulfil our dreams.

ABSTRACT

The wettability condition of a reservoir rock is known to have a significant impact on the multiphase flow characteristics of the subsurface fluid-rock system by controlling critical attributes such as fluid saturation distribution, capillary pressure, relative permeability and displacement efficiency. Therefore, for any given system, it is paramount to gain an in-depth understanding of how possible natural variations in wettability may alter the dynamic behaviour of the underground system over the intermediate to long term. Furthermore, where necessary, the ability to effectively modify this critical parameter in the reservoir has implications in a range of areas such as mitigating liquid banking/blockage around hydrocarbon production wells, CO₂ geosequestration, enhanced hydrocarbon recovery, and separation of CO₂ using porous media.

Due to the diverse functionalities of silane coupling agents, application of these chemicals have gained substantial attention in the area of material surface modification in various industries. The ability to create cross-links between inorganic (e.g., quartz) and organic (e.g., alkyl groups) materials by applying these chemicals have demonstrated applications which are not limited to improving adhesiveness, mechanical strengthening, inorganic material modification, thermal resistivity, electrical properties, water resistivity, etc. To achieve the objectives of this research, the surface chemistry of four different sandstone rock types were modified using five different silane agents through both conventional and scCO₂-based silylation routes. A combination of X-ray photoelectron spectroscopy (XPS) analysis and contact angle measurements was utilized to evaluate and compare the surface coverage and effectiveness of the mentioned techniques. Subsequently, given the negligible impact of the treatments on the pore sizes/network of the rock samples, spontaneous imbibition and core-flooding experiments were conducted before and after treatment to understand the effects of wettability alteration on the multiphase flow characteristics of the fluid-rock system.

The XPS results demonstrated that superior chemical surface coverage was achieved through scCO₂-based silylation as compared to that of the conventional techniques that use liquid solvents such as toluene as the silane carrier. Moreover, contact angle measurements were indicative of a strong change in wettability state of the treated sandstone surfaces from strongly water-wet to strongly CO₂-wet. Furthermore, spontaneous imbibition experiments before and after treatment showed a considerable reduction in the rate and volume of water uptake in the post-treatment samples. The core-flooding results indicated that the effective permeability to the water phase was significantly increased, demonstrating higher water removal from the rock

matrix (i.e., lower S_{wr}). Subsequently, the gas (i.e., $scCO_2$) relative permeability was substantially enhanced after treatment.

This research helps to fill an existing gap in the published literature by providing reliable experimental evidence about the effect of wettability on dynamic multiphase flow characteristics of CO_2 -brine system. For this, the relative permeabilities and residual saturations are measured under the two extremes of strongly water-wetting and strongly CO_2 -wetting conditions while keeping other system parameters (e.g., rock properties) unchanged. Furthermore, the outcomes of this research reveal the benefits of the novel $scCO_2$ -based treatment technique in achieving an effective surface modification.

PUBLICATIONS BY THE AUTHOR

1. **Arjomand, Eghan**, Christopher D Easton, Matthew Myers, Wendy Tian, Ali Saeedi, and Colin D Wood. 2020. “Changing Sandstone Rock Wettability with Supercritical CO₂-Based Silylation.” *Energy and Fuels*. doi: 10.1021/acs.energyfuels.9b03431.
2. **Arjomand, Eghan**, Matthew Myers, Nasser Mohammed Al Hinai, Colin D. Wood, and Ali Saeedi. 2020. “Modifying the Wettability of Sandstones Using Nonfluorinated Silylation: To Minimize the Water Blockage Effect.” *Energy and Fuels*. doi: 10.1021/acs.energyfuels.9b03432.

Table of Contents

DECLARATION.....	i
ACKNOWLEDGMENT.....	iii
ABSTRACT.....	v
PUBLICATIONS BY THE AUTHOR.....	vii
List of Figures.....	xi
List of Tables.....	xvi
Abbreviations/Symbols.....	xvii
Chapter 1 Introduction.....	1
1.1 Background and Problem Description.....	1
1.2 Research Objective.....	2
1.3 Organization of Thesis.....	3
Chapter 2 Literature Review.....	5
2.1 Introduction.....	5
2.2 Fundamentals of Wettability.....	5
2.3 Effect of Wettability on Multiphase Flow in Porous Media.....	7
2.3.1 Fluid Phase Saturation and Distribution.....	7
2.3.2 Relative Permeability.....	9
2.3.3 Capillary Pressure.....	15
2.4 Wettability Evaluation Techniques.....	18
2.4.1 Contact Angle Method.....	19
2.4.2 Amott Method.....	20
2.4.3 USBM Method.....	22
2.4.4 Spontaneous Imbibition.....	23
2.4.5 Other Techniques.....	24
2.5 Wettability of Sandstone Rocks.....	24
2.6 Wettability Alteration by Chemical Treatment.....	26
2.6.1 Surfactant Application.....	26
2.6.2 Low Salinity Flooding.....	27
2.6.3 Nanoparticle Treatment.....	27
2.6.4 Fluorinated Chemical Application.....	28
2.6.5 Silylation.....	29

2.6.5.1	Conventional Silylation.....	31
2.6.5.2	Supercritical Fluid Silylation	32
2.7	Subsurface Applications of CO ₂	35
Chapter 3	Experimental Setup, Materials and Methodology.....	38
3.1	Experimental Equipment.....	38
3.1.1	High Pressure-Temperature Visual Cell	38
3.1.2	High Throughput Surface Modification Setup.....	40
3.1.3	X-Ray Photoelectron Spectroscopy	42
3.1.4	Core-Flooding Setup	43
3.1.5	Nuclear Magnetic Resonance.....	48
3.2	Materials	50
3.2.1	Fluids and Chemicals	50
3.2.2	Rock Samples.....	52
3.3	Experimental Methodology.....	54
3.3.1	Sample Preparation	54
3.3.1.1	Rock Discs and Powder	54
3.3.1.2	Core Plug Preparation and Preliminary Measurements	55
3.3.2	NMR Measurements	57
3.3.3	Cloud Point Pressure Measurements.....	58
3.3.4	Rock Discs and Powder Treatment Process.....	59
3.3.4.1	Conventional Silylation Technique.....	59
3.3.4.2	Silylation in Supercritical CO ₂	60
3.3.5	Mutual Pre-Saturation of CO ₂ and Brine	61
3.3.6	X-Ray Photoelectron Spectroscopy Measurements	63
3.3.7	Contact Angle Measurements	63
3.3.8	Spontaneous Imbibition Measurements	65
3.3.9	Core-Flooding Experiments	66
Chapter 4	Experimental Results, Interpretation and Discussion	71
4.1	Cloud Point Pressure Measurement Results	71
4.2	X-Ray Photoelectron Spectroscopy	74
4.2.1	Supercritical CO ₂ -based Silylation	74
4.2.2	Conventional vs. Supercritical CO ₂ -based Silylation	75
4.3	Contact Angle Measurement and Wettability Alteration Evaluation.....	78
4.3.1	Supercritical CO ₂ -based Silylation	78

4.3.2	Conventional vs. Supercritical CO ₂ -based Silylation	80
4.4	Effect of scCO ₂ -based Silylation on Spontaneous Imbibition	81
4.5	Core-Flooding Experiments	84
4.6	NMR Results.....	91
Chapter 5	Conclusions, Recommendations and Outlook for Future Work	93
5.1	Conclusions.....	93
5.2	Recommendations and outlook for future work.....	95
References	96
APPENDIX A	Supporting Information	116
APPENDIX B	Official Permissions and Copyrights	137
APPENDIX C	Attributions of Co-authors.....	139

List of Figures

Figure 2.1. Pore-scale demonstration of the effect of wettability conditions of a rock formation on fluid distribution within pores. Water-wet (left), where the water phase covers the pore surfaces and occupies smaller pores, and the hydrocarbon is held in the centre of the larger pores. Oil-wet (right), which is the opposite condition of water-wet system and water remains in the centre of the larger pores, and oil covers the grain surfaces and remains in smaller pores. Mixed-wet (middle), where oil has expelled the native water from some of the pores but not all of them (modified from Abdallah <i>et al.</i> 2007).....	6
Figure 2.2. Single-phase flow through porous media (Darcy’s law)	9
Figure 2.3. Left: Steady-state relative permeability curves for oil and water for water-wet and oil-wet systems (modified from Jennings 1957). Right: The relative permeability curves for different wettability conditions at the same initial water saturation (modified from Owens and Archer 1971)	12
Figure 2.4. Effect of wettability on water fractional flow at constant viscosity ratio. Water-wet (blue curve), oil-wet (red curve) and mixed-wet (green curve). (modified from, Ahmed 2001). The tangent lines drawn from S_{wir} to the water fractional flow curves corresponds to the water fractional flow encountered at water break through and the shock-front water saturation.	15
Figure 2.5. Capillary desaturation curves during drainage (solid lines) and imbibition (dashed lines) processes for air-water system. Strongly water-wet system (blue) and weakly water-wet (red lines) systems (modified from Bradford and Leij 1995).	18
Figure 2.6. Schematic of force field acting on a three-phase substrate-water-scCO ₂ system.....	20
Figure 2.7. Capillary pressure (P_c) versus water saturation (S_w) curves as measured during an Amott test (modified from Morrow 1990). This graph will also be used to describe USBM technique in following Section 2.4.3.	21
Figure 2.8. Simplified mechanism of silylation reaction (modified from Sánchez-Vicente <i>et al.</i> 2014)	29
Figure 2.9. Reaction efficiency of silylation agents on inorganic materials (modified from Sanli and Erkey 2015)	30
Figure 2.10. P-V diagram of pure CO ₂ system, where the single, two-phase and supercritical regions are emphasised. The isotherms are represented by dashed lines. (modified from Erkey 2011)	33
Figure 2.11. CO ₂ emissions, 1990-2019 (modified from IEA 2020).....	36
Figure 2.12. Map of CO ₂ sequestration facilities, pilot projects, and long-term storage potential in geologic formations (modified from Kelemen <i>et al.</i> 2019).....	37
Figure 3.1. The high pressure-temperature visual cell apparatus used to measure cloud point pressure and contact angle (Vinci IFT-700).	38
Figure 3.2. The schematic diagram of IFT-700 apparatus.....	39
Figure 3.3. The High Throughput Surface Modification (HTSM) used for scCO ₂ silylation. a) HTSM cell. b) Demonstration of sample distribution in the stand/racking system. c) The schematic of HTSM experimental setup.	41

Figure 3.4. AXIS Ultra X-ray photoelectron spectroscopy (KRATOS).....	43
Figure 3.5. The core-flooding system used in this study.	43
Figure 3.6. The schematic diagram of the core-flooding setup.....	44
Figure 3.7. a) The schematic cross-section of the standard biaxial HCH core-holder, b) Picture of the end plug design configuration.	45
Figure 3.8. Combinational sleeve sequence. a) Core sample. b) Teflon tape layer. c) Aluminium foil layer. d) Heat-shrink sleeve. e) Viton sleeve. f) Core sample placement fixed at both ends.....	46
Figure 3.9. a) Data acquisition software. b) Pressure transducer.....	48
Figure 3.10. The Nuclear Magnetic Resonance (NMR) spectrometer used in this research (GeoSpec2).....	50
Figure 3.11. Chemical structure of selected silanes. a) DD_TS, b) CPhe_TS, c) BHEA_TS, d) GPTS, e) CPTS, f) APTES.	51
Figure 3.12. Geographical distribution of petroleum reservoirs: a) Siliciclastic reservoirs, b) Carbonate reservoirs (modifies from Ehrenberg and Nadeau 2005).	53
Figure 3.13. Prepared GB samples. Powder for chemical surface modification tests (left) and polished disc for contact angle measurements (right).....	54
Figure 3.14. Dean-Stark apparatus (used for core plug and rock disc washing).....	55
Figure 3.15. The high-pressure apparatus used to fully saturate the core plugs with synthetic brine.....	56
Figure 3.16. The stirred reactor used to mutually saturate the brine and CO ₂	62
Figure 3.17. (a) Spontaneous imbibition test setup. (1) Pressure relieve valve (0.2 MPa), (2) Graduated neck, (3) Sample holder. (b) Imbibed brine displacing air bubbles from a water-wet core plug.....	65
Figure 4.1. BHEA_TS cloud point pressure measurement in the visual cell. The intensity of the light passing through the cell decreases as the pressure approaches the cloud point value.	72
Figure 4.2. Visible deposition of ammonium carbamate during depressurization resulting from a chemical reaction of scCO ₂ with APTES.	73
Figure 4.3. The XPS elemental quantification (expressed as atomic %) of Gray Berea substrate before and after treatment. (Graph contains data for Control Sample and aged through scCO ₂ method with CPTS, CPhe_TS, BHEA_TS, GPTS and DD_TS).	74
Figure 4.4. The XPS elemental quantification (expressed as atomic %) of Gray Berea substrate before and after treatment. (Graph contains data for Control Sample and aged through scCO ₂ method with CPTS, CPhe_TS, BHEA_TS, GPTS and DD_TS).	76
Figure 4.5. Selected, representative, high resolution C 1s XPS spectra with peak fitting with a 5 component system for Grey Berea [(a) Control, (b) BHEA_TS in toluene and (c) BHEA_TS in scCO ₂]. Tentative assignments for components are as follows: C1 + C2: C-C, C-H, C-Si; C3: C-O, C-N; C4: C=O, N-C=O, O-C-O; C5: CO ₃ , COOR.....	77
Figure 4.6. Contact angle measurements to show the alteration made by the scCO ₂ -based silylation of the sandstone rock samples [(a) Gray Berea, (b) Upper Gray Berea, (c) Bandera Brown, and (d) Bentheimer].	79

Figure 4.7. Contact angle measurements to show the alteration made by the conventional silylation of the sandstone rock samples [(a) Gray Berea, (b) Upper Gray Berea, (c) Bandera Brown, and (d) Bentheimer]. 81

Figure 4.8. Spontaneous brine imbibition versus time in GB.2, pre-treatment (red triangle) and post-treatment (blue diamond). 82

Figure 4.9. Experimental differential pressure (denoted by Exp) vs. pore volumes of CO₂ injected through the GB.2 sandstone sample pre- (blue cross symbol) and post-silylation (red plus symbol) with 2 wt. % of CPTS (inset compares the breakthrough points) Solid and dashed black lines represent the numerical simulation history matched differential pressure for pre- and post-silylation, respectively (denoted by Sim). 85

Figure 4.10. Differential pressure vs. pore volumes of brine injected through the GB.2 sandstone sample pre- (blue cross symbol) and post-silylation (red plus symbol) with 2 wt. % of CPTS (inset compares the breakthrough points). 86

Figure 4.11. Experimental brine recovery profiles during scCO₂ injection for pre-treatment (blue diamond symbol), post-treatment (red triangle symbol) for GB.2 (denoted by Exp). Solid and dashed black lines represent the numerical simulated brine recovery for pre- and post-treatment, respectively (denoted by Sim). 87

Figure 4.12. Relative permeability curves for the primary drainage conducted on pre-treated (triangle symbol) and post-treated (circle symbol) for GB.2 sample. 90

Figure 4.13. NMR derived incremental brine volume for pre- and post-treated GB.2. 92

Figure A. 1. XPS elemental quantification expressed as atomic % of Upper Gray Berea substrate and modified samples. (Graph contains data for Control Sample and aged through scCO₂ method with CPTS, CPhe_TS, BHEA_TS, GPTS and DD_TS). Note: Not all the elements present in the substrates are included in the graphs. 120

Figure A. 2. XPS elemental quantification expressed as atomic % of Bandera Brown substrate and modified samples. (Graph contains data for Control Sample and aged through scCO₂ method with CPTS, CPhe_TS, BHEA_TS, GPTS and DD_TS). Note: Not all the elements present in the substrates are included in the graphs. 120

Figure A. 3. XPS elemental quantification expressed as atomic % of Bentheimer substrate and modified samples. (Graph contains data for Control Sample and aged through scCO₂ method with CPTS, CPhe_TS, BHEA_TS, GPTS and DD_TS). Note: Not all the elements present in the substrates are included in the graphs. 121

Figure A. 4. XPS elemental quantification expressed as atomic % of Upper Gray Berea substrate and modified samples. (Graph contains data for Control Sample (hashed bars) and aged through Conventional method (solid bars) and scCO₂ method (dotted bars) with BHEA_TS and GPTS). Note: Not all the elements present in the substrates are included in the graphs. 121

Figure A. 5. XPS elemental quantification expressed as atomic % of Bandera Brown substrate and modified samples. (Graph contains data for Control Sample (hashed bars) and aged through Conventional method (solid bars) and scCO₂ method (dotted bars) with BHEA_TS and GPTS). Note: Not all the elements present in the substrates are included in the graphs. 122

Figure A. 6. XPS elemental quantification expressed as atomic % of Bentheimer substrate and modified samples. (Graph contains data for Control Sample (hashed bars) and aged through conventional method (solid bars) and scCO₂ method (dotted bars) with BHEA_TS and GPTS). Note: Not all the elements present in the substrates are included in the graphs. 122

Figure A. 7. Spontaneous brine imbibition vs. time in GB.1, pre-treatment (red triangle) and post-treatment (blue diamond). 123

Figure A. 8. Spontaneous brine imbibition vs. time in GB.3, pre-treatment (red triangle) and post-treatment (blue diamond). 123

Figure A. 9. Spontaneous brine imbibition vs. time in GB.4, pre-treatment (red triangle) and post-treatment (blue diamond). 124

Figure A. 10. Experimental differential pressure (denoted by Exp) vs. pore volumes of CO₂ injected through the GB.1 sandstone sample pre- (blue cross symbol) and post-silylation (red plus symbol) with 2 wt. % of CPTS (inset compares the breakthrough points) Solid and dashed black lines represent the numerical simulation history matched differential pressure for pre- and post-silylation, respectively (denoted by Sim). 125

Figure A. 11. Differential pressure vs. pore volumes of brine injected through the GB.1 sandstone sample pre- (blue cross symbol) and post-silylation (red plus symbol) with 2 wt. % of CPTS (inset compares the breakthrough points). 126

Figure A. 12. Experimental differential pressure (denoted by Exp) vs. pore volumes of CO₂ injected through the GB.3 sandstone sample pre- (blue cross symbol) and post-silylation (red plus symbol) with 2 wt. % of CPTS (inset compares the breakthrough points). Solid and dashed black lines represent the numerical simulation history matched differential pressure for pre- and post-silylation, respectively (denoted by Sim). 127

Figure A. 13. Differential pressure vs. pore volumes of brine injected through the GB.3 sandstone sample pre- (blue cross symbol) and post-silylation (red plus symbol) with 2 wt. % of CPTS (inset compares the breakthrough points). 128

Figure A. 14. Experimental differential pressure (denoted by Exp) vs. pore volumes of CO₂ injected through the GB.4 sandstone sample pre- (blue cross symbol) and post-silylation (red plus symbol) with 2 wt. % of CPTS (inset compares the breakthrough points). Solid and dashed black lines represent the numerical simulation history matched differential pressure for pre- and post-silylation, respectively (denoted by Sim). 129

Figure A. 15. Differential pressure vs. pore volumes of brine injected through the GB.4 sandstone sample pre- (blue cross symbol) and post-silylation (red plus symbol) with 2 wt. % of CPTS (inset compares the breakthrough points). 130

Figure A. 16. Experimental brine recovery factor during scCO₂ injection for pre-treatment (blue diamond symbol) and post-treatment (red triangle symbol) for GB.1 (denoted by Exp). Solid and dashed black lines represent the numerical simulated brine recovery for pre- and post-treatment, respectively (denoted by Sim). 131

Figure A. 17. Experimental brine recovery factor during scCO₂ injection for pre-treatment (blue diamond symbol) and post-treatment (red triangle symbol) for GB.3 (denoted by Exp). Solid and dashed black lines represent the numerical simulated brine recovery for pre- and post-treatment, respectively (denoted by Sim). 132

Figure A. 18. Experimental brine recovery factor during scCO₂ injection for pre-treatment (blue diamond symbol) and post-treatment (red triangle symbol) for GB.4 (denoted by Exp). Solid and dashed black lines represent the numerical simulated brine recovery for pre- and post-treatment, respectively (denoted by Sim). 133

Figure A. 19. Relative permeability curves for the primary drainage conducted on pre-treated (triangle symbol) and post-treated (circle symbol) for GB.1 sample. 134

Figure A. 20. Relative permeability curves for the primary drainage conducted on pre-treated (triangle symbol) and post-treated (circle symbol) for GB.3 sample. 134

Figure A. 21. Relative permeability curves for the primary drainage conducted on pre-treated (triangle symbol) and post-treated (circle symbol) for GB.4 sample. 135

Figure A. 22. NMR derived incremental brine volume for pre- and post-treated GB.1. 135

Figure A. 23. NMR derived incremental brine volume for pre- and post-treated GB.3. 136

Figure A. 24. NMR derived incremental brine volume for pre- and post-treated GB.4. 136

List of Tables

Table 2.1. Craig's (1971) general rules for determining wettability from relative permeabilities	12
Table 3.1. Basic properties of selected silane agents used in this research.....	52
Table 3.2. Mineral composition of selected rock samples	53
Table 3.3. Basic petrophysical properties of core plugs used during core-flooding experiments.	56
Table 3.4. The calculated mass of individual silanes to achieve a 2 wt. % solution within the HTSM cell (volume of 1000 cc).....	61
Table 4.1. Calculated mass of individual silanes to make up a 2 wt. % solution in the visual cell (internal volume of 20 cc) and the corresponding measured cloud point pressures.....	73
Table 4.2. A summary of the pre- and post-treatment spontaneous imbibition test results.	83
Table 4.3. Brine and CO ₂ effective and endpoint relative permeability and brine residual saturation before and after chemical treatment.	86
Table 4.4. Best-fit relative permeability parameters for the history matched core-floods using the Sigmund and McCaffery (1979) model.....	89
Table A. 1. Elemental Quantification for Gray Berea derived from XPS survey spectra. Listed are the mean values based on 2 analysis points.	116
Table A. 2. Elemental Quantification for Upper Gray Berea derived from XPS survey spectra. Listed are the mean values based on 2 analysis points.	117
Table A. 3. Elemental Quantification for Bandera Brown derived from XPS survey spectra. Listed are the mean values based on 2 analysis points.	118
Table A. 4. Elemental Quantification for Bentheimer derived from XPS survey spectra. Listed are the mean values based on 2 analysis points.	119

Abbreviations/Symbols

A	Cross-sectional area
ADSA	Axisymmetric drop shape analysis
API	American petroleum institute
APTES	(3-aminopropyl)triethoxysilane
atm	Atmosphere
B_0	Static magnetic field
B_1	Oscillating magnetic field
BB	Bandera brown
BE	Binding energy
BHEA_TS	3-[bis(2-hydroxyethyl)amino]propyl-triethoxysilane solution
BPR	Back-pressure regulator
BT	Bentheimer
BVI	Bulk volume irreducible
BVW	Bulk volume movable
CBW	Clay-bound water
cc	Cubic centimetre
CCF	Chromatography column filter
CCS	Carbon capture and storage
cm^2	Centimetre squared
$\text{cm}^3 \cdot \text{s}^{-1}$	Cubic centimetre per second
CO_2	Carbon dioxide
CP	Cloud point
cP	Centipoise
CPhE_TS	(4-chlorophenyl)triethoxysilane
CPMG	Carr–Purcel–Meiboom–Gill
CPTS	(3-chloropropyl)triethoxysilane
CVD	Chemical vapour deposition
D	Darcy
DD_TS	Dodecyltriethoxysilane
DI	Deionized
EOR	Enhanced Oil Recovery
ESCA	Electron spectroscopy for chemical analysis
EtOH	Ethanol
eV	Electron-volts
FFI	Free-fluid index
FS	Full Scale
f_w	Water fractional flow
g	Gravitational acceleration constant
GB	Gray Berea
GPTS	(3-glycidyoxypropyl)triethoxysilane
h	Plank's constant
H	Contact angle hysteresis
HI	Hydrogen index

hr	Hour
HMDS	Hexamethyldisilazane
HTGE	High throughput gravimetric extraction
HTSM	High throughput surface modification
I_{AH}	Amott-Harvey index
ID	Internal diameter
IFT	Interfacial Tension
in	inch
I_o	Amott oil wettability index
I_w	Amott water wettability index
K	Degrees Kelvin
k	Absolute permeability
KE	Kinetic energy
k_i	Effective permeability for individual fluids (i)
k_{ri}	Relative Permeability for individual fluids (i)
kV	Kilo-volt
L	Length
LSWI	Low salinity water injection
mA	Milliamps
max	maximum
mBar	Millibar
MeOH	Methanol
MHz	Megahertz
MIE	Multi-ion exchange
min	Minute
ml	Millilitre
mN/m	Millinewton/metre
mol	Mole
m_p	Mass of solute in solvent
MPa	Mega Pascal
ms	Millisecond
Mt/yr	Millionton per year
N_E	Number of echo
NIST	National Institute of Standards and Technology
nm	Nanometre
NMR	Nuclear magnetic resonance
NPs	Nanoparticles
N_{USBM}	USBM wettability number
OD	Outside diameter
OH	Hydroxyl group
OTS	Octadecyltrichlorosilane
P	Pressure
P_c / P_d	Capillary pressure / Displacement pressure
P_c	Critical pressure
pH	Acidity or basicity of a solution
P_{nw}	Non-wetting phase pressure

ppm	Parts per million
Psi	pounds per square inch
PV	Pore volume
P_w	Wetting phase pressure
q_i	Flow rate (i denotes individual fluids, i.e., water, oil, gas)
R	Effective pore radius
RF	Radio frequency
RPM	Rotation per minute
s	Second
S_i	Fluid saturation (i denotes individual fluids, i.e., water, oil, gas)
SAMs	Self-assembled monolayers
SCADA	Supervisory control and data acquisition
scCO ₂	Supercritical carbon dioxide
SCF	Supercritical Fluid
SI	Spontaneous imbibition
SNR	Signal-to-noise ratio
S_{ro}	Residual oil saturation
SS	Steady-state
S_{wr}	Residual water saturation
T	temperature
T_c	Critical temperature
T_1	Spin-lattice relaxation time
T_2	Spin-spin relaxation time
T_w	Inter-experimental delay time
UGB	Upper Gray Berea
USS	Unsteady-state
V	Volume
v	Light frequency
W	Watt
wt. %	weight percent
XPS	X-ray photoelectron spectroscopy
X_{sol}	Weight ratio of solute to solvent
ΔP	Differential pressure
°C	Degrees Centigrade
μL	Microliter
μ	Viscosity
μs	micro second
ρ	Density
ρ_e	Surface relaxivity
σ	Interfacial Tension
τ	Echo-spacing time
Θ	Contact angle
Θ_Y	Young's contact angle

Chapter 1 Introduction

One major focus point of this research work has been to compare the multiphase flow characteristics of the CO₂-brine-rock system under the two wettability states of strongly water-wet and CO₂-wet. To achieve this goal, a novel supercritical CO₂-based (scCO₂-based) silylation technique has been developed and tested, that could be used to induce the necessary wettability alteration to porous sandstone rocks under elevated pressure and temperature. The primary objective of the current chapter is to set the scene by giving a brief background to the problem at hand, presenting a snapshot of the objectives pursued by this research and finally providing a brief picture of how this thesis is organised.

1.1 Background and Problem Description

Fluid flow through porous media is a critical subject area pertaining to subsurface operations and in particular, those related to hydrocarbon recovery and CO₂ geosequestration (Avraam and Payatakes 1995; Speight 2017). The ability to control or maintain fluid flow behavior is central to a broad range of critical petroleum engineering-related tasks such as field development, reservoir management, hydrocarbon production and fluid injection. Therefore, for example, early characterization of multiphase fluid flow will serve to constrain related uncertainties and assist in predicting future performance and possible problems, thus, allowing engineers to determine the best course of action (Higdon 2013).

Successful implementation of environmental strategies such as carbon capture and storage (CCS) also hinges on a comprehensive understanding of multiphase fluid flow properties (Iglauer *et al.* 2017). A number of researchers have demonstrated that in a water-hydrocarbon-rock system, higher amounts of hydrocarbon can be produced if the formation wettability shifts towards a more water-wet state (Anderson 1987; Jadhunandan and Morrow 1995). Assuming a similar scenario to be valid for a water-CO₂-rock system, the mobility of CO₂ plume would increase as the rock formation deviates towards a less water-wetting condition. Subsequently, the upward migration of CO₂ can cause a substantial reduction in the containment security of the formation (Arif *et al.* 2017; Iglauer *et al.* 2015).

When a porous medium is filled with multiple fluid phases (water, oil and gas), the flow of a given phase within the pores is not primarily a function of the medium permeability alone as predicted by Darcy's equation in its original form applicable to single-phase flow. Given the multiphase nature of such a system, the transport is also a function of the saturation level and relative permeability of a given phase, the interactions of fluids with the pore surfaces and the

geometry of the fluid-filled part of the pore space (John *et al.* 2015). The above factors are then strongly influenced by the wettability of the medium (Morrow 1990; McCaffery and Bennion 1974; Jackson, Valvatne, and Blunt 2005). For example, for a water-oil system, the relative permeability of the oil phase increases as the wettability of the rock shifts towards a neutral or more water-wet state (Jadhunandan and Morrow 1995; Sari *et al.* 2017; Nwideo *et al.* 2017). As another general example, from a pore-scale perspective, the way various mechanisms entrap the wetting phase is somewhat different from how the non-wetting phase is rendered immobile in the pores. At the end of a drainage displacement, the wetting phase is left behind primarily in the form of thin-film covering pore surfaces and within the smaller range of pore sizes. However, at the conclusion of an imbibition displacement, the residual non-wetting phase is trapped mainly due to the snap-off mechanism in the form of blobs and ganglia in the centre of the large pores (Land 1968; Dullien 1992; Holtz 2002).

Although the impact of wettability alteration on multiphase fluid flow characteristics of the oil-brine-rock system has been evaluated and discussed in the literature extensively, a similar experimental study on evaluating the same for the CO₂-brine-rock system under representative dynamic conditions seems to be nonexistent. The lack of representative experimental data is particularly evident from the recently published studies where authors opted to use hypothetical data in their numerical simulation work (Al-Khdheawi *et al.* 2017a; 2017b; Al-Khdheawi *et al.* 2018). One major concern with using such data, as opposed to a field or experimentally measured data, is the introduction of further uncertainties which then create operational challenges and undermine the ability to make informed decisions. Therefore, there is a pressing need for a representative experimental study to evaluate the relationship between wettability and multiphase fluid flow characteristics under reservoir conditions for CO₂-brine-rock system. The above has been done in this study using a structured and systematic approach to alter wettability, providing a unique opportunity to evaluate wettability effects while keeping other influencing factors (e.g., rock petrophysical properties) effectively unchanged. This study is not using model surfaces (e.g., quartz crystals) which are typically used in the literature. Using model surfaces, while valuable, would yield results not representative of reservoir conditions. In this research, the silylation treatment approach has been adopted to modify the wettability of natural sandstone rocks using a novel scCO₂-based silylation technique for the first time.

1.2 Research Objective

Given the above general background and problem description, the following key objectives have been pursued by this research work:

- Qualitative investigation of solubility performance of a number of selected silylation agents in scCO₂.
- Comparison between two different silylation techniques, namely, conventional and supercritical fluid-based, in achieving the best surface coverage necessary for the sought wettability alteration.
- Investigating the degree of wettability alteration for a number of sandstone rocks, as controlled by the effectiveness of chemical modification attained through scCO₂-based versus conventional silylation techniques.
- Investigating the effect of wettability alteration on dynamic multiphase flow characteristics of scCO₂-brine-sandstone systems, such as residual saturations and relative permeabilities. This would also yield the much-needed representative experimental data about the effect of wettability state of sandstone rocks on the flow properties of the CO₂-brine fluid system.

1.3 Organization of Thesis

This thesis consists of five chapters. In Chapter 2 (Literature Review), first, the fundamentals of surface wettability and its effect on multiphase flow in porous media are discussed. Subsequently, a number of techniques applied in the technical community to evaluate the surface wettability are reviewed. Then, various approaches that may be followed to change the wettability of a rock are described. Finally, as the particular topic of interest in the current research, silylation technique as a means for surface treatments and wettability alteration is discussed by providing a detailed review of the previously published works in this area.

Chapter 3 (Experimental Setup, Materials and Methodology), divided in two major sections presenting a detailed description of experimental apparatuses and material used during this research followed by a detailed outline of the experimental procedures followed in conducting the intended experiments.

Chapter 4 (Experimental Results, Interpretation and Discussion), presents the experimental results obtained along with their detailed analysis, interpretation and discussions.

Finally, in Chapter 5 (Conclusions, Recommendations and Outlook for Future Work), includes a condensed summary of the research findings together with a number of recommendations for possible future investigations.

It is worth noting that Chapter 4 (Experimental Results, Interpretation and Discussion) is compiled primarily based on the author's journal publications, which have been reproduced in this thesis as an individual chapter. The reader may wish to refer PUBLICATIONS BY THE AUTHOR section for the titles of the published works.

Chapter 2 Literature Review

2.1 Introduction

In this chapter, a comprehensive introduction to wettability phenomena and the effect on multiphase flow characteristics within porous media is presented, followed by an outline of different techniques (qualitative and quantitative) applied to assess the wettability state of a solid surface. Next, a number of different techniques employed to change the wettability state of reservoir rocks are discussed, which includes silylation (the technique adopted for this research). Finally, this chapter will conclude with a brief overview of the thermodynamic properties of CO₂, which is the primary experimental fluid used in this work.

2.2 Fundamentals of Wettability

Wettability is defined as the tendency of one fluid to wet or spread over a solid surface in the vicinity of another immiscible fluid phase (Speight 2017; Craig 1971). The general multiphase flow characteristics of a porous medium are controlled by this intrinsic surface property, which is one of the fundamental physicochemical parameters of the system. In a system where three fluid phases are present (water, oil and gas), depending on the preferential affinity of the solid surface to any of the fluids, the surface can be termed as hydrophilic (water-wet), oleophilic (oil-wet) or lyophobic (gas-wet), respectively. As demonstrated in Figure 2.1, at the pore-scale, the wetting phase covers the surface of the rock grains and occupies the smaller pores due to their high capillary pressure that opposes the intrusion of the non-wetting phase. On the other hand, the non-wetting phase, which can be present as a continuous phase across several pores, occupies the centre of the pores and is surrounded by a thin film of the wetting phase keeping it away from pore surfaces (Anderson 1986). In addition to the strong wetting tendency of a surface towards a specific fluid phase, fractional-wettability and mix-wettability terms have also been extensively used in the area of reservoir characterization (Brown and Fatt 1956; Salathiel 1973). Fractional-wettability refers to the local variation of wettability within a single rock formation, attributed to the range of minerals covering the rock pore surfaces, which can result in heterogeneous surface chemistries and fluid-phase adsorption capacities (Wolthers, Charlet, and Van Cappellen 2008). Mixed-wettability is one of the relatively common wettability states of a reservoir formation if more than one fluid phase is present (Figure 2.1, middle image). Considering that initially a reservoir pore space is filled with native water prior to the hydrocarbon migration, the pore surfaces are at equilibrium with the formation water and therefore have a strong hydrophilic tendency (Kyte, Naumann, and Mattax 1961). Once the

hydrocarbon migrates through to the target formation, it displaces the native water from the larger pores; however, it cannot penetrate the smallest pores due to high capillary forces. Subsequently, as demonstrated in Figure 2.1 (middle image), the smallest pores remain water-wet, and the surfaces of the larger pores which now contain the hydrocarbon phase may be altered to an oleophilic state (Abdallah *et al.* 2007). In fact, the polar and heavy component of the oil such as asphaltenes can interact with the surface minerals of the formation and adsorb onto the surface, and subsequently lead to the wettability alteration of the rock formation (Agbalaka *et al.* 2008). A study by Hirasaki (1991) demonstrated that the wettability of a brine-oil-rock system would be directly influenced by the thickness of the wetting phase (water in this case) film covering the rock surface, meaning that the surface remains water-wet if a stable and thick water film remains on the surface. On the other hand, a possible fissure within an unstable water film covering the surface allows for the polar components of the oil to adsorb onto the rock surface, and the subsequent deposition may lead to possible wettability alteration of the surface towards a less water-wetting state. A number of factors which are known to contribute to the degree of wettability alteration through this process are the brine composition occupying the pore space, the grain surface mineral chemistry and the hydrocarbon chemical composition (William G Anderson 1986). More than 50% of remaining oil reserves are those of carbonate nature which are generally oil-wet (Chilingar and Yen 1983). In contrast, the tendency towards water-wetness is observed more in sandstone reservoirs, except for those formations which contain a considerable amount of clay minerals distributed on the sandstone surfaces (K. Ma *et al.* 2013).

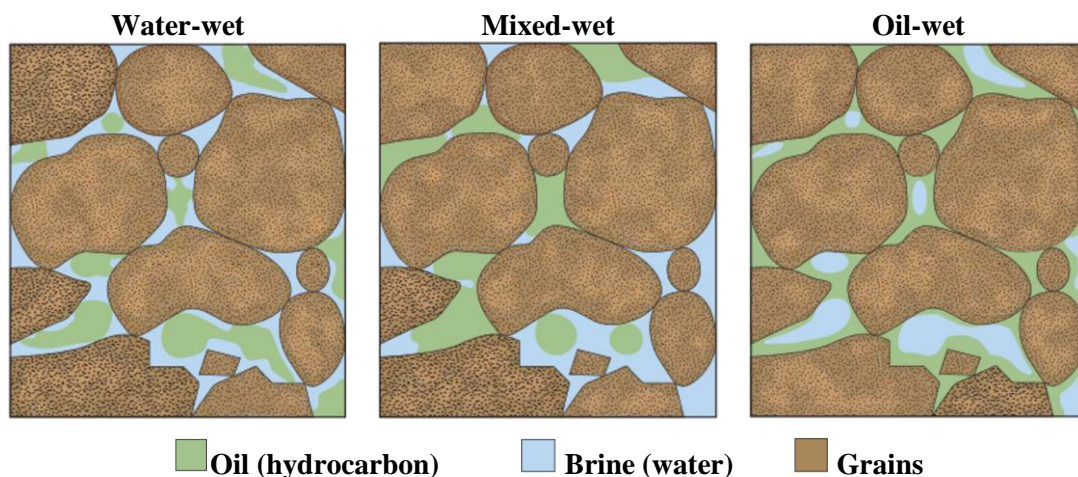


Figure 2.1. Pore-scale demonstration of the effect of wettability conditions of a rock formation on fluid distribution within pores. Water-wet (left), where the water phase covers the pore surfaces and occupies smaller pores, and the hydrocarbon is held in the centre of the larger pores. Oil-wet (right), which is the opposite condition of water-wet system and water remains in the centre of the larger pores, and oil covers the grain surfaces and remains in smaller pores. Mixed-wet (middle), where oil has expelled the native water from some of the pores but not all of them (modified from Abdallah *et al.* 2007)

2.3 Effect of Wettability on Multiphase Flow in Porous Media

In terms of reservoir properties, a number of dominant aspects of multiphase flow characteristic are controlled by the wettability state of the porous formation, such as the residual fluid saturation, immiscible fluid distribution, relative permeability of the fluid phases and the capillary pressure of the rock formation (Anderson 1986; Anderson 1987; Morrow 1990; Chaudhary *et al.* 2013; Jackson *et al.* 2005). The following sections will provide insight into each of the mentioned parameters which are directly influenced by the wettability state of a rock formation.

2.3.1 Fluid Phase Saturation and Distribution

Multiphase fluid distribution within a reservoir rock formation has a direct impact on the production potential of the reservoir, and the fluid distribution is in turn influenced by the wettability of the formation. Wettability would control how fluids position themselves relative to each other under static and dynamic conditions. Therefore, it can influence many reservoir scale processes from the hydrocarbon migration from the source rock to enhanced hydrocarbon recovery processes including water or gas flooding as well as other subsurface processes such CO₂ geosequestration and natural gas storage (Morrow 1990).

Numerous studies have investigated the effect of rock wettability on multiphase flow in oil reservoirs under various wettability states including strongly water-wet, mixed-wet and strongly oil-wet conditions. During the primary hydrocarbon recovery, the wettability of the system is one of the main factors that determines the recovery efficiency of a reservoir. In a strongly water-wet system, during water-flooding (or imbibition of water from an active aquifer), the water penetrates the smallest pores and moves the hydrocarbon through the larger pores. If a desirable viscosity ratio between the two immiscible phases is in place (which controls the fractional multiphase flow), a stable displacement pattern would be achieved during which the oil phase passes uniformly through the centre of the larger pores, while water proceeds along the walls of the pores and within the smaller pores where no oil is present (Raza *et al.* 1968; Donaldson and Thomas 1971; Agbalaka *et al.* 2008). Although under the scenario mentioned above the oil front flows in a uniform and stable manner, some of the oil would still become immobile and trapped in the centre of pores surrounded by water (Morris and Wieland 1963). Furthermore, it has been demonstrated that in a strongly water-wet system, most of the mobile hydrocarbon tends to be produced before the water breakthrough with no substantial hydrocarbon recovery taking place after the breakthrough, meaning that any post-breakthrough water injection may not contribute to further oil recovery (Jadhunandan and Morrow 1995; Donaldson and Thomas 1971; Morris and Wieland 1963). In other words, the ultimate oil

recovery would be almost equal to the oil recovery at breakthrough (i.e., for water-wet systems $S_{ro_{breakthrough}} \cong S_{ro_{ultimate}}$).

The fluid distribution in a strongly oil-wet system follows an almost opposite trend to that of the strongly water-wet systems. In strongly oil-wet reservoirs, the oil phase fills the smallest pores and covers the grain surfaces, while the water phase is located in the centre of the larger pores. Primary oil recovery in these systems are reported to be the lowest, owing to a low relative permeability of the oil compared to that of water, which is explicitly a function of wettability. During a water-drive primary recovery, unlike strongly water-wet system, a non-uniform water-front would create fingers and channels, as promoted by less restricted flow of water in the centre of the larger pores whose surfaces are coated with oil (wetting phase). Hence, under the scenario depicted above, a substantial amount of oil would be left behind in smaller pores and cavities and as a film covering pore surfaces in larger pores (Erie C Donaldson and Thomas 1971). Generally, in strongly oil-wet systems, the oil recovery at water breakthrough is considerably lower than that of their strongly water-wet counterparts. However, unlike water-wet systems, the ultimate oil recovery can be substantially more than that achieved at water breakthrough (W Anderson 1987). A work by Jennings has revealed the effect of wettability on the residual oil saturation during water-flooding in a water-wet versus an oil-wet porous medium when both media were initially 100% saturated with a synthetic oil. During water-flooding experiments, the breakthrough occurred at water saturations of 75% and 53% pore volume (PV) for water-wet and oil-wet samples, respectively, which is a clear indication of the expected early water breakthrough in the oil-wet system. However, after a longer-term water-flooding, the ultimate oil recoveries were reached at comparable water saturations of 85% and 81% PV for water-wet and oil-wet systems, respectively. As concluded by Jennings, the oil recovery for the oil-wet system gradually increases with a considerable amount of water injected through the system during breakthrough times, whereas for the water wet-system, the increase in oil recovery is not appreciable once water breakthrough occurs (i.e., for oil-wet systems $S_{ro_{breakthrough}} \gg S_{ro_{ultimate}}$) (Jennings 1957).

As explained earlier, unlike strongly water- or oil-wet surfaces, a mixed-wet porous medium can have a preferential wetting tendency towards water or oil. Generally in mixed-wet reservoirs, the smallest pores remain water-wet, and the larger pores are rendered oil-wet. Since the mixed-wet porous media have the best of both strong water- and oil-wet systems, commonly, the ultimate recovery from these systems are higher (i.e., lower residual oil saturation). This is attributed to the lower amount of trapped hydrocarbon in large pores as seen in water-wet systems and lower volume of oil trapped in smaller pores as experienced in oil-wet systems (Anderson 1987). It must be noted that to achieve a low residual oil saturation in mixed-wet

systems, similar to oil-wet systems, a considerable amount of water needs to be injected into the formation after the water breakthrough to achieve the potential ultimate recovery of the field (Salathiel 1973). In an experimental study, Humphry *et al.* (2014) investigated the effect of wettability on residual oil saturation in a number of sandstone rocks with different wettability conditions. They concluded that in their experiments, as the wettability of the sandstones moved from strongly water-wet to mixed-wet, the residual oil saturation decreased from 50% to 15%. Similar outcomes were observed by other researchers who have reported higher oil recoveries for mixed-wet reservoirs compared with strongly water-wet or oil-wet systems (McDougall and Sorbie 1995; Larpudomlert *et al.* 2014; Morrow 1990; Abeysinghe *et al.* 2012).

2.3.2 Relative Permeability

In order to understand and optimise subsurface processes such as production or injection in a given fluid-rock system (e.g., a hydrocarbon reservoir), it is necessary to evaluate the multiphase flow characteristics of the system. Considering a hydrocarbon reservoir upon discovery, having high porosity and high in-situ hydrocarbon saturation may not be necessarily reflective of the high quality of the reservoir. In general, the above-mentioned properties primarily control static fluid distribution and may not (directly) control the fluid flow characteristics of the subsurface system. Instead, those petrophysical properties (e.g., permeability (k)) that control the passage and transmission of the fluid/s within the reservoir matrix and subsequently through to the production wells (or to the reservoir from injection wells) control the dynamics of the system. In 1856, Henry Darcy developed an empirical law which describes the single-phase fluid flow in a porous medium. Through experimentation, he concluded that flow rate of a fluid passed through a porous medium is proportional to the cross-sectional area and the pressure gradient across the medium and inversely proportional to the viscosity of the fluid used and the length of the medium (Figure 2.2). Darcy named the proportionality constant of his equation the permeability (k) which is described using *Darcy* as a unit (Equation (2.1)).

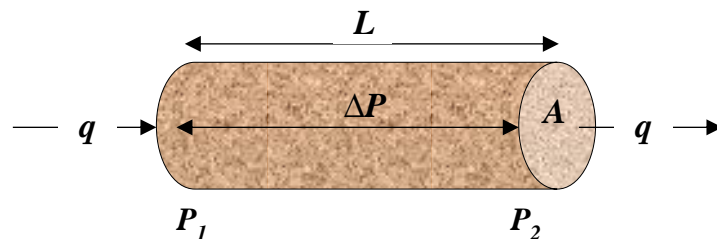


Figure 2.2. Single-phase flow through porous media (Darcy's law)

$$q = \left(\frac{k * A}{\mu * L} \right) * \Delta P \quad (2.1)$$

where q and μ are the flow rate ($\text{cm}^3 \cdot \text{s}^{-1}$) and viscosity (cP) of the fluid, respectively, A and L are the cross-sectional area (cm^2) and length of the medium (cm), respectively, ΔP is the differential pressure (atm) across the length of the medium, and k is the permeability (D) of the medium.

While Equation (2.1) appears straightforward, several assumptions need to be considered in order to apply the Darcy's law:

- The porous medium must be 100% saturated with a single incompressible fluid phase.
- The flow in the porous media must follow a laminar flow pattern.
- Steady-state flow regime must prevail.
- There must be no chemical interactions between the fluid and the surface of the pores.

As mentioned above, Darcy's Law is only applicable if the pore space of the porous medium is 100% saturated with a single fluid, and therefore k quantifies the absolute permeability of the medium. However, usually, there is more than one fluid phase (a combination of water, oil and gas) is present in any petroleum reservoir. Subsequently, Darcy's Law could not be directly applied in its simple form to describe fluid flow in such systems. Muskat *et al.* made some observations about the multiphase flow through porous media and proposed an empirical modification to the original Darcy's Law that could account for the flow of multiple immiscible fluids in the porous rock formations (Muskat *et al.* 1937). The study demonstrated that while more than one fluid phase would flow through a conductive porous space, each phase would possess its unique permeability trend, which would be a function of several factors. The above resulted in the introduction of the term *Effective permeability* (k_i , where the subscript i refers to each individual fluid, e.g., water, oil or gas), which referred to the conductivity of a porous medium to a single fluid in the presence of other immiscible fluid phase/s. Subsequently, another term was driven from the effective permeability and referred to as the *Relative permeability* (k_{ri} , where the subscript i refers to each individual fluid, e.g., water, oil or gas). The relative permeability was defined as the ratio of the effective permeability of a given fluid phase to the absolute permeability (k) of the medium. Integration of the effective permeability term into the Darcy's Law resulted in the following equation that could be used to quantify multiphase flow:

$$q_i = \left(\frac{(k * k_{ri}) * A}{\mu_i * L} \right) * \Delta P_i \quad (2.2)$$

where subscript “*i*” refers to each fluid phase (e.g., water, oil and gas) flowing through a porous medium.

In a dynamic fluid-rock system where more than one fluid is present, a number of factors affect the permeability to each individual phase. A list of such factors may include fluid saturation, interfacial tension, fluid viscosity, fluid displacement flow rate, capillary end effect, temperature, in-situ stress, flow direction, clay content and type, fluid saturation history (hysteresis) and wettability of the rock surface (Bennion *et al.* 1998; Crotti and Rosbaco 1998; Payatakes *et al.* 1996; Bennion *et al.* 1993; Chen *et al.* 1998). As stated in the previous chapter, two primary objectives of this research are to develop an effective technique to chemically alter the wettability of a rock’s pore space and then examine the effect of such wettability alteration on the multiphase flow characteristics of rock samples. Therefore, from the above-mentioned list of factors, only the effect of surface wettability on relative permeability will be discussed in more details in the following section.

Quantification and analysis of the wettability alteration of a system through relative permeability curve construction is challenging and time-consuming. Nevertheless, a number of researchers have performed core-flooding experiments under the various wettability states of a particular porous medium in an attempt to evaluate the potential relationship between the relative permeabilities of various fluid phases and the wettability tendency of the medium. Jennings (1957) measured the relative permeabilities of oil and water for a synthetic porous sample under water-wet and oil-wet conditions. His experiments were of steady-state type where water was injected into the core samples initially saturated with oil. The resultant relative permeability curves normalized for absolute rock permeability measured at 100% oil saturation are presented in Figure 2.3 (left). For a water-wet system (circular markers- black and green lines), the water endpoint relative permeability at residual oil saturation (S_{or}) is below 40% whereas, at the same S_{or} , the endpoint relative permeability of water for an oil-wet system (diamond markers- red and blue lines) is almost 80%. Furthermore, the relative permeability cross-over points for the water-wet and oil-wet systems fall at 65% and 35% water saturation, respectively. The cross-over point indicates that, for instance, in a water-wet system, for water and oil to have the same relative permeabilities, the water saturation has to be at 65%, on the other hand in an oil-wet system, a water saturation of 35% results in the same relative permeabilities for the two phases. In other words, in a water-wet system, a higher wetting phase (i.e., water) saturation is required for water and oil to flow at the same relative permeability.

The endpoint relative permeabilities (for water and oil) and the relative permeabilities cross-over points reported by Jennings (1957) are in line with the general rules specified by Craig's (1971) (Table 2.1).

Table 2.1. Craig's (1971) general rules for determining wettability from relative permeabilities

	Water-wet	Oil-wet
Initial water saturation	Usually greater than 20 to 25% PV	Generally less than 15% PV
Relative permeability cross-over point (i.e., saturation at which relative permeability for water and oil are equal)	Greater than 50% water saturation	Less than 50% water saturation
Relative permeability to water at maximum water saturation (i.e., residual oil saturation); normalized to effective oil permeability at residual water saturation	Generally less than 30%	Greater than 50% and approaches 100%

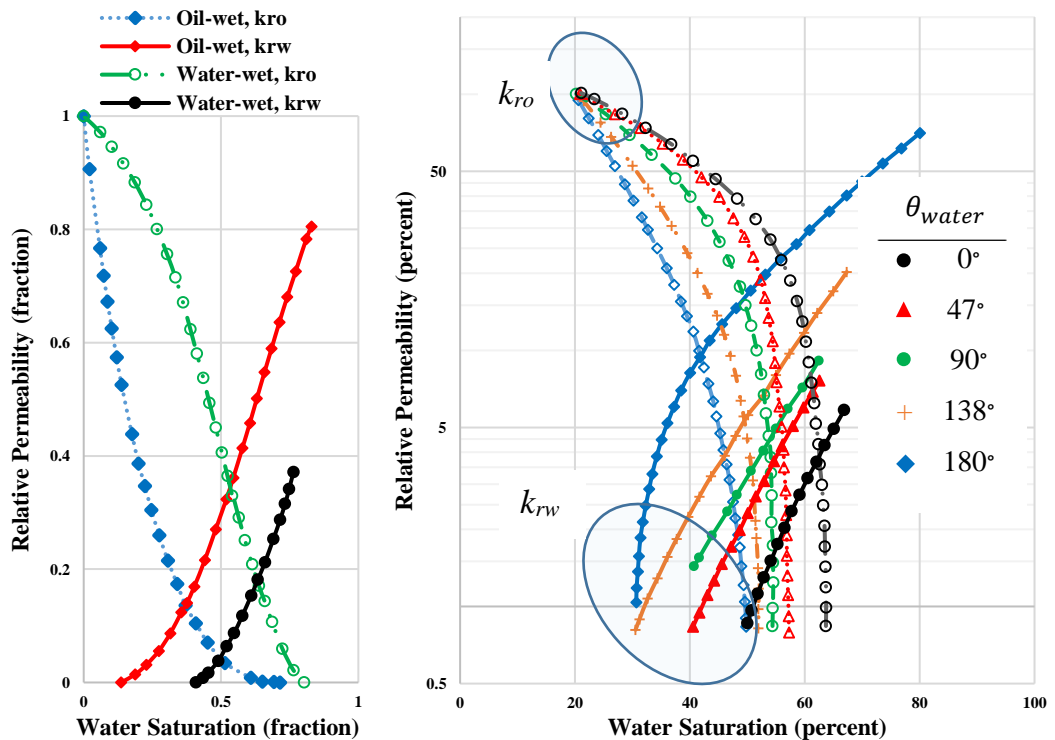


Figure 2.3. Left: Steady-state relative permeability curves for oil and water for water-wet and oil-wet systems (modified from Jennings 1957). Right: The relative permeability curves for different wettability conditions at the same initial water saturation (modified from Owens and Archer 1971)

In another study, Owens and Archer (1971) investigated the effect of wettability on the relative permeabilities of water and oil in strongly water-wet to strongly oil-wet sandstone rocks. The wettability condition of the surfaces were first evaluated through contact angle measurements, for which the water contact angles of 0° and 180° indicated strongly water- and oil-wet systems, respectively. A steady-state flooding procedure (water injection) was then performed on each sample at an irreducible water saturation (S_{wir}) of 20%. Their measured relative permeabilities are presented in Figure 2.3 (right), where, similar to Jennings, the relative permeability data were normalized to the absolute permeability of oil for each system. They concluded that as the wettability of the system varies from strongly water-wet ($\Theta = 0^\circ$ - circular marker, black lines) towards strongly oil-wet ($\Theta = 180^\circ$ diamond marker, blue lines), the relative permeability of water increases whilst the relative permeability of oil declines. Furthermore, as the rocks become more oil-wet, the cross-over point for relative permeability curves shift towards a less water saturation condition. For instance, when $\Theta = 0^\circ$, the cross-over point falls at 65% water saturation, whereas the corresponding point for $\Theta = 180^\circ$, falls at 45% water saturation.

Both of the above-mentioned studies indicated that as the wettability of a rock surface changes from strongly water-wet to strongly oil-wet, the relative permeability of water increases while the relative permeability of the oil decreases. Additionally, they indicated that, in a water-wet medium and at S_{wir} , the relative permeability of oil (non-wetting phase) could approach unity (100%). These conclusions are attributed to the particular distribution of the immiscible fluid phases within the rock pore space, which in turn is governed by the wettability of the rock. As explained in Section 2.3.1, in a water-wet medium, the wetting phase (water) fills the smallest pores and covers the grain surfaces, whereas the non-wetting phase (oil) is located in the centre of the larger pores. Subsequently, during an imbibition process (i.e., water injection), the water tends to flow through the smallest pores and close to the pore surfaces, both of which impose high restrictions on water flow. On the other hand, the oil phase moves through the centre of the largest pores feeling the least resistance to its flow. In addition, even at the end of the imbibition flood (i.e., at residual non-wetting phase (oil) saturation), the permeability of the wetting-phase (water) is still low. That is because the residual non-wetting phase is usually trapped in the centre of the large pores and induces a considerable resistance to the flow of the wetting phase. On the other hand, at the end of a drainage flood (at residual wetting-phase saturation), the non-wetting phase relative permeability approached the unity, which can be again attributed to the locations in which the wetting-phase is trapped (i.e., smallest pores and as a thin film covering grains), imposing the least resistance to the non-wetting phase flow (Owens and Archer 1971; Jennings 1957; Craig 1971; Heiba *et al.* 1983). It is worth noting that

an imbibition process is referred to the increase in wetting phase saturation, whereas the drainage process refers to the decrease in wetting phase saturation.

So far in this section, it has been demonstrated that in a water-oil-rock system, as the wettability shifts towards more oil-wet state, the water relative permeability increases while the oil relative permeability decreases. This can indicate that under dynamic conditions, if all other system parameters remain unchanged, the oil productivity (flow rate) tends to be lower in oil-wet systems compared to that for their water-wet counterparts (Agbalaka *et al.* 2008). In 1941, Leverett developed the fractional flow theory for an immiscible water flood in porous media, which is defined as the ratio of water flow rate to the total flow rate (2.3).

$$f_w = \left(\frac{q_w}{q_w + q_o} \right)_{S_w} \quad (2.3)$$

where, f_w is the water fractional flow as a function of water saturation (S_w), and q_w and q_o are the water and oil flow rates respectively. By integrating the Darcy's equation (2.2) into Equation (2.3), the following equation is obtained:

$$f_w = \left(\frac{1}{1 + \frac{\mu_w}{\mu_o} * \frac{k_{ro}}{k_{rw}}} \right)_{S_w} \quad (2.4)$$

where, μ_w and μ_o are the viscosity (cP) of water and oil, respectively, and k_{rw} and k_{ro} are also the relative permeability of water and oil, respectively. Therefore, Equation (2.4) is a function of viscosity ratio, the relative permeabilities of the immiscible fluid phases and the water saturation at any given time. As indicated earlier, the relative permeability is an explicit function of saturation and an implicit function of wettability condition of a porous medium, subsequently, the fractional flow becomes an implicit function of the wettability state of the rock formation (Anderson 1987; Agbalaka *et al.* 2008). Assuming the viscosity ratio of the fluids remains unchanged, the fractional flow is essentially controlled by the wettability condition of the rock. A graphical demonstration of water fractional flow for a constant viscosity ratio and variable wettability conditions is presented in Figure 2.4. Welge (1951), demonstrated that the point of tangency for a tangent line drawn from S_{wir} to the water fractional flow curve corresponds to the water fractional flow encountered at water breakthrough and the shock-front water saturation (the water saturation seen at the

production side of the system at the time of breakthrough). For instance, considering the curve for the water-wet system (blue curve), the tangent line intersects the curve at water saturation of 60%. At this point, the water fractional flow is as high as 78%. On the other hand, for the oil-wet system (red curve), the tangent intersects the curve at 26% water saturation and corresponds to 57% water fractional flow at breakthrough. Referring back to Equation (2.4), if the viscosity ratio is kept constant, and the wettability of the rock shifts towards a more oil-wet condition, the relative permeability of oil would be reduced while the relative permeability of water would improve, and subsequently, the water fractional flow would increase. Such effects tend to create an unstable flood front and result in an early breakthrough of water in oil-wet reservoirs (Agbalaka *et al.* 2008; McDougall and Sorbie 1995).

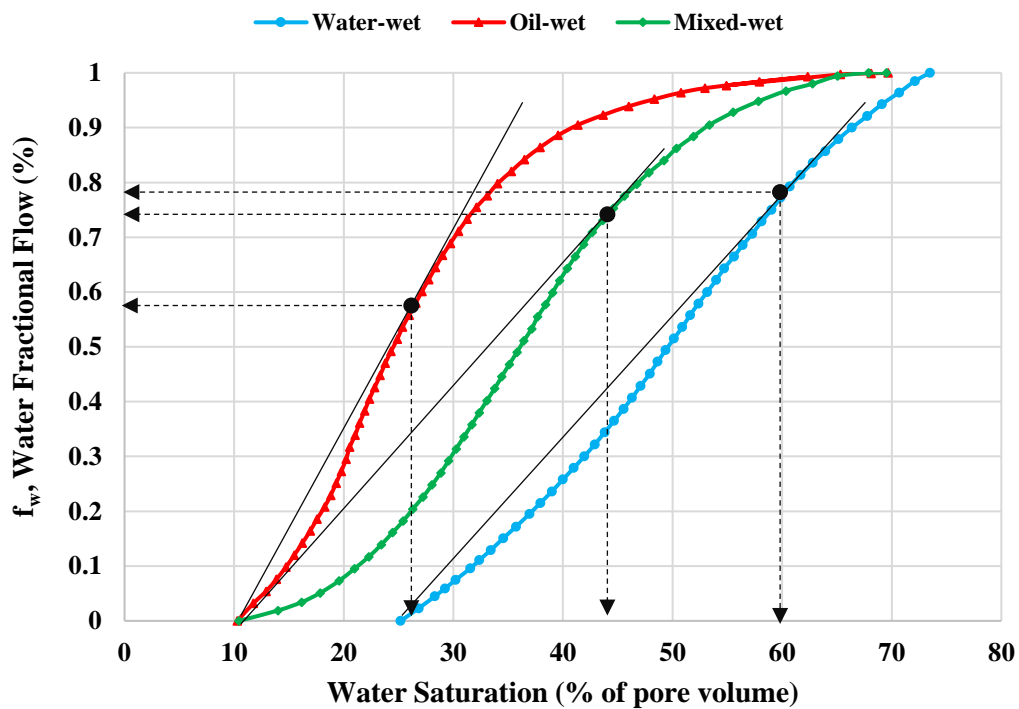


Figure 2.4. Effect of wettability on water fractional flow at constant viscosity ratio. Water-wet (blue curve), oil-wet (red curve) and mixed-wet (green curve). (modified from, Ahmed 2001). The tangent lines drawn from S_{wir} to the water fractional flow curves corresponds to the water fractional flow encountered at water break through and the shock-front water saturation.

2.3.3 Capillary Pressure

Capillary pressure (P_c) is defined as the discontinuity in pressure at the interface of two immiscible fluids that are in contact. This parameter is dependent on the curvature of the interface between the two fluids (governed by the wettability and interfacial tension) and their

saturations. In porous media, the capillary forces are directly influenced by pore geometry, interfacial and surface tensions of the fluids and the surface, and the wetting tendency of the pore surface. In such media, in order for an invading non-wetting fluid to displace the defending wetting fluid, the pressure in the non-wetting fluid is required to be larger than that of the wetting phase by an amount equal to P_c . In general, the balance between these forces is responsible for the capillary rise or depression of the fluids inside a capillary tube (Anderson 1987).

Accordingly, the capillary pressure in the simplest form can be demonstrated by the following equation:

$$P_c = P_{nw} - P_w \quad (2.5)$$

where, P_{nw} and P_w are the non-wetting and wetting phase pressures, respectively. The capillary pressure can also be defined by the well-known Laplace equation:

$$P_c = P_{nw} - P_w = \frac{2\sigma_{nw,w} \cos \theta}{R} \quad (2.6)$$

where:

- $\sigma_{nw,w}$ = interfacial tension (IFT) between non-wetting and wetting fluids
- θ = the measured contact angle of wetting phase and surface
- R = the effective pore radius

It must be noted that Equation (2.6) is applicable for a single capillary tube with a defined diameter. However, in a rock formation, various pore throat diameters may be present, and subsequently, a porous rock may be considered as a bundle of capillary tubes (Purcell 1949). Therefore, since every given pore throat size would have a particular capillary force (assuming all the other parameters such as fluid saturation, IFT, wettability, etc. remaining constant), a complete desaturation capillary curve is required to fully characterize the capillarity of the porous rock (Humphry *et al.* 2014). As per Equation (2.6), assuming the interfacial tension between the immiscible fluids and pore throat sizes of a rock remain unchanged, an alteration of the wettability state of the reservoir rock (contact angle) may have a pronounced effect on the distribution of fluids within the reservoir. Figure 2.5 demonstrates the shift in the capillary pressure curve for a water-air-sandstone system when wettability changes from a strongly

water-wet (blue lines) to a weakly water-wet (red lines) state. Furthermore, from a qualitative point of view, Figure 2.5 demonstrate the potential differences between the imbibition (solid lines) and drainage (dashed lines) capillary pressure curves of a fluid-rock system. The following additional points may be inferred from the capillary pressure curves presented in Figure 2.5, (Ahmed 2001):

- ***Drainage curves (solid lines):***
 - At 100% water saturation, for the strongly water-wet system, the minimum pressure required for the non-wetting phase to enter the largest pore throat is considerably larger compared to the weakly water-wet system. This minimum capillary pressure is referred to as capillary entry pressure or displacement pressure (P_d).
 - In general, for any given saturation of the wetting fluid, in a strongly water-wet system, the pressure required for the non-wetting phase to drain-out the wetting phase is higher compared to that for the weakly water-wet system. This difference becomes more pronounced towards higher values of capillary pressure corresponding to smaller pore sizes. Hence the curvature of the capillary pressure curve is less for the weakly water-wet system.
 - Towards the end of the drainage process, any increase in the capillary pressure does not contribute to any further water saturation reduction, and the curve approaches vertical asymptote. This point corresponds to the irreducible water saturation. The irreducible water saturation for the weakly water-wet system is lower than that for the strongly water-wet system. This is attributed to the ability of the non-wetting fluid to invade smaller pores and expel water from them under a weakly water-wet state.

- ***Imbibition curves (dashed lines):***
 - During the imbibition process (i.e., increase in water saturation with decrease in the capillary pressure), for the strongly water-wet system, the water saturation increases considerably for a small decrease in capillary pressure, whereas in the weakly water-wet system, this increase is more subtle (steeper overall slope in a weakly water-wet system). This is attributed to the affinity of the strongly water-wet system to imbibe water spontaneously due to higher capillary forces.

- When the capillary pressure reaches zero, the water saturation is higher for a strongly water-wet system compared to a weakly water-wet system. This is due to the ability of water to imbibe inside the smallest pores and expel the air, whereas, in a weakly water-wet system, water may not penetrate the smallest air-filled pores, subsequently, resulting in lower water saturation.

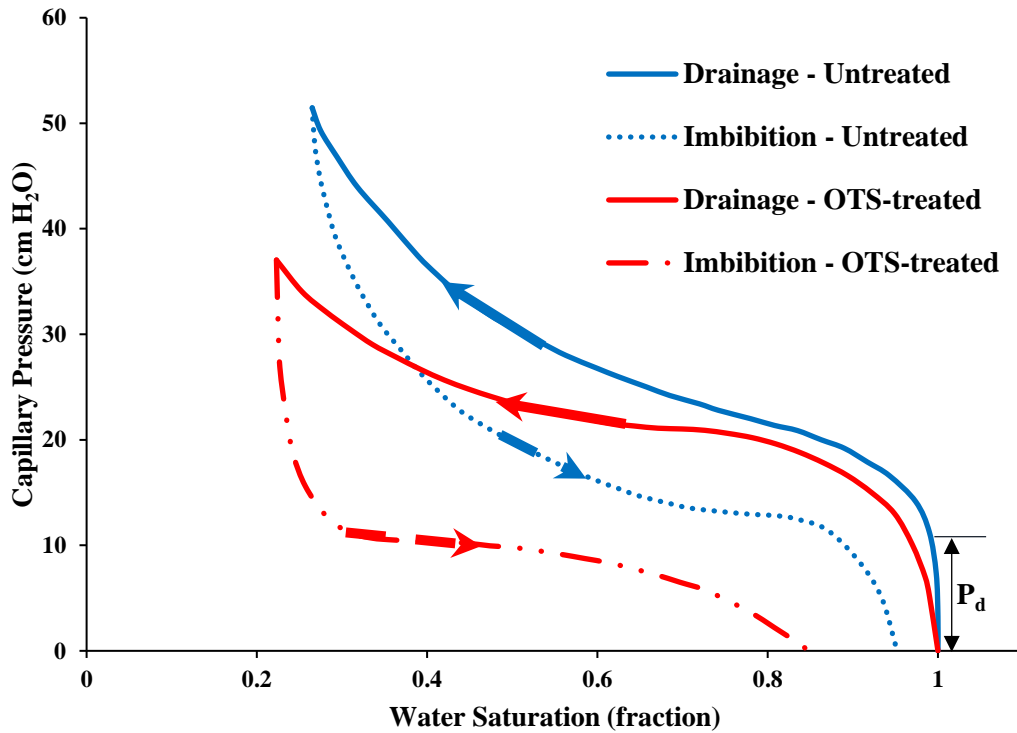


Figure 2.5. Capillary desaturation curves during drainage (solid lines) and imbibition (dashed lines) processes for air-water system. Strongly water-wet system (blue) and weakly water-wet (red lines) systems (modified from Bradford and Leij 1995).

2.4 Wettability Evaluation Techniques

As mentioned earlier, the wettability of a reservoir rock has a considerable impact on the multiphase flow characteristics of the formation, including the fluid phase saturation distribution, relative permeability, capillary pressures, etc. Therefore, an accurate evaluation of the wettability state of a rock formation under representative conditions is an essential element of the reservoir characterization process. The above has led to the development of a number of qualitative/quantitative approaches and techniques to assess this surface property. The current section of this chapter provides a brief outline of the most common techniques used to evaluate the wettability of solids in general surface or porous structure.

2.4.1 Contact Angle Method

Contact angle measurement is one of the most widely utilized quantitative technique in wettability evaluation of a solid substrate. This method can accommodate for experiments conducted under high pressure and temperature, which is especially important for deep geological systems containing gas-liquid-solid configuration such as hydrocarbon reservoirs and CO₂ geosequestration sites (William Anderson 1986). In addition, contact angle measurements have been extensively applied to analyse the effect of pressure, temperature and fluids' chemistry on the wettability of rock surface (Shojai Kaveh *et al.* 2012; 2014; Arif *et al.* 2015; Al-Yaseri *et al.* 2016). To date, a number of contact angle measurements techniques have been introduced, out of which, the sessile drop and captive drop are the most widely utilized methods in petroleum industry (Mccaffery and Mungan 1970; A.W. and R.J. 1979; William Anderson 1986).

Contact angle measurements of a three-phase vapour-liquid-solid system is a function of three interfacial tensions (Figure 2.6) as first presented by Young's equation:

$$\cos \theta_Y = \frac{(\sigma_{sv} - \sigma_{sl})}{\sigma_{lv}} \quad (2.7)$$

where, σ_{sv} , σ_{sl} and σ_{lv} represent the solid-vapour, solid-liquid and liquid-vapour interfacial tensions, respectively and θ_Y is the Young's contact angle (Figure 2.6). Theoretically, the above relationship implies that the contact angle is based on the force balanced between the solid and the liquid drop at the triple-phase contact line, where the forces in question are generated from the interfacial and surface tensions between the phases in contact (Packham 2005). In addition, the adhesion force which is the product of $\sigma_{lv} * \cos \theta_Y$ can be used to calculate the capillary number (Equation (2.8)) which is an important parameter in evaluation of the relative permeability and residual saturations during multiphase flow in a porous medium (Anderson 1986; D. Yang *et al.* 2008).

$$N_{ca} = \frac{\mu v}{\sigma_{lv} * \cos \theta_Y} \quad (2.8)$$

Where, v is the velocity of the injected fluid.

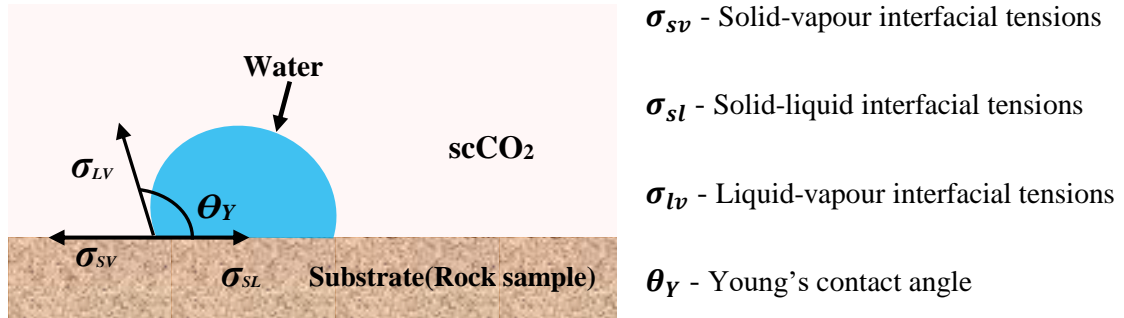


Figure 2.6. Schematic of force field acting on a three-phase substrate-water-scCO₂ system

Although the contact angle measurement is one of the most commonly utilized techniques in wettability evaluation, a number of factors may affect the accuracy of this technique such as surface chemical heterogeneity (Brandon and Marmur 1996), surface roughness (Eick *et al.* 1975), surface contamination (Iglauer *et al.* 2014) and adsorption/desorption of liquid molecules (Carré *et al.* 1996). Practically, some degree of roughness is present on all surfaces, which results in creating non-equivalent advancing (θ_a) and receding (θ_r) contact angles on a test surface (Kwok and Neumann 1999). The difference between θ_a and θ_r is termed the contact angle hysteresis (H). To reduce the effect of the hysteresis on measured contact angle data (i.e., reducing hysteresis), well-polished and homogeneous surfaces such as pure minerals (e.g., mica, calcite, etc.) are used which may be good representatives of actual lithology of rock formations (Morrow 1990; D. Yang *et al.* 2008). The measured contact angle on such surfaces is termed “*apparent contact angle*” which represents the average wettability state of a real specimen (Anderson 1986; Lin *et al.* 1993)

As demonstrated in Figure 2.6, within a multiphase test condition, generally, the Young's contact angle is measured through the denser phase, which corresponds to the wettability of the given substrate. In a brine-rock-CO₂ system, the rock is strongly water-wet for $\theta_Y < 50^\circ$, weakly water-wet for $50^\circ < \theta_Y < 70^\circ$, intermediate-wet for $70^\circ < \theta_Y < 110^\circ$, weakly CO₂-wet for $110^\circ < \theta_Y < 130^\circ$ and strongly CO₂-wet for $130^\circ < \theta_Y < 180^\circ$ (Iglauer and Pentland 2017).

2.4.2 Amott Method

Another most commonly practiced quantitative measurement techniques to evaluate the wettability of a porous medium is the Amott test (Amott 1958). In this technique, two fluids of interest are sequentially displaced through forced and spontaneous displacement in a porous rock in the following order (assuming an oil-water fluid system and that the rock core plug is initially 100% saturated with water):

- Forced displacement of water from pore space by oil (using a centrifuge or forced injection in a Hassler core-holder), until initial water saturation is reached (Primary drainage-forced)
- Spontaneous imbibition of water to displace the oil (Primary imbibition-spontaneous)
- Forced displacement of oil by water through centrifuge or forced injection (Primary imbibition-forced)
- Spontaneous drainage of oil to displace water (Secondary drainage-spontaneous)
- Forced displacement of water by oil (Secondary drainage-forced)

It is worth noting that some of the technical terminology used in the above procedure and Figure 2.7 assumes that the rock is water-wet; however, the overall general procedure outlined and subsequent analysis of the experimental results as presented shortly remain valid regardless.

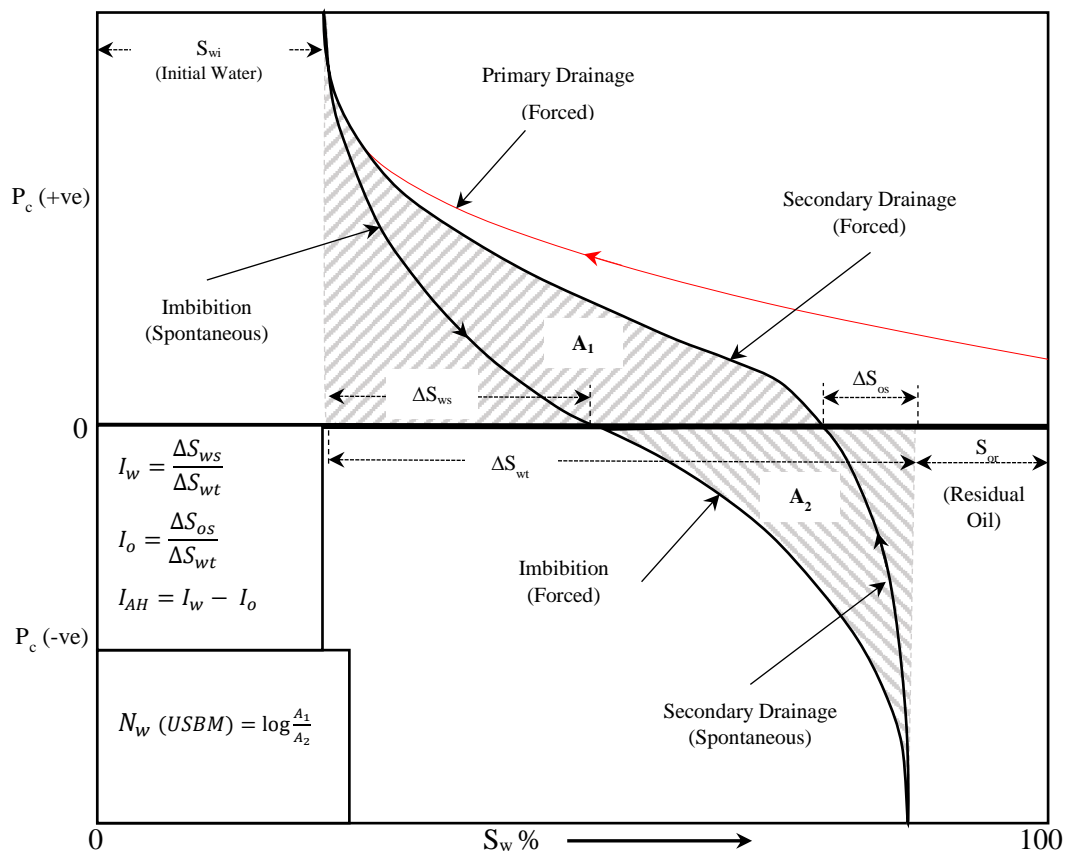


Figure 2.7. Capillary pressure (P_c) versus water saturation (S_w) curves as measured during an Amott test (modified from Morrow 1990). This graph will also be used to describe USBM technique in following Section 2.4.3.

The amount of fluids produced and the corresponding capillary pressure during each step is measured periodically, so the wettability condition of the porous medium can be evaluated. The wettability indices to water (I_w) and oil (I_o) are then calculated from the following equations:

$$I_w = \frac{\Delta S_{ws}}{\Delta S_{wt}} \quad (2.9)$$

$$I_o = \frac{\Delta S_{os}}{\Delta S_{wt}} \quad (2.10)$$

where, ΔS_{ws} and ΔS_{os} are the spontaneous changes in water and oil saturation, respectively, and ΔS_{wt} is the total change in the water saturation within the rock through both spontaneous and forced displacements (Morrow 1990). The Amott indices indicate that the rock is strongly water-wet when $I_w = 1$ and $I_o = 0$, and strongly oil-wet when $I_w = 0$ and $I_o = 1$. A major drawback of Amott test is its insensitivity towards mixed/neutral wettability conditions, in which case, a modified version can be applied to overcome this problem. The Amott-Harvey index (I_{AH}) was introduced to express the wettability of the rock with a single value ranging from -1 to +1 by combining the I_w and I_o as follows:

$$I_{AH} = I_w - I_o \quad (2.11)$$

Subsequently, based on the Amott-Harvey index (Equation (2.11)), the rock is considered to be:

- Water-wet when $0.3 \leq I_{AH} \leq 1.0$
- Weakly water-wet when $0 \leq I_{AH} \leq 0.3$
- Weakly oil-wet when $-0.3 \leq I_{AH} \leq 0$
- Oil-wet when $-1 \leq I_{AH} \leq -0.3$

One other major issue with the Amott test is its potentially time consuming spontaneous displacements, making the overall test to take substantially longer time to complete compared with the contact angle measurement technique.

2.4.3 USBM Method

The USBM (U.S. Bureau of Mines) method is another quantitative measurement technique which is widely applied for rock wettability assessment (Donaldson *et al.* 1969). Similar to the

Amott test, wettability measurement using the USBM method consists of consecutive drainage and imbibition cycles in a similar fashion to that depicted in Figure 2.7 (both spontaneous and forced processes). In this technique, the work required to displace the wetting or non-wetting fluid phases from the pore space is analysed. During the drainage process, initially, the sample at its initial water (wetting phase) saturation (S_{wi}) is immersed in an Amott cell filled with oil (non-wetting phase) and subjected to spontaneous imbibition. Subsequently, the sample is placed inside a sample-holder filled with oil and subjected to forced phase displacement in a centrifuge with an incremental increase in speed (i.e., increased force). From the forced displacement, capillary pressure data are obtained, and finally, the work required for water displacement by oil is measured from the area under the curve (Figure 2.7 – A_1). Similar procedures are then repeated during imbibition steps, where, the oil and water are displaced and displacing fluids, respectively. The area under the imbibition curve (A_2) indicates the work required for water to displace oil in the system (Figure 2.7). Finally, the logarithm of the ratio between the areas under the capillary pressure curves define the USBM wettability number (N_{USBM}):

$$N_{(USBM)} = \log \frac{A_1}{A_2} \quad (2.12)$$

Subsequently, the wettability of the system from the USBM number is characterized as follows:

- If $N_{USBM} > 0$, the system is water-wet
- If $N_{USBM} < 0$, the system is oil-wet
- If $N_{USBM} \approx 0$, the system is near neutral-wet

The main advantage of the USBM technique over the Amott test is its demonstrated sensitivity for near neutral-wettability systems; however, since similar to the Amott test the samples are subjected to high centrifugal force, only consolidated cores samples can be tested in this technique, which limits the application of the USBM test (Anderson 1986).

2.4.4 Spontaneous Imbibition

Spontaneous imbibition (SI) is an indirect method for evaluating the wettability of a system based on the rate of imbibition of fluids or the total amount of fluids imbibed into a porous medium. The above is based on the fact that the spontaneous imbibition is controlled by the capillary pressure and largely influenced by wettability (Zhang *et al.* 2007). Depending on the

expected wettability state of a core sample, the spontaneous displacement test is performed by either immersing the oil (or gas) saturated core sample in water, or the water saturated core in oil (or gas). The amount and rate of fluid displaced is then measured and plotted against time to evaluate wettability (Xie and Morrow 2001). The amount and rate of imbibition depend on a number of parameters, including rock wettability, interfacial tension (IFT), and saturation history (MA *et al.* 1999). According to the accepted conventions, in a strongly water-wet system, capillary pressure is considered positive, and water would imbibe into the rock until residual non-wetting saturation (S_{nwr}) is reached. In contrast, the capillary pressure is considered negative when the rock is strongly non-water-wet (e.g., oil-wet), hence oil would spontaneously imbibe into the rock and displace water in the test (Tiab and Donaldson 2012).

The advantage of this technique over the Amott and USBM test is evident, knowing that both of the mentioned methods have limited applicability if the wettability of the system falls within a certain range. The Amott method does not appropriately distinguish between the systems with high wettability index, and collectively describes the system as strongly water-wet. Additionally, this test tends to be insensitive for near-neutral wettability formation (Anderson 1986). In the USBM test, the residual oil saturation achieved through spontaneous imbibition is not recognised (MA *et al.* 1999). In spontaneous imbibition experiments, appropriate wettability characterization can be achieved through both the rate and the amount of fluid produced during the earlier period of recovery (MA *et al.* 1999).

2.4.5 Other Techniques

Multiphase flow characteristics analysis of a fluid-rock system can provide a qualitative assessment of wettability state of a given formation. As explained in Section 2.3.2, for example, the relative permeabilities are heavily and directly influenced by the wettability (Iglauer *et al.* 2017). For instance, as discussed before, in a water-oil-rock system, where water and oil are wetting and non-wetting phases, respectively, the relative permeability to water increases as the system shifts towards less water-wetting state while the relative permeability to oil phase (the non-wetting phase) decreases as demonstrated in Figure 2.3 (Jennings 1957; Craig 1971).

2.5 Wettability of Sandstone Rocks

As mentioned earlier (Section 2.2), in general, sandstone reservoirs are considered to be strongly water-wet. The pore space of this reservoir rock would be in equilibrium with the formation brine for a prolonged period of time prior to the migration of hydrocarbon phase to its pore space (in case of a hydrocarbon bearing reservoir); consequently, the rock surface tends to be hydrophilic (Kyte *et al.* 1961). Once the hydrocarbon migrates into the previously brine

filled formation, a number of interactions might take place, which may result in naturally occurring wettability alteration of the pore space towards a less water-wetting state. Parameters such as brine pH and salinity, acid/base number of formation fluids, hydrocarbon components, and rock mineralogy (e.g., clay content) may have a considerable effect on the eventual wettability condition of a sandstone formation (Xie *et al.* 2002; Buckley *et al.* 1996; Buckley and Liu 1998; Liu and Buckley 1999). Buckley and Liu (1998) proposed four main mechanisms which explain the possible interactions of water-oil-rock systems and their effect on the wettability of sandstone rocks: polar interactions, surface precipitation, acid/base interactions, and ionic bonding. Polar interactions can occur on a clean surface through the interactions of the polar components of the oil and the surface. Surface precipitation can occur when the oil is unable to keep its heavy components (e.g., asphaltenes) in solution, and subsequently, they may precipitate and cover the rock surface. Commonly, a more oil-wet rock condition is attributed to the heavier component of the crude oil (Denekas *et al.* 1959). Wettability alteration through acid/base interactions can occur in systems where the hydrocarbon possesses low acid numbers and high base numbers, whereas, ionic bond interactions take place if the hydrocarbon possesses low base numbers and high acid numbers (Buckley *et al.* 1996). The wettability alteration through these techniques is achieved by reducing the water film stability on the rock pore surfaces.

Wettability state of a sandstone formation may be of great interest for subsurface processes that do not involve a hydrocarbon phase, such as CO₂ geosequestration in deep aquifers. Deep saline aquifers are known to be good candidates for CO₂ geosequestration (Bikkina 2011). A number of studies have investigated the wettability condition of brine-CO₂-sandstone systems and concluded that generally, in the presence of CO₂, sandstone formations tend to be strongly hydrophilic and in some cases weakly water-wet. Krevor *et al.* (2012) investigated the trapping capacity of sandstone formations through relative permeability analysis of brine-CO₂-rock system and concluded that such systems would be good candidates for CO₂ geosequestration because they demonstrate strong water-wetting tendency. Their founding was further confirmed by Pini *et al.* (2012), who also demonstrated the water-wetting tendency of sandstone formations in the presence of CO₂. However, they indicated that as the pressure increases, the rock wettability diverts towards weakly hydrophilic, which was attributed to the reduction in the interfacial tension (IFT) between the fluid phases (Georgiadis *et al.* 2011). Chiquet *et al.* (2007) studied the wettability alteration of caprock towards weakly water-wet in the presence of CO₂ and attributed this effect to the reduction of brine pH due to dissolution of CO₂ in brine at elevated pressures. Subsequently, the increased brine acidity contributed to the reduction of the electrostatic attraction and stability of water film on the sandstone surface, thus impacting the interfacial repulsion between phases (McGrail and Schaef 2005; Sharma and Yen 1984).

Effect of ionic strength on the wettability of silica surfaces has also been investigated (Jung and Wan 2012). This study concluded that the wettability for silica diverts from strongly water-wet state ($\theta \approx 0^\circ$) for pure water, to a less water-wet condition ($\theta \approx 19.6 \pm 2.1^\circ$) when 5 mol of NaCl was used to prepare the brine. In another research, Chalbaud *et al.* (2009) demonstrated that the ionic strength has a direct effect on the interfacial tension between brine and CO₂, which can potentially impact the wettability of the rock formation. Sandstone formations owe their water-wetness tendency to the presence of surface silicon dioxide (SiO₂). Quartz, which is one of the polymorphs of silicon dioxide, constitutes a majority of sandstone's mineralogy, and once exposed to water, hydroxyl (-OH) groups can be generated with concentrations ranging from 0 to 4.6 OH/nm² (Zhuravlev 2000). The wettability of a sandstone formation is proportionally influenced by the concentration of the surface hydroxyl groups due to its high polarity nature, subsequently, the surface becomes more water-wet with increased concentrations of this species on the rock surface (Iglauer *et al.* 2017).

2.6 Wettability Alteration by Chemical Treatment

One of the areas of interest in the oil and gas industry is wettability alteration of reservoir rocks to render the rock surface wettability to accommodate for an intended requirement. For instance, in enhanced oil recovery (EOR) it is more favourable if the rock surface is more water-wet rather than oil-wet (Morrow 1990; Ravari *et al.* 2011; Sari *et al.* 2017; Nwidae *et al.* 2017). Similarly, in CO₂ geosequestration applications, a more water-wet rock formation can provide improved residual CO₂ trapping. Furthermore, a water-wet caprock would provide a superior sealing in a CO₂ geosequestration site, hence improving the structural trapping mechanism of CO₂ (Al-Khdheawi *et al.* 2017; Iglauer and Pentland 2017). In some cases, it is more favourable to render the rock formation from a lyophilic state to more gas-wetting conditions. For instance, in gas reservoirs which suffer from water blockage or hydrocarbon condensate banking, the gas flow rate would dramatically be reduced, impacting on the well deliverability substantially (McCain and Alexander 1992; Barnum *et al.* 1995). In the case of the absence of favourable wettability state for the above-mentioned situations, if feasible, wettability alteration may be an option to consider. The following sections outline a number of chemicals and techniques used to render the wettability of rock surfaces for various applications.

2.6.1 Surfactant Application

Surfactants are amphiphilic molecules (containing both hydrophilic and hydrophobic moieties) composed of a polar group (ionic or nonionic) and hydrophobic chains (usually alkyl chains) (Pinazo *et al.* 2019). Surfactants are used in various applications and processes, owing to their dual molecular structure, which makes them active at interfaces. These compounds have

been extensively investigated in oil and gas industries, and have demonstrated promising applications in EOR for hydrocarbon producing fields with high trapped oil saturation (e.g., oil-wet formations). It has been revealed that reduction in IFT and wettability alteration (from oil-wet to more water-wet state) are the two main mechanisms behind the effectiveness of surfactants as EOR agents (Chegenizadeh *et al.* 2017; Standnes and Austad 2000; Giraldo *et al.* 2013). The efficiency of a surfactant application in achieving its objectives is influenced by a number of factors of which the most dominant are, the surfactant classifications/types (anionic, cationic, nonionic, biosurfactant and zwitterionic surfactants), the solvent used in surfactant preparation, native fluids characteristics (e.g., reservoir's brine salinity, hydrocarbon characteristics), operational conditions (pressure and temperature), surfactant concentration, and the chemical characteristics of the reservoirs rock (Chegenizadeh *et al.* 2017; Gupta and Mohanty 2010; Schramm 2000; Karnanda *et al.* 2013).

2.6.2 Low Salinity Flooding

Low salinity water injection (*LSWI*) has become one of the major research areas in EOR for both sandstone and carbonate reservoirs, because of its added advantages over conventional seawater or formation water injection. *LSWI* has attracted the attention of field operators because of its affordability, availability, ease of injection in the oil bearing zones, minimal capital and operational costs and proven applicability to displace medium to high *API* crude oil with high efficiency. To date, a number of possible mechanisms associated with *LSWI* have been proposed by researchers, which generally constitute fluid-fluid and rock-fluid interactions (Al-Shalabi and Sepehrnoori 2016). Wettability alteration has been proposed as the main EOR mechanism during *LSWI* in carbonate rocks. It has been demonstrated that the electrical double layer expansion caused by multi-ion exchange (MIE) during *LSWI* contributes to wettability alteration of carbonate rocks (Strand *et al.* 2003; Yousef *et al.* 2012; Sari *et al.* 2019). In sandstone formations, researchers have proposed that during *LSWI*, multi-ion exchange, salt-in effect, pH effect and fines migration are the main mechanisms contributing to the increased oil recovery (Lager *et al.* 2008; Rezaeidoust *et al.* 2009; Austad *et al.* 2010; Bernard 1967; Alotaibi and Nasr-El-Din 2009).

2.6.3 Nanoparticle Treatment

Nanoparticles (NPs) have attracted significant attention of researchers in oil and gas industry because of their properties. Nanoparticles come in diverse chemical composition, surface area, shape and size (Oberdörster *et al.* 2005). Depending on their chemical composition, and the surfactant used to create the nano-fluids, they can be hydrophilic, hydrophobic or lyophobic, making them attractive for various applications (Nel *et al.* 2009). Nanoparticles have found

applications in a number of subsurface processes including the CO₂ geosequestration, viscosity and interfacial tension control during heavy oil recovery, drilling fluid optimization and wettability alteration of hydrocarbon reservoirs (Al-Anssari *et al.* 2017; Al-Anssari *et al.* 2017a; LI *et al.* 2007; Ponmani *et al.* 2016; Jin *et al.* 2017; Zhang *et al.* 2016). During the nanoparticle treatment of a porous structure, it has been proposed that five phenomena may take place including nanoparticle transportation, adsorption, desorption, aggregation and blocking (Li and Torsaeter 2015). Once the nanoparticles arrive at deposition sites (pore surfaces), forces such as double-layer and London-van der Waals would assist with their adsorption/desorption (Lecoanet *et al.* 2004). In the context of surface wettability alteration, the efficiency of a nanoparticle treatment depends on a number of factors including, solid surface chemistry, nanoparticle characteristics, and operational conditions such as temperature, pressure and deposition aging time (Täuber *et al.* 2013; Moghaddam *et al.* 2015; Al-Anssari *et al.* 2016; Zhang *et al.* 2015).

2.6.4 Fluorinated Chemical Application

Fluorinated chemicals are synthetic compounds of organic chemicals in which the hydrogen atoms (or alkyl tails) are substituted by halogen fluorine tails, which results in the production of fluorinated hydrophobes (Craddock 2018). These chemicals have been applied to alter the wettability of reservoir rocks. They can be used in the form of fluorinated surfactants, polymers, polymeric surfactant, or nanoparticles fluorinated surfactants (Li and Firoozabadi 2000; Fahes and Firoozabadi 2007; Murphy and Hewat 2008; Mousavi *et al.* 2013; Karandish *et al.* 2015; Naghizadeh *et al.* 2020). In the context of wettability alteration of solid surfaces such as the rock pore surfaces, it is well understood that such treated surfaces owe their wettability shift to the very low surface free energy induced by the fluorinated chemicals (Huang *et al.* 2004), making the surfaces to be more lyophobic. A number of researches have shown that the treatment of the near wellbore region with fluorinated chemicals in gas reservoirs which suffer from water blockage or condensate banking can result in significant well productivity improvement (Zhang *et al.* 2014; Lee *et al.* 2008). Wang *et al.* (2015) investigated the effectiveness of wettability alteration of sandstone rocks from liquid-wetting to preferentially gas-wetting state by applying a number of fluorinated surfactants at elevated temperature. They concluded that the wettability alteration of the lyophilic pore space towards preferentially gas-wetting was strongly influenced by the reduced surface free energy from 70 to 3.29 mN/m. Despite the promising application of fluorinated chemicals in EOR and production optimisation, there are a number of concerns associated with their use. Fluorinated chemicals persist in the environment, due to the strong chemical bonding between the fluorine and carbon atoms, subsequently, the chemical stability of their molecule tends to be very high, making them highly

resistive to biodegradation (Stahl *et al.* 2011). Subsequently, fluorinated chemicals pose a threat to the environment and human health. Furthermore, synthesising fluorinated compounds are known to be expensive and may not be cost-effective in many applications (Li *et al.* 2011; Craddock 2018).

2.6.5 Silylation

Silylation process is one of the most commonly applied surface modification techniques. This process takes place when active hydrogen of an organic or inorganic molecule is substituted by a silyl group (R_3Si-) from a silane agent (Roth 1972). The active hydrogen groups from the test substrates are usually classified as $-OH$ (phenol, alcohol, carboxylic acid), $-SH$ (thiol) or $-NH$ (urea, amine, amide). In general, organosilanes are presented in the form of R_nSiX_{4-n} , where, R is the non-hydrolysable organic group which possesses the functionality, and X is either a halogen, alkoxy, acyloxy, or amino group (Combes *et al.* 1999b; Pape 2006). Mechanistically, during surface treatment, the X group containing hydrolysable group undergoes hydrolysis as triggered by the water present in either the applied solvent, water moisture in the test environment or the adsorbed water on the treated substrate's surface. The hydrolysis process creates hydroxyl moieties ($-OH$) in the silylation agent which can then react with the hydroxyl groups (e.g., surface silanol groups ($Si-OH$) on hydrolysed quartz surfaces) on the substrate to create strong covalent bonds with concomitant water creation ($Si-O-Si + H_2O$). Subsequently, the R group (silanes' functional group) extended from the surface impart the physical and chemical functionality based on the required application (Tripp and Hair 1993; Voort and Vansant 1996; Arkles *et al.* 2014). A simplified depiction of the mechanisms involved during the silylation process on a quartz (SiO_2) surface is presented in Figure 2.8.

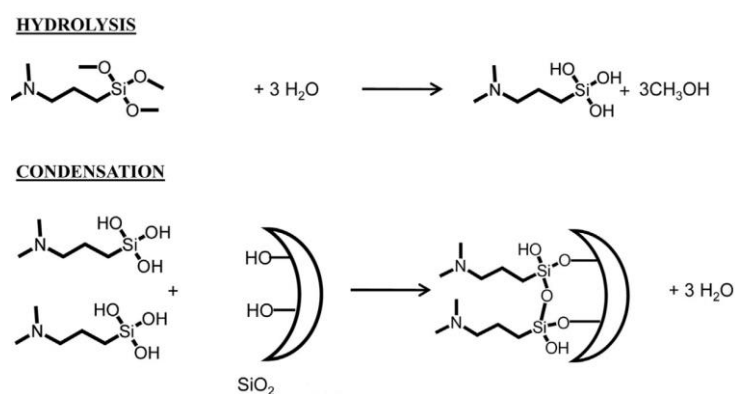


Figure 2.8. Simplified mechanism of silylation reaction (modified from Sánchez-Vicente *et al.* 2014)

It's worth noting that the surface silylation may be accompanied by a number of other side processes. For instance, the condensation of organosilanes molecules on the substrate and self-

assembled polymerization (oligomers creation) within the silane solution may occur prior or during the hydrolysis and silane's chemical bonding to the surface (Tripp and Hair 1993; Arkles *et al.* 2014). Self-assembled polymerization occurs when the adjacent silane molecules interact and form a monolayer on the surface of the test substrate prior to surface reactions. A number of factors such as the amount of water present during the silylation process, selected solvent, and the silylation agent's characteristics affect the competition between self-assembled polymerization and the surface reactions; subsequently, it is essential to consider all of these variables prior to the surface treatment (Ulman 1996; Voort and Vansant 1996; Sánchez-Vicente *et al.* 2014).

The surface groups of the test substrate also play an important role in controlling the silylation efficiency. In general, organosilanes can create stable bonds with the oxide of inorganic materials. For instance, oxides of materials such as silicon, aluminium and copper can create strong bonds with the silylation agents, whereas the reaction of silanes with materials such as lead and carbon is considerably lower. This behaviour highlights the importance of the surface hydroxyl groups in the silylation process. Figure 2.9 provides a guide on the effectiveness level of silylation reactions on various inorganic material (Sanli and Erkey 2015).

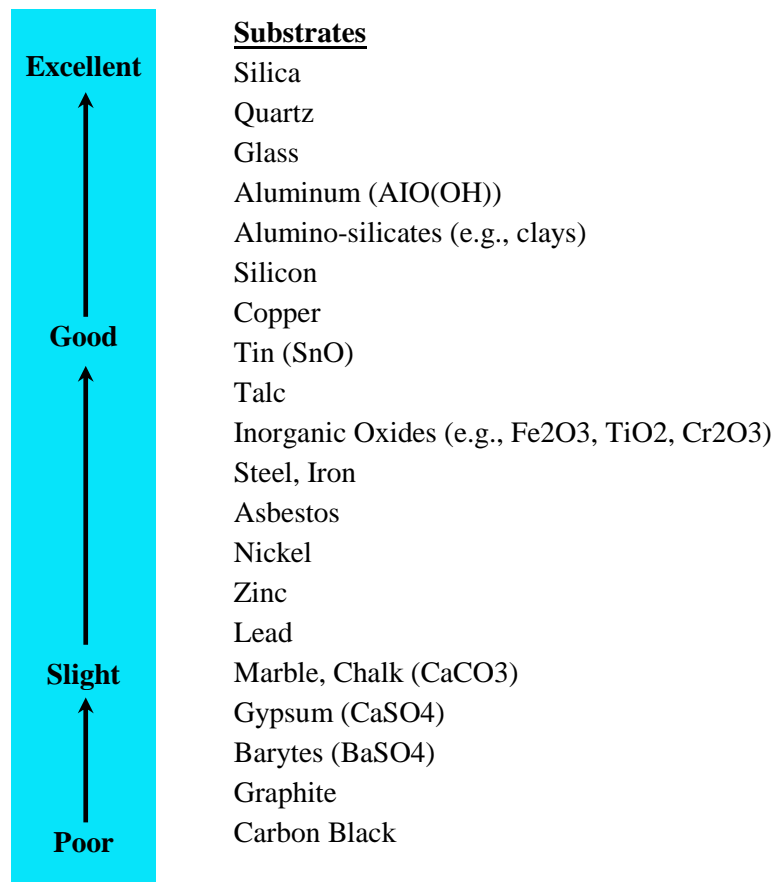


Figure 2.9. Reaction efficiency of silylation agents on inorganic materials (modified from Sanli and Erkey 2015)

2.6.5.1 Conventional Silylation

There are two techniques used in conventional silylation of surfaces. The first method involves placing the substrate in contact with the silane-solvent mixture. The silylation agent is usually mixed with aqueous solvents; however, in some cases where the silylation agent demonstrates minimal solubility in aqueous solvents, organic solvents such as toluene, tetrahydrofuran and benzene etc., is used to prepare the mixture (Aissaoui *et al.* 2012; Jakša *et al.* 2013; Soliveri *et al.* 2014). In this technique (regardless of the type of solvent used), surface silylation does not occur directly (post-synthesis is required); hence, further reactions take place prior to covalent bonding of the silane molecules to the surface (Tripp and Hair 1992a; 1992b). Initially, hydrolysis of silane is initiated with the water present in the mixture, and the self-assembled polymerization takes place within the silane solution. The amount of water in the system determines the degree of hydrolysis and self-polymerization (oligomer creation). Subsequently, the created oligomers precipitate and physisorb to the surface, from which the chemical reactions between the oxides of the surface and the hydrolysed silane molecules take place. One of the main drawbacks of this technique is the pre-polymerization of the silanes before reacting with the surface groups, which results in a non-uniform multilayer surface coverage and pore blocking (López-aranguren *et al.* 2012). Despite the mentioned inherited disadvantages of silylation with silane-solvent mixture, a number of researchers have demonstrated that uniform self-assembled monolayers (SAMs) can be obtained through this route, given that the test conditions are optimised. Wang and Lieberman (2003) investigated the SAMs of octadecyltrichlorosilane (OTS) on silica surfaces. Their work demonstrated that a uniform monolayer can be obtained when a number of factors such as the amount of water in the solution, sample aging time in the mixture and surface pre-treatment are closely monitored and controlled. Their finding was in agreement with that of other researchers who have drawn similar conclusions (Tripp and Hair 1992a; Aissaoui *et al.* 2012; Jakša *et al.* 2013). Other disadvantages of silylation through liquid mixtures are the general toxicity of the solvents, prolonged reaction times and the inability of silane-solution to reach small pores due to high capillary forces and relatively high viscosity of the mixtures (Adam *et al.* 2009; Kartal and Erkey 2010).

An alternative conventional silylation method is the chemical vapour deposition (CVD). In this method, surface functionalization takes place by vaporization of silylation agent in a controlled high-temperature and low-pressure closed chamber (Soliveri *et al.* 2014). The actual silylation process in CVD follows similar steps as those described for the solution silane deposition; however, in this route, the amount of water present in the environment and on the substrate surface are closely controlled. Since there is no free water present with the silylation

agent prior to surface deposition, the silane does not undergo self-polymerization in the solution; subsequently, more uniform SAMs would be created on a substrate's surface (Yadav *et al.* 2014; Soliveri *et al.* 2014). A number of parameters can be taken into consideration in order to create a more uniform monolayer on a surface during CVD route, such as dehumidification of the chemical deposition environment, reduction in the deposition temperature and time, and the application of monofunctional silylation agents (Diebold and Clarke 2012). One major advantage of CVD surface treatment over solution-phase treatment is the rapid deposition and bonding of silanes to the surface (Fadeev and McCarthy 1999). Gao and McCarthy (2008) applied trimethylchlorosilane and tetrachlorosilane to functionalize silicon wafer using the CVD route. Their work demonstrated that a chemical treatment time as short as 2 min was sufficient to effectively alter the surface characteristics of the silicon wafer. Other advantages of CVD route over solution-phase deposition are, eliminating the concerns around the solvent recovery and disposal (which are associated with high operational cost, low efficiency and severe environmental pollution (Lazghab *et al.* 2015)), possible reproducible functionalized surfaces with higher chemical surface coverage and density, more homogenous covalently bonded chemicals and reducing the use of solvent to rinse the surface after treatments, since this technique is less susceptible to chemical solution impurities (Voort and Vansant 1996; F. Zhang *et al.* 2010; Zhu *et al.* 2012). A major disadvantage of this technique is the high temperature ($T > 70\text{ }^{\circ}\text{C}$) and low pressure ($P_r > 5\text{ torr}$) operational conditions which would limit the application envelope of this technique (Tripp and Hair 1993; Fadeev and McCarthy 1999; Deniz Sanli and Erkey 2015).

2.6.5.2 Supercritical Fluid Silylation

Chemical surface modification through supercritical fluids (SCF)-based silylation has attracted the attention of researchers in recent years. In this route, the surface of a substrate is exposed to a silylation agent dissolved in a SCF. Similar hydrolysis and surface covalent bonding mechanisms as those outlined for the conventional techniques would take place in this method; however, the SCF-based silylation process has several advantages over the conventional techniques, and will be elaborated on in the following sections. One of the most commonly used solvents for SCF-based silylation is supercritical CO_2 (scCO_2). The scCO_2 demonstrates a number of desirable chemical and physical properties, besides being naturally abundant, nontoxic and non-flammable (Desimone 2014; Tenorio *et al.* 2018). This solvent is highly tunable with liquid-like density, gas-like viscosity and high diffusivity, making its application very appealing because it reduces the limitation of diffusion and mass-transfer, especially if tight porous media chemical modification is of interest (Gu *et al.* 2006; López-aranguren *et al.* 2012). Having a relatively mild critical pressure and temperature ($P_c = 7.38$

MPa, $T_c = 304.1$ K) is another significant characteristic of $scCO_2$, which can be easily achieved on an industrial scale. Figure 2.10 illustrates the P-V-T diagram for the pure CO_2 system. It is evident from the diagram that the pressure has substantial impact on the density of $scCO_2$ close to the critical point, thus, a slight variation in system's pressure can result in considerable change in its density. Such variations in $scCO_2$ density can potentially impact its solvation capacity (Khaw *et al.* 2017; Peach and Eastoe 2014). Furthermore, $scCO_2$ can easily be separated from the surface after treatment and leaves the surface solvent-free, which is another advantage of silylation through $scCO_2$ -based route (Combes *et al.* 1999b; López-Periago *et al.* 2014).

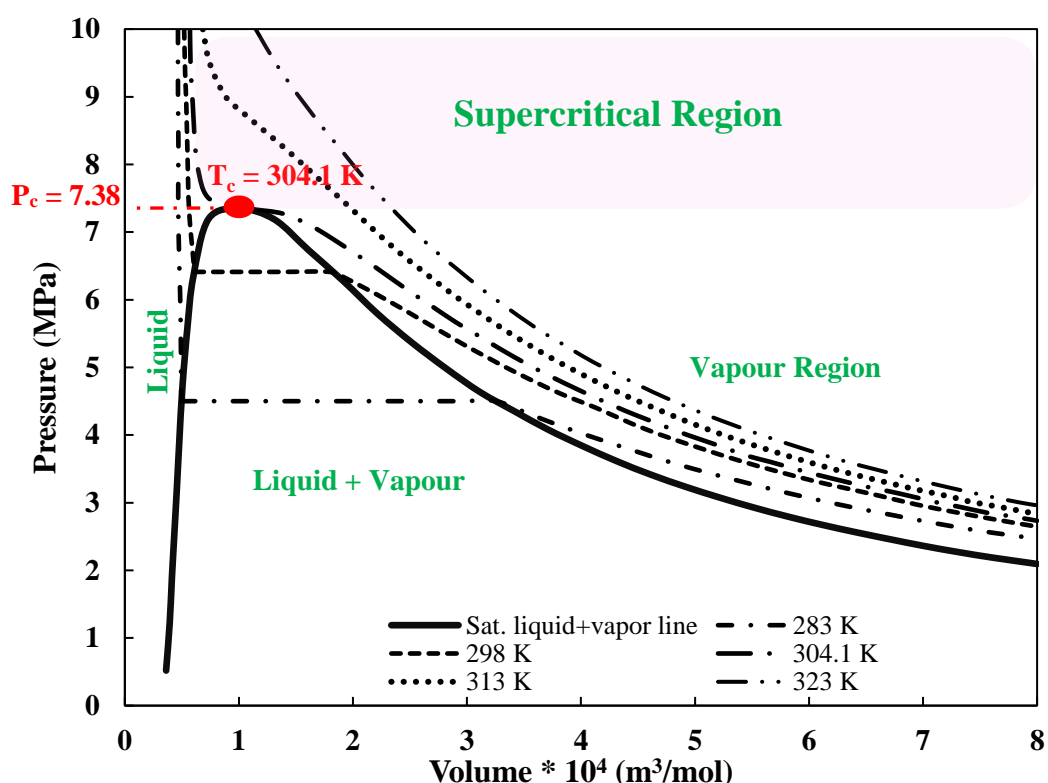


Figure 2.10. P-V diagram of pure CO_2 system, where the single, two-phase and supercritical regions are emphasised. The isotherms are represented by dashed lines. (modified from Erkey 2011)

With respect to the earlier mentioned advantages offered through $scCO_2$ -based silylation, a wide range of silane agents has been employed in chemical modification of different oxide surfaces (e.g., SiO_2 , TiO_2 , Al_2O_3 , etc.) through this technique (Combes *et al.* 1999b; Cao *et al.* 2001; Gu *et al.* 2006; Vyhmeister *et al.* 2013; Tenorio *et al.* 2018). Yarita, Nomura, and Horimoto (1996) applied hexamethyldisilazane in chemical surface modification of silica gel in both conventional and $scCO_2$ -based routes, who then analysed the performance of each technique by high-performance liquid chromatography as well as pyridine/phenol test in supercritical fluid chromatography. Their work demonstrated that the chemical surface

coverages were $3.91 \mu\text{mol}/\text{m}^2$ and $4.13 \mu\text{mol}/\text{m}^2$ for conventional and scCO_2 -based silylation, respectively. They proposed that the enhanced surface coverage in scCO_2 -base route was probably due to lower viscosity and higher diffusion rate, which contributed to the faster mass-transfer of the silane- scCO_2 solution. Kartal and Erkey (2010) chemically modified the silica aerogels by hexamethyldisilazane (HMDS)- scCO_2 mixtures. They concluded that the functionalization of the silica aerogel was not only limited to the surface of substrates, but also the pore space of silica aerogel demonstrated the same level of surface modification, which was attributed to the high diffusion rate of HMDS molecules to aerogel disc's pore space.

Sánchez-Vicente *et al.* (2014) studied the chemical surface modification of mesoporous silica SBA-15 with tertiary aminosilane in conventional and scCO_2 -based silylation. Their experimental data indicated that the scCO_2 -based silylation could result in a grafting density of $2.6 \text{ mmol}\cdot\text{g}^{-1}$ after only 2 hr of treatment. In fact, they demonstrated that 30 min of scCO_2 -based silylation could yield a similar grafting density as that achieved with a conventional technique in 24 hr of treatment ($1.9 \text{ mmol}\cdot\text{g}^{-1}$ and $1.7 \text{ mmol}\cdot\text{g}^{-1}$ for scCO_2 -based and conventional treatments, respectively). Zemanian *et al.* (2001) analysed the deposition of mercaptopropyltrimethoxysilane self-assembled monolayers in mesoporous silica through conventional and SCF-based routes. Their work demonstrated that the surface population density of the chemical agent in scCO_2 -based treatment was considerably higher than that of the solution-based deposition (6.5 versus 4.6 silanes/ nm^2). Additionally, they indicated that in scCO_2 -based technique, full surface coverage with higher quality monolayer was completed in as short as 5 min, whereas during the conventional method, an extended period of treatment time was required (over 10 hr), followed by days of post-treatment and drying. Higher surface coverage density of SCF-based technique was attributed to reduced surface defects. Pinholes and dangling hydroxyls are the two main defects associated with the monolayer surface coverage. It was demonstrated that higher treatment pressure would fill out the pinhole defects during the scCO_2 -based route. Additionally, the high pressure treatment conditions in scCO_2 route would assist with ironing-out the dangling hydroxyls which create wrinkles and bumps in the monolayer's morphology (pre-polymerization in liquid solution). Subsequently, by reducing the impact of these two defects, higher monolayer quality and silane population density could be obtained through scCO_2 -based treatment (Zemanian *et al.* 2001; Diebold and Clarke 2012).

The accessibility of silylation agent to surface hydroxyl groups is considered to be one of the dominant factors in determining the efficiency of surface functionalization with silanes, thus, increasing the surface hydroxyl moieties increases the reaction sites for silane-surface covalent bonding proportionally (Sanli and Erkey 2015). In 2005, McCool and Tripp demonstrated that the inaccessible surface hydroxyl groups are in fact accessible when scCO_2

was used as a solvent and reaction medium. In addition, they showed that the octadecyldimethylchlorosilane could react with the isolated hydroxyl groups when scCO₂ was used as a solvent, whereas, these reactions would not be possible when liquid solvents were used. Although CO₂ suffers from dissolving polar and ionic species due to its linear molecule and quadrupole moment (Peach and Eastoe 2014), it has been demonstrated that residual adsorbed water on the silica surface could be extracted by scCO₂, exposing the isolated and inaccessible silanol moieties (Gu *et al.* 2006; Sánchez-Vicente *et al.* 2014).

This chapter so far has covered the fundamentals of wettability followed by a discussion as to how wettability may influence multiphase flow in porous rocks. Then a number of methods used to evaluate the wettability state of reservoir rocks were reviewed. Also, in the current section, various methods applied to alter the wettability of material surfaces have been presented. In the preceding few pages, silylation with the use of supercritical CO₂ as an option for chemically modifying surfaces was discussed. The purpose of this last part is to elaborate on an essential link as to how a scCO₂-based silylation may be of relevance given the current state of the relevant industry.

2.7 Subsurface Applications of CO₂

There are a number of important subsurface operations that involve the extensive use of CO₂. Such operations have enhanced the experience, knowledge and confidence of the relevant technical community in handling, injection and understanding the behaviour of the injected CO₂ which would be present in the subsurface environment in its supercritical state. According to the International Energy Agency (IEA) reports (IEA 2020), during the past two decades, the CO₂ emissions have increased from 20.5 Gt/yr to 33.3 Gt/yr (Figure 2.11), and this emission is forecasted to reach 42 Gt/yr by the year 2040 (Center For Climate And Energy Solutions 2020). Additionally, this report indicates that CO₂ contributes to as high as three-quarters of greenhouse gas emissions, responsible for a measurable rise in global atmospheric temperature (Ritchie and Roser 2019). CCS has been proposed and used to some extent as a viable option to mitigate and reduce CO₂ emissions. In this technique, the unwanted gas is captured, compressed and then injected and stored into a suitable geological formation. There are a number of active and under development pilot or commercial-scale CO₂ geosequestration projects worldwide (Figure 2.12).

The first commercial-scale CCS project (Sleipner saline aquifer in the North Sea) commenced in 1996 and has injected CO₂ into a sandstone formation located beneath a low permeability caprock. This project demonstrated that 1 Mt/yr can be injected into subsurface sedimentary reservoirs and stored safely (Baklid *et al.* 1996). The Salah (Algeria) CO₂ storage

project started in 2004 and injected 1.2 Mt/yr of CO₂ into a depleted oil reservoir. In the USA, a pilot geosequestration project (Cranfield Project – Mississippi) began in 2008, which is now injecting over 1.5 Mt/yr CO₂ into the Tuscaloosa Sandstone Formation. At the Snøhvit project in the Barents Sea, since the field became operational in 2008, 0.7 Mt/yr of CO₂ has been injected into Tubasan Sandstone Formation reservoirs (Eiken *et al.* 2011). In Western Australia, the Gorgon and South West Hub projects, at full capacity, are going to store 3-4 Mt/yr and 5-6 Mt/yr of CO₂, respectively, which will make them the largest CO₂ geosequestration project worldwide (Chevron 2019; Government of Western Australia - Department of Mines and Petroleum 2013). In addition to the above, there numerous other operational/proposed pilot or commercial projects scattered around the world as depicted in Figure 2.12.

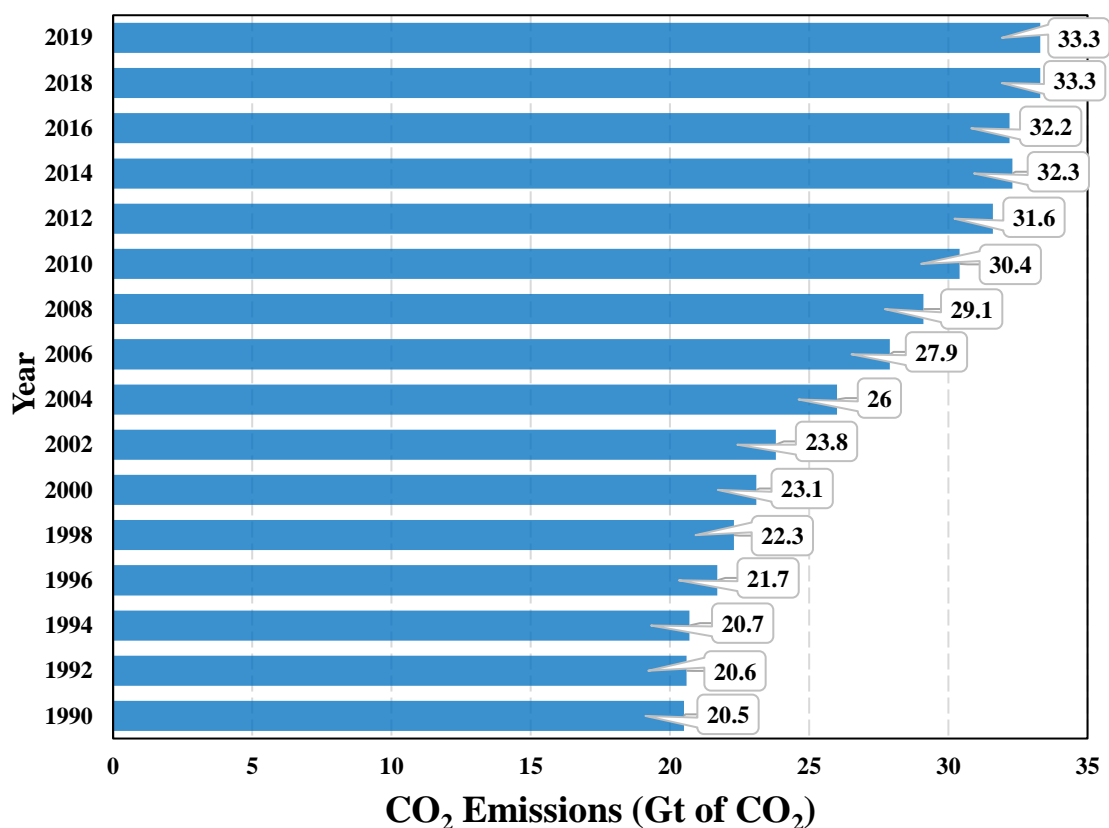
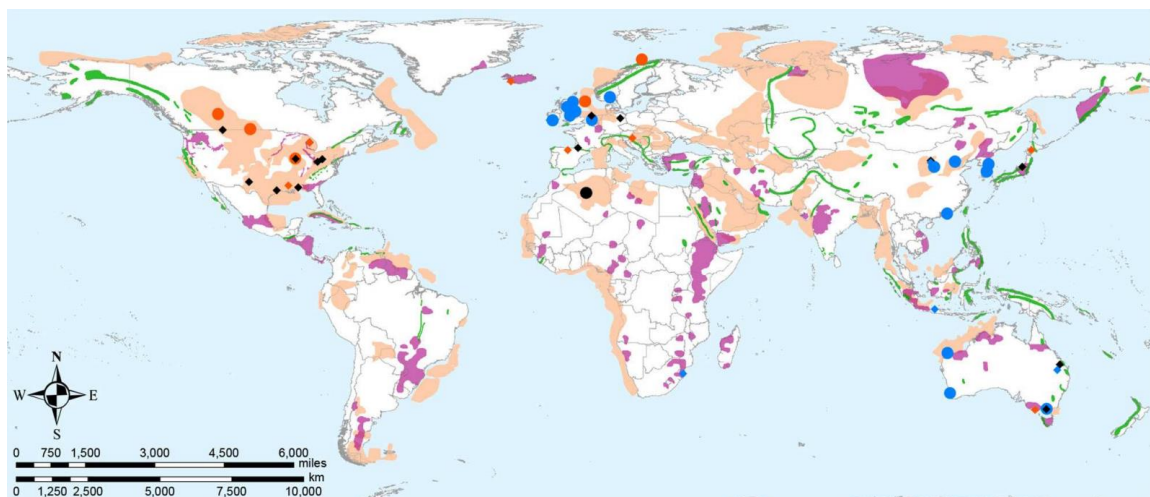


Figure 2.11. CO₂ emissions, 1990-2019 (modified from IEA 2020)

The use of CO₂ in EOR has also been studied extensively in the laboratory scale and implemented in a number of successfully field scale cases resulting in a considerable incremental recovery. In fact, where possible, it would be highly advantageous to combine geological storage of CO₂ with EOR, as the produced oil can help with offsetting the cost associated with CCS (Cook 2007). So far CO₂-EOR has been applied in more than 74 oil fields in the USA (IEA Greenhouse Gas R&D Programme 2004). The pilot CO₂-EOR project in Sundown Slaughter Unit (Texas, USA) commenced in 1976, which achieved an incremental

tertiary oil recovery of 19.6% of original oil in place by 1984 (Folger and Guillot 1996). In 1983, a commercial-scale CO₂ miscible flood commenced in the Means Field in Andrews County (Texas, USA), which increased the estimated oil recovery factor of this field from 25% to 50% (Stiles and Magruder 1998; Kuuskraa 2008). Canada has also operated a number of successful projects including the Weyburn and Joffre Viking. In fact, the first commercial CO₂-EOR project in Canada was implemented in Joffre Viking in 1984, which is estimated to give an additional oil recovery of up to 25% (Pyo *et al.* 2003). The Weyburn project (Saskatchewan, Canada) is another successful example of field-scale CO₂ injection for the combined purpose of EOR and geosequestration. In this project which commenced in 2000, about 1 Mt/yr of CO₂ was injected into an oil reservoir resulting in an increase in the daily oil production from 8000 barrels to nearly 30000 barrels (Emberley *et al.* 2004; The Prasino Group 2012).



CO₂ sequestration facilities, projects, and opportunities

Large scale facilities		Pilot projects		CO ₂ sequestration	
●	Completed	◆	Completed	■	Highly prospective sedimentary reservoirs
●	Operating	◆	Operating	■	Basaltic formations
●	Future	◆	Future	■	Ultramafic formations

Figure 2.12. Map of CO₂ sequestration facilities, pilot projects, and long-term storage potential in geologic formations (modified from Kelemen *et al.* 2019)

Chapter 3 Experimental Setup, Materials and Methodology

To achieve the particular objectives set for this research, as outlined in Chapter 1 (Introduction), various types of experiments were conducted. This chapter is to present the necessary information about the experimental plan followed in three consecutive main sections; a brief introduction of the major equipment used in conducting various experiments, a detailed description of the materials (rock samples, chemicals and fluids) used and finally the experimental procedures followed in conducting the planned experiments.

3.1 Experimental Equipment

3.1.1 High Pressure-Temperature Visual Cell

The cloud point (CP) pressure of a binary system and the wettability state of rock surfaces are among the important parameters requiring evaluation in this study. The CP pressure provides information on the lowest possible pressure for a binary system (e.g., silane-scCO₂) at a given temperature, for which the mixture exists as a single-phase state. For this research, the visual cell included in Vinci IFT-700 apparatus (Figure 3.1) was used to measure the necessary CP pressure data. This visual cell is also designed to assess the wettability condition of a rock substrate. This instrument can operate under elevated pressure (P) and temperature (T) conditions (up to 70 MPa and 473 K, respectively).



Figure 3.1. The high pressure-temperature visual cell apparatus used to measure cloud point pressure and contact angle (Vinci IFT-700).

Figure 3.2 depicts the IFT apparatus schematic and consists of six main modules: 1. high pressure-temperature viewing cell, 2. pressure and temperature controlling system, 3. hand

pumps, 4. high definition digital camera (CR-GEN0-M1020, DALSA Genie, Canada), 5. light source, and 6. supervisory control and data acquisition (SCADA) system. The main body of the viewing cell (20 ml capacity) is made of Hastelloy C, which is highly corrosion-resistant. The viewing windows are made of sapphire glass, providing adequate strength to contain the pressurized fluids at high-temperature conditions. In addition, the sapphire glass does not react with chemicals used in various experimental investigations. The two hand pumps (10 ml each) are used to adjust the bulk fluid pressure and to produce liquid droplets (for wettability analysis). The SCADA is the main module that controls the light source intensity (which illuminates the viewing cell), heating system and the camera settings. Produced images from the experiments are then analysed using Vinci software specifically designed for this equipment (embedded in the SCADA). This software is used to extract the contact angle value for the brine-gas-rock system (Figure 3.2) as well as the interfacial tension (IFT) of immiscible fluids (i.e., gas and brine). The software can also measure both sessile and captive drop contact angles on a test surface.

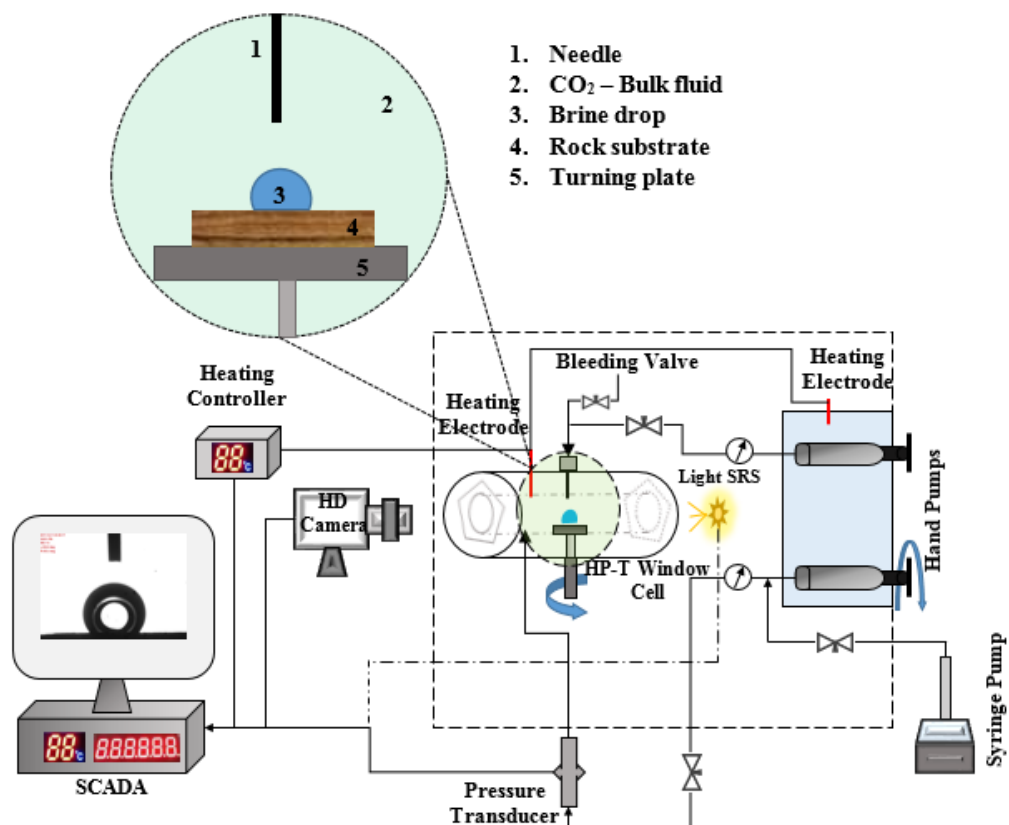


Figure 3.2. The schematic diagram of IFT-700 apparatus.

3.1.2 High Throughput Surface Modification Setup

The apparatus and technique used to chemically modify the surfaces of the rock samples in scCO₂ were adopted from an existing high throughput gravimetric extraction (HTGE) technique. The HTGE technique has been developed by Bray *et al.* (2005) which allows for rapid parallel solubility tests on a number of chemicals in supercritical fluids. The final procedure specifically designed for this research is referred to as the high throughput surface modification (HTSM) technique, which was used to treat multiple rock samples in a single silane-scCO₂ mixture environment at once (Figure 3.3). This equipment consists of two main parts, namely the extraction cell body and the sample holder stand/racking system (Figure 3.3-**a** and **b**, respectively). The extraction cell body has a 1000 ml capacity and is made of stainless steel (grade 316) which can be used for elevated pressures and temperatures (up to 69 MPa and 453 K) investigations. The racking system can accommodate up to 40 rock samples at a time and is designed in a way that samples can be randomly distributed over five levels along the height of the cell. This configuration allows to validate the chemical concentration uniformity of a mixture within the cell by testing the chemical composition of a particular rock sample taken from different levels after treatment (e.g., a sample taken from lower levels could be compared to another taken from higher levels). Borosilicate open-ended glass tubes (ID = 6.5 mm, L = 60 mm) were used to hold the rock samples in the holder column. To avoid the rock powder from falling out of the tubes but allowing for the silane-scCO₂ mixture to easily pass through, the tube bottoms were plugged with permeable quartz frits.

The necessary CO₂ injection for the HTSM procedure was supplied from a high pressure and temperature accumulator. An air-driven gas compressor (Haskel, AGT-30/75, USA) was used to fill up and pressurize the accumulator and the HTSM cell. A high precision syringe pump (BTSP 500-5, Vinci Technologies, France) was then used to inject CO₂ from the accumulator through the HTSM cell at a constant flow rate. A dome-loaded back-pressure regulator (Equilibar, USA) was used at the cell's outlet to keep the pressure constant during CO₂ injection. The outflow silane-scCO₂ mixture was passed through a water trap and then released into a fume cupboard (Figure 3.3-**c**). To maintain a constant temperature at prescribed test condition, the HTSM cell was placed inside a fan-forced oven for the duration of the experiment.



a)



b)

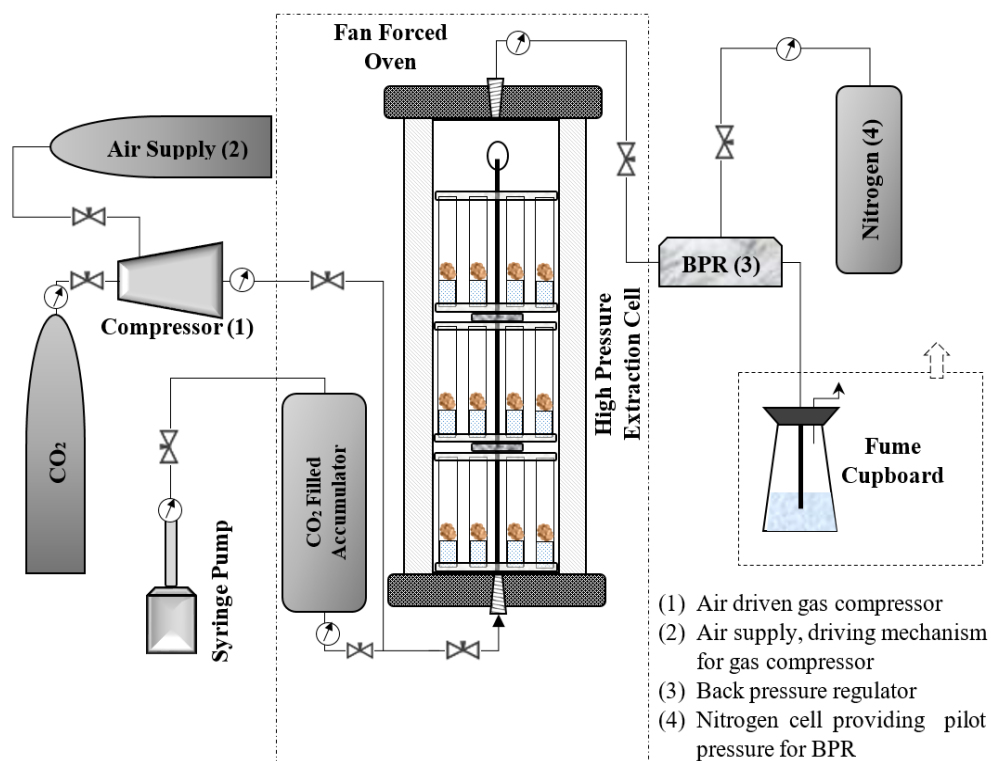


Figure 3.3. The High Throughput Surface Modification (HTSM) used for $scCO_2$ silylation. a) HTSM cell. b) Demonstration of sample distribution in the stand/racking system. c) The schematic of HTSM experimental setup.

3.1.3 X-Ray Photoelectron Spectroscopy

As indicated earlier, this work involves treating rock samples with silanes using a scCO_2 -based silylation technique. To evaluate the efficiency of this technique, it is necessary to characterize and analyse the surface chemistry of the rock substrates pre- and post-treatment. To achieve this objective, X-ray photoelectron spectroscopy (XPS) was used to map the rock surfaces' elemental compositions and associated chemical state.

X-ray photoelectron spectroscopy is a widely used surface analysis technique to characterize the surface chemical composition (with a characterization depth of 2 to 5 nm) through the generation of photoelectrons by exposing the surface to X-ray radiation. By measuring the ejected electron's energy and the energy shift, one can identify the elemental composition and chemical bonding, respectively. This technique is also referred to as electron spectroscopy for chemical analysis (ESCA) if the chemical bonding of the surface is analysed, which is of interest in analysing organic materials on the surface.

The XPS can be utilized to obtain surface elemental analysis as well as chemical state, which is achieved by dividing the electron energy level of an atom into two types. The first type reflects the highest electron energy level and is located on the first electron orbit of an atom ($1s$) and is referred to as the core level. The second type is referred to as a valance level and reflects the electron energy in the outer electron orbits of an atom ($2s$, $2p$, etc.). For example, when pure carbon is subjected to XPS analysis, a high-intensity peak and two peaks with lower intensity will be recorded with different binding energies. The high-intensity peak corresponds to the core level binding energy (BE - 284.8 eV), and the two lower intensity peaks refer to the energy released from the valance levels, which are weakly bonded to the atom. The chemical bonding in molecules are formed when the valance levels of an atom react with the valance levels of another atom to create a new species, and subsequently, the BE peaks will shift slightly corresponding to the presence of different chemical states.

During this research, elemental analyses tests were carried out on the pre- and post-treatment sandstone samples with an AXIS Ultra X-ray photoelectron spectroscopy (KARATOS) located at CSIRO (Melbourne, Australia) as shown in Figure 3.4. Further information on this setup and its specific parameters settings as considered for this research will be presented in the upcoming experimental procedure section of this chapter (Section 3.3.6).



Figure 3.4. AXIS Ultra X-ray photoelectron spectroscopy (KRATOS)

3.1.4 Core-Flooding Setup

Core-flooding is widely used in experimental evaluation of multiphase flow in porous rocks. The custom-made core-flooding setup used for this study is shown in Figure 3.5. The system is capable of operating at elevated pressure and temperature conditions (up to 70 MPa and 473 K, respectively). It can be utilized in various core-flooding scenarios, including horizontal/vertical injection, single-phase/multi-phase flow (two-phase relative permeability and recovery measurement), and steady/unsteady-state injections.



Figure 3.5. The core-flooding system used in this study.

Figure 3.6 is a schematic of the core-flooding system (shown in Figure 3.5) together with other auxiliary equipment attached to it. To keep the equipment safe against mechanical failure, rust and corrosion, high tensile strength and corrosion-resistant materials (e.g., 2507 super duplex stainless steel and Hastelloy C-276) are used in the manufacturing of the metal parts of

the system (e.g., core-holder body, flow lines, fittings, etc.). The above considerations were necessary due to the use of acidic and potentially corrosive fluids (e.g., saline brine-CO₂ mixture) during experiments.

Overall, this system can be divided into six main modules, namely: core-holder, injection pumps, fluid accumulators, the supervisory control and data acquisition (SCADA) system, heating system and back-pressure regulator. In order to achieve the necessary thermal equilibrium during each experiment, the core-holder, the accumulators, and the flow lines connecting them together that hold the injection fluids are kept inside a convection fan-force oven.

To accommodate for multiphase injection, three accumulators were connected in parallel, and their outlets were connected to the inlet port of the core-holder as shown in Figure 3.6. Each accumulator has a floating piston which isolates the hydraulic fluid (water) from the injection fluid (silane-scCO₂, live brine, scCO₂). All the accumulators have a 1000 ml capacity, which is sufficient for uninterrupted fluid injection during a flow cycle. Two high precision syringe pumps (BTSP 500-5, Vinci Technologies, France) were used in order to pressurize the accumulators and subsequently inject the desired fluid/fluids into the core-holder. A 0.5 micron sintered line filter was installed just before the core-holder inlet to remove any fine materials from the injection lines, which may potentially damage the rock sample.

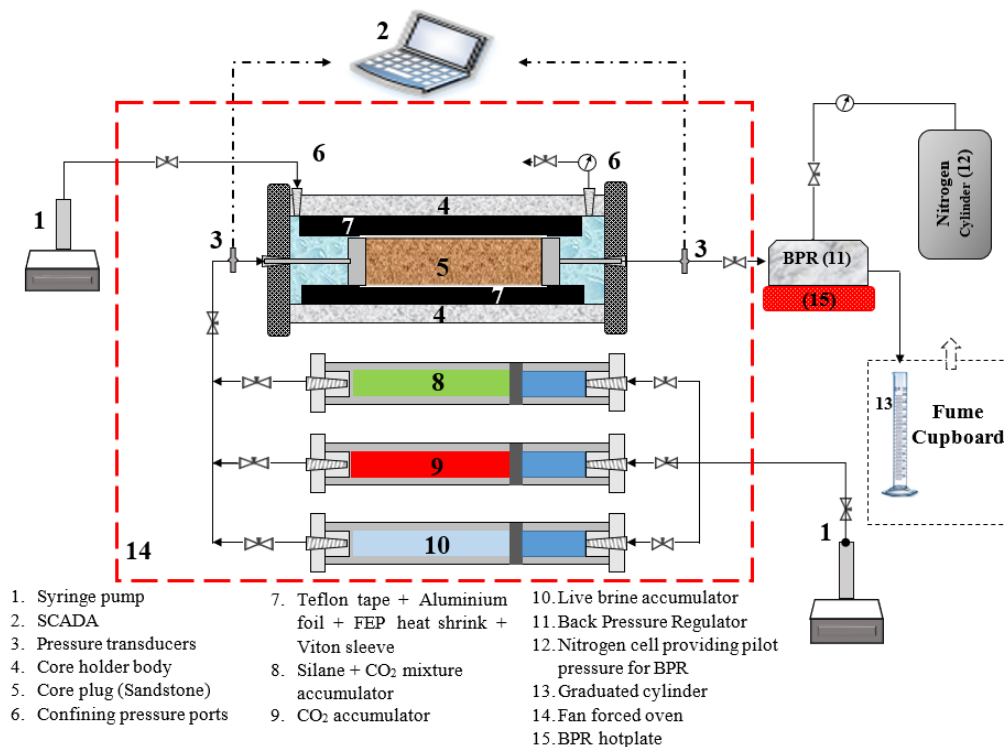


Figure 3.6. The schematic diagram of the core-flooding setup.

The core-holder used in this research was a Core Laboratories standard biaxial HCH series. A schematic of the core-holder is presented in Figure 3.7-a. This type of core-holder is referred to as standard biaxial type because the same radial and axial pressures are applied on the core sample from the confining fluid in the annular space. The radial pressure is applied along the length of the core sample by means of the radial Viton sleeve, and the axial pressure is exerted to the end of the core sample using a floating end plug (Figure 3.7). A ¼" high-pressure tubing is connected to the centre of the floating end plug and passed through the end-cap of the core-holder which can slide in and out as required. This degree of freedom allows for different lengths of core plugs to be used in the core-holder, as well as keeping the end plug in contact with the rock sample throughout the experiment (Figure 3.8-f).

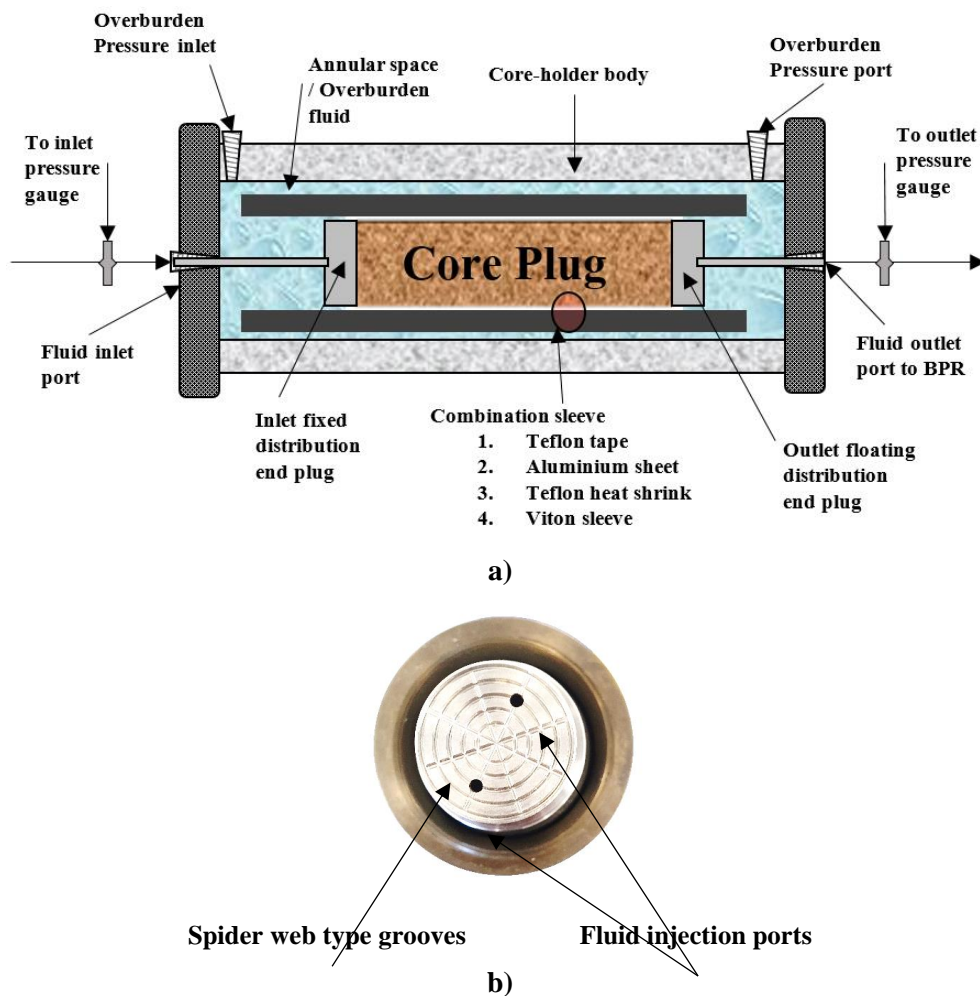


Figure 3.7. a) The schematic cross-section of the standard biaxial HCH core-holder, b) Picture of the end plug design configuration.

Figure 3.7-b demonstrates the distribution end plugs' design configuration. As it can be seen, the spider-web-pattern groove is implemented, which uniformly distributes the injection fluid

across the entire face of the rock sample. Additionally, the inlet distribution end plug has two injection ports which may be utilized if a simultaneous injection of two fluids is required.

Due to the high diffusivity of injected supercritical CO₂ into an ordinary flexible Viton core sleeve which can cause sleeve failure (e.g., explosive decompression), a multilayer sleeve configuration was used. The possible movement of CO₂ not only affects the integrity of the sleeve but can also affect the accuracy of the material balance calculations (high accuracy is essential for fluids saturation determination inside the core sample). The multilayer combination sleeve sequence adapted for this research is shown in Figure 3.8-b to e. First, a layer of Teflon tape is wrapped around the core sample followed by a layer of aluminium foil and then Teflon heat-shrink, and finally, the sample was placed inside a Viton sleeve.

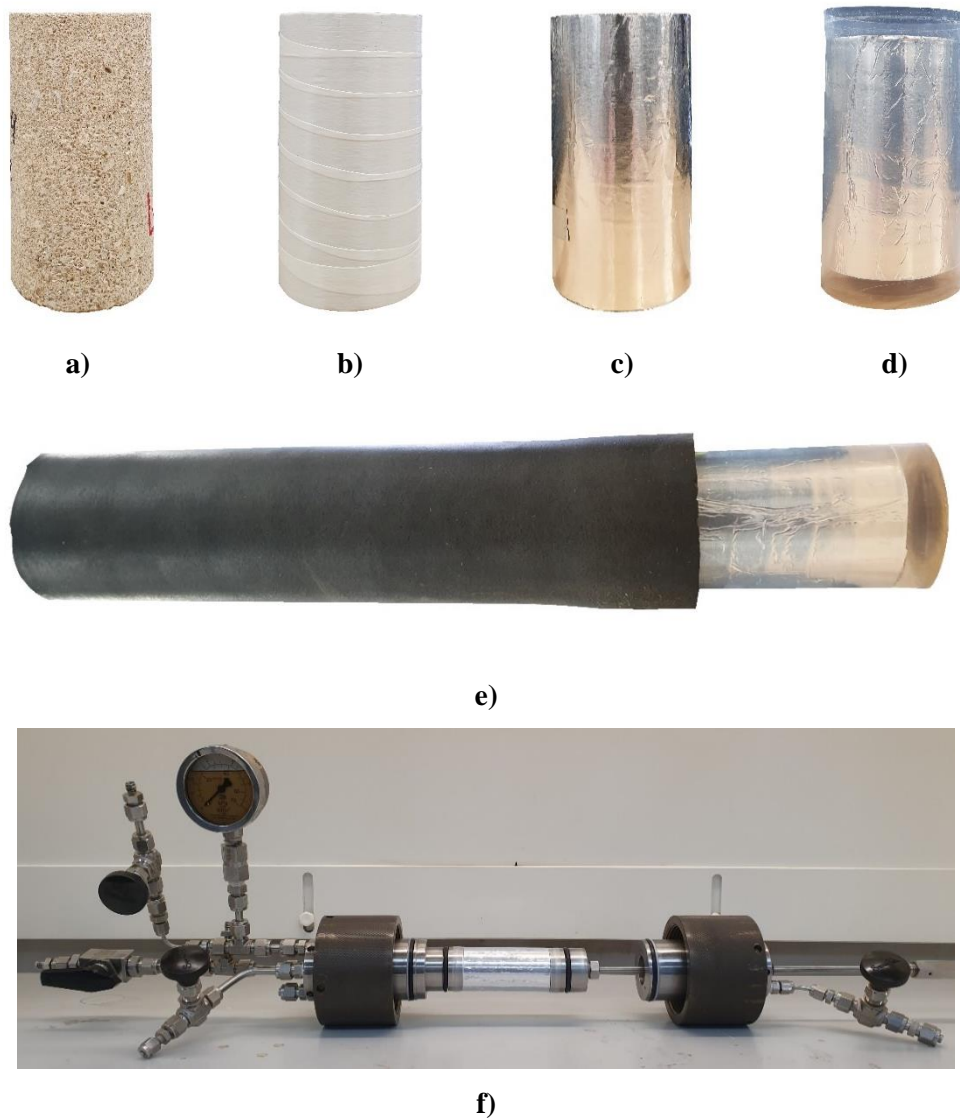


Figure 3.8. Combinational sleeve sequence. a) Core sample. b) Teflon tape layer. c) Aluminium foil layer. d) Heat-shrink sleeve. e) Viton sleeve. f) Core sample placement fixed at both ends.

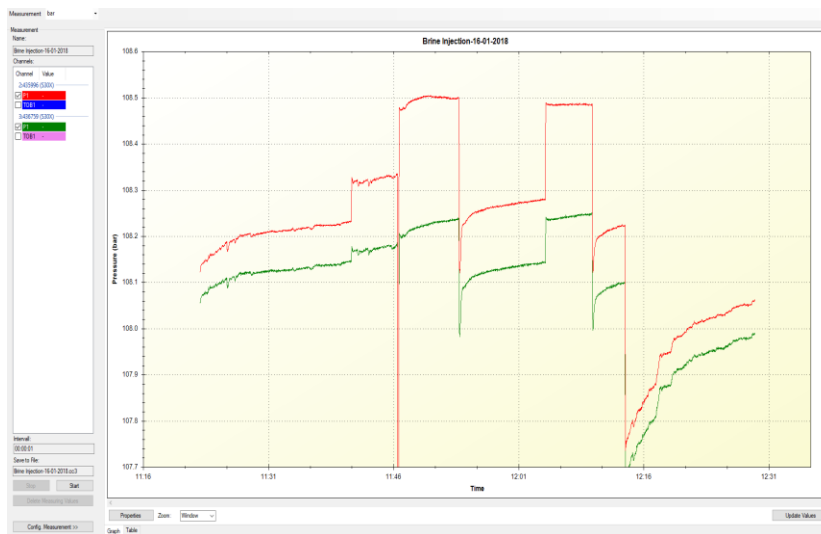
Confining pressure is applied through the injection of fluid via the overburden injection port. There are two confining pressure ports (fluid injection and air/fluid purging Figure 3.7-a) incorporated in a standard biaxial core-holder. A high precision syringe pump (ISCO 100D, Teledyne; 0.1% FS pressure accuracy) was used to pressurize the confining fluid, and it was kept connected to the system throughout the experiment duration in order to keep the overburden pressure constant in an unlikely event of slight temperature variations.

To prevent backflow of the produced fluids into the core plug and to keep the pore pressure constant for the duration of the core-flooding experiments, the downstream of the core-holder was connected to a dome-type back-pressure regulator (BPR). The advantage of using this type of BPR over other types (e.g., spring-loaded BPR) is its ability to handle multiphase flow injection with very high precision and quick response to changing process conditions. Additionally, this type of BPR is compatible with highly aggressive chemicals. A cylindrical gas reservoir filled with pressurized nitrogen was used to apply the required reference pressure (equal to the desired experimental value) on the diaphragm within the BPR. The use of nitrogen gas as a BPR's pilot pressure over liquids is advantageous as its high compressibility can help provide smooth pressure regulation, and its pressure will fluctuate less compared to liquid with slight temperature variations. It is worth noting that due to thermodynamic properties of CO₂, freeze-up can occur within the BPR when CO₂ is expanded rapidly through a small opening to atmospheric condition (Liu, Maruyama, and Matsusaka 2010). The occurrence of freeze-up can potentially plug the regulator's orifices and substantially affect the pressure readings. This problem was effectively eliminated by heating the BPR with an adjustable temperature hotplate (Figure 3.6).

Two types of data were recorded during the core-flooding experiments: volume of the effluent brine and the differential pressure across the core plug. These data can be analysed together to examine the multiphase flow characteristics such as relative permeability, fluid residual saturation, qualitative analysis of the rocks wettability state, etc. The effluent brine was collected and monitored continuously in a graduated tube placed at the BPR's outlet. At the start of any fluid injection stage, the effluent brine volume was recorded after short time intervals (e.g., every 30s) but as the experiment progressed, the frequency of the volume recordings could be decreased if the experimental circumstances allow (e.g., every 5 min). This particular volume reading strategy is considered optimum because at the beginning of a flooding stage, only the fluid that is initially saturating the core sample is produced and therefore saturation change in the sample versus time is rapid. However, once the breakthrough occurs, both fluids would be produced simultaneously, which means that the saturation change would occur at a slower pace. Given the fact that only two fluid phases (CO₂ and brine) were used in

the flooding experiments, it was only necessary to record the production of brine. The amount of CO₂ produced versus time can then be calculated readily using a simple material balance calculation.

The differential pressure across the core sample was monitored and recorded using two high precision pressure transducers (Keller, series 33X, 0.01% FS accuracy, Switzerland) installed at each end of the core plug. The data logging software can record the measured pressure data as frequent as one reading per second (Figure 3.9).



a)



b)

Figure 3.9. a) Data acquisition software. b) Pressure transducer

3.1.5 Nuclear Magnetic Resonance

The application of NMR has become a valuable tool in various fields such as medical, biology, chemistry and physics since its discovery in 1946 by Bloch *et al.*. Nuclear magnetic resonance refers to the respond of any nucleus which has an odd number of neutrons, protons or both (such as, hydrogen (¹H), which has non-zero spin), when it is located within a static magnetic field (B₀) and then excited by a radio frequency (RF) oscillating magnetic field (B₁) perpendicular to the B₀. The signals recorded during NMR measurements are generated from the nuclear spins with the applied magnetic field, subsequently, important petrophysical information such as fluid quantity, fluid properties, total and effective porosity and pore size distribution, permeability, bulk volume irreducible (BVI), free-fluid index (FFI) also referred to as bulk volume movable (BVM) and clay-bound water (CBW) can be obtained from NMR relaxation time response (Dunn *et al.* 2002; Coates *et al.* 1999). Relaxation time refers to a time

constant related to the return of nuclear spins to their original positions once the oscillating magnetic field (B_1) is removed.

In general, to study a porous medium, a low-field NMR spectrometer is used to measure the longitudinal or spin-lattice (T_1) and transverse or spin-spin (T_2) relaxation times. The T_2 relaxation time as measured for a porous medium is a factor of parameters such as bulk fluid, pore fluid diffusion and surface transverse relaxation processes (T_{2_bulk} , $T_{2_diffusion}$, $T_{2_surface}$) and is driven by the following equation:

$$\frac{1}{T_2} = \frac{1}{T_{2_bulk}} + \frac{1}{T_{2_diffusion}} + \frac{1}{T_{2_surface}} \quad (3.1)$$

Theoretical analysis indicates that the system is referred to be within fast diffusion limits if the T_2 relaxation occurs at the pore surfaces (solid-fluid interface). Subsequently, the $T_{2_diffusion}$ contribution in Equation (3.1) would become negligible. In addition, when T_2 is measured for a fluid-filled porous medium, T_{2_bulk} would be considerably larger than $T_{2_surface}$, and again the contribution of this term in the above equation can be ignored (Coates *et al.* 1999). Therefore, for such systems, the measured T_2 would become directly proportional to $T_{2_surface}$, which is a function of the surface-to-volume ratio of pores within a rock specimen. The measured transverse relaxation time for such conditions are considered to reflect the pore size distribution of the rock sample relative to the fluid type and is expressed as:

$$\frac{1}{T_2} = \rho_e \left(\frac{S}{V} \right)_{pore} \quad (3.2)$$

where, ρ_e is the surface relaxivity (determined empirically) and $\left(\frac{S}{V} \right)_{pore}$ is the ration of pore surface to fluid volume (fully-fluid saturated pore volume).

Evaluating the T_2 relaxation characteristics of core plugs are important in this research since the changes to the pore size distribution of the treated and untreated plugs before and after core-flooding can be investigated and quantified. The changes in apparent pore size distribution, as inferred from alteration to T_2 values, can originate from possible mineral dissolution or precipitation, fines migration and clay swelling as induced by the flooding process and/or wettability alteration of the pore surfaces induced by the chemical treatment. In order to obtain the above-outlined information, NMR measurements on pre- and post-treated core plugs were

carried out using a low field GeoSpec 2-53 instrument (Oxford Instruments, UK) located in CSIRO (Perth, Australia) as shown in Figure 3.10.

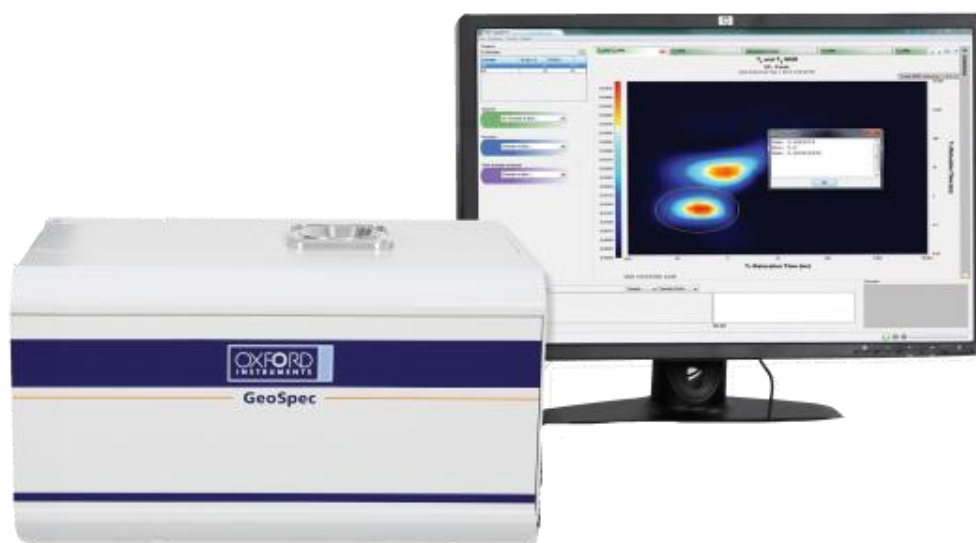


Figure 3.10. The Nuclear Magnetic Resonance (NMR) spectrometer used in this research (GeoSpec2)

3.2 Materials

3.2.1 *Fluids and Chemicals*

In order to achieve the objectives of this research as outlined in Chapter 1 (Introduction), six different types of non-fluorinated silanes were used. Dodecyltriethoxysilane (DD_TS, 99% pure), (3-chloropropyl)triethoxysilane (CPTS, 95% pure), (3-glycidyloxypropyl)triethoxysilane (GPTS, 98% pure), (4-chlorophenyl)triethoxysilane (CPhe_TS, 97% pure), 3-[bis(2-hydroxyethyl)amino]propyl-triethoxysilane solution (BHEA_TS, 65% in ethanol), and (3-aminopropyl)triethoxysilane (APTES, 99% pure) were all purchased from Sigma Aldrich. The chemical structure and basic properties of these selected silane agents are presented in Figure 3.11 and Table 3.1, respectively. These silanes can be categorized into three types of organosilanes, as decided based on their chemical composition build-up. Group one (CPTS and CPhe_TS) contain halogen moieties, group two (BHEA_TS and APTES) contain amino moieties and group three (DD_TS and GPTS) possess alkoxy moieties in their chemical structures (Sanli and Erkey 2015).

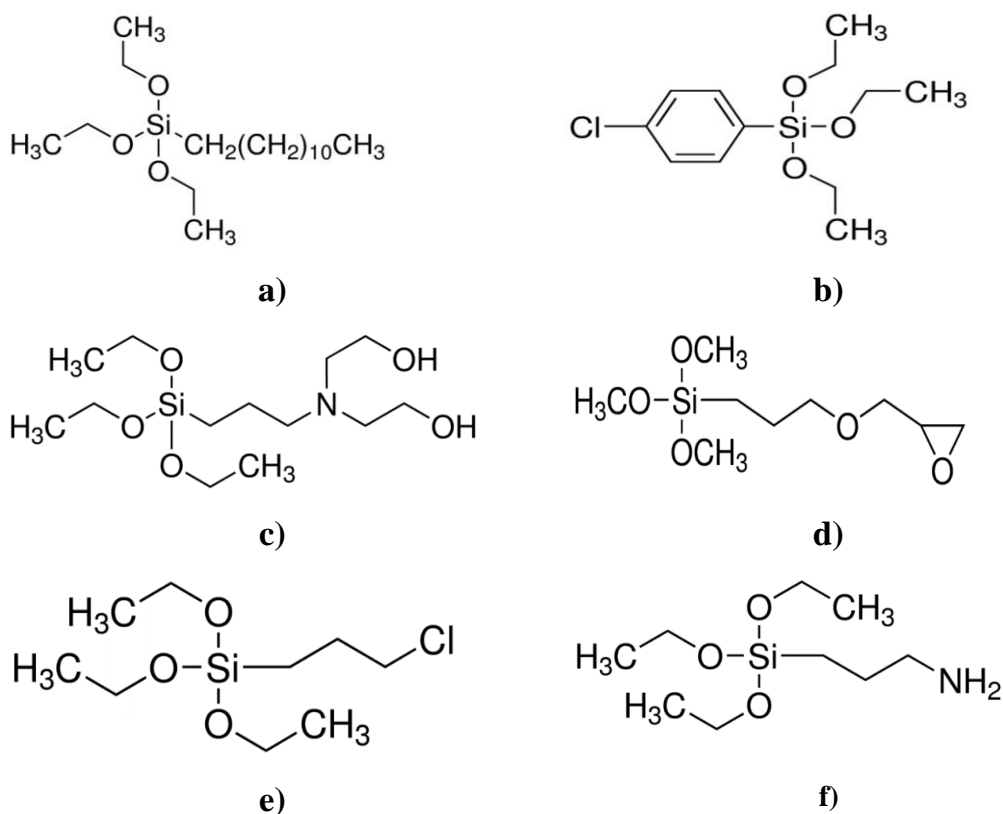


Figure 3.11. Chemical structure of selected silanes. a) DD_TS, b) CPhe_TS, c) BHEA_TS, d) GPTS, e) CPTS, f) APTES.

In addition to the main chemicals (organosilanes) mentioned above, five fluids were also used in various stages of the work as outlined below:

1. dead (degassed) synthetic brine with a total dissolved solid (TDS) of 60,000 ppm which was prepared in the laboratory by dissolving 0.54 mol of Cl⁻, 0.27 mol of Na⁺ and 0.14 mol of K⁺ in ultrapure deionized (DI) water. The above TDS is an arbitrary value chosen based on a number of publications, which indicate that this concentration corresponds to a high salinity formation brine (Robertson 2007; Mahzari and Sohrabi 2014),
2. high-purity grade carbon dioxide (99.9 mol% - BOC gas, Australia),
3. supercritical CO₂ saturated with water vapour,
4. brine saturated with CO₂ (the procedure followed for mutual saturation of CO₂ and brine is explained in Section 3.3.5),
5. silane-scCO₂ binary mixture.

The necessary PVT properties (e.g., mutual solubility of water and CO₂ and viscosities) for the above fluids under experimental conditions were obtained from a number of literature resources and databases including the National Institute of Standards and

Technology Interactive online models (Kestin *et al.* 1981; Lemmon *et al.*). In the case of a silane-scCO₂ binary mixture, some of its properties such as the cloud point pressure at the desired conditions were measured in the laboratory whose particular measurement procedure will be discussed in a later section (Section 3.3.3). For restoring and cleaning the rock samples, high-purity organic solvents including toluene (99.5 mol%), ethanol (EtOH, 95 mol%) and methanol (MeOH, 99.8 mol%) were purchased from Chem-Supply, Rowe Scientific and Univar, respectively. All the above mentioned chemicals were used as received without further purification.

Table 3.1. Basic properties of selected silane agents used in this research

Silane Agents	Chemical Formula	Boiling Point (K)	M _w (g/mol)	Silane density (g/ml) at 298 K
a) DD_TS	C ₁₈ H ₄₀ O ₃ Si	383.15	332.59	0.875
b) CPhe_TS	C ₁₂ H ₁₉ ClO ₃ Si	357.15	274.82	1.069
c) BHEA_TS	C ₁₃ H ₃₁ NO ₅ Si	-----	309.47	0.92
d) GPTS	C ₁₂ H ₂₆ O ₅ Si	417.15	278.42	1.004
e) CPTS	C ₉ H ₂₁ ClO ₃ Si	494.15	240.80	1
f) APTES	C ₉ H ₂₃ NO ₃ Si	490.15	221.37	0.946

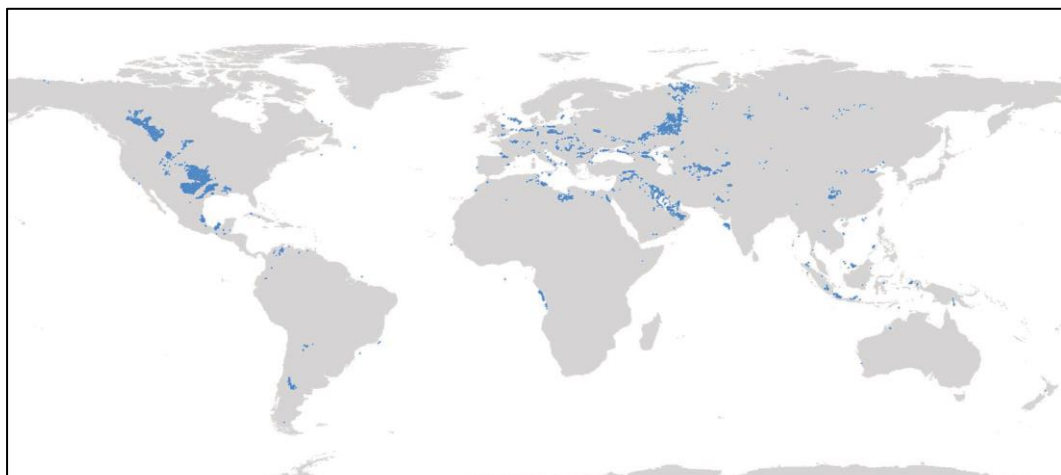
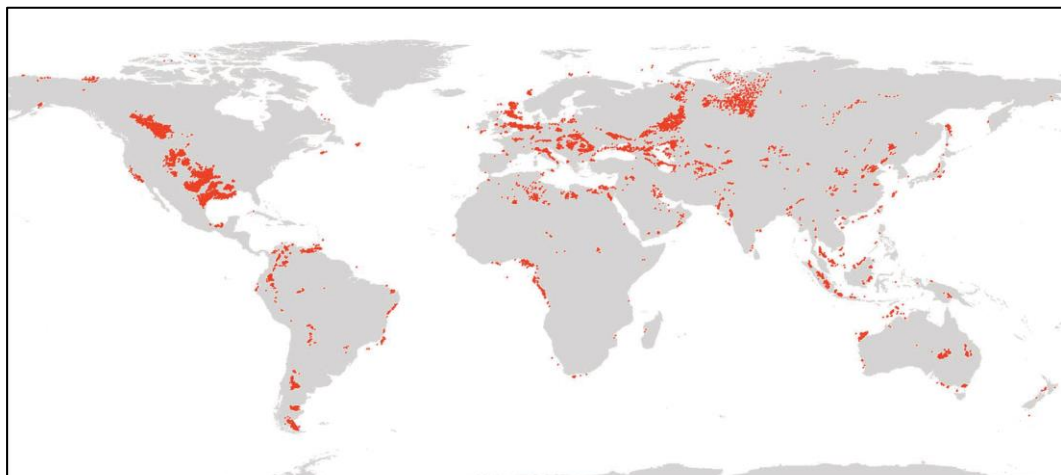
3.2.2 Rock Samples

Geological surveys indicate that as high as 78% of Earth's continental crust has siliciclastic sedimentary characteristics with the remaining having carbonate characteristics (Rudnick, R.L. & Gao 2003). Siliciclastic sedimentary formations consist of 47% sandstone and 53% shale (Saeedi 2005). In addition, the majority of hydrocarbon reservoirs worldwide are located within siliciclastic formations (with quartz as their main mineral composition). Figure 3.12 demonstrates the distribution of such reservoirs based on their lithology category (adopted after Ehrenberg and Nadeau 2005). As a result, due to the abundance of this rock formation in hydrocarbon fields and their considerable potential application for CO₂ geosequestration, the wettability investigation and multiphase flow characterization of these formations are very important. Therefore, four sandstone rock types with different mineral compositions and petrophysical properties were purchased from the USA (Kocurek Industries-Texas) which included Gray Berea (GB), Upper Gray Berea (UGB), Bentheimer (BT) and Bandera Brown (BB). The mineral composition of these rocks are presented in Table 3.2, with quartz making

up the major mineral composition (64% to 98%) of the samples. All four rock types were used during the first phase of this research, which focused on wettability alteration using silane treatments. For the second phase of the work (core-flooding experiments), only four Gray Berea core plugs with similar permeabilities were selected.

Table 3.2. Mineral composition of selected rock samples

Rock Types	Quartz	Albite	Kaolinite	Calcite	Muscovite	Clinchlore	Ankerite	Microcline
Gray Berea (GB)	63.9	8.5	2.1	-	3.8	0.6	18	3.1
Upper Gray Berea (UGB)	89.3	1.5	2.2	-	1.6	0.4	-	5.1
Bentheimer (BT)	98.1	-	0.6	-	-	-	-	1.3
Bandera Brown (BB)	74.4	10.5	2.6	6.3	3.9	2.3	-	-



a)

Figure 3.12. Geographical distribution of petroleum reservoirs: a) Siliciclastic reservoirs, b) Carbonate reservoirs (modifies from Ehrenberg and Nadeau 2005).

3.3 Experimental Methodology

The remaining sections of this chapter provide a detailed outline of a number of experimental procedures followed in obtaining the necessary data and information for this research work. These procedures were devised based on the standard protocols presented in various literature sources.

3.3.1 Sample Preparation

3.3.1.1 Rock Discs and Powder

A major part of this research was performed on finely grinded rock powder and highly-polished rock discs. For the purpose of quantifying the effectiveness of various organosilane chemical treatments, thin slices were cut from the four rock types named in Section 3.2.2. Some of these slices were grinded into a powder form. The reason for powdering the rock samples was to have a higher surface area per unit volume of the rock, and subsequently, provide more reactive sites for the sought silylation processes. For contact angle measurements, the remaining slices were polished with a fine-grit sandpaper (P3000) to reduce the surface roughness as much as possible, to reduce the effect of surface roughness and hysteresis during these measurements. An example of prepared rock powder (left) and disc (right) for GB rock type is presented in Figure 3.13.



Figure 3.13. Prepared GB samples. Powder for chemical surface modification tests (left) and polished disc for contact angle measurements (right).

After preparing the powder samples, in order to eliminate any possible contaminations, first, the samples were rinsed with toluene and dried inside an oven. The dried samples were then placed inside chromatography column filters (CCFs) (ID = 16 mm, volume = 20 ml) and flushed with 200 cc of DI water followed by 30 cc of MeOH and finally flushed with 200 cc of DI water. A microspatula was used to stir the solids inside the CCF during the washing process. The cleaned/washed samples were then dried inside an oven at 333 K for 24 hours or until their weights stabilized. The procedure to remove contaminations from rock discs was similar to that used for the core plugs, as explained in Section 3.3.1.2.

3.3.1.2 Core Plug Preparation and Preliminary Measurements

The core plugs and rock discs used in this research were reasonably clean as they were extracted directly from outcrops; however, they were still cleaned in a Dean-Stark apparatus with toluene and methanol to remove any possible contaminants (Gluyas and Swarbrick 2004). Core plugs and discs were placed in the Dean-Stark apparatus, as demonstrated in Figure 3.14 and heated to maintain a consistent solvent reflux for 48 hr. The samples were then dried in an oven at 333 K for 24 hr or until their weight stabilized. This temperature was chosen based on the fact that exposing the samples to a high temperature during washing and drying can cause dehydration of any clay components within their matrix resulting in irreversible damage to their pore structure (Gluyas and Swarbrick 2004). The dried core plugs were then cooled down to room temperature and their dimensions were measured with a calliper tool (Table 3.3).



Figure 3.14. Dean-Stark apparatus (used for core plug and rock disc washing).

The gas porosity and permeability of clean samples were measured using the AP-608 automated porosi-permeameter (Coretest Inc., USA). The instrument applies the Boyle's law and a pressure decay technique to measure the porosity and Klinkenberg-corrected permeability, respectively. Additionally, this instrument is capable of measuring the mentioned parameters under confining pressures of up to 69 MPa. Low pressure nitrogen gas (1.4 MPa) is

applied as pore fluid, due to its high diffusivity and non-damaging/non-toxic nature. Gas porosity and permeability of the four GB rocks used in core-flooding experiments are presented in Table 3.3 as measured using the mentioned instrument. The data provided in Table 3.3 is for the confining pressure of 27.6 MPa, which is equal to the overburden pressure applied to the core plugs during the core-flooding experiments.

Table 3.3. Basic petrophysical properties of core plugs used during core-flooding experiments.

	Sample ID	Confining Pressure (MPa)	Length (cm)	Diameter (cm)	Nitrogen permeability (mD)	Nitrogen porosity (%)	Pore volume (cc)
Gray Berea	GB.1	27.6	7.62	3.81	193.5	19.15	16.6
	GB.2		7.64	3.82	223.85	19	16.6
	GB.3		7.62	3.815	188.6	18.88	16.5
	GB.4		7.61	3.8	205	19.1	16.5

After measuring their porosity and permeability, the core plugs were placed inside specially designed saturation cells (Figure 3.15) to have them fully saturated with a degassed synthetic brine (Section 3.2.1). Subsequently, their pore size distribution was evaluated (in the form of T_2 distribution) using low field NMR (Section 3.1.5).



Figure 3.15. The high-pressure apparatus used to fully saturate the core plugs with synthetic brine.

Prior to brine saturation, the dry weights of the core plugs were measured with a high precision digital scale. The core plugs were then placed inside the saturation cells and vacuumed for a period of 24 hr. This time frame allows for the trapped air within the pore space of the rock samples to be removed. Subsequently, degassed brine was injected into the cells at $0.7 \text{ MPa}\cdot\text{min}^{-1}$ until reaching the desired pressure of 20.7 MPa. At this condition, the system was aged for 48 hr. At the conclusion of the saturation process, the pressure of the cells was gradually reduced to atmospheric condition, and the samples were extracted, and their weights were immediately measured. The combination of increased weight of the samples with the density of the degassed brine was then used to calculate the pore volume of the plugs. These results were found to be in good agreement with those obtained from gas porosimeter apparatus.

3.3.2 *NMR Measurements*

Nuclear magnetic resonance measurements were performed on fully brine saturated core plugs and those used in spontaneous imbibition experiments as tested before and after silane treatments. In this exercise, transverse T_2 relaxation time measurements were carried out using the Carr–Purcell–Meiboom–Gill (CPMG) pulse sequence (Carr and Purcell 1954). As indicated earlier, the NMR data for the fully brine saturated core plugs were used to determine the possible pore size distribution changes caused by the core-flooding experiments pre- and post-treatment. Similar data obtained for spontaneous imbibition experiments were mainly used to accurately detect the ultimate volume of brine imbibed into a sample during these experiments. The following steps were carried out during each NMR tests:

- The connected porosity is directly derived from the NMR signal amplitude, which is proportional to the hydrogen index (HI) of the fluid present in the sample. The NMR amplitude is calibrated using a known volume of brine, assuming a hydrogen index of one (Kenyon 1997). Since the same brine is used for all the experiments, any porosity changes in the tested samples would be therefore directly proportional to the calibrated NMR amplitude and HI.
- To eliminate any temperature-related errors, all rock samples were placed inside air-tight containers and then submerged inside a temperature-controlled water-bath at $35 \text{ }^\circ\text{C}$ (corresponding to the magnet temperature) to equilibrate for few hours before placing them in the NMR machine.
- Subsequently, to minimise possible sample dehydration due to atmospheric air exposure, each sample was tightly wrapped with an elastic cling film. Any possible free

water on the cling wrap surface was removed prior to placing the sample inside the NMR probe.

- The sample was placed inside the NMR magnet chamber using a Teflon sample holder with no NMR signal. The CPMG sequence was optimised for the tested samples with having the minimum signal-to-noise ratio (SNR) of 300, a number of echoes (N_E) set at 30702, an echo-spacing time (τ) of 57 μ s, and an inter-experimental delay time (T_w) of 5250 ms. This CPMG setting satisfies the $T_{2,max} / 3 \tau \leq N_E$ criteria which is required for the detection of full T_2 components (Coates *et al.* 1999).

3.3.3 Cloud Point Pressure Measurements

The application of visual observation at high pressure and temperature to measure the CP pressure of a miscible substance in supercritical fluids has been widely reported in the literature (Tan *et al.* 2009; Pérez *et al.* 2008). The solubility of the selected silane agents in scCO₂ was assessed using CP pressure measurements conducted in the high pressure-temperature visual cell is shown in Figure 3.1, following a procedure designed based on the above-mentioned literature.

To remove any possible contamination, prior to initiating any experiment, the visual cell was washed extensively with toluene and methanol and rinsed with DI water and then dried inside an oven at 333 K. The schematic of the high pressure-temperature visual cell is presented in Figure 3.2. To achieve a 2 wt. % fully dissolved silane in scCO₂, an accurate amount of silane was injected onto the turning plate inside the visual cell (Fadeev and McCarthy 2000; D Sanli and Erkey 2013). The following equation was used in order to determine the mass of silane required in scCO₂ to create a 2 wt. % mixture (Zhang *et al.* 2011):

$$X_{sol.} = \frac{m_p}{m_p + \rho_{CO_2} \cdot (V_{cell} - \frac{m_p}{\rho_p})} \quad (3.3)$$

where, X_{sol} is the weight ratio of the soluble silane in scCO₂ (2 wt. % in this work), m_p (g) and ρ_p (g/ml) are the mass and the density of the silane which is dissolved in scCO₂ respectively, V_{cell} is the volume of the visual cell which is equal to 20 cc, and ρ_{CO_2} (g/ml) is the density of scCO₂ at the prescribed pressure and temperature ($P = 21$ MPa, $T = 333$ K). The density of scCO₂ at desired conditions was obtained from the thermodynamic properties for CO₂ (Lemmon *et al.*). The required mass of each silane for this study was calculated using Equation (3.3), and the calculated values are given in Table 4.1.

After placing the silane sample in the cell, it was vacuumed for 20 min, followed by purging the system with a low pressure CO₂ injected at a low flow rate. A syringe pump (BTSP 500-5, Vinci Technologies, France) was then used to increase the cell pressure with CO₂ at a slow rate (0.5 MPa.min⁻¹) to minimise the thermal instability. At this stage, heating of the system was initiated to reach and then maintain a constant temperature of 333 K (this temperature was applied for all the experiments). The pressure of the system was raised to the point at which all the silane was dissolved in scCO₂, and a transparent single-phase binary mixture was achieved (\approx 21 MPa). The system was kept at this condition for 60 min to reach thermal equilibrium.

To determine the cloud point pressure of a mixture, the pressure of the cell was decreased at a 1.4 MPa.min⁻¹ rate. A lower depressurization rate (0.4 MPa.min⁻¹) was used by Al Hinai *et al.* (2017) who investigated the solubility of polymers in natural gas for gas thickening applications; however, due to the very low molecular weight of the selected silanes in this work, that rate proved to be inapplicable, and the transition at the cloud point pressure was not visible. Since this technique is a visual method, the cloud point pressure was estimated to be equal to the system pressure at which the back of the visual cell was no longer visible through the cell glass window (90% reduction in light intensity). This procedure was repeated three times for every silane to validate the reproducibility of the results, which was confirmed to be within \pm 0.25 MPa accuracy. A high speed/high definition camera was used to constantly monitor the visual cell during CP pressure measurements.

3.3.4 Rock Discs and Powder Treatment Process

Two different techniques of conventional solvent-based and scCO₂-based silylation were adopted to treat the samples with the selected silanes. Since one of the major objectives of this research is to assess the viability of scCO₂-based silylation in treating real rock formations, it was important to make qualitative and quantitative comparison between the two techniques.

3.3.4.1 Conventional Silylation Technique

Conventional silylation of the rocks in the powder and disc forms was performed according to a procedure designed based on those presented in the literature, and a summary of which is provided below (Voort and Vansant 1996; Duchet *et al.* 2000; Ko, Shin, and Choi 2011). Toluene was used as the solvent to create a 2 wt. % silane solution. The desired amount of the selected silane was placed inside a glass beaker followed by addition of the appropriate amount of toluene which was subsequently stirred for 20 min with a magnetic stirrer. A rock sample (powder or discs) was then submerged into the mixture, and the beaker was capped to eliminate any solvent loss. The system containing the solution and the rock sample was stirred for an

additional 30 min, and finally, the sealed beaker was placed inside an oven at 333 K for 24 hr to age. At the conclusion of the aging process, the sample was extracted from the beaker and flushed with 30 cc of toluene to remove any residual and unreacted silanes from the rock's surface. The sample was then placed inside a beaker filled with 30 cc of EtOH to remove the residual toluene. It was then placed inside a CCF and flushed with 300 cc of DI water, followed by 30 cc of MeOH and finally rinsed with an additional 200 cc of DI water. The washed sample was then placed inside an oven at 333 K for 24 hr to dry. This extensive washing and drying process of the treated samples would remove any unreacted silane or solvent residue from the rock surface. Any potential changes observed during the surface characterization procedures (e.g., XPS tests, contact angle measurements) would then be solely due to the chemically bounded silane.

3.3.4.2 Silylation in Supercritical CO₂

For the scCO₂-based silylation, various rock types (e.g., GB, UGB, etc.) in different forms (e.g., rock powder or polished disc) can be treated simultaneously in one silane-scCO₂ mixture inside the HTSM setup described in Section 3.1.2. This is advantageous over the conventional treatment technique where, if multiple rock samples are placed in a beaker, cross-contamination through the liquid solvent may occur. In order to silylate the rock surfaces inside a silane-scCO₂ mixture, techniques similar to the scCO₂-based silylation introduced in the literature were applied (Combes, *et al.* 1999b; Yoshida *et al.* 2001; Vyhmeister *et al.* 2013; Sánchez-Vicente *et al.* 2014; Bray *et al.* 2005). Equation (3.3) was used to determine the necessary amount of a selected silane (see Table 3.4) to create a 2 wt. % silane in scCO₂ mixture, for a 1000 ml volume at test conditions (HTSM - Figure 3.3). Clean and dry rock powders were placed inside glass tubes which were plugged at the bottom with permeable quartz frits. The glass tubes were then randomly distributed and secured in the setup's racking system as shown in Figure 3.3-b. Additionally, the rock discs were randomly suspended within the system. At this stage, the HTSM cell was tightly assembled and put under vacuum for 30 min. Subsequently, the controlled release of CO₂ into the cell at a low flow rate was initiated. With the aid of an auxiliary gas compressor and a syringe pump, the cell was then pressurized to 8.3 MPa at room temperature (~296 K). The pressurized cell was then transferred to an oven and heated at 333 K for 24 hr to age the samples in the silane-scCO₂ mixture. It is worth noting that, at this final temperature, the pressure of the cell elevated further to 27 MPa, which is above the CP pressure (as will be presented in results, Section 4.1), resulting in a single-phase mixture.

Table 3.4. The calculated mass of individual silanes to achieve a 2 wt. % solution within the HTSM cell (volume of 1000 cc).

	Silane Agents					
	DD_TS	CPhE_TS	BHEA_TS	GPTS	CPTS	APTES
Mass of silane in HTSM (g)	14.73	14.78	14.74	14.76	14.76	14.75

After the 24 hr of sample aging process, the HTSM cell was flushed with two litres of clean scCO₂ at 20 cc.min⁻¹, to remove any excess silane-scCO₂ mixture from the cell into the water trap at its outlet and then vented via fume cupboard (Figure 3.3-c). As indicated earlier, to ensure that the pressure inside the HTSM cell would remain constant at 27 MPa during this process, a dome-type BPR was placed at the outlet of the HTSM cell. Subsequently, the BPR set pressure was reduced gradually at 0.35 MPa.min⁻¹ until reaching ambient conditions. After depressurization, the rock samples were extracted and thoroughly washed and dried following a procedure similar to that described in Section 3.3.4.1. The chemically modified rock powders and rock discs were then used for surface chemical analysis (XPS tests) and wettability alteration evaluation (contact angle measurements), respectively.

3.3.5 Mutual Pre-Saturation of CO₂ and Brine

It was necessary to eliminate the two-way mass transfer between the dead brine and dry CO₂ in the high pressure and temperature experiments involving these two fluids. Therefore, both phases were pre-equilibrated with each other at test conditions (T = 333 K and P = 21 MPa) using a procedure that will be described in this section. Some complications which may arise if the two phases are not mutually saturated include:

- One of the main constraints during contact angle measurements is the immiscible nature of the two fluid phases (i.e., scCO₂ and brine in this work) brought in contact. In the case of the mass transfer taking place between the two phases, the size of the droplet introduced into the test cell would keep changing until equilibrium may be reached. During this time, the observed changes in the contact angle may not be a true reflection of the wettability state of a substrate surface being tested but mainly caused by the droplet size variation (Shojai Kaveh *et al.* 2014; Yang *et al.* 2008).
- During core-flooding experiments, if the brine and CO₂ are not mutually saturated, phase vaporization and diffusion will affect the accuracy of saturation and recovery calculations. As a result, the residual saturation of the pore fluids will be misjudged, and subsequently, the derivation and construction of relative permeability curves would

be significantly affected. Additionally, depending on the salinity of the injected brine, if the vaporization of brine continues, a phenomenon known as the salting-out effect can develop. The salting-out effect can alter the flow characteristics of the formation by inducing additional pressure drop in the porous medium (Berntsen *et al.* 2019).

A stirred reactor shown in Figure 3.16 (Autoclave Reactor, $T_{\max} = 423 \text{ K}$, $P_{\max} = 35 \text{ MPa}$) was used to mutually saturate the degassed brine and CO_2 at in-situ pressure and temperature conditions. Initially, 600 ml of degassed brine was placed inside the reactor, and the remaining air inside the reactor chamber was vacuumed. Subsequently, the reactor was pressurized using a syringe pump in combination with an air-driven gas compressor connected to a CO_2 gas supply. The compressor was used to raise the reactor pressure to the desired experimental value, but the syringe pump was primarily used to maintain the pressure inside the reactor during the subsequent equilibration process. Just before the commencement of CO_2 injection, the reactor's temperature was increased to the required test value (333 K), and the rotation speed of the stirring impeller mechanism was set at 200 RPM. Once the required temperature and pressure conditions were reached, the mixing continued for further two hours until the two fluid phases were fully equilibrated. This was indicated by the pressure stability and zero flow rate reading of the syringe pump connected to the system. At the conclusion of the above process, the CO_2 -saturated brine was transferred at constant pressure into a fluid accumulator through the bottom port of the reactor, and similarly, the water vapour-saturated CO_2 was displaced into a second accumulator. These two accumulators formed part of the core-flooding setup and were placed inside an oven at constant test temperature (333 K) to keep the saturated fluids in thermal equilibrium. At times, the accumulators containing the pre-equilibrated brine and CO_2 were also used for contact angle measurements.



Figure 3.16. The stirred reactor used to mutually saturate the brine and CO_2 .

3.3.6 X-Ray Photoelectron Spectroscopy Measurements

As indicated earlier, the X-ray photoelectron spectroscopy (XPS) analysis was used to analyse the surface chemistry of the powdered rock samples and qualitatively assess the efficiency of each of the two silylation techniques used in this work. In this work, a standard XPS measurement procedure was adopted from the literature (Koegler *et al.* 2014; Kaur *et al.* 2015). The XPS analysis was performed using an AXIS Nova and AXIS Ultra-DLD spectrometers (Kratos Analytical Inc., Manchester, UK) with a monochromated Al K α source at a power of 180 W (15 kV \times 12 mA), a hemispherical analyser operating in the fixed analyser transmission mode and a standard aperture (analysis area: 0.3 mm \times 0.7 mm). The total pressure in the main vacuum chamber during analysis was typically between 10⁻⁹ and 10⁻⁸ mbar. Survey spectra were acquired at a pass energy of 160 eV. To obtain more detailed information about the chemical structure, oxidation states etc., high resolution spectra were recorded from individual peaks at 40 eV pass energy (yielding a typical peak width for polymers of < 1.0 eV).

The powder samples were filled into shallow wells of a custom-built sample holder and analysed at a nominal photoelectron emission angle of 0° with respect to the surface normal. However, the actual emission angle is ill-defined in the case of particles and powders (ranging from 0° to 90°) the sampling depth may range from 0 nm to approximately 10 nm. For quantification of the XPS results, data processing was performed using Casa XPS processing software version 2.3.15 (Casa Software Ltd., Teignmouth, UK). The dominant elements present were identified from the survey spectra. The atomic concentrations of the detected elements were calculated using integral peak intensities and the sensitivity factors supplied by the manufacturer. Binding energies were referenced to the C 1s peak at 284.8 eV (i.e., adventitious carbon). The precision (i.e., reproducibility) of the initially acquired XPS data depends on the signal-to-noise ratio but is usually better than 5%. The latter is relevant when comparing similar samples against each other.

3.3.7 Contact Angle Measurements

Contact angle measurements allow the wettability of a specific surface to be evaluated qualitatively (Kwok and Neumann 1999). As indicated earlier, this technique was employed here to assess the change in the wettability state of the rock discs pre- and post-treatments using the IFT-700 apparatus (Figure 3.1). An axisymmetric drop shape analysis (ADSA) technique integrated into the instrument's SCADA software was utilized to measure the dynamic and equilibrium contact angle of a sessile droplet under high pressure and temperature conditions (Chen *et al.* 1998). Here, the dynamic contact angle measurement refers to a non-thermodynamically equilibrated system in which the two fluid phases may diffuse into one

another which may subsequently influence the contact angle measurements (Yang *et al.* 2008). In this research, both dynamic and equilibrated systems were utilized; however, the dynamic results will not be elaborated on due to the limitation of these results as explained under Section 3.3.5.

As mentioned earlier, surface roughness has a direct impact on contact angle measurements; therefore, it was crucial to have similar surface roughness on the corresponding pre- and post-treated rock samples. To achieve this, the rock discs (Figure 3.13) after polishing were split into smaller useable portions. A number of these portions were used to analyse their un-treated surfaces, and the rest with the same surface roughness were treated with silanes as explained in Section 3.3.4. The following procedure was followed in conducting the contact angle measurements on the pre- and post-treatment samples:

1. Prior to performing any experiment, the apparatus was thoroughly washed and dried to remove any possible contamination. A piece of a rock disc was then secured with epoxy resin onto the cell's turning plate. The turning plate provided the possibility of 360° rotation of the substrate that may be essential for a detailed examination of the deposited fluid droplet. The high pressure-temperature visual cell containing the sample (Figure 3.2) was then secured inside the apparatus's heating system.
2. The system was vacuumed out and purged with low pressure CO₂ to remove air from the visual cell and all the flow lines. Then, the system was pressurized with CO₂ and heated until it reached the experimental conditions of 21 MPa and 333 K, where it was kept for 60 min to reach equilibrium. This equilibrium was indicated by a constant pressure reading and a zero flow rate of the syringe pump. It must be noted that, during the contact angle measurements, the bulk fluid was the pre-saturated scCO₂ phase and the droplet fluid was the pre-saturated brine.
3. A hand pump was used to produce the brine droplet on the rock substrate through the capillary needle. For this, the clean empty hand pump was filled with CO₂-saturated brine. To prevent the evolution of CO₂ from brine during the filling process, the hand pump was initially pressurized to the experimental condition (21 MPa) with CO₂ through one of the ports of a three-way valve. Then using a second port on the valve, the CO₂-saturated brine stored inside an accumulator (Section 3.3.5) was injected into the hand pump at constant pressure.
4. Once all components of the system reached stability, a brine droplet ($\approx 7 \mu\text{L} \pm 2\mu\text{L}$) was produced through a capillary needle and placed on top of the horizontally mounted substrate.

The contact angle of brine on the substrate was then monitored and recorded periodically. To confirm that there was no mass transfer occurring between the two fluid phases, all the contact angle data reported in this research was recorded after 10 min from the time the brine droplet was deposited on a substrate surface.

3.3.8 Spontaneous Imbibition Measurements

In addition to the contact angle measurements, spontaneous imbibition experiments were used to evaluate the wettability state of the rock samples before and after chemical treatments. Given the larger size of the samples used for these experiments (i.e., core plugs), their results are less prone to analytical errors and may be considered to be overall more representative in evaluating the true wettability state of a rock sample. The experiments were carried out inside a high-temperature Amott cell (Vinci Technologies, France) as shown in Figure 3.17. The pressure relief valve installed on top of the cell allows for experiments to be carried out at pressures and temperatures of up to 0.2 MPa and 393 K, respectively. It is important to note that the spontaneous imbibition experiments were carried out in atmospheric conditions, where the scCO₂ phase is substituted with air. Despite the differences in the fluid properties of scCO₂ and air, when normalized, the air in ambient condition can provide a relatively close qualitative approximation of scCO₂-brine-rock configuration (Herring *et al.* 2014).

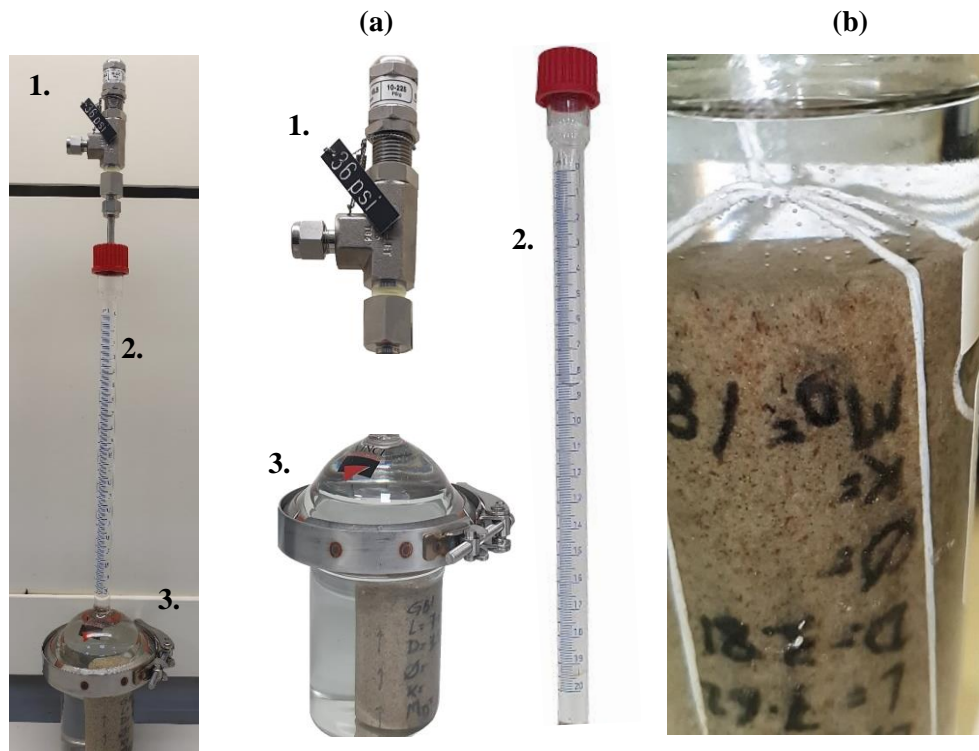


Figure 3.17. (a) Spontaneous imbibition test setup. (1) Pressure relieve valve (0.2 MPa), (2) Graduated neck, (3) Sample holder. (b) Imbibed brine displacing air bubbles from a water-wet core plug.

Prior to an experiment, the Amott cell and the core plug were washed and dried as outlined in Section 3.3.1.2. After drying, the weight of the clean sample was measured and recorded. Subsequently, the sample was placed inside the cell that was then filled with brine to the top of the cell neck, where the last calibration mark (0 ml) is located. The elapsed time is then tracked with the volume of brine imbibed into the pore space until equilibrium has been established. Periodically, over 14 days for each sample, the imbibed brine volume was recorded against time. At the conclusion of 14 days, the core plug was extracted and re-weighted immediately. This weight was required to cross-check and estimate the brine volume imbibed in the core sample. In addition, the NMR test was performed on the plug after spontaneous imbibition experiment as another technique of checking the volume of the imbibed brine. After the NMR measurements, the sample was washed and dried in preparation for core-flooding experiments (Section 3.3.9).

3.3.9 Core-Flooding Experiments

Brine-CO₂ core-flooding was performed to investigate the effect of wettability alteration on the fluid flow characteristics of the core plugs. The main output of these experiments included the differential pressure across the core plugs and the brine saturation profile, both of which were recorded against time during the flooding experiments. Subsequently, these data were used to numerically history match and construct the relative permeability curves for the two fluid phases.

Convictional core-flooding may be conducted using a steady-state (SS) or an unsteady-state (USS) technique with each methodology having their own advantages and disadvantages. This research used an USS procedure; however, a brief description of the SS method is also provided below.

In the steady-state method, the core plug is fully saturated with one phase and then flooded in consecutive steps, mostly using a simultaneous injection of the two phases of interest. During this process, the fractional flow of the second phase is increased successively. In the last step, only the second fluid phase is injected. For each step, the injection continues until steady-state conditions are established, which means stable and constant pressure drop across the sample and having an identical inlet and outlet flow rates for the injection fluids. At this point, the Darcy's equation (2.2) can be used to directly calculate the relative permeabilities of both phases. The experiment may be referred to as a drainage or imbibition displacement depending on whether the fractional flow of the non-wetting or wetting fluid increases, respectively, as the experiment proceeds. The main disadvantages of this technique include:

- It is assumed that at the end of each step, a uniform saturation profile exists along the length of the core sample. This may not be an accurate assumption in some specific cases, for example, when gravitational or capillary forces are dominant during flooding.
- It may take days or even weeks for each injection step to reach the desirable steady-state conditions making this technique extremely time consuming.

The unsteady-state displacement technique refers to the injection of only one fluid phase at a time. Generally, the sample is fully saturated with one phase followed by the injection of the second phase at a constant flow rate (or constant pressure). The injection will continue until a pseudo-steady-state is established, at which the pressure drop across the sample remains constant, and the only produced phase at the outlet of the system is the injection fluid. The experiment may be referred to as a drainage or imbibition process depending on whether the injection phase is the non-wetting or wetting phase, respectively. During flooding, the pressure drop across the sample, as well as the volume of produced fluids are recorded regularly, and through analytical or numerical methods, the relative permeability curves can be obtained. The foundation of data analysis in unsteady-state technique is the Buckley-Leverett theory for linear displacement of immiscible and incompressible fluids. In this technique, at each time step, the relative permeabilities, the flow rate, the viscosity ratio of fluids and the capillary pressure are related to the fluid saturation (Hanarpour and Mahmood 1988). The most commonly used methods to analyse data from an USS technique are Welge, Johnson-Bossler-Naumann, and Jones-Roszelle (Johnson *et al.* 1959; Jones and Roszelle 1978; Hanarpour and Mahmood 1988).

The main advantage of this method over the steady-state method is that a set of relative permeability curves can be obtained in a very short period of time (as short as a few hours). Nevertheless, there are also some issues associated with this technique which may affect the final results. Operational problems such as viscous fingering, capillary end effects, and channelling in heterogeneous cores are challenging to monitor and account for properly. In systems where the mobility of the displacing fluid is not considerably higher than that of the displaced fluid, the time period between the injection fluid's breakthrough and a complete flood-out is usually very short. Subsequently, the relative permeability curves can only be obtained for a small range of movable saturations. Additionally, in unsteady-state method, it is crucial to make an accurate measurement of the breakthrough time. Slight inaccuracy in breakthrough time measurement can create a substantial error in relative permeability data (Hanarpour and Mahmood 1988).

In this research, the unsteady-state injection technique was utilized with the specific steps followed outlined below:

1. After the conclusion of preliminary experiments (e.g., gas porosity/permeability tests, NMR measurements and spontaneous imbibition experiments), a clean and dry core plug was placed inside a multilayer sleeve as explained in Section 3.1.4. Figure 3.8 presented the configuration of the multilayered sleeve, where the rock sample was first wrapped with a layer of Teflon tape followed by a layer of aluminium, Teflon heat shrinkage, and finally inserted into a Viton sleeve.
2. Then, the fixed end plug of the core-holder was inserted inside the Teflon heat shrink and Viton sleeve. It is important to assure that the end plug surface makes complete contact with the end face of the core plug. Then the sample-end plug assembly was inserted into the core-holder, and the respective end-cap was secured. The adjustable end plug (outlet side) was then inserted into the combinational sleeve, and its associated end-cap was secured in place.
3. Next, the annulus space between the Viton sleeve and the internal diameter of the core-holder was slowly filled with water from one end of the core-holder, and the air present in the annulus space was expelled from the other end via a bleeding port. Once the injected water appeared from the bleeding port, it was plugged, and the confining pressure was raised gradually using further water injection until reaching 6.9 MPa (this pressure represents the net effective pressure of the experiment). In order to confirm the absence of cross-flow of the confining fluid into the core sample, the system was kept at this condition for 2 hr while observing the volume reading of the syringe pump used to maintain the confining pressure. Any instability in the volume reading may indicate a leak.
4. Once the leak test was complete, the inlet and outlet of the core-holder were connected to respective connections to establish a closed system. The outlet of the core-holder was connected to the system BPR pre-set to the pore pressure of 21 MPa. The heating system was then initiated, and the temperature was raised to the desired experimental value (333 K). Heating up the core-holder would increase the confining pressure excessively (by thermal expansion of the confining fluid). However, the syringe pump connected to the system collected the expanded fluid from the core-holder and kept the pressure constant.
5. Once the confining pressure and the temperature stabilized, the air inside the core plug and the flow-lines were vacuumed for 24 hr. The vacuum process was monitored using the pressure readings from both ends of the sample.

6. Subsequently, the sample was saturated with degassed brine and the pore pressure raised to the full in-situ value (21 MPa). Meanwhile, the confining pressure was also increased to its respective experimental value (27.9 MPa). It is important to fully saturate and pressurize the core plug and flow-lines with a degassed brine first. If the CO₂-saturated brine was to be injected directly after vacuuming, its dissolved CO₂ would evolve undermining the validity of the subsequent measurement steps. The system was then left for 24 hr to achieve thermal and pressure stability. During this time the pore and confining pressures were maintained using syringe pumps. The pumps' volume reading would also provide an indication of any possible leak that may take place in the system.
7. In the next step, five pore volumes (PV) of the CO₂-saturated brine was injected into the system to remove the degassed brine from the sample pore space. Subsequently, a multiple flow rate method was applied to measure the absolute permeability of the core sample by injecting the pre-equilibrated brine. At each flow rate, the injection continued until the pressure drop across the sample stabilized. The Darcy's Law was then applied to the measured data to calculate the absolute permeability of the sample.
8. At this stage, the sample was ready for the primary drainage displacement phase (assuming the system is water-wet, and the scCO₂ is the non-wetting phase). Water vapour-saturated scCO₂ (for simplicity, water vapour-saturated scCO₂ will be referred to as scCO₂) was injected at a constant flow rate of 2 cc.min⁻¹ until steady-state conditions were reached, at which the differential pressure across the sample remained constant, and no more brine was produced. Throughout the injection phase, the pressure drop across the sample as well as the brine production was monitored and recorded regularly. When the complete flood-out was reached, the residual saturation of brine was calculated by applying material balance. To construct the relative permeability curves for the drainage phase, a numerical history matching method was applied to the recorded data.
9. Next step was the primary imbibition process, where the core sample was flooded with the pre-equilibrated brine. Similar to the drainage step, the brine was injected into the sample at a constant flow rate of 2 cc.min⁻¹ until steady-state conditions were reached. Brine recovery and pressure drop data were again recorded as the main outputs of this step. At this point, all necessary data for the pre-silylation stage of the investigation had been generated, and the sample was ready for chemical treatment.

10. Subsequently, the system was depressurized by reducing the pore pressure to atmospheric and the confining pressure to 6.9 MPa, and then the system was put under vacuum for 24 hr.
11. As will be elaborated on in the next chapter of the thesis (Section 4.1), the minimum pressure required for the silane-CO₂ mixture to remain in a single-phase state at 60 °C was approximately 10.4 MPa which is well below the pore pressure used (21 MPa), guaranteeing the silane to remain in solution during the flooding experiments. To avoid any phase separation during silane-CO₂ injection, it is essential to raise the pore pressure to the experimental condition prior to injecting the silane-CO₂ mixture. The pore pressure was increased to experimental condition with scCO₂, following which seven pore volumes of pre-mixed scCO₂ with the selected silane (2 wt. %) was injected through the system at a constant flow rate of 2 cc.min⁻¹. The system was then left at this condition for 24 hr to age and for the silylation process to take place.
12. After the aging process, to remove any untreated silane from the pore space, the system was flushed with another seven pore volumes of clean and dry scCO₂ (not saturated with water-vapour). The system was then gradually depressurized to atmospheric condition.
13. At this stage, the system was ready for post-treatment flooding. The earlier described steps 5 to 9 were repeated to measure the post-silylation multiphase flow properties of the rock sample.

It must be noted that, after performing the first two core-flooding experiments (on GB.1 and GB.3 core samples), it was suspected that the pronounced presence of salt on the pore surfaces may have reduced the reaction of silane reagent with the rock surface, reducing the effectiveness of the silylation process. To eliminate the above deficiency, one more step was added to the remaining core-flooding experiments (on GB.2 and GB.4 core plugs) in which, prior to step 10, the core plug was flushed with five PV of a low salinity brine (2,000 ppm) before proceeding to subsequent steps.

14. At the conclusion of Step 13, the system was depressurized, and the core sample was extracted from the core-holder and prepared for other experiments, including post-treatment NMR measurement and spontaneous imbibition test (sections 3.3.2 and 3.3.8).

Chapter 4 Experimental Results, Interpretation and Discussion

This chapter presents the results of the various experimental work carried out in this research, together with their detailed interpretation and discussion. As outlined before, the experiments covered phase behaviour study, surface chemical alteration and analysis, quantitative analysis of surface wettability alteration through contact angle measurements, qualitative wettability alteration analysis through spontaneous imbibition experiments and finally, evaluation of the effect of wettability alteration on the multiphase flow characteristics of the CO₂-brine-rock system using a number of sandstone core plugs. In addition to the above, NMR measurements were also conducted on the core plugs to investigate any possible alteration to their pore size distribution caused by the wettability alteration process.

4.1 Cloud Point Pressure Measurement Results

In this research, the surface chemical modification was performed within a silane-scCO₂ mixture environment, therefore, it was essential to investigate the phase behaviour of the mixture at the experimental condition. To achieve this, cloud point pressure for the selected silanes were measured at 333 K, as explained in Section 3.3.3. The cloud point pressure is an indication of the minimum pressure required for the binary mixture to remain in a single-phase state.

As mentioned earlier in experimental procedure (Section 3.3.3), a 2 wt. % silane-scCO₂ binary mixture was used for all the experiments. The amount of an individual silane required to create this concentration was governed by its molecular weight when considering all the remaining variables such as pressure, temperature and the solvent remain the same. Subsequently, Equation (3.3) was applied to calculate the weight of silanes needed for the corresponding visual cell volume to achieve the 2 wt. % binary mixture. The required mass for each silane as calculated using the above method is presented in the first row of Table 4.1. As can be seen from this table, since the molecular weight of all six silanes are similar, the required mass for these silanes varies slightly.

The images captured during the cloud point pressure measurement for BHEA_TS inside the visual cell are presented in Figure 4.1. At the beginning, the pressure is well above the cloud point pressure, and there is a clear single-phase silane-scCO₂ mixture (Figure 4.1-a). When the pressure is further reduced, the phase separation starts to take place (Figure 4.1-b-c). The cloud

point pressure is reached once the light intensity is reduced by 90%, as shown in Figure 4.1-d (Al Hinai *et al.* 2017). Finally, as the pressure is decreased below the supercritical condition, all the silanes return to the liquid phase.

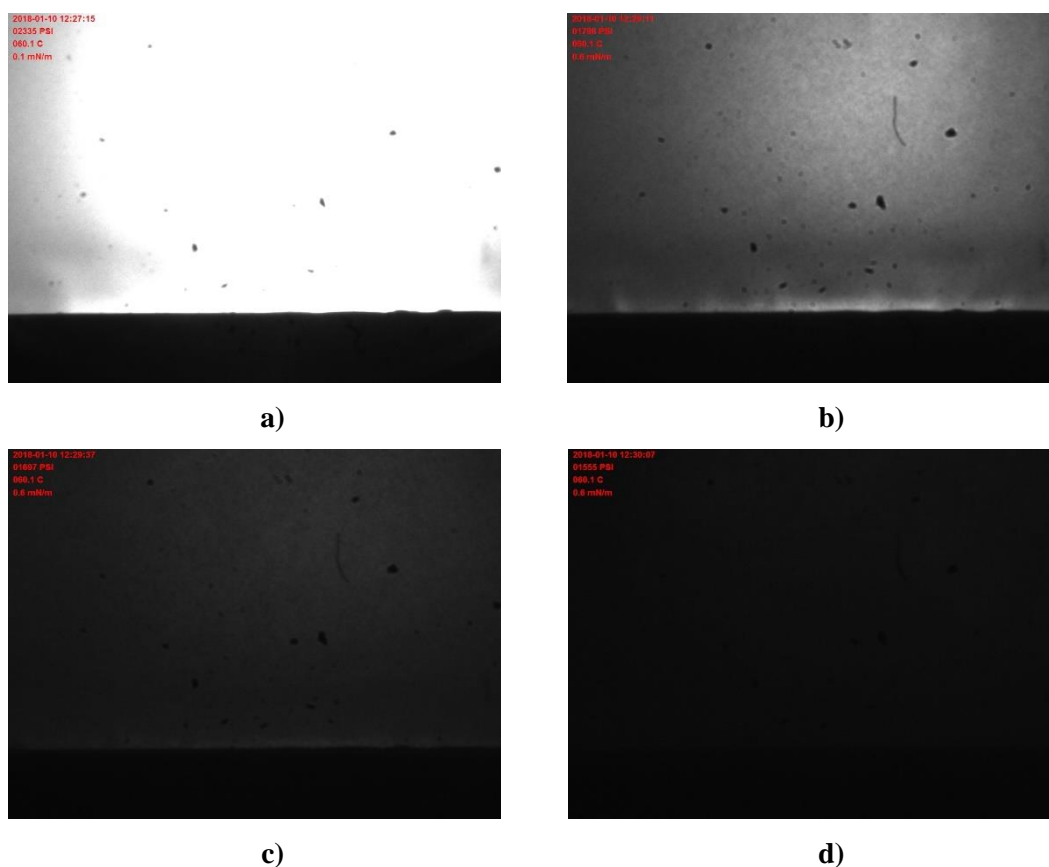
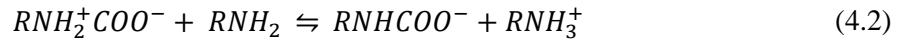


Figure 4.1. BHEA_TS cloud point pressure measurement in the visual cell. The intensity of the light passing through the cell decreases as the pressure approaches the cloud point value.

Except for APTES, all the remaining silanes (DD_TS, CPhe_TS, CPTS and GPTS) in this research followed a similar trend during cloud point pressure measurements. Once the depressurization of APTES-scCO₂ mixture commenced, there was a clear solid precipitation at the bottom of the visual cell (Figure 4.2). This could be attributed to the formation of ammonium carbamate, due to chemical reaction of primary amine groups in APTES with scCO₂. Under the dry condition, the two neighbouring amine groups in the silane react with scCO₂ to form a zwitterion which leads to carbamate formation (Sanz *et al.* 2010). The possible mechanisms for this reaction are presented below:





Since the formation of the solid ammonium carbamate was regarded as unfavourable towards meeting the objectives of this research (pore filling/blockage effect), the APTES was eliminated and was not included in further experiments.



Figure 4.2. Visible deposition of ammonium carbamate during depressurization resulting from a chemical reaction of scCO₂ with APTES.

Given a silane is soluble in supercritical fluids (SCF), one of the factors which has an impact on its solubility is its molecular weight (Kirby and McHugh 1999). As the molecular weight of polymers decreases their solubility increases, and hence their cloud point pressure in a gas decreases (Johnston *et al.* 1998). The measured CP pressures for the non-polymeric silanes used in this research are presented in the second row of Table 4.1. The measured CP pressure data indicate that the selected silanes were soluble at relatively low pressures and had very similar cloud point pressures attributed to their very low but similar molecular weights. As indicated earlier, the objective of the CP pressure measurements and solubility studies were to obtain the minimum pressure required to have a fully dissolved silane in scCO₂ at constant temperature. Subsequently, this information was used to determine the experimental conditions to be used for the silane-scCO₂ chemical treatment process inside the HTSM cell (Section 3.3.4.2) and core-flooding experiments (Section 3.3.9).

Table 4.1. Calculated mass of individual silanes to make up a 2 wt. % solution in the visual cell (internal volume of 20 cc) and the corresponding measured cloud point pressures.

	Silane Agents					
	DD_TS	CPhE_TS	BHEA_TS	GPTS	CPTS	APTES
Mass of silane (g)	0.2964	0.2955	0.2949	0.2953	0.2952	0.2942
CP Pressure (MPa) at 333 K	10.40	10.90	10.72	10.00	9.80	----

4.2 X-Ray Photoelectron Spectroscopy

4.2.1 Supercritical CO₂-based Silylation

Elemental quantification derived from XPS survey spectra of the samples demonstrated that all the substrate were successfully modified with the various silanes with each rock demonstrating similar, trends (full XPS elemental quantification for all the samples are presented in APPENDIX - Table A. 1 to Table A. 4). Generally, for the elements solely attributed to the rock samples and not present in the silane reagents (e.g., *Al* and *Fe*), there is a decrease in their intensity measured for the silylated samples as compared with the control sample, also in general, the atomic concentration of carbon increases for all the samples after silylation. For instance, as can be seen for the Gray Berea substrate (Figure 4.3), when CPTS and CPhe_TS are applied to the surface, the *C* concentration increases from 9.99 % to 12.79 % for CPTS and to 16.99 % for CPhe_TS. The difference in carbon concentration between these two samples is attributed, at least in part, to the larger number of carbon atoms in CPhe_TS compared to CPTS. Furthermore, *Al* is reduced from 9.04 atomic % in the control sample to 8.16 and 7.67 atomic % for CPTS and CPhe_TS, respectively, while an increase in the chloride concentration is due to the silylating reagent.

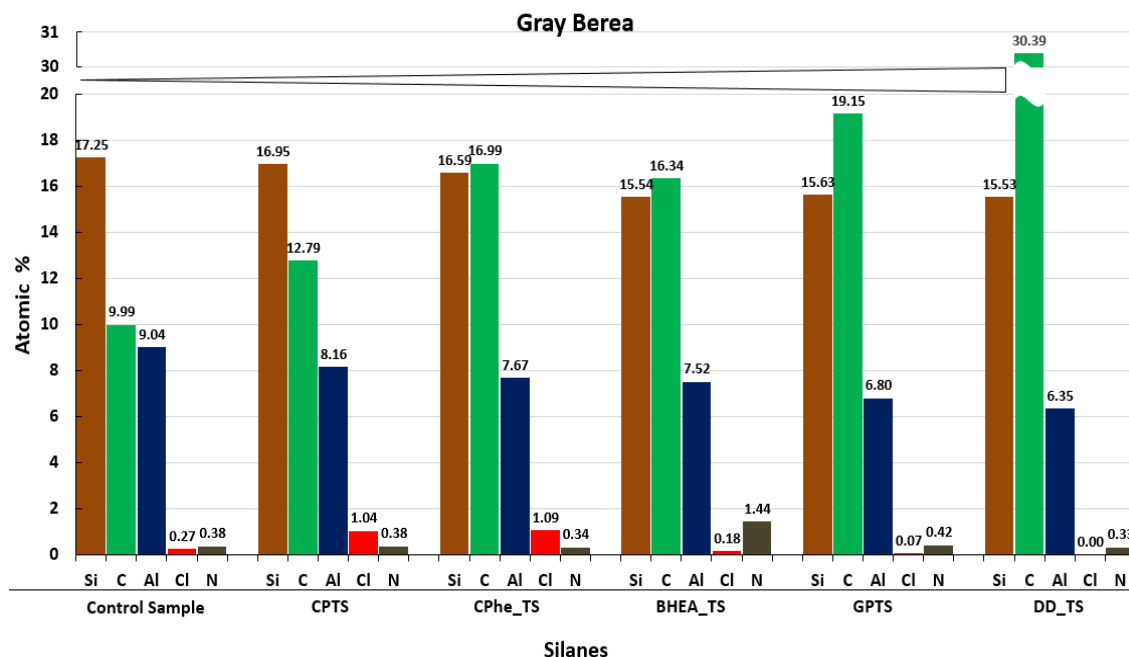


Figure 4.3. The XPS elemental quantification (expressed as atomic %) of Gray Berea substrate before and after treatment. (Graph contains data for Control Sample and aged through scCO₂ method with CPTS, CPhe_TS, BHEA_TS, GPTS and DD_TS).

When BHEA_TS is applied to the Grey Berea, the nitrogen concentration increases from 0.38 atomic % for the control sample to 1.44 atomic % for the treated sample, which is attributed to the presence of amine group in this particular silane (Kartal and Erkey 2010; Chowdhury *et al.* 2013; Combes *et al.* 1999b). For the Gray Berea sandstone, DD_TS results in the highest carbon concentration at 30.39 atomic %, while the suppression of the substrate signal is the most significant for *Al* and *Cl*, which are reduced to 6.35 and 0.00 atomic %, respectively. These results are consistent with expectations because DD_TS has the most *C* atoms per silane unit. Similar trends can be observed for all of the other rock surfaces, with related graphs presented in APPENDIX Figure A. 1 to Figure A. 3.

4.2.2 Conventional vs. Supercritical CO₂-based Silylation

Regardless of the silylation technique employed in modifying the surface chemistry, the mechanisms dictating how the silanes may interact with a surface remain the same (Fadeev and McCarthy 2000, 1999; Combes *et al.* 1999b). However, the efficiency of the technique in achieving acceptable coverage over the surface may vary depending on the actual approach followed and the carrier solvent/fluid used. XPS elemental quantification was conducted on all the substrates modified through conventional silylation method for comparison with scCO₂-based silylation. Figure 4.4, Figure A. 4, Figure A. 5, and Figure A. 6 compares the two silylation methods (conventional vs. scCO₂-based) for all rock samples treated with GPTS and BHEA_TS. In all cases, the treated samples had a larger concentration of *C* and smaller concentration of *Al* compared to the control sample, consistent with the addition of a carbon-rich overlayer on the top surface of the substrate. For both GPTS and BHEA_TS, the scCO₂-based silylation (GPTS-scCO₂ and BHEA_TS-scCO₂) leads to a larger concentration of *C* and a smaller concentration of *Al* when compared with the results of the conventional silylation (GPTS-Conventional and BHEA_TS-Conventional).

In general, the above comparison reveals that using scCO₂ as a carrier during the silylation process would produce comparable or better results than the conventional solvents such as toluene. The scCO₂-based method provides improved mass transfer and faster diffusion due to the considerably lower viscosity of scCO₂ compared to organic solvents leading a more effective delivery of the silanes to a treated surface. This is expected to have contributed towards higher surface chemical adsorption for the case of using scCO₂ as the carrier. Furthermore, as an added advantage, this technique provides solvent-free surfaces after treatment (Sanli and Erkey 2015; Cao, Fadeev, and McCarthy 2001; Sánchez-Vicente *et al.* 2014).

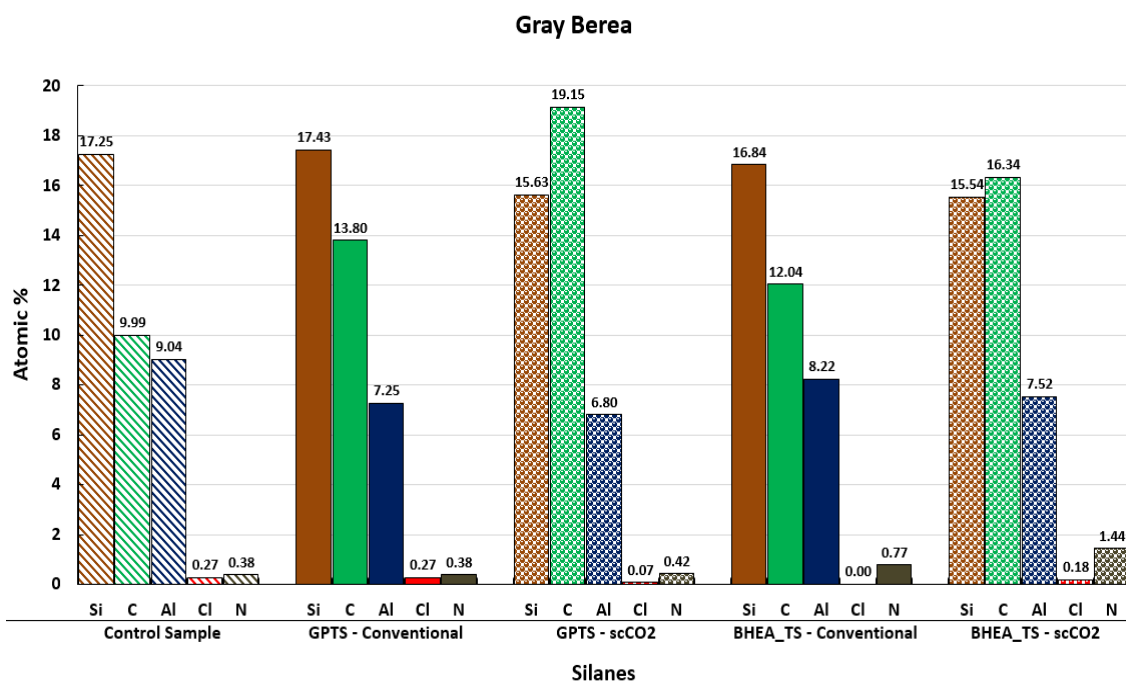
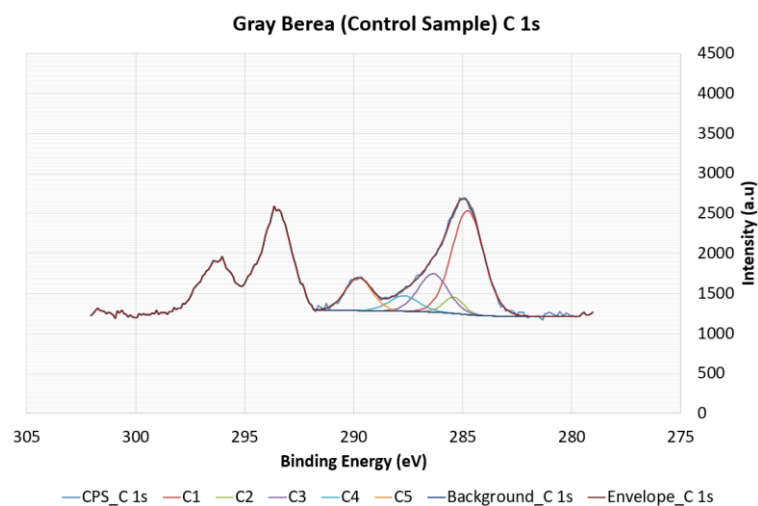


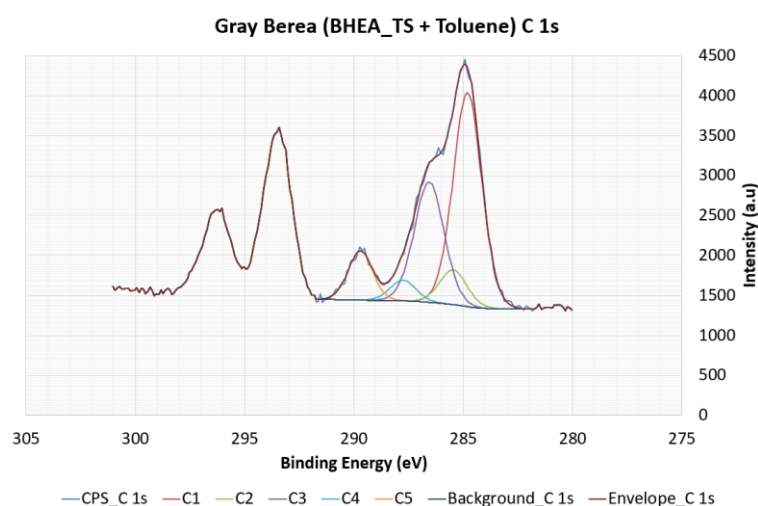
Figure 4.4. The XPS elemental quantification (expressed as atomic %) of Gray Berea substrate before and after treatment. (Graph contains data for Control Sample and aged through scCO₂ method with CPTS, CPhe_TS, BHEA_TS, GPTS and DD_TS).

Evaluating the *Si/C* ratio values for BHEA_TS treated Gray Berea samples provides a means to assess the effectiveness and surface coverage of the two methods. BHEA_TS with a *Si/C* value of 0.08, and the uncoated control with a *Si/C* value of 2.39, it is expected that addition of a silane overlayer would lead to a decrease in *Si/C*. Comparing the *Si/C* values for the two silylation methods, the scCO₂ (0.95) sample has a lower value than the conventional method (1.26), thus providing evidence that the scCO₂ provides improved surface coverage.

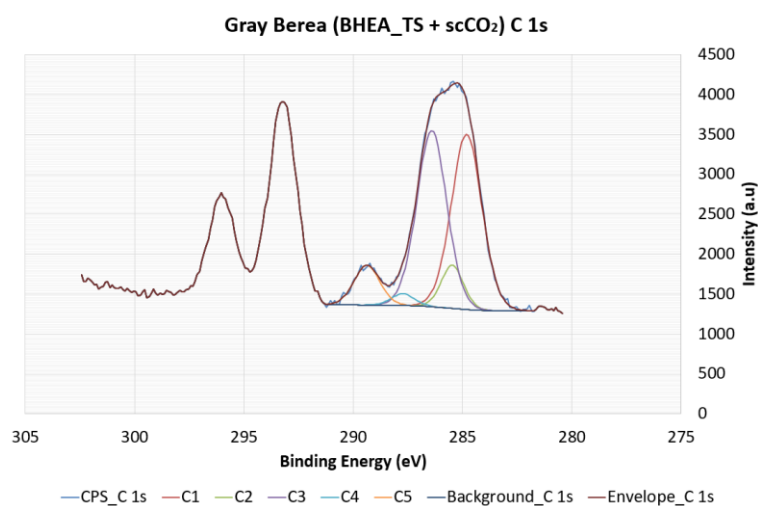
Further insight into the comparison of the two silylation methods can be gained from examination of the high resolution *C 1s* spectra. The spectra presented in Figure 4.5 were fitted using a 5 component using a GL(30) lineshape and a Shirley background. For the control sample, the spectral envelope is consistent with that of adventitious carbon, with the *C 1* peak at 284.8 eV attributed to *C-C* and *C-H*. This is the dominant species that would exist in the sandstone sample, but other inorganic carbon, e.g., carbonate from the Ankerite phase, likely contribute intensity to this spectrum. For the treated samples in both cases, the peak at approximately 286.5 eV (e.g., *C3*: *C-N* and *C-O*) increases relative to the *C 1* peak, and this is attributed to the presence of both *C-N* and *C-O* groups within the BHEA_TS molecule. In the case of scCO₂ treatment, this enhancement is even more pronounced, providing additional evidence that scCO₂ is leading to improved surface coverage relative to toluene treatment (Jakša, Štefane, and Kovač 2013). This demonstrates the surface chemistry that provides more information for atomic percentages and shows that *C-N* and *C-O* groups are present.



(a)



(b)



(c)

Figure 4.5. Selected, representative, high resolution C 1s XPS spectra with peak fitting with a 5 component system for Grey Berea [(a) Control, (b) BHEA_TS in toluene and (c) BHEA_TS in scCO₂]. Tentative assignments for components are as follows: C1 + C2: C-C, C-H, C-Si; C3: C-O, C-N; C4: C=O, N-C=O, O-C-O; C5: CO₃, COOR.

4.3 Contact Angle Measurement and Wettability Alteration Evaluation

4.3.1 Supercritical CO₂-based Silylation

A major mineral component of the substrates used in this study was quartz (Table 3.2). According to previous studies, hydroxylated quartz is a high-energy solid with negatively charged surface groups that can readily attract water molecules (Arkles 2015; Zdziennicka, Szymczyk, and Jańczuk 2009a; Hilner *et al.* 2015a; C. Chen *et al.* 2015; Zhuravlev 1986). Organosilanes have the ability to change the surface properties of a material by covalently bonding to the surface. They may interact with a substrate via strong physical adsorption or by creating a stable covalent bond with the substrate (Xie and Muscat 2005; Arkles *et al.* 2014; López-Periago *et al.* 2014). The surface silylation increases the hydrophobicity of the surface by reducing the high-energy hydroxyl sites for water adsorption and by incorporating organic nonpolar groups (Kim, Arkles, and Pan 2009).

As indicated before (Section 3.3.7), contact angle measurement was used in this research to qualitatively evaluate the degree of wettability alteration in different sandstone rocks silylated with five different organosilanes using a scCO₂-based approach. These measurements were all conducted using scCO₂-brine fluid system under the experimental conditions of 333 K and 21 MPa (Figure 4.6). The brine was pre-equilibrated with CO₂ and all of the control samples were strongly water-wet with contact angles ranging from 6° to 16°. These results are in line with similar studies showing quartz (rock substrate used in this work are composed of 64% to 98% quartz (Table 3.2)) surfaces are strongly water-wet in the presence of CO₂. Saraji *et al.* reported a contact angle of 17.14° at 11.7 MPa and 333 K for quartz-scCO₂-brine system (Saraji *et al.* 2013). Furthermore, Shojai Kaveh *et al.* demonstrated the Bentheimer-scCO₂-brine system to be strongly water-wet (P = 12.74 MP, T = 318 K, and $\Theta \approx 18^\circ$), which is in line with our findings (Shojai Kaveh *et al.* 2014). Previous studies on wettability tendency of pure quartz in CO₂-brine system indicated that with, increased pressure, the wettability of quartz tends to shift from strongly water-wet to less water-wet condition (Al-Yaseri *et al.* 2016; Saraji *et al.* 2013; Arif *et al.* 2015), which is attributed to the reduced surface charges of quartz under the low pH value of the pre-equilibrated brine at elevated pressures. The brine pH reduces from 7 at 0 (partial) CO₂ pressure to 3 at elevated pressures (as a result of dissolution of CO₂ in brine), which has a direct effect on reducing the quartz (negative) surface charges to zero (McGrail and Schaefer 2005). The reduction in surface charges at low pH diminishes the electrostatic forces of quartz and, subsequently, destabilizes the water film covering the surface, which leads to reduced water wetness of quartz at higher pressures (Tokunaga 2012; Jung and Wan 2012). However, the sandstone rocks used in this work contain a number of different minerals, which react differently in CO₂-brine system. Unlike pure quartz, the surface charges of sandstone approaches zero at

pH of ~ 8 , and at lower pH values, the surface becomes more positively charged, which enhances the electrostatic attractions and, subsequently, increases the water film stability on the sandstone surfaces (i.e., enhanced water wettability) (Sharma and Yen 1984; Shojai Kaveh *et al.* 2014).

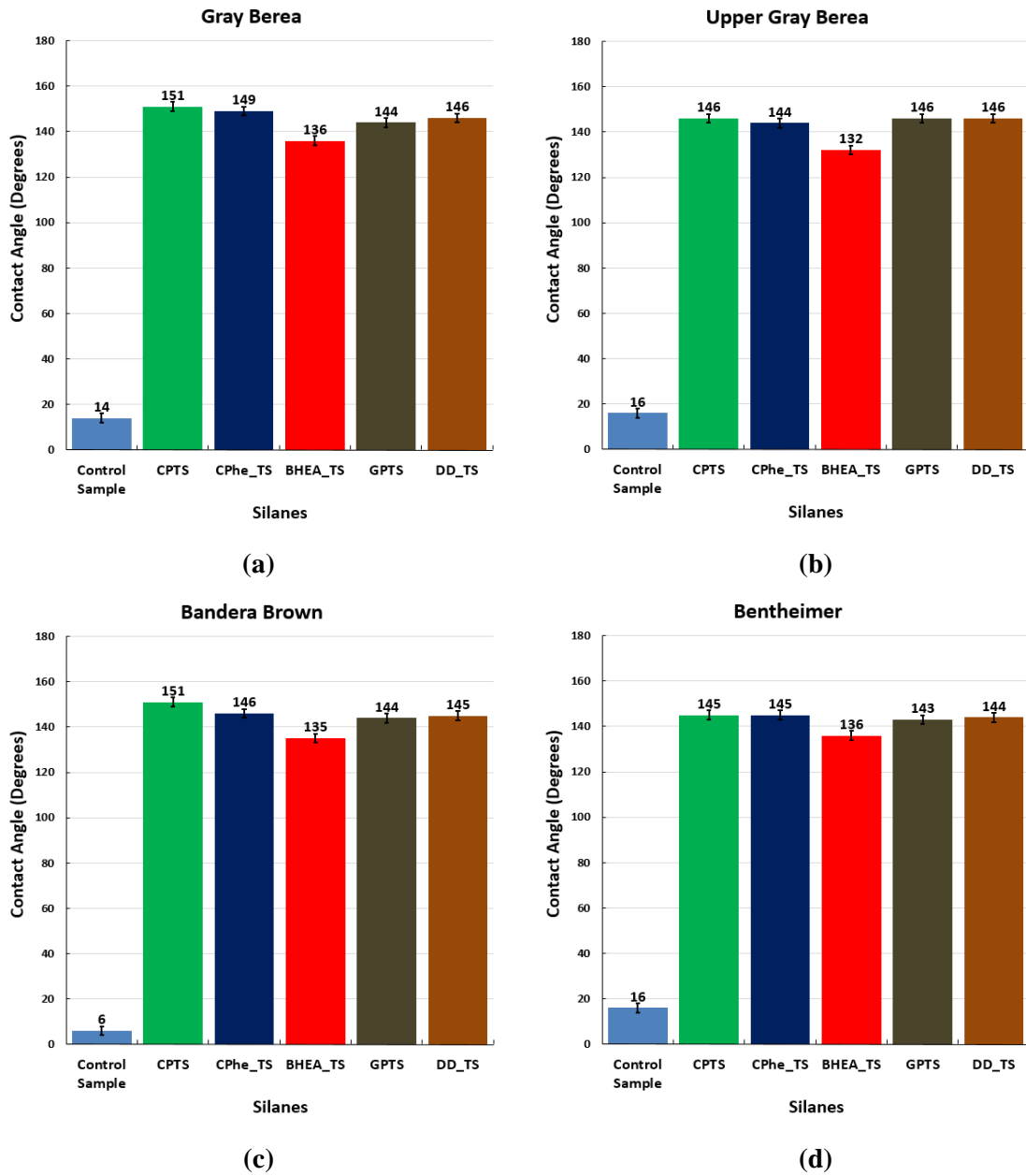


Figure 4.6. Contact angle measurements to show the alteration made by the scCO₂-based silylation of the sandstone rock samples [(a) Gray Berea, (b) Upper Gray Berea, (c) Bandera Brown, and (d) Bentheimer].

Generally, organosilanes used in this work rendered the surface of the rock samples tested hydrophobic to various degrees. The results presented in Figure 4.6 indicate that the highest degree of hydrophobicity was obtained with CPTS and CPhe_TS. Silanes GPTS and DD_TS displayed the second best wettability improvement towards CO₂ on all surfaces, with contact

angles ranging from 143° to 146°; however, the changes between each silane were minimal. Silane BHEA_TS, which contains an amino group and several hydroxyl groups (aside from the methoxy groups that are reactive), induced the least level of hydrophobicity among the silanes tested, with an average contact angle of 135°. The amine present in BHEA_TS could interact with scCO₂ to possibly form a carbamate, which would affect the rock-scCO₂-brine wettability (Combes *et al.* 1999b). The hydrophobicity of a surface modified with organosilanes is governed by the organic substituent on the silanes, the degree of surface coverage, residual unsaturated groups (both from the silane and the surface), and the distribution and orientation of silane on the surface (Arkles 2015). In addition to the hydrophobic alkyl chain in organosilanes, chlorosilanes contain halogen, which can increase the hydrophobicity of the coated surfaces (Priimagi *et al.* 2013; Cavallo *et al.* 2016).

4.3.2 Conventional vs. Supercritical CO₂-based Silylation

All functionalized substrates modified with silanes (with the exception of BHEA_TS) using toluene as a carrier also exhibited a hydrophobic surface (Figure 4.7). However, our data revealed that, for all surfaces treated using the scCO₂-based method, the CO₂ wettability was higher (i.e., higher hydrophobicity) compared to those treated using the conventional method, with the largest difference observed for Bentheimer treated in GPTS ($\Delta\theta \approx 5.6\%$). As a result, silanes may not have gained access to small air-filled cavities and pores scattered over the surface. Hence, the overall silane coverage for these samples may have been further reduced when treated using conventional solvents. The accessibility of pores and cavities would be improved with the use of the scCO₂-based silylation method because scCO₂ has high diffusivity and low viscosity, which can help to deliver the silanes into the cavities and pores more effectively (Zemanian *et al.* 2001; Mccool and Tripp 2005).

It was found that not all the silanes selected for this work would be suitable for use with toluene as a carrier. After deposition of BHEA_TS on the discs of all the rock types, there was clear visual evidence that oligomerization/polymerization had occurred (gel formation). We hypothesize that the amine groups in BHEA_TS could have catalyzed the hydrolysis of the methoxy groups, causing longer molecular chains to form on the surface of the rock. This is the reason why amine-based silanes are often deposited in the vapour phase, although, under certain conditions, it is possible to deposit from the solution phase (Yadav *et al.* 2014). Further investigation is required to validate this hypothesis, but this is beyond the scope of this study.

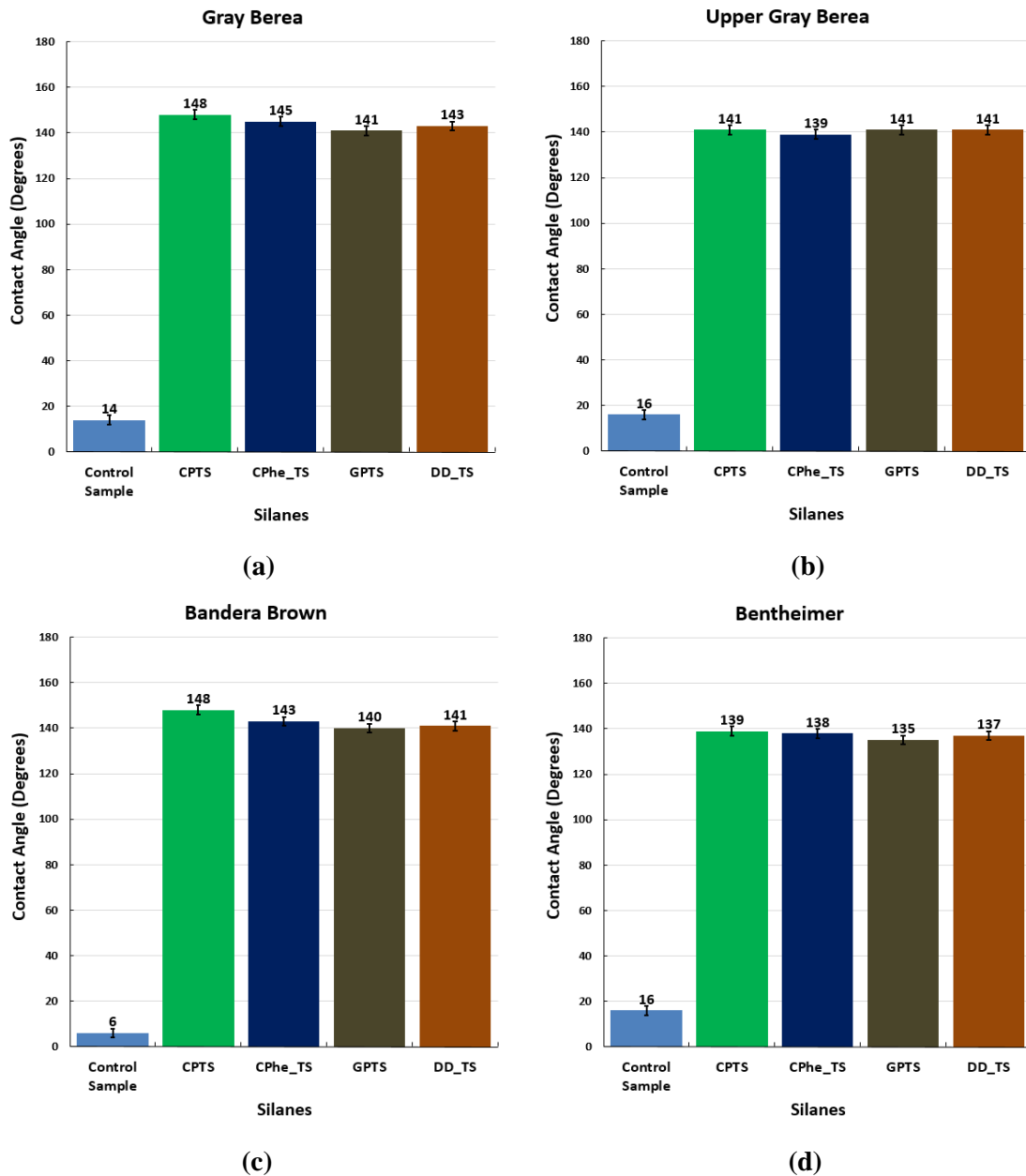


Figure 4.7. Contact angle measurements to show the alteration made by the conventional silylation of the sandstone rock samples [(a) Gray Berea, (b) Upper Gray Berea, (c) Bandera Brown, and (d) Bentheimer].

4.4 Effect of scCO₂-based Silylation on Spontaneous Imbibition

The effectiveness of wettability alteration via in-situ treatment in reducing water uptake in core plugs was investigated through spontaneous imbibition experiments. The results of the spontaneous imbibition of brine versus time in the pre- and post-treated GB.2 sample is presented in Figure 4.8. It is evident that the treated GB.2 imbibed less brine during the course of the experiment (10.7 ml of imbibed brine or final $S_w = 58.9\%$) compared to the pre-treated sample (12.7 ml of imbibed brine or final $S_w = 76.4\%$). Furthermore, by looking closer at the early stages of the experiment, it can be observed that the pre-treated sample has a substantially

higher imbibition rate and reaches a plateau during the first 10 min, and then the rate drops considerably for the remaining experimental time. In contrast, the post-treated sample demonstrates a considerably lower imbibition rate until reaching its plateau after approximately 17 hr. A similar trend was observed in GB.4; however, only minor differences in spontaneous brine imbibition were observed for the other samples (APPENDIX - Figure A. 7, Figure A. 8 and Figure A. 9).

In the research by MA. *et al.* into the wettability characterization from spontaneous imbibition tests, it is indicated that the rate at which the non-wetting phase saturation decreases during such tests is a function of fluids' viscosity ratio, the pore space structure, interfacial tension, core surface boundary condition, and the wettability of the rock surface (MA *et al.* 1999). However, the considerable difference between the performance of our pre- and post-treated samples in uptaking brine is primarily attributed to change in wettability of the samples from strongly water-wet to a less water-wetting condition. That is because all parameters other than wettability were kept constant between our pre- and post-treatment experiments.

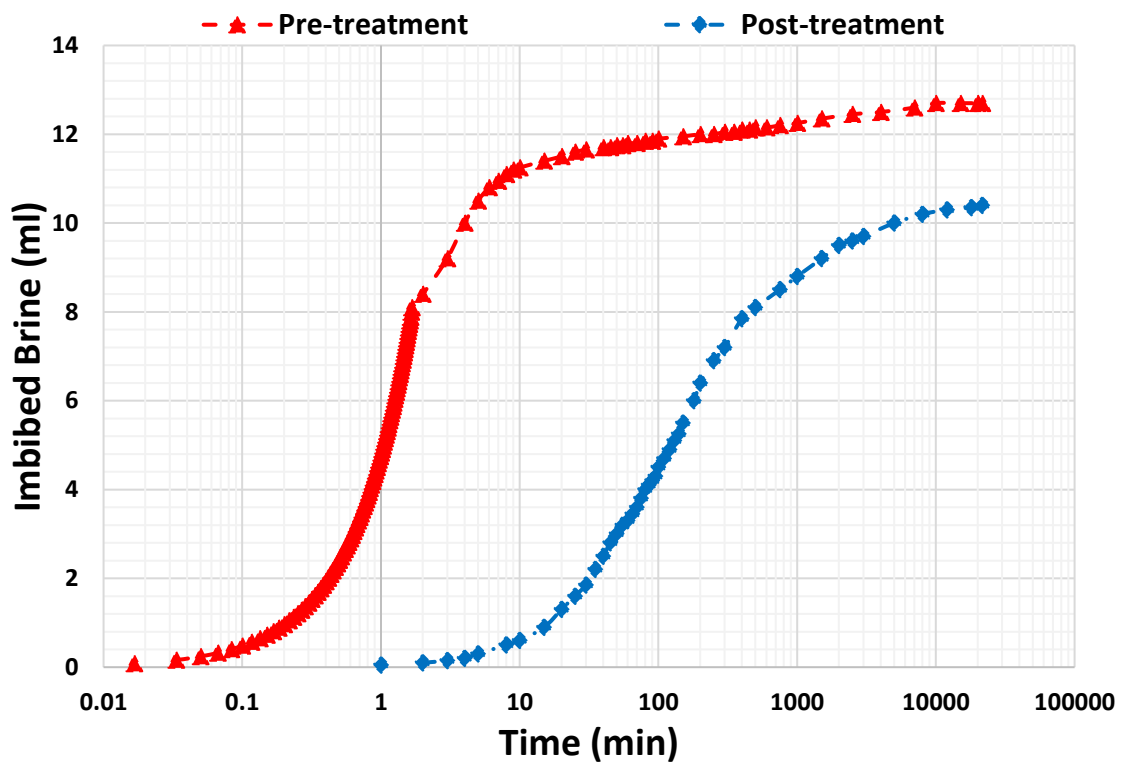


Figure 4.8. Spontaneous brine imbibition versus time in GB.2, pre-treatment (red triangle) and post-treatment (blue diamond).

A summary of the spontaneous imbibition test results for all the core samples is presented in Table 4.2. Despite all the samples exhibiting similar trends, it is evident that after surface silylation a smaller shift in the final water saturation was obtained with samples GB.1 and GB.3

(31.1% and 40.6%, respectively) compared with that achieved with samples GB.2 and GB.4 (50.6% and 58.9%, respectively). As mentioned earlier, after the first two experiments conducted on GB.1 and GB.3, a slight modification was applied in the experimental procedure prior to silylation of GB.2 and GB.4. This modification was done to reduce the negative effect of possible salt precipitation on the pore surfaces prior to the injection of a silane-scCO₂ mixture. The following section provides further elaboration on the wettability alteration process and the rationale behind the above-mentioned procedure modification.

Table 4.2. A summary of the pre- and post-treatment spontaneous imbibition test results.

Sample IDs	Pre-treatment		Post-treatment		Change in Brine Saturation (%)
	Imbibed Brine (ml)	Brine Saturation (%)	Imbibed Brine (ml)	Brine Saturation (%)	
GB.1	12.35	75.6	11.1	68.9	8.86
GB.2	12.7	76.4	10.4	41.1	46.21
GB.3	12.75	77.4	11.25	59.4	23.31
GB.4	12.45	75.5	10.4	49.4	34.57

The wettability of a solid surface with complex chemistry, such as a rock, is strongly influenced by the interactions of fluids with the surfaces; hence, it is important to characterize the surface species of rock samples before undergoing wettability related studies (Shojai Kaveh *et al.* 2014). The main mineral species found in the GB rocks in this study is quartz (see Table 3.2), which according to previous studies, possess negatively charged surface groups (in the presence of water) and high free surface energy (Chen *et al.* 2015; Zdziennicka *et al.* 2009b; Hilner *et al.* 2015b). Subsequently, due to the high polarity of water, water molecules are attracted to the highly charged quartz surface (Hilner *et al.* 2015b; Arkles 2015). Furthermore, it has been well established that in the presence of water, the surface silica (SiO₂) readily reacts with water molecules to form silanol (Si-OH) groups (i.e., the surface becomes hydrated, which promotes water wettability) and to remove these species from the surface, high temperatures and dry conditions must be employed (e.g., temperatures exceeding 475 K and a completely dry environment) (Yang *et al.* 2005; Ma *et al.* 2005; Rovetta and Blacic 1989; Hair 1975). Given the comparatively mild test conditions in this study, the presence of silanol species on the quartz surface is inevitable, and consequently the surface is strongly water-wet. Hence, by coating the hydroxyl groups (-OH) on the surface and reducing the free surface energy of the pore walls, the wettability of the surface can be shifted (Kim *et al.* 2009; Zhuravlev 1986). Application of an appropriate organosilane reduces the water wetness of the surface not only by shielding the hydroxyl groups on the surface but also by incorporating non-polar organic moieties through silylation (Kim *et al.* 2009; Hara *et al.* 2012). However, it must be noted that the effectiveness of silylation is governed by the accessibility of the silane to the surface and the reactivity of the

surface with the organosilane reagent (Kim *et al.* 2009; Gun *et al.* 2000; Combes *et al.* 1999b). The degree of surface coverage of the treatment is governed by the population and accessibility of the hydroxyl groups; consequently, by inadvertently inhibiting these surface species, the silylation coverage could be reduced to varying degrees. For instance, given that the pre-treated samples were flooded with the experimental brine before silylation, a relatively high salt concentration used at this stage with GB.1 and GB.3 could have impacted the reactive sites on their pore surfaces and subsequently reduced the silane coverage. When a lower salinity brine was used to flush and wash out the pore spaces of GB.2 and GB.4 prior to injecting the silane-scCO₂ mixture, more of the hydroxyl groups became available with which the silane agent could react. This can explain the higher shift observed in the final water saturation obtained with samples GB.2 and GB.4 (i.e., lower post-treatment water-wetness) relative to GB.1 and GB.3.

4.5 Core-Flooding Experiments

To understand how the wettability alteration may impact the multiphase flow, detailed scCO₂-brine core-flooding experiments were conducted on the four rock samples used in this study. Figure 4.9 and Figure 4.10 compare the pre- and post-treatment differential pressure profiles across sample GB.2 for the scCO₂ and brine injection stages, respectively. For all four profiles, as expected, the differential pressure begins to increase from the onset of CO₂/brine introduction into the inlet face of the sample, reaching a peak right before breakthrough, after which it starts to decrease, initially fast but more gradual during the latter stages. As indicated by a change in the differential pressure profiles plotted for the scCO₂ injection stage (see Figure 4.9), the scCO₂ breakthrough, as determined from the pressure profiles, is delayed due to the wettability alteration. Additionally, the final quasi-steady-state differential pressure for the post-treated rock is lower than that for the untreated one. The final readings of the differential pressures translate to about a 19% increase in the post-treatment scCO₂ endpoint relative permeability ($\Delta k_{rCO_2}' / k_{rCO_2}' = +19\%$).

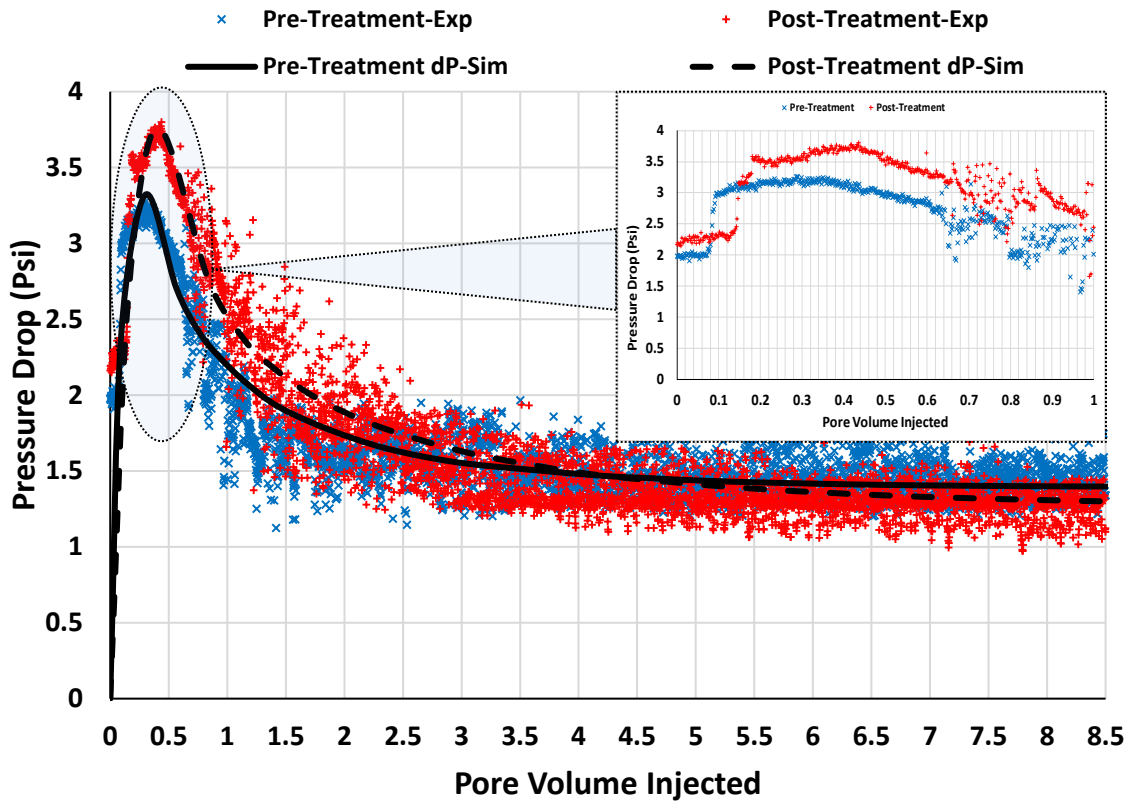


Figure 4.9. Experimental differential pressure (denoted by Exp) vs. pore volumes of CO₂ injected through the GB.2 sandstone sample pre- (blue cross symbol) and post-silylation (red plus symbol) with 2 wt. % of CPTS (inset compares the breakthrough points) Solid and dashed black lines represent the numerical simulation history matched differential pressure for pre- and post-silylation, respectively (denoted by Sim).

A similar trend to that described for the CO₂ injection stage is detected in the differential pressure profiles during the brine injections (Figure 4.10). In general, the differential pressures recorded during the brine injection before treatment are noticeably higher compared to those for the post-treatment, especially towards the end of the two experiments. As clearly visible in the inset, the wettability alteration has delayed the occurrence of brine breakthrough. Further effects of the treatment on the petrophysical and multiphase flow characteristics of the sample are evaluated by calculating the change in its absolute, effective, and relative permeabilities (Table 4.3). As can be seen from Table 4.3, the effective permeability and endpoint relative permeability to brine show noticeable increases after treatment ($\Delta k_{rw}'/k_{rw}' = +61\%$), which is a clear consequence of the induced wettability alteration in this rock sample. Similar differential pressure characteristics as described above for sample GB.2 were observed for the other samples (see Figure A. 10, Figure A. 11, Figure A. 12, Figure A. 13, Figure A. 14 and Figure A. 15).

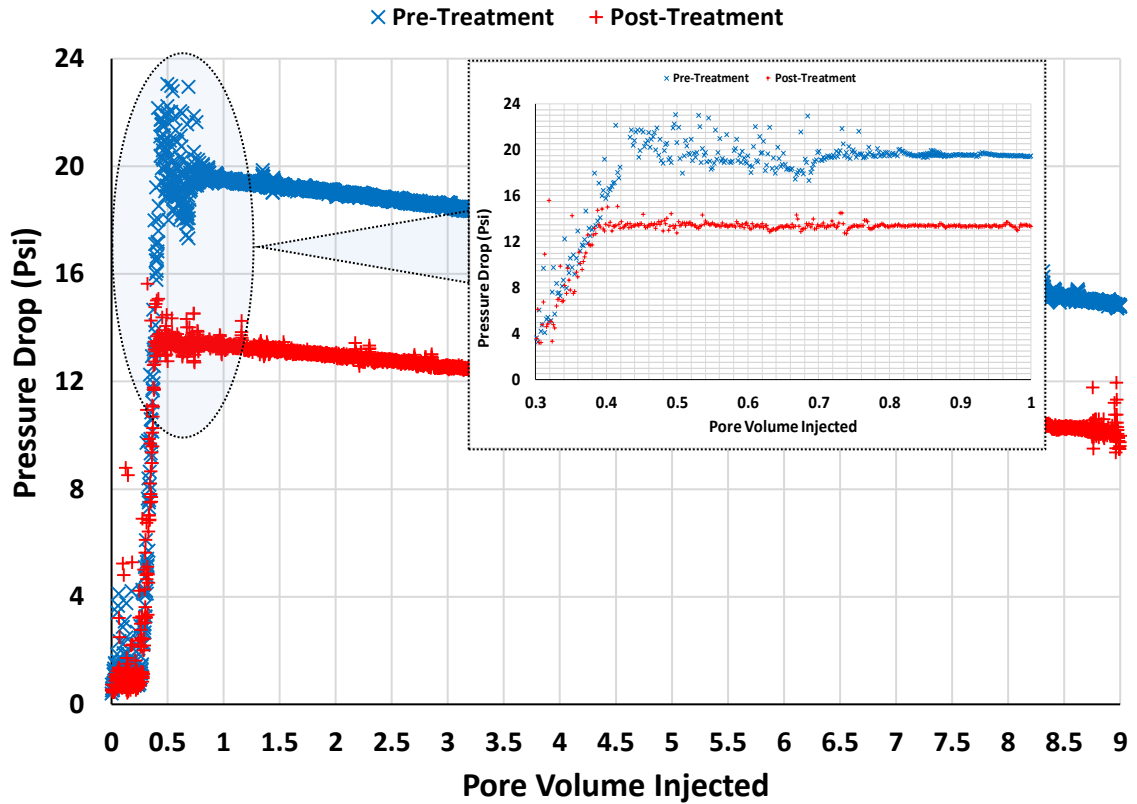


Figure 4.10. Differential pressure vs. pore volumes of brine injected through the GB.2 sandstone sample pre- (blue cross symbol) and post-silylation (red plus symbol) with 2 wt. % of CPTS (inset compares the breakthrough points).

Ultimate brine recovery (see Figure 4.11 and Figure A. 16 - Figure A. 18) was measured by collecting the effluent brine, and subsequently, residual brine saturations were calculated at the end of the drainage floods conducted on the pre- and post-treated samples (see Table 4.3). As can be seen from Table 4.3 and Figure 4.11, the residual brine saturation for GB.2 was reduced from 61.5% to 45.5% due to the silylation treatment, which translates to a 26% improvement in the brine displacement by scCO₂. Similar behaviour in the differential pressure response and brine recovery factors was also observed for samples GB.1, GB.3 and GB.4.

Table 4.3. Brine and CO₂ effective and endpoint relative permeability and brine residual saturation before and after chemical treatment.

Sample IDs	Pre-Treatment				Post-Treatment			
	CO ₂ Injection			Brine Injection	CO ₂ Injection			Brine Injection
	k_{abs} (mD)	k_{rCO_2}'	S_{wri} (%)	k_{rw}'	k_{abs} (mD)	k_{rCO_2}'	S_{wri} (%)	k_{rw}'
GB.1	61	0.28	55	0.148	59	0.35	41	0.22
GB.2	93	0.16	61.5	0.124	86	0.19	45.5	0.2
GB.3	53	0.25	63	0.25	48	0.286	53	0.33
GB.4	74	0.196	61.5	0.147	65	0.25	45.5	0.28

The differential pressure and fluids saturation data recorded during the primary drainage floods were used to generate the relative permeability curves for the pre- and post-treated core samples. Such data for GB.2 are presented in Figure 4.12 (similar data for GB.1, GB.3 and GB.4 are presented in Figure A. 19, Figure A. 20 and Figure A. 21, respectively). The respective relative permeability data were calculated using a numerical history matching technique (Bennion and Bachu 2008; Archer and Wong 1973; Sigmund and McCaffery 1979) for which Sendra software from PRORES AS was used.

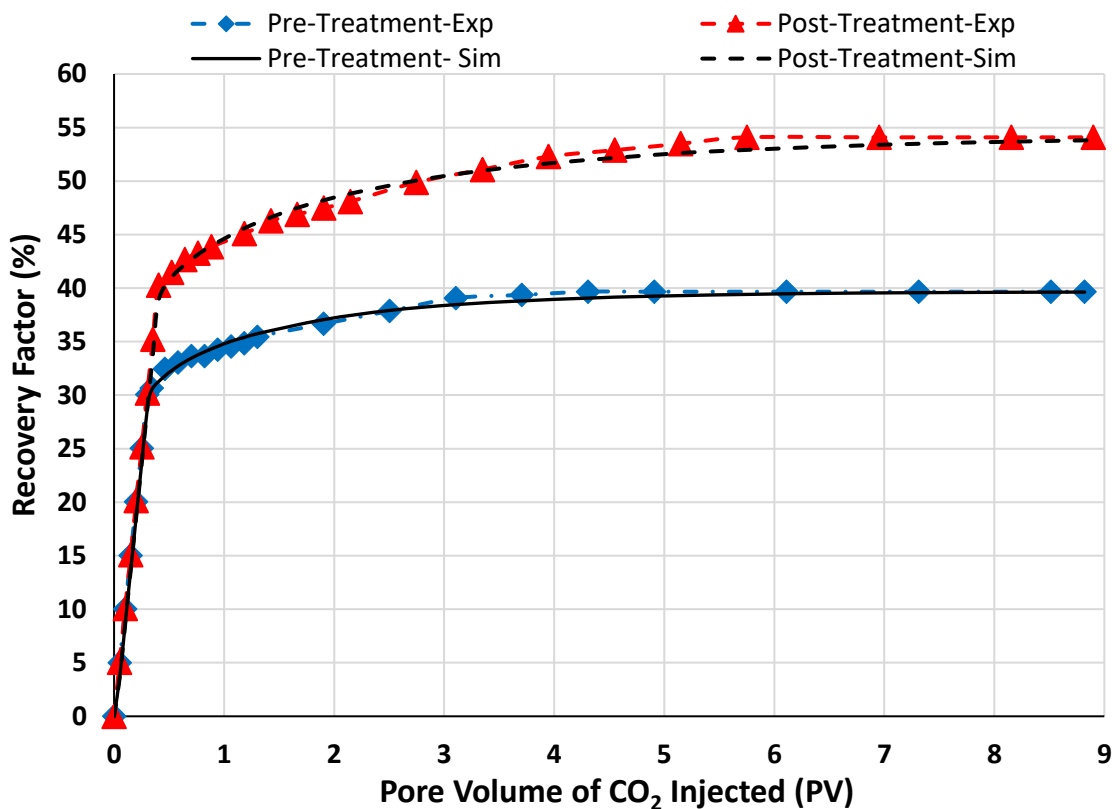


Figure 4.11. Experimental brine recovery profiles during scCO₂ injection for pre-treatment (blue diamond symbol), post-treatment (red triangle symbol) for GB.2 (denoted by Exp). Solid and dashed black lines represent the numerical simulated brine recovery for pre- and post-treatment, respectively (denoted by Sim).

To integrate the spatially dependent experimental data with time and generating the relative permeability curves, a two-phase, 1-dimensional black oil simulation model with a routine automated history matching technique, which is implemented in Sendra software was applied. It is worth noting that this technique has a number of advantages over other relative permeability derivation methods such as JBN (Johnson, Bossler, and Naumann 1959). Other methods can calculate such data for post breakthrough portion of the laboratory experiments and therefore would require the extrapolation of the data before that, whereas, in the above mention technique, relative permeability data can be directly derived for the full range of movable saturations

(Abbas 2016). Additionally, unlike some other commonly used techniques, the above method accounts for the capillary pressure effect during the history matching process. If the capillary pressure data are not available, for history matching and modelling process, a suitable model can be chosen within the software package. Lastly, since one of the commonly employed relative permeability correlations (LET, Corey, Sigmund and McCaffery, etc.) is used during the history matching, the resultant relative permeability data can be readily integrated into a full field numerical simulation model.

A number of history match routines were tried on the experimental data obtained using different models (LET, Corey, Sigmund and McCaffery, etc.) to obtain the relative permeability curves. In the end, the closest match was obtained using the Sigmund and McCaffery (1979) model. Subsequently, this optimal model was adopted for analysing the core-flooding data (Saeedi *et al.* 2016).

The three equations presented below are used in the Sigmund and McCaffery (1979) to empirically correlate the fluid phase saturations to the relative permeability data:

$$S_w^* = \frac{S_w - S_{wi}}{1 - S_{wi} - S_{gi}} \quad (4.3)$$

$$k_{rw} = k_{rw}^0 \frac{(S_w^*)^{N_w} + AS_w^*}{1 + A} \quad (4.4)$$

$$k_{rg} = k_{rg}^0 \frac{(1 - S_w^*)^{N_g} + B(1 - S_w^*)}{1 + B} \quad (4.5)$$

where, S_w^* is the normalized water saturation, S_w is the water saturation measured during the experiment, S_{wi} and S_{gi} are the residual water and gas saturations respectively, k_{rw}^0 and k_{rg}^0 are the endpoint relative permeabilities for water and gas respectively and finally, N_w , N_g , A and B are the empirical constants used for the calculation of relative permeabilities. The values for the empirical parameters which produced the best match of experimental data are presented in Table 4.4. The history matched curves for GB.2 (pre- and post-treatment differential pressure and brine recovery) are presented in Figure 4.9 and Figure 4.11 (refer to APPENDIX figures for GB.1, GB.3 and GB.4 history match data). Relative permeability data for GB.2 are presented in Figure 4.12 (similar data for GB.1, GB.3 and GB.4 are presented in Figure A. 19, Figure A. 20 and Figure A. 21, respectively)

Table 4.4. Best-fit relative permeability parameters for the history matched core-floods using the Sigmund and McCaffery (1979) model.

Sample ID	N_w	N_g	A	B
GB.1 Pre-treatment	7.6632	3.08277	0.23413	0.00435
GB.1 Post-treatment	6.0258	4.35972	0.189827	0.029713
GB.2 Pre-treatment	3.60224	3.33202	0.122618	0.010885
GB.2 Post-treatment	4.19813	3.38595	0.11366	0.028578
GB.3 Pre-treatment	4.00664	2.98626	0.149121	0.007186
GB.3 Post-treatment	3.71125	2.85487	0.176508	0.020602
GB.4 Pre-treatment	3.34198	4.82534	0.162858	0.001
GB.4 Post-treatment	3.8303	2.98214	0.210274	0.007608

By comparing the curves included in Figure 4.12, it is evident that the rock sample became less water-wet; for every CO_2 saturation point, compared to the pre-treatment stage, a higher relative permeability to water is observed for the post-treated sample. Furthermore, despite having a higher endpoint CO_2 relative permeability, the post-treatment relative permeability to CO_2 is considerably lower along the range of saturations that the two pre- and post-treatment CO_2 relative permeability curves share. In addition, the crossover point of a set of relative permeability curves (i.e., the point at which the permeability for both fluid phases are equal) is a significant indicator of wettability, and a shift of this point along the saturation axis (x -axis) indicates how the wettability of the system may have been altered. Wang *et al.* investigated the effect of temperature on relative permeability and displacement efficiency for a waxy oil reservoir and concluded that by lowering the temperature the system became more oil-wet. This effect was observed through the movement of the relative permeability crossover point along the water saturation axis towards lower water saturations, which meant water would flow easier at lower saturations (Wang *et al.* 2019). In another study, the effect of low salinity water flooding (LSWF) in enhanced oil recovery was investigated (Suijkerbuijk *et al.* 2014). The authors concluded that the target rock formation became more water-wet when LSWF was applied by comparing the crossover point of relative permeability curves for the high salinity water flooding (HSWF) with that of the LSWF in an oil-brine system. As indicated in this publication, the crossover point for the HSWF occurred at 61% water saturation compared to 70% water saturation for the LSWF, indicating that when the relative permeability of oil and brine are equal, the water would require to have a higher saturation to flow during LSWF (Suijkerbuijk *et al.* 2014).

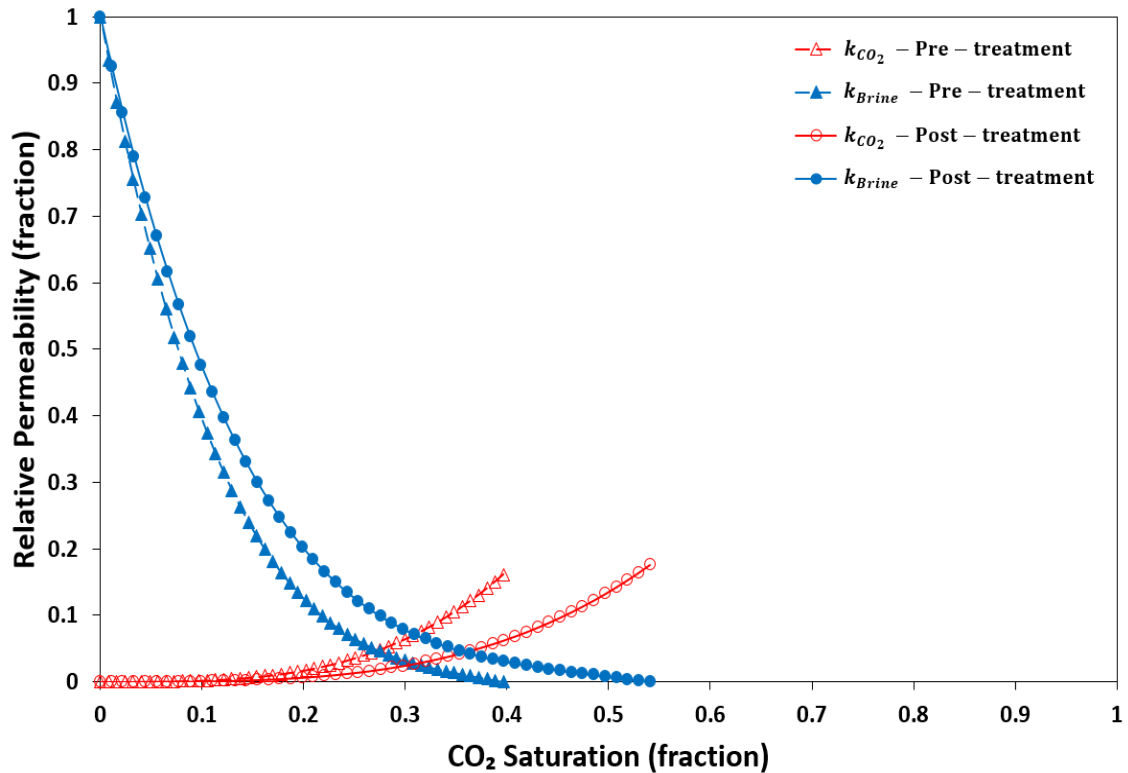


Figure 4.12. Relative permeability curves for the primary drainage conducted on pre-treated (triangle symbol) and post-treated (circle symbol) for GB.2 sample.

A similar comparison was made in this study between the crossover points of the pre- and post-treatment relative permeability curves to qualitatively evaluate the effect of the induced wettability change on the relative permeability of the two fluid phases. From Figure 4.12, it is apparent that after treatment the crossover point has moved towards a higher CO₂ saturation along the x -axis, which can be translated to a change in wettability of the sample toward a less water-wetting state. Similar results were observed for the rest of the rock samples (GB.1, GB.3 and GB.4). Gray Berea.2 and GB.4 demonstrated larger changes in brine relative permeability compared to GB.1 and GB.3. The endpoint relative permeability of brine was enhanced by approximately 61% and 90.5% for GB.2 and GB.4, respectively, while improvement for GB.1 and GB.3 were approximately 49% and 32%, respectively. As explained previously, the effect of salt precipitation on the rock surface may have limited the available reactive sites for the silane reagent to create a bond and subsequently reduced the degree of alkyl hydrophobic attachment to the surface, leading to a higher surface free energy. By flushing samples GB.2 and GB.4 with a low salinity brine prior to the silylation process, more of the mentioned surface silanol groups would become available for creating bonds with the silane reagent. In addition, a comparison between the pre- and post-treatment absolute permeability of the samples indicates that the treatment did not affect this parameter significantly in contrast to the change in brine's relative permeability. The brine absolute permeability of the samples reduced in the range of 3% to 12% with the highest reduction in absolute permeability observed with sample GB.4, which also

indicated the highest change in brine relative permeability improvement of approximately 90%. Silane functionalization of the pore throats in the sample is likely the main cause for any reduction in absolute permeability, which again is an indication that flushing the core with low salinity brine was beneficial for silylation.

4.6 NMR Results

Transverse magnetic relaxation time (T_2) distribution of the fully brine saturated cores pre- and post-treatment were analysed to investigate any possible alteration in pore size distribution. Furthermore, in addition to the recorded volume reading data from the spontaneous imbibition tests, NMR measurements were conducted on the samples after 14 days of imbibition, to control the bias and increase the reliability of the calculated final imbibed brine saturation. Figure 4.13 shows the T_2 spectra generated using the NMR measurements conducted at the above-mentioned saturation stages for GB.2. As mentioned earlier, T_2 distribution of a porous rock may be directly related to the pore size distribution of the rock. As revealed by Figure 4.13, three distinct peaks can be detected from the T_2 spectrum recorded for the fully brine saturated GB.2 at 0.4, 11, and 251 ms, which correspond to three different pore size groups of smallest, medium and largest pore sizes, respectively. By comparing the pre- and post-flooding, it can be seen that the pre- and post-flooding curve are similar, indicating only a minor change in the pore structure. Comparing the T_2 distributions for the fully brine saturated pre- and post-treatment, there is a slight drop in incremental volume at 251 ms (corresponding to the largest pore sizes) as well as a small shift in the transverse relaxation time from 251 ms (pre-treatment) to 225 ms (post-treatment). The functionalization of the pore space with the silane reagent is expected to decrease the porosity only very slightly (i.e., only a monolayer of the functionalization would cover the pore surfaces), therefore, these changes are most likely attributed to the effects of wettability changes on the NMR relaxation mechanism (Freedman *et al.* 2003). Similarly, for the T_2 distribution for the spontaneous imbibition tests, the T_2 curves for pre- and post-treatment samples follow a similar trend. The T_2 distributions basically overlap for the small and medium size pores, but there is a significant change in the incremental volume for the larger pores. This is probably due to a subtle wettability effect on the NMR relaxation but a major one due to a change in the level of pore space filling during the spontaneous imbibition process. Comparison of the T_2 curve of the spontaneously brine saturated sample with that of the fully saturated sample indicates that once the spontaneous imbibition process reaches an equilibrium state, most of the air is trapped within the larger pores. Finally, the cumulative brine volumes within the pore space of the pre- and post-treated GB.2 as measured by NMR tests were 12.57 and 10.45 ml, respectively. These volumes closely match the recorded final data from the spontaneous imbibition tests. Similar trends to those described above for

GB.2 were observed for the rest of the Gray Berea cores (GB.1, GB.3 and GB.4) used, and the relevant data are presented in Figure A. 22, Figure A. 23 and Figure A. 24.

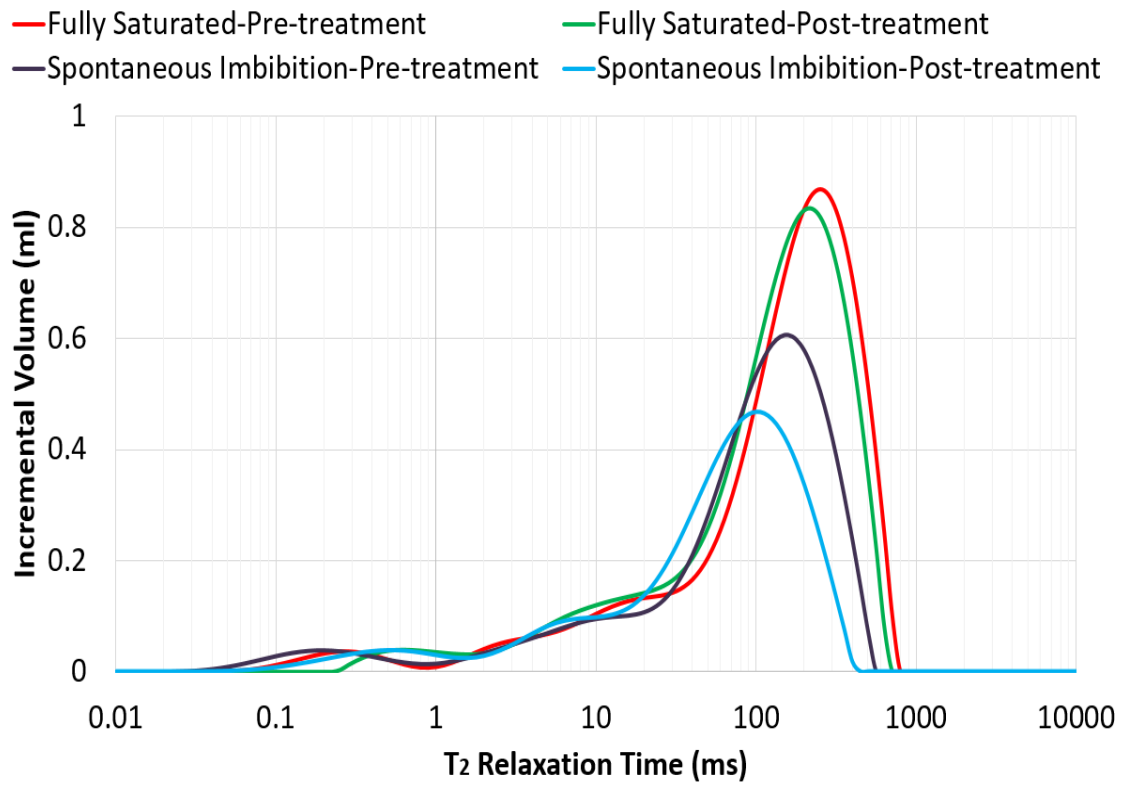


Figure 4.13. NMR derived incremental brine volume for pre- and post-treated GB.2.

Chapter 5 Conclusions, Recommendations and Outlook for Future Work

5.1 Conclusions

A major objective of this work was to develop and test a novel scCO₂-based silylation technique in which supercritical fluids can be used as a carrier solvent for wettability alteration of sandstone reservoir rocks using a range of silane agents. A comprehensive critical analysis of measured XPS data was used to evaluate the effectiveness of the chemical surface coverage as attained using two different deposition routes (Conventional versus scCO₂-based treatments). In order to assess the influence of silylation agents on the degree of wettability alteration of the treated rock substrates, contact angle measurements were employed. To help achieving the other major objective of this research, multiphase flow characteristics of the scCO₂-brine-rock system was evaluated before and after the wettability alteration using a combination of core-flooding and spontaneous imbibition experiments. This resulted in the generation of the much needed experimental data about the effect of wettability on the multiphase flow behaviour of CO₂-brine system under representative conditions.

The followings are the major conclusions drawn from the activities performed in this research, a brief summary of which was presented above.

- Quantitative experimental analysis:
 - Chemical solubility experiments (cloud point pressure measurements) at 333 K indicated that, despite CO₂ not being the strongest solvent, it was capable of dissolving the selected silylation agents (five out of the six selected silanes in this work) at reasonably low pressures (\approx 10 MPa). This outcome indicates that silylation of rock formation through scCO₂-based route can be achieved for a wide range of applications from mild to harsh conditions.
 - Surface chemical analysis using XPS indicated that the scCO₂-based silylation technique would yield a higher degree of surface modification compared to the conventional technique. The above was evident for all of the five silane agents and four rock types tested. This conclusion was found to be consistent with previous research which employed different types of oxide surfaces (e.g., AlO₂, TiO₂, silica mesoporous material, etc.).

- Quantitative experimental data analysis showed that the rock surfaces treated with silane-scCO₂-based mixture would exhibit a higher degree of wettability alteration compared to those treated in conventional solutions. Contact angle measurements indicated that all the sandstone surfaces were strongly water-wet ($6^\circ \leq \Theta \leq 16^\circ$) prior to chemical treatments. Post-treatment, all treated surfaces demonstrated superhydrophobic ($132^\circ \leq \Theta \leq 151^\circ$) behaviour in the presence of scCO₂, with the highest changes evident in those treated using silane-scCO₂ mixtures.
- Qualitative experimental analysis on multiphase flow characteristics of CO₂-brine-sandstone system pre- and post-treatments indicated that:
- The rate of spontaneous brine imbibition into the post-treatment sandstones substantially decreased, demonstrating a shift from strongly water-wet towards weakly water-wet condition. Furthermore, in those samples, the final brine saturation at the conclusion of spontaneous imbibition experiments was considerably less, further confirming the wettability alteration towards a less water-wet state.
 - The calculated relative permeability curves for the drainage floods demonstrated that the post-treatment relative permeability to brine phase was consistently higher. On the other hand, over the pre-treatment mobile saturation range, the post-treatment relative permeability to scCO₂ was lower. However, due to the delayed scCO₂ breakthrough and higher final brine recovery (i.e., lower S_{wr}) for post-treatment samples, the endpoint relative permeability of scCO₂ for these samples was higher. Finally, as expected, the silane treatment caused a clear shift in the crossover point of the relative permeability curves as attributed to the induced wettability alteration. Taking the above points into account, it can be inferred that this treatment technique has the potential to effectively and permanently mitigate water blockage problem around hydrocarbon production wells.
 - During the imbibition displacement, the post-treatment endpoint relative permeability to brine was found to be significantly higher, which is again a clear consequence of the induced wettability alteration in the rock samples.
 - The effect of prior salt precipitation over the quartz surface on the silylation process was qualitatively assessed. The main sites for silane chemical bonding to the quartz surfaces are the silanol groups. In the presence of excess salt deposits, these moieties would be shielded, and therefore the chemical bonding would diminish. In this work,

it was demonstrated that flushing a rock sample's pore space with low salinity brine would remove the salt deposits making these reactive moieties available again for silane molecules to create strong bonds to the quartz surface.

- Comparison between NMR's transverse magnetic relaxation time (T_2) distribution of rock samples pre- and post-treatment indicated that, despite the noticeable wettability alteration achieved through scCO₂-based silylation, the change in the pore size distribution of the core plugs were negligible. These findings were further confirmed by a minimal change in the absolute permeability of the core plugs as measured in the dry state before and after treatments.

5.2 Recommendations and outlook for future work

This study successfully demonstrated the potential of in-situ application of scCO₂-based silylation of sandstone rocks at elevated pressure and temperature. Additionally, it unravelled multiphase flow characteristics of scCO₂-brine-sandstone pre- and post-treatment, which is of paramount importance in such systems. The following recommendations may be followed for any future research built upon the findings of this work:

- The experimental works for this research were performed in a single pressure and temperature condition. It is recommended to perform similar work on a wider range of experimental conditions to assess the possible effect of such variables on the results.
- The core plugs used for fluid displacement experiments all had a similar range of porosity and permeability. Since such parameters influence the multiphase flow characteristic of CO₂-brine, conducting similar experiments on a wider range of porosity and permeability would be beneficial to improve the result of this work.
- The focus of this study was on wettability alteration of sandstone rocks; however, a considerable portion of hydrocarbon reservoirs and saline aquifers are located in carbonate formations (22% of Earth's crust is built of carbonate rocks). Therefore, conducting similar experimental work on carbonate rocks may be strong interest in the technical community.

References

- A.W., Neumann, and Good R.J. 1979. *Techniques of Measuring Contact Angles*. Surface and Colloid Science: Springer, Boston, MA. <https://doi.org/https://doi.org/10.1007>.
- Abbas, Mamudu. 2016. "An Extension of Johnson, Bossler and Neumann JBN Method for Calculating Relative Permeabilities." *Proceedings - SPE Annual Technical Conference and Exhibition 2016–Janua*.
- Abdallah, Wael, Jill S. Buckley, Andrew Carnegie, John Edwards, Bernd Herold, Edmund Fordham, Arne Graue, et al. 2007. "Fundamentals of Wettability." *Oilfield Review*, 44–61. https://www.slb.com/~media/Files/resources/oilfield_review/ors07/sum07/p44_61.pdf.
- Abeyasinghe, Kumuduni Prasangika, Ingebret Fjelde, and Arild Lohne. 2012. "Dependency of Remaining Oil Saturation on Wettability and Capillary Number." *Society of Petroleum Engineers - SPE Saudi Arabia Section Technical Symposium and Exhibition 2012*, no. 1973: 201–12. <https://doi.org/10.2118/160883-ms>.
- Adam, Farook, Hasnah Osman, and Kasim Mohammed Hello. 2009. "The Immobilization of 3-(Chloropropyl)Triethoxysilane onto Silica by a Simple One-Pot Synthesis." *Journal of Colloid and Interface Science* 331 (1): 143–47. <https://doi.org/10.1016/j.jcis.2008.11.048>.
- Agbalaka, Chinedu, Abhijit Y. Dandekar, Shirish L. Patil, Santanu Khataniar, and James R. Hemsath. 2008. "The Effect of Wettability on Oil Recovery: A Review." *SPE Asia Pacific Oil and Gas Conference and Exhibition 2008 - "Gas Now: Delivering on Expectations"* 1: 73–85. <https://doi.org/10.2118/114496-ms>.
- Ahmed, Tarek. 2001. *Reservoir Engineering Handbook*. 2nd Ed. Houston: Gulf Professional Publishing.
- Aissaoui, Nesrine, Latifa Bergaoui, Jessem Landoulsi, Jean François Lambert, and Souhir Boujday. 2012. "Silane Layers on Silicon Surfaces: Mechanism of Interaction, Stability, and Influence on Protein Adsorption." *Langmuir* 28 (1): 656–65. <https://doi.org/10.1021/la2036778>.
- Al-Anssari, Sarmad., Muhammad. Arif, Shaobin. Wang, Ahmed. Barifcani, Maxim. Lebedev, and Stefan. Iglauer. 2017a. "Wettability of Nano-Treated Calcite/CO₂/Brine Systems: Implication for Enhanced CO₂ Storage Potential." *International Journal of Greenhouse Gas Control* 66 (November 2016): 97–105. <https://doi.org/10.1016/j.ijggc.2017.09.008>.
- Al-Anssari, Sarmad, Muhammad Arif, Shaobin Wang, Ahmed Barifcani, Maxim Lebedev, and Stefan Iglauer. 2017b. "CO₂ Geo-Storage Capacity Enhancement via Nanofluid Priming." *International Journal of Greenhouse Gas Control* 63 (May): 20–25. <https://doi.org/10.1016/j.ijggc.2017.04.015>.
- Al-Anssari, Sarmad, Ahmed Barifcani, Shaobin Wang, Lebedev Maxim, and Stefan Iglauer. 2016. "Wettability Alteration of Oil-Wet Carbonate by Silica Nanofluid." *Journal of Colloid and Interface Science* 461: 435–42. <https://doi.org/10.1016/j.jcis.2015.09.051>.

- Al-Khdheawi, Emad A., Stephanie Vialle, Ahmed Barifcani, Mohammad Sarmadivaleh, and Stefan Iglauer. 2017a. "Impact of Reservoir Wettability and Heterogeneity on CO₂-Plume Migration and Trapping Capacity." *International Journal of Greenhouse Gas Control* 58: 142–58. <https://doi.org/10.1016/j.ijggc.2017.01.012>.
- . 2017b. "Influence of Rock Wettability on CO₂ Migration and Storage Capacity in Deep Saline Aquifers." *Energy Procedia* 114 (November 2016): 4357–65. <https://doi.org/10.1016/j.egypro.2017.03.1587>.
- . 2018. "Enhancement of CO₂ Trapping Efficiency in Heterogeneous Reservoirs by Water-Alternating Gas Injection." *Greenhouse Gases: Science and Technology* 8 (5): 920–31. <https://doi.org/10.1002/ghg.1805>.
- Al-Shalabi, Emad W., and Kamy Sepehrnoori. 2016. "A Comprehensive Review of Low Salinity/Engineered Water Injections and Their Applications in Sandstone and Carbonate Rocks." *Journal of Petroleum Science and Engineering* 139: 137–61. <https://doi.org/10.1016/j.petrol.2015.11.027>.
- Al-Yaseri, Ahmed Z., Maxim Lebedev, Ahmed Barifcani, and Stefan Iglauer. 2016. "Receding and Advancing (CO₂+brine+quartz) Contact Angles as a Function of Pressure, Temperature, Surface Roughness, Salt Type and Salinity." *Journal of Chemical Thermodynamics* 93: 416–23. <https://doi.org/10.1016/j.jct.2015.07.031>.
- Alotaibi, M. B., and H. A. Nasr-El-Din. 2009. "Chemistry of Injection Water and Its Impact on Oil Recovery in Carbonate and Clastic Formations." *Proceedings - SPE International Symposium on Oilfield Chemistry* 1 (2001): 512–21. <https://doi.org/10.2118/121565-ms>.
- Amott, E. 1958. "Observations Relating to the Wettability of Porous Rock." *Petroleum Transactions, AIME* 216: 156–62.
- Anderson, W.G. 1987. "Wettability Literature Survey-Part 4: Effects of Wettability on Capillary Pressure." *Journal of Petroleum Technology*, no. October: 1283–1300. <https://doi.org/10.2118/15271-PA>.
- Anderson, W.G. 1987. "Wettability Literature Survey-Part 5: The Effects of Wettability on Relative Permeability." *Journal of Petroleum Technology*, 1453–68.
- Anderson, W. 1987. "Wettability Literature Survey-Part 6: Effect of Wettability on Waterflooding." *Journal of Petroleum Technology*, no. December: 1605–22. <https://doi.org/10.2118/16471-PA>.
- Anderson, William. 1986. "Wettability Literature Survey-Part 2 : Wettability Measurement." *Journal of Petroleum Technology*, 1246–62.
- Anderson, William G. 1986. "Wettability Literature Survey-Part 1 : Rock / Oil /Brine Interactions and the Effects of Core Handling on Wettability." *Journal of Petroleum Technology*, no. October: 1125–40. <https://doi.org/10.2118/13932-PA>.
- Archer, J. S., and S. W Wong. 1973. "Use of a Reservoir Simulator To Interpret Waterflood Data Laboratory." *SPE Journal* 3551 (13): 343–47.

- Arif, Muhammad, Ahmed Z. Al-Yaseri, Ahmed Barifcani, Maxim Lebedev, and Stefan Iglauer. 2015. "Impact of Pressure and Temperature on CO₂-brine-mica Contact Angles and CO₂-brine Interfacial Tension: Implications for Carbon Geo-Sequestration." *Journal of Colloid and Interface Science* 462: 208–15. <https://doi.org/10.1016/j.jcis.2015.09.076>.
- Arif, Muhammad, Maxim Lebedev, Ahmed Barifcani, and Stefan Iglauer. 2017. "CO₂ Storage in Carbonates: Wettability of Calcite." *International Journal of Greenhouse Gas Control* 62 (May): 113–21. <https://doi.org/10.1016/j.ijggc.2017.04.014>.
- Arkles, Barry. 2015. "Hydrophobicity, Hydrophilicity and Silane Surface Modification." *Gelest Inc, Morrisville, PA*, 2015.
- Arkles, Barry, Annalese Maddox, Mani Singh, Joel Zazyczny, and Janis Matisons. 2014. "Silane Coupling Agents: Connecting Across Boundaries, 3rd Edn." *Gelest Inc, Morrisville, PA*, 2014. www.gelest.com.
- Austad, Tor, Alireza RezaeiDoust, and Tina Puntervold. 2010. "Chemical Mechanism of Low Salinity Water Flooding in Sandstone Reservoirs." *Proceedings - SPE Symposium on Improved Oil Recovery* 1: 679–95. <https://doi.org/10.2523/129767-ms>.
- Avraam, D.G., and A.C. Payatakes. 1995. "Flow Regimes and Relative Permeabilities during Steady-State Two-Phase Flow in Porous Media." *Journal of Fluid Mechanics* 293 (January): 207–36. <https://doi.org/10.1017/S0022112095001698>.
- Baklid, Alan, Ragnhild Korbol, and Geir Owren. 1996. "Sleipner Vest CO₂ Disposal, CO₂ Injection Into A Shallow Underground Aquifer." *Society of Petroleum Engineers*, 269–77. <https://doi.org/https://doi.org/10.2118/36600-MS>.
- Barnum, R. S., F. P. Brinkman, T. W. Richardson, and A. G. Spillette. 1995. "Gas Condensate Reservoir Behaviour: Productivity and Recovery Reduction Due to Condensation." *Proceedings - SPE Annual Technical Conference and Exhibition* Sigma: 677–87. <https://doi.org/10.2523/30767-ms>.
- Bennion, B., G. Sarioglu, M. Chan, T. Hirata, D. Courtnage, and J. Wansleben. 1993. "Steady-State Bitumen-Water Relative Permeability Measurements at Elevated Temperatures in Unconsolidated Porous Media." In *SPE: International Thermal Operations Symposium*, Society of Petroleum Engineers. California.
- Bennion, D. Brant, and Stefan Bachu. 2008. "Drainage and Imbibition Relative Permeability Relationships for Supercritical CO₂/Brine and H₂S/Brine Systems in Intergranular Sandstone, Carbonate, Shale, and Anhydrite Rocks." *SPE Reservoir Evaluation and Engineering* 11 (3): 487–96. <https://doi.org/doi:10.2118/99326-PA>.
- Bennion, D.B., F.B. Thomas, A.K.M. Jamaluddin, and T. Ma. 1998. "The Effect of Trapped Critical Fluid Saturations on Reservoir Permeability and Conformance." *Hycal Energy Research Laboratories Ltd* 98 (8).
- Bernard, George G. 1967. "Effect of Floodwater Salinity on Recovery of Oil from Cores Containing Clays." *Society of Petroleum Engineers - SPE California Regional Meeting, CRM 1967*.

<https://doi.org/10.2523/1725-ms>.

- Berntsen, Andreas, Jelena Todorovic, Martin Røphaug, Malin Torsæter, Elvia Anabela Chavez Panduro, and Kamila Gawel. 2019. "Salt Clogging during Supercritical CO₂ Injection into a Downscaled Borehole Model." *International Journal of Greenhouse Gas Control* 86 (April): 201–10. <https://doi.org/10.1016/j.ijggc.2019.04.009>.
- Bikkina, Prem Kumar. 2011. "Contact Angle Measurements of CO₂-Water-Quartz/Calcite Systems in the Perspective of Carbon Sequestration." *International Journal of Greenhouse Gas Control* 5 (5): 1259–71. <https://doi.org/10.1016/j.ijggc.2011.07.001>.
- Bloch, F, WW Hansen, and M Packard. 1946. "Nuclear Induction." *Physical Review* 69: 127. <https://doi.org/10.1103/PhysRev.70.460>.
- Bradford, Scott A., and Feike J. Leij. 1995. "Wettability Effects and Scaling Two- and Three-Fluid Capillary Pressure-Saturation Relations." *Environmental Science and Technology* 29 (6): 1446–55.
- Brandon, Simon, and Abraham Marmur. 1996. "Simulation of Contact Angle Hysteresis on Chemically Heterogeneous Surfaces." *Journal of Colloid and Interface Science* 183 (2): 351–55. <https://doi.org/10.1006/jcis.1996.0556>.
- Bray, Christopher L, Bien Tan, Colin D Wood, and Andrew I Cooper. 2005. "High-Throughput Solubility Measurements of Polymer Libraries in Supercritical Carbon Dioxide." *Journal of Materials Chemistry* 15 (4): 456–59. <https://doi.org/10.1039/b415343j>.
- Brown, Robert J.S., and Irving Fatt. 1956. "Measurements of Fractional Wettability of Oil Fields Rocks by the Nuclear Magnetic Relaxation Method." *Society of Petroleum Engineers - Fall Meeting of the Petroleum Branch of AIME, FM 1956*. <https://doi.org/10.2523/743-g>.
- Buckley, J. S., and Y. Liu. 1998. "Some Mechanisms of Crude Oil/Brine/Solid Interactions." *Journal of Petroleum Science and Engineering* 20 (3–4): 155–60. [https://doi.org/10.1016/S0920-4105\(98\)00015-1](https://doi.org/10.1016/S0920-4105(98)00015-1).
- Buckley, Jill S., Christophe Bousseau, and Yu Liu. 1996. "Wetting Alteration by Brine and Crude Oil: From Contact Angles to Cores." *SPE Journal* 1 (3): 341–50. <https://doi.org/10.2118/30765-PA>.
- Cao, Chuntao, Alexander Y Fadeev, and Thomas J Mccarthy. 2001. "Reactions of Organosilanes with Silica Surfaces in Carbon Dioxide." *Langmuir* 17: 757–61. <https://doi.org/10.1021/la000849t>.
- Carr, H Y, and E M Purcell. 1954. "Effects of Diffusion on Free Precession Experiments." *Physical Review* 94 (3): 630–38.
- Carré, Alain, Jean-Claude Gastel, and Martin E Shanahan. 1996. "Viscoelastic Effects in the Spreading of Liquids." *Nature* 379: 432–434. <https://doi.org/10.1038/379432a0>.
- Cavallo, Gabriella, Pierangelo Metrangolo, Roberto Milani, Tullio Pilati, Arri Priimagi, Giuseppe Resnati, and Giancarlo Terraneo. 2016. "The Halogen Bond." *Chemical Reviews* 116 (4): 2478–2601. <https://doi.org/10.1021/acs.chemrev.5b00484>.
- Center For Climate And Energy Solutions. 2020. "Global Emissions." Center For Climate And Energy Solutions - C2ES. 2020. <https://www.c2es.org/content/international-emissions/> (accessed May 20,

2020).

- Chalbaud, C, M Robin, J-m Lombard, F Martin, P Egermann, and H Bertin. 2009. "Interfacial Tension Measurements and Wettability Evaluation for Geological CO₂ Storage." *Advances in Water Resources* 32 (1): 98–109. <https://doi.org/10.1016/j.advwatres.2008.10.012>.
- Chaudhary, Kuldeep, M. Bayani Cardenas, William W. Wolfe, Jessica A. Maisano, Richard A. Ketcham, and Philip C. Bennett. 2013. "Pore-Scale Trapping of Supercritical CO₂ and the Role of Grain Wettability and Shape." *Geophysical Research Letters*. <https://doi.org/10.1002/grl.50658>.
- Chegenizadeh, Negin, Ali Saeedi, and Xie Quan. 2017. "Most Common Surfactants Employed in Chemical Enhanced Oil Recovery." *Petroleum* 3 (2): 197–211. <https://doi.org/10.1016/j.petlm.2016.11.007>.
- Chen, Cong, Ning Zhang, Weizhong Li, and Yongchen Song. 2015. "Water Contact Angle Dependence with Hydroxyl Functional Groups on Silica Surfaces under CO₂ Sequestration Conditions." *Environmental Science & Technology* 49 (24): 14680–87. <https://doi.org/10.1021/acs.est.5b03646>.
- Chen, Her Yuan, Dewi Triarti Hidayati, and Lawrence W. Teufel. 1998. "Estimation of Permeability Anisotropy and Stress Anisotropy from Interference Testing." In *Proceedings - SPE Annual Technical Conference and Exhibition*. Vol. 1999–Sept. New Orleans, Louisiana. <https://doi.org/10.2523/49235-ms>.
- Chen, P, D. Y Kwok, R. M Prokop, O. I del Rio, S. S Susnar, and A. W Neumann. 1998. "Axisymmetric Drop Shape Analysis (ADSA) and Its Applications." *Studies in Interface Science* 6 (C): 61–138. [https://doi.org/10.1016/S1383-7303\(98\)80019-7](https://doi.org/10.1016/S1383-7303(98)80019-7).
- Chevron. 2019. "Gorgon Carbon Dioxide Injection Project Gorgon Project Overview." <https://australia.chevron.com/-/media/australia/publications/documents/gorgon-co2-injection-project.pdf>.
- Chilingar, George V., and T. F. Yen. 1983. "Some Notes on Wettability and Relative Permeabilities of Carbonate Reservoir Rocks, II." *Energy Sources* 7 (1): 67–75. <https://doi.org/10.1080/00908318308908076>.
- Chiquet, P, D Broseta, and S Thibeau. 2007. "Wettability Alteration of Caprock Minerals by Carbon Dioxide." *Geofluids* 7: 112–22. <https://doi.org/10.1111/j.1468-8123.2007.00168.x>.
- Chowdhury, Firoz Alam, Hidetaka Yamada, Takayuki Higashii, Kazuya Goto, and Masami Onoda. 2013. "CO₂ Capture by Tertiary Amine Absorbents: A Performance Comparison Study." *Industrial & Engineering Chemistry Research* 52 (24): 8323–31. <https://doi.org/10.1021/ie400825u>.
- Coates, G.R., L. Xiao, and G.M Prammer. 1999. *NMR Logging Principles & Applications*. Halliburton Energy Services.
- Combes, J. R., L. D. White, and C. P. Tripp. 1999a. "Chemical Modification of Metal Oxide Surfaces in Supercritical CO₂: In Situ Infrared Studies of the Adsorption and Reaction of Organosilanes on Silica." *Langmuir*. <https://doi.org/10.1021/la990495+>.
- Combes, J R, L D White, and C P Tripp. 1999b. "Chemical Modification of Metal Oxide Surfaces in

- Supercritical CO₂: In Situ Infrared Studies of the Adsorption and Reaction of Organosilanes on Silica.” *Langmuir* 15 (2): 7870–75.
- Cook, Peter. J. 2007. “Inquiry into Geosequestration.” *House of Representative Science and Innovation Committee*. <http://www.aph.gov.au/house/committee/scin/geosequestration/subs/sub36.pdf>.
- Craddock, Henry A. 2018. *Oilfield Chemistry and Its Environmental Impact*. John Wiley & Sons.
- Craig, Forrest F. 1971. *The Reservoir Engineering Aspects of Waterflooding*. Volume 3 ed. Society of Petroleum Engineers, Richardson, Texas.
- Crotti, M. A., and J. A. Rosbaco. 1998. “Relative Permeability Curves: The Influence of Flow Direction and Heterogeneities. Dependence of End Point Saturations on Displacement Mechanisms.” *Proceedings - SPE Symposium on Improved Oil Recovery*, 39–45. <https://doi.org/10.2523/39657-ms>.
- Darcy, Henry. 1856. “Les Fontaines Publiques de La Ville de Dijon.” *The Public Fountains of the City of Dijon* Dalmont. (Paris).
- Denekas, M.O, C.C Mattax, and G.t Davis. 1959. “Effect of Crude Oil Componenets on Rock Wettability.”
- Desimone, Joseph M. 2014. “Practical Approaches to Green Solvents.” *Science* 297 (5582): 799–803. <https://doi.org/10.1126/science.1069622>.
- Diebold, Roger M., and David R. Clarke. 2012. “Smooth, Aggregate-Free Self-Assembled Monolayer Deposition of Silane Coupling Agents on Silicon Dioxide.” *Langmuir* 28 (44): 15513–20. <https://doi.org/10.1021/la303377w>.
- Donaldson, Erie C, and Rexd Thomas. 1971. “Microscopic Observations and of Oil Displacement Systems in Water-Wet and Oil-Wet Systems.” *Society of Petroleum Engineers*. <https://doi.org/10.2118/3555-MS>.
- Donaldson, Erle C., Rex D. Thomas, and Philip B. Lorenz. 1969. “Wettability Determination and Its Effect on Recovery Efficiency.” *SPE Journal*, 13–20. <https://doi.org/10.2118/2338-PA>.
- Duchet, Jannick, Jean François Gerard, Jean Paul Chapel, and Bernard Chabert. 2000. “Grafting of Alkylchlorosilanes onto Silica from Solution for Adhesion Enhancement.” *Journal of Adhesion Science and Technology* 14 (5): 691–718. <https://doi.org/10.1163/156856100742834>.
- Dullien, Francis A. L. 1992. *Porous Media: Fluid Transport and Pore Structure*. New York: Academic Press.
- Dunn, Keh J., David J. Bergman, and Gerald A. LaTorraca. 2002. *Nuclear Magnetic Resonance Petrophysical and Logging Applications*. Vol. 32. Elsevier. [https://doi.org/10.1016/S0950-1401\(02\)80001-5](https://doi.org/10.1016/S0950-1401(02)80001-5).
- Ehrenberg, S. N., and P. H. Nadeau. 2005. “Sandstone vs. Carbonate Petroleum Reservoirs: A Global Perspective on Porosity-Depth and Porosity-Permeability Relationships.” *AAPG Bulletin* 89 (4): 435–45. <https://doi.org/10.1306/11230404071>.
- Eick, J. D., R. J. Good, and A. W. Neumann. 1975. “Thermodynamics of Contact Angles. II. Rough Solid

- Surfaces.” *Journal of Colloid And Interface Science* 53 (2): 235–48. [https://doi.org/10.1016/0021-9797\(75\)90010-7](https://doi.org/10.1016/0021-9797(75)90010-7).
- Eiken, Ola, Philip Ringrose, Christian Hermanrud, Bamshad Nazarian, Tore A. Torp, and Lars Høier. 2011. “Lessons Learned from 14 Years of CCS Operations: Sleipner, In Salah and Snøhvit.” *Energy Procedia* 4: 5541–48. <https://doi.org/10.1016/j.egypro.2011.02.541>.
- Emberley, S., I. Hutcheon, M. Shevalier, K. Durocher, W. D. Gunter, and E. H. Perkins. 2004. “Geochemical Monitoring of Fluid-Rock Interaction and CO₂ Storage at the Weyburn CO₂-Injection Enhanced Oil Recovery Site, Saskatchewan, Canada.” *Energy* 29 (9–10): 1393–1401. <https://doi.org/10.1016/j.energy.2004.03.073>.
- Erkey, Can. 2011. *Supercritical Fluids and Organometallic Compounds: From Recovery of Trace Metals to Synthesis of Nanostructured Materials*. Amsterdam: Elsevier Science.
- Fadeev, Alexander Y., and Thomas J. McCarthy. 1999. “Trialkylsilane Monolayers Covalently Attached to Silicon Surfaces: Wettability Studies Indicating That Molecular Topography Contributes to Contact Angle Hysteresis.” *Langmuir* 15 (11): 3759–66. <https://doi.org/10.1021/la981486o>.
- Fadeev, Alexander Y., and Thomas J. McCarthy. 2000. “Self-Assembly Is Not the Only Reaction Possible Between Alkyltrichlorosilanes and Surfaces: Monomolecular and Oligomeric Covalently Attached Layers of Dichloro- and Trichloroalkylsilanes on Silicon.” *Langmuir* 16 (18): 7268–74. <https://doi.org/10.1021/la000471z>.
- Fahes, Mashhad Mousa, and Abbas Firoozabadi. 2007. “Wettability Alteration to Intermediate Gas-Wetting in Gas-Condensate Reservoirs at High Temperatures.” *SPE Journal* 12 (04): 397–407. <https://doi.org/10.2118/96184-pa>.
- Folger, L. K., and S. N. Guillot. 1996. “A Case Study of the Development of the Sundown Slaughter Unit CO₂ Flood Hockley County, Texas.” *Society of Petroleum Engineers - Permian Basin Oil and Gas Recovery Conference, OGR 1996*, 381–93. <https://doi.org/10.2523/35189-ms>.
- Freedman, R., N. Heaton, M. Flaum, G. J. Hirasaki, C. Flaum, and M. Hürlimann. 2003. “Wettability, Saturation, and Viscosity from NMR Measurements.” *SPE Journal* 8 (4): 317–27. <https://doi.org/10.2118/87340-PA>.
- Gao, Lichao, and Thomas J. McCarthy. 2008. “(CH₃)₃SiCl/SiCl₄ Azeotrope Grows Superhydrophobic Nanofilaments.” *Langmuir* 24 (2): 362–64. <https://doi.org/10.1021/la7025297>.
- Georgiadis, Apostolos, Geoffrey Maitland, J. P. Martin Trusler, and Alexander Bismarck. 2011. “Interfacial Tension Measurements of the (H₂O + CO₂) Ternary System at Elevated Pressures and Temperatures.” *Journal of Chemical and Engineering Data* 56 (12): 4900–4908. <https://doi.org/10.1021/je200825j>.
- Giraldo, Juliana, Pedro Benjumea, Sergio Lopera, Farid B. Cortés, and Marco A. Ruiz. 2013. “Wettability Alteration of Sandstone Cores by Alumina-Based Nanofluids.” *Energy and Fuels* 27 (7): 3659–65. <https://doi.org/10.1021/ef4002956>.
- Gluyas, Joe, and Richard Swarbrick. 2004. *Petroleum Geoscience*. Blackwell Publishing, Oxford.

- Government of Western Australia - Department of Mines and Petroleum. 2013. "South West CO₂ Geosequestration Hub: Project Activity and Progress Report," no. June. <https://www.globalccsinstitute.com/archive/hub/publications/155608/south-west-co2-geosequestration-hub-project-activity-progress-report.pdf>.
- Gu, Wei, Carl P Tripp, Recei V March, In Final, and Form April. 2006. "Reaction of Silanes in Supercritical CO₂ with TiO₂ and Al₂O₃," no. 16: 5748–52. <https://doi.org/10.1021/la060571q>.
- Gun, V M, M S Vedamuthu, G L Henderson, and J P Blitz. 2000. "Mechanism and Kinetics of Hexamethyldisilazane Reaction with a Fumed Silica Surface" 170: 157–70. <https://doi.org/10.1006/jcis.2000.6934>.
- Gupta, R., and K. K. Mohanty. 2010. "Temperature Effects on Surfactant-Aided Imbibition into Fractured Carbonates." *SPE Journal* 15 (3): 587–97. <https://doi.org/10.2118/110204-pa>.
- Hair, Michael. L. 1975. "Hydroxyl Groups on Silica Surface." *Journal of Non-Crystalline Solids* 19: 299–309.
- Hanarpour, M., and S. M. Mahmood. 1988. "Relative-Permeability Measurements: An Overview." *JPT, Journal of Petroleum Technology* 40 (8): 963–66.
- Hara, Kenji, Saiko Akahane, Jerzy W. Wiench, Breina R. Burgin, Nobuhiro Ishito, Victor S.Y. Lin, Atsushi Fukuoka, and Marek Pruski. 2012. "Selective and Efficient Silylation of Mesoporous Silica: A Quantitative Assessment of Synthetic Strategies by Solid-State NMR." *Journal of Physical Chemistry C* 116 (12): 7083–90. <https://doi.org/10.1021/jp300580f>.
- Heiba, A. A., H. T. Davis, and L. E. Scriver. 1983. "Effect of Wettability on Two-Phase Relative Permeabilities and Capillary Pressures." *Society of Petroleum Engineers*. <https://doi.org/10.2118/12172-MS>.
- Herring, Anna L., Linnéa Andersson, D. L. Newell, J. W. Carey, and Dorthe Wildenschild. 2014. "Pore-Scale Observations of Supercritical CO₂ Drainage in Bentheimer Sandstone by Synchrotron x-Ray Imaging." *International Journal of Greenhouse Gas Control* 25: 93–101. <https://doi.org/10.1016/j.ijggc.2014.04.003>.
- Higdon, J J L. 2013. "Multiphase Flow in Porous Media." *Fluid Mechanics* 730: 1–4. <https://doi.org/10.1017/jfm.2013.296>.
- Hilner, E., M. P. Andersson, T. Hassenkam, J. Matthiesen, P. A. Salino, and S. L.S. Stipp. 2015a. "The Effect of Ionic Strength on Oil Adhesion in Sandstone - The Search for the Low Salinity Mechanism." *Scientific Reports* 5: 1–9. <https://doi.org/10.1038/srep09933>.
- Hilner, E, M. P Andersson, T Hassenkam, J Matthiesen, P. A Salino, and S. L.S Stipp. 2015b. "The Effect of Ionic Strength on Oil Adhesion in Sandstone - The Search for the Low Salinity Mechanism." *Scientific Reports* 5: 1–9. <https://doi.org/10.1038/srep09933>.
- Hinai, Nasser M. Al, A. Saeedi, Colin D. Wood, R. Valdez, and Lionel Esteban. 2017. "Experimental Study of Miscible Thickened Natural Gas Injection for Enhanced Oil Recovery." *Energy & Fuels* 31 (5): 4951–65. <https://doi.org/10.1021/acs.energyfuels.7b00314>.

- Hirasaki, G.J. 1991. "Wettability: Fundamentals and Surface Forces." *SPE Formation Evaluation*.
<https://doi.org/10.2118/17367-PA>.
- Holtz, M.H. 2002. "Residual Gas Saturation to Aquifer Influx: A Calculation Method for 3-D Computer Reservoir Model Construction." In *SPE Gas Technology Symposium, Calgary, Alberta, Canada*. Society of Petroleum Engineers Inc. <https://doi.org/10.2118/75502-ms>.
- Huang, Pei Yuan, Yu Chou Chao, and Yih Tyan Liao. 2004. "Preparation of Fluoroacrylate Nanocopolymer by Miniemulsion Polymerization Used in Textile Finishing." *Journal of Applied Polymer Science* 94 (4): 1466–72. <https://doi.org/10.1002/app.21054>.
- Humphry, K J, B M J M Suijkerbuijk, H A van der Linde, S G J Pieterse, and S K Masalmeh. 2014. "Impact of Wettability on Residual Oil Saturation and Capillary Desaturation Curves." *Petrophysics* 55 (4): 313–18.
- IEA. 2020. "Global CO2 Emissions in 2019." International Energy Agency. 2020. <https://www.iea.org/articles/global-co2-emissions-in-2019> (accessed May 20, 2020).
- IEA Greenhouse Gas R&D Programme. 2004. "IEA GHG Weyburn CO2 Monitoring and Storage Project."
- Iglauer, Stefan, Ahmed Zarzor Al-yaseri, Reza Rezaee, and Maxim Lebedev. 2015. "CO2 Wettability of Caprocks: Implications for Structural Storage Capacity and Containment Security." *Geophysical*, no. Figure 1: 9279–84. <https://doi.org/10.1002/2015GL065787>.Received.
- Iglauer, Stefan, C. H. Pentland, and A Busch. 2017. "CO2 Wettability of Seal and Reservoir Rocks and the Implications for Carbon Geo-Sequestration." *Water Resources Research*, 1–18. <https://doi.org/10.1002/2016WR019804>.Received.
- Iglauer, Stefan, Abdulsalam Salamah, Mohammad Sarmadivaleh, Keyu Liu, and Chi Phan. 2014. "Contamination of Silica Surfaces: Impact on Water-CO2-Quartz and Glass Contact Angle Measurements." *International Journal of Greenhouse Gas Control* 22: 325–28. <https://doi.org/10.1016/j.ijggc.2014.01.006>.
- Jackson, Matthew D., Per H. Valvatne, and Martin J. Blunt. 2005. "Prediction of Wettability Variation within an Oil/Water Transition Zone and Its Impact on Production." *SPE Journal* 10 (2): 184–95. <https://doi.org/10.2118/77543-pa>.
- Jadhunandan, P P, and N R Morrow. 1995. "Effect of Wettability on Waterflood Recovery for Crude-Oil / Brine / Rock Systems." *SPE Reservoir Engineering*, no. Spe 22597: 40–46.
- Jakša, G., B. Štefane, and J. Kovač. 2013. "XPS and AFM Characterization of Aminosilanes with Different Numbers of Bonding Sites on a Silicon Wafer." *Surface and Interface Analysis* 45 (11): 1709–13. <https://doi.org/10.1002/sia.5311>.
- Jennings, H. Y. 1957. "Surface Properties of Natural and Synthetic Porous Media." *Producers Monthly* 21 (5): 20–24.
- Jin, Jiafeng, Yanling Wang, Tuan A.H. Nguyen, Anh V. Nguyen, Mingzhen Wei, and Baojun Bai. 2017. "The Effect of Gas-Wetting Nano-Particle on the Fluid Flowing Behavior in Porous Media." *Fuel*

- 196 (November 2016): 431–41. <https://doi.org/10.1016/j.fuel.2017.01.083>.
- John, Poate, Tissa Illangasekare, Hossein Kazemi, and Robert Kee. 2015. *Pore Scale Phenomena - Frontiers in Energy and Environment*. Colorado, USA: World Scientific.
- Johnson, E. F., D. P. Bossler, and V. O. Naumann. 1959. “Calculation of Relative Permeability from Displacement Experiments.” *Petroleum Transactions, AIME* 206: 370–72.
- Johnston, K. P., M. Fang, M. L. O’Neill, Q. Cao, S. H. Jureller, J. L. Kerschner, S. P. Wilkinson, and C. D. Smith. 1998. “Solubility of Homopolymers and Copolymers in Carbon Dioxide.” *Industrial & Engineering Chemistry Research* 37 (8): 3067–79. <https://doi.org/10.1021/ie980010x>.
- Jones, S. C., and W. O. Roszelle. 1978. “Graphical Techniques for Determining Relative Permeability From Displacement Experiments.” *JPT, Journal of Petroleum Technology* 30 (5): 807–17. <https://doi.org/10.2118/6045-PA>.
- Jung, Jong-Won, and Jiamin Wan. 2012. “Supercritical CO₂ and Ionic Strength Effects on Wettability of Silica Surfaces: Equilibrium Contact Angle Measurements.” *Energy & Fuels* 26 (9): 6053–59. <https://doi.org/10.1021/ef300913t>.
- Jung, Jong Won, and Jiamin Wan. 2012. “Supercritical CO₂ and Ionic Strength Effects on Wettability of Silica Surfaces: Equilibrium Contact Angle Measurements.” *Energy and Fuels* 26 (9): 6053–59. <https://doi.org/10.1021/ef300913t>.
- Karandish, G. R., M. R. Rahimpour, S. Sharifzadeh, and A. A. Dadkhah. 2015. “Wettability Alteration in Gas-Condensate Carbonate Reservoir Using Anionic Fluorinated Treatment.” *Chemical Engineering Research and Design* 93 (June): 554–64. <https://doi.org/10.1016/j.cherd.2014.05.019>.
- Karnanda, Wimpy, M. S. Benzagouta, Abdulrahman AlQuraishi, and M. M. Amro. 2013. “Effect of Temperature, Pressure, Salinity, and Surfactant Concentration on IFT for Surfactant Flooding Optimization.” *Arabian Journal of Geosciences* 6 (9): 3535–44. <https://doi.org/10.1007/s12517-012-0605-7>.
- Kartal, Ayşe Meriç, and Can Erkey. 2010. “Surface Modification of Silica Aerogels by Hexamethyldisilazane-Carbon Dioxide Mixtures and Their Phase Behavior.” *Journal of Supercritical Fluids* 53: 115–20. <https://doi.org/10.1016/j.supflu.2009.11.004>.
- Kaur, Gagan, Raju Adhikari, Peter Cass, Mark Bown, Margaret D.M. Evans, Aditya V. Vashi, and Pathiraja Gunatillake. 2015. “Graphene/Polyurethane Composites: Fabrication and Evaluation of Electrical Conductivity, Mechanical Properties and Cell Viability.” *RSC Advances* 5 (120): 98762–72. <https://doi.org/10.1039/c5ra20214k>.
- Kelemen, Peter, Sally M. Benson, Hélène Pilorgé, Peter Psarras, and Jennifer Wilcox. 2019. “An Overview of the Status and Challenges of CO₂ Storage in Minerals and Geological Formations.” *Frontiers in Climate* 1 (November): 1–20. <https://doi.org/10.3389/fclim.2019.00009>.
- Kenyon, W. E. 1997. “Petrophysical Principles of Applications of NMR Logging.” *The Log Analyst* 38 (2): 21–43.
- Kestin, Joseph, H. Ezzat Khalifa, and Robert J. Correia. 1981. “Tables of the Dynamic and Kinematic

- Viscosity of Aqueous NaCl Solutions in the Temperature Range 25-150 °C and the Pressure Range 0.1-35 MPa.” *Journal of Physical and Chemical Reference Data* 10 (1): 71–88. <https://doi.org/10.1063/1.555641>.
- Khaw, Kooi Y., Marie O. Parat, Paul N. Shaw, and James R. Falconer. 2017. “Solvent Supercritical Fluid Technologies to Extract Bioactive Compounds from Natural Sources: A Review.” *Molecules* 22 (7). <https://doi.org/10.3390/molecules22071186>.
- Kim, Y. M., B. Arkles, and Y. Pan. 2009. “The Role Of Polarity In The Structure Of Silanes Employed In Surface Modification.” *Silanes and Other Coupling Agents, Volume 5* 5: 51–64. <http://booksandjournals.brillonline.com/content/books/10.1163/ej.9789004165915.i-348.37>.
- Kirby, Christopher F., and Mark A. McHugh. 1999. “Phase Behavior of Polymers in Supercritical Fluid Solvents.” *Chemical Reviews* 99 (2): 565–602. <https://doi.org/10.1021/cr970046j>.
- Ko, Young Gun, Seung Su Shin, and Ung Su Choi. 2011. “Primary, Secondary, and Tertiary Amines for CO₂ Capture: Designing for Mesoporous CO₂ Adsorbents.” *Journal of Colloid and Interface Science* 361 (2): 594–602. <https://doi.org/10.1016/j.jcis.2011.03.045>.
- Koegler, Peter, Paul Pasic, James Gardiner, Veronica Glattauer, Peter Kingshott, and Helmut Thissen. 2014. “Polymerizable Peptide Copolymer Coatings for the Control of Biointerfacial Interactions.” *Biomacromolecules* 15 (6): 2265–73. <https://doi.org/10.1021/bm500386y>.
- Krevor, Samuel C.M., Ronny Pini, Lin Zuo, and Sally M. Benson. 2012. “Relative Permeability and Trapping of CO₂ and Water in Sandstone Rocks at Reservoir Conditions.” *Water Resources Research* 48 (2): 1–16. <https://doi.org/10.1029/2011WR010859>.
- Kuuskraa, Vello a. 2008. “Maximizing Oil Recovery Efficiency and Sequestration of CO₂ with ‘Next Generation’ CO₂-EOR.” In *Society of Petroleum Engineers*.
- Kwok, D Y, and A W U Neumann. 1999. “Contact Angle Measurement and Contact Angle Interpretation.” *Advances in Colloid and Interface Science* 81: 167–249.
- Kyte, J. R, V. O Naumann, and C.C Mattax. 1961. “Effect of Reservoir Environment on Water-Oil Displacements.” *Journal of Petroleum Technology*, 579–82.
- Lager, A., K. J. Webb, C. J.J. Black, M. Singleton, and K. S. Sorbie. 2008. “Low Salinity Oil Recovery - An Experimental Investigation.” *Petrophysics* 49 (1): 28–35.
- Land, Carlon S. 1968. “Calculation of Imbibition Relative Permeability for Two- and Three-Phase Flow From Rock Properties.” *Society of Petroleum Engineers Journal* 243: 149–56. <https://doi.org/10.2118/1942-pa>.
- Larpudomlert, Ruthut, Victor A. Torrealba, Zuleima T. Karpyn, and Phillip Halleck. 2014. “Experimental Investigation of Residual Saturation in Mixed-Wet Porous Media Using a Pore-Scale Approach.” *Journal of Petroleum Exploration and Production Technology* 4 (2): 175–87. <https://doi.org/10.1007/s13202-013-0076-8>.
- Lazghab, Myriam, Khashayar Saleh, Pierre Guigon, and À Si. 2015. “A New Solventless Process to Hydrophobize Silica Powders in Fluidized Beds.” *AIChE Journal* 61 (3): 857–66.

<https://doi.org/10.1002/aic>.

- Lecoanet, H el ene F., Jean Yves Bottero, and Mark R. Wiesner. 2004. "Laboratory Assessment of the Mobility of Nanomaterials in Porous Media." *Environmental Science and Technology* 38 (19): 5164–69. <https://doi.org/10.1021/es0352303>.
- Lee, Sangwha, Joon Seo Park, and T. Randall Lee. 2008. "The Wettability of Fluoropolymer Surfaces: Influence of Surface Dipoles." *Langmuir* 24 (9): 4817–26. <https://doi.org/10.1021/la700902h>.
- Lemmon, Ew, Mo McLinder, and DG Friend. n.d. "Thermophysical Properties of Fluid Systems." NIST Chemistry WebBook, NIST Standard Reference Database Number 69, Eds., P.J. Linstorm, W.G. Mallard. <https://doi.org/10.18434/T4D303>.
- Leverett, M. C. 1941. "Capillary Behavior in Porous Solids." *Society of Petroleum Engineers*, 152–69. <https://doi.org/10.2118/941152-G>.
- Li, Kewen, and Abbas Firoozabadi. 2000. "Experimental Study of Wettability Alteration to Preferential Gas-Wetting in Porous Media and Its Effects." *SPE Reservoir Evaluation & Engineering* 3 (02): 139–49. <https://doi.org/10.2118/62515-pa>.
- Li, Kewen, Yijiang Liu, Hongwen Zheng, Guixiong Huang, and Ganqin Li. 2011. "Enhanced Gas-Condensate Production by Wettability Alteration to Gas Wetness." *Journal of Petroleum Science and Engineering* 78 (2): 505–9. <https://doi.org/10.1016/j.petrol.2011.08.001>.
- Li, Shidong, and Ole Torsaeter. 2015. "The Impact of Nanoparticles Adsorption and Transport on Wettability Alteration of Intermediate Wet Berea Sandstone." In *SPE Middle East Unconventional Resources Conference and Exhibition*. <https://doi.org/10.2118/172943-MS>.
- LI, Wei, Jian hua ZHU, and Jian hua QI. 2007. "Application of Nano-Nickel Catalyst in the Viscosity Reduction of Liaohe Extra-Heavy Oil by Aqua-Thermolysis." *Ranliao Huaxue Xuebao/Journal of Fuel Chemistry and Technology* 35 (2): 176–80. [https://doi.org/10.1016/S1872-5813\(07\)60016-4](https://doi.org/10.1016/S1872-5813(07)60016-4).
- Lin, F.Y.H., D. Li, and A.W. Neumann. 1993. "Effect of Surface Roughness on the Dependence of Contact Angles on Drop Size." *Journal of Colloid And Interface Science* 159: 86–95.
- Liu, Ling, and Jill S. Buckley. 1999. "Alteration of Wetting of Mica Surfaces." *Journal of Petroleum Science and Engineering* 24 (2–4): 75–83. [https://doi.org/10.1016/S0920-4105\(99\)00050-9](https://doi.org/10.1016/S0920-4105(99)00050-9).
- Liu, Yi Hung, Hiroyuki Maruyama, and Shuji Matsusaka. 2010. "Agglomeration Process of Dry Ice Particles Produced by Expanding Liquid Carbon Dioxide." *Advanced Powder Technology* 21 (6): 652–57. <https://doi.org/10.1016/j.apt.2010.07.009>.
- L opez-aranguren, P, J Saurina, L F Vega, and C Domingo. 2012. "Microporous and Mesoporous Materials Sorption of Tryalkoxysilane in Low-Cost Porous Silicates Using a Supercritical CO2 Method." *Microporous and Mesoporous Materials* 148: 15–24. <https://doi.org/10.1016/j.micromeso.2011.06.035>.
- L opez-Periago, Ana M., Wendy Sandoval, and Concepci on Domingo. 2014. "Chemical Modification of Nanometric TiO2 Particles by Anchoring Functional Silane Molecules in Supercritical CO2." *Applied Surface Science* 296: 114–23. <https://doi.org/10.1016/j.apsusc.2014.01.058>.

- MA, S.M., Morrow, N.R, Zhang, X., Zhou X. 1999. "Characterization of Wettability from Spontaneous Imbibition Measurements." *Jcpt* 38 (13). <https://www.onepetro.org/download/journal-paper/PETSOC-99-13-49?id=journal-paper%2FPETSOC-99-13-49>.
- Ma, Kun, Leyu Cui, Yezi Dong, Tianlong Wang, Chang Da, George J. Hirasaki, and Sibani Lisa Biswal. 2013. "Adsorption of Cationic and Anionic Surfactants on Natural and Synthetic Carbonate Materials." *Journal of Colloid and Interface Science* 408 (1): 164–72. <https://doi.org/10.1016/j.jcis.2013.07.006>.
- Ma, Yuchen, A. S. Foster, and R. M. Nieminen. 2005. "Reactions and Clustering of Water with Silica Surface." *Journal of Chemical Physics* 122 (14): 1–9. <https://doi.org/10.1063/1.1878652>.
- Mahzari, Pedram, and Mehran Sohrabi. 2014. "Crude Oil/Brine Interactions and Spontaneous Formation of Microdispersions in Low Salinity Water Injection." *Proceedings - SPE Symposium on Improved Oil Recovery* 2 (2009): 731–45. <https://doi.org/10.2118/169081-ms>.
- McCaffery, F.G., and D.W. Bennion. 1974. "The Effect Of Wettability On Two-Phase Relative Permeabilities." *Journal of Canadian Petroleum Technology* 13 (04): 42–53. <https://doi.org/10.2118/74-04-04>.
- Mccaffery, F.G., and N. Mungan. 1970. "Contact Angle and Interfacial Tension Studies of Some Hydrocarbonwater-Solid Systems." *Journal of Canadian Petroleum Technology* 9 (3): 185–96.
- McCain, W. D., and R. A. Alexander. 1992. "Sampling Gas-Condensate Wells." *Society of Petroleum Engineers SPE*, no. August. <https://doi.org/10.2118/942013-g>.
- McCool, Ben, and Carl P Tripp. 2005. "Inaccessible Hydroxyl Groups on Silica Are Accessible in Supercritical CO₂." *Journal of Physical Chemistry B* 109: 8914–19. <https://doi.org/10.1021/jp050192q>.
- McDougall, S. R., and K. S. Sorbie. 1995. "Impact of Wettability on Waterflooding: Pore-Scale Simulation." *SPE Reservoir Engineering (Society of Petroleum Engineers)* 10 (3): 208–13. <https://doi.org/10.2118/25271-PA>.
- McGrail, Peter B., and Todd H. Schaefer. 2005. "Direct Measurements of PH and Dissolved CO₂ in H₂O-CO₂ Brine Mixtures to Supercritical Conditions." *Greenhouse Gas Control Technologies* 2: 2169–73. <https://doi.org/10.1016/B978-008044704-9/50294-9>.
- Morris, Earl. E, and Denton. R Wieland. 1963. "A Microscopic Study of the Effect of Variable Wettability Conditions on Immiscible Fluid Displacement." *Society of Petroleum Engineers*. <https://doi.org/10.2118/704-MS>.
- Morrow, Norman R. 1990. "Wettability and Its Effect on Oil Recovery." *JPT, Journal of Petroleum Technology* 42 (12): 1476–84. <https://doi.org/10.2118/21621-PA>.
- Mousavi, M. A., Sh Hassanajili, and M. R. Rahimpour. 2013. "Synthesis of Fluorinated Nano-Silica and Its Application in Wettability Alteration near-Wellbore Region in Gas Condensate Reservoirs." *Applied Surface Science* 273: 205–14. <https://doi.org/10.1016/j.apsusc.2013.02.014>.
- Murphy, Peter M., and Tracy Hewat. 2008. "Fluorosurfactants in Enhanced Oil Recovery." *The Open*

- Petroleum Engineering Journal* 1 (1): 58–61. <https://doi.org/10.2174/1874834100801010058>.
- Muskat, M., R.D. Wyckoff, H. G. Botset, and M. W. Meres. 1937. “Flow of Gas-Liquid Mixtures through Sands.” *Society of Petroleum Engineers*, no. 7: 69–96. <https://doi.org/10.2118/937069-G>.
- Naghizadeh, Arefeh, Reza Azin, Shahriar Osfouri, and Rouhollah Fatehi. 2020. “Wettability Alteration of Calcite and Dolomite Carbonates Using Silica Nanoparticles Coated with Fluorine Groups.” *Journal of Petroleum Science and Engineering* 188 (December 2019): 106915. <https://doi.org/10.1016/j.petrol.2020.106915>.
- Nazari Moghaddam, Rasoul, Alireza Bahramian, Zahra Fakhroueian, Ali Karimi, and Sharareh Arya. 2015. “Comparative Study of Using Nanoparticles for Enhanced Oil Recovery: Wettability Alteration of Carbonate Rocks.” *Energy and Fuels* 29 (4): 2111–19. <https://doi.org/10.1021/ef5024719>.
- Nel, A., L. Mädler, D. Velegol, T. Xia, E. Hoek, P. Somasundaran, F. Klaessig, V. Castranova, and M. Thompson. 2009. “Understanding Biophysicochemical Interactions at the Nano–bio Interface.” *Nature Mater* 8 (7): 543–557. <https://doi.org/10.1038/nmat2442>.
- Nwidee, Lezorgia N., Maxim Lebedev, Ahmed Barifcani, Mohammad Sarmadivaleh, and Stefan Iglauer. 2017. “Wettability Alteration of Oil-Wet Limestone Using Surfactant-Nanoparticle Formulation.” *Journal of Colloid and Interface Science* 504: 334–45. <https://doi.org/10.1016/j.jcis.2017.04.078>.
- Oberdörster, Günter, Eva Oberdörster, and Jan Oberdörster. 2005. “Nanotoxicology: An Emerging Discipline Evolving from Studies of Ultrafine Particles.” *Environmental Health Perspectives* 113 (7): 823–39. <https://doi.org/10.1289/ehp.7339>.
- Owens, W. W., and D. L. Archer. 1971. “The Effect of Rock Wettability on Oil-Water Relative Permeability Relationships.” *Journal of Petroleum Technology* 251: 873–78. <https://doi.org/doi:10.2118/3034-PA>.
- Packham, D. E. 2005. *Handbook of Adhesion*. 2nd ed. John Wiley & Sons.
- Pape, Peter G. 2006. *Silylating Agents*. *Kirk-Othmer Encyclopedia of Chemical Technology*. 5th ed. USA: Lindner.
- Payatakes, A. C., D. G. Avraam, and G. N. Constantindes. 1996. “Flow Regimes and Relative Permeabilities during Steady State Two-Phase Flow in Porous Media.” *Journal of Fluid Mechanics* 293.
- Peach, Jocelyn, and Julian Eastoe. 2014. “Supercritical Carbon Dioxide: A Solvent like No Other.” *Beilstein Journal of Organic Chemistry* 10: 1878–95. <https://doi.org/10.3762/bjoc.10.196>.
- Pérez, Eduardo, Albertina Cabanas, Juan A.R. Renuncio, Yolanda Sánchez-Vicente, and Concepción Pando. 2008. “Cosolvent Effect of Methanol and Acetic Acid on Dibenzofuran Solubility in Supercritical Carbon Dioxide.” *Journal of Chemical and Engineering Data* 53 (11): 2649–53. <https://doi.org/10.1021/jc800574v>.
- Pinazo, Aurora, Lourdes Pérez, M^a del Carmen Morán, and Ramon Pons. 2019. *Arginine-Based Surfactants: Synthesis, Aggregation Properties, and Applications*. *Biobased Surfactants*. Second

- Edi. Elsevier Inc. <https://doi.org/10.1016/b978-0-12-812705-6.00013-7>.
- Pini, Ronny, Samuel C.M. Krevor, and Sally M. Benson. 2012. "Capillary Pressure and Heterogeneity for the CO₂/Water System in Sandstone Rocks at Reservoir Conditions." *Advances in Water Resources* 38: 48–59. <https://doi.org/10.1016/j.advwatres.2011.12.007>.
- Ponmani, Swaminathan, R. Nagrajan, and Jitendra R. Sangwai. 2016. "Effect of Nanofluids of CuO and ZnO in Polyethylene Glycol and Polyvinylpyrrolidone on the Thermal, Electrical, and Filtration-Loss Properties of Water-Based Drilling Fluids." *SPE Journal* 21: 405–15. <https://doi.org/10.2118/178919-PA>.
- Priimagi, Arri, Gabriella Cavallo, Pierangelo Metrangolo, and Giuseppe Resnati. 2013. "The Halogen Bond in the Design of Functional Supramolecular Materials: Recent Advances." *Acc. Chem. Res.* 46 (11): 2686–95. <https://doi.org/10.1021/ar400103r>.
- Purcell, W.R. 1949. "Capillary Pressures - Their Measurement Using Mercury and the Calculation of Permeability Therefrom." *Journal of Petroleum Technology* 1 (02): 39–48. <https://doi.org/10.2118/949039-g>.
- Pyo, K, N Damián-Díaz, M Powell, and J Van Nieuwkerk. 2003. "CO₂ Flooding in Joffre Viking Pool." *Petroleum Society's Canadian International Petroleum Conference*.
- Ravari, Reza Rostami, Skule Strand, and Tor Austad. 2011. "Combined Surfactant-Enhanced Gravity Drainage (SEGD) of Oil and the Wettability Alteration in Carbonates: The Effect of Rock Permeability and Interfacial Tension (IFT)." *Energy and Fuels* 25 (5): 2083–88. <https://doi.org/10.1021/ef200085t>.
- Raza, S. H, L. E Treiber, and D. L Archer. 1968. "Wettability of Reservoir Rocks and Its Evaluation." *Prod. Mon.; (United States)* 32 (4).
- Rezaeidoust, A., T. Puntervold, S. Strand, and T. Austad. 2009. "Smart Water as Wettability Modifier in Carbonate and Sandstone: A Discussion of Similarities/Differences in the Chemical Mechanisms." *Energy and Fuels* 23 (9): 4479–85. <https://doi.org/10.1021/ef900185q>.
- Ritchie, Hannah, and Max Roser. 2019. "CO₂ and Greenhouse Gas Emissions." Our World in Data. 2019. <https://ourworldindata.org/co2-and-other-greenhouse-gas-emissions> (accessed May 20, 2020).
- Robertson, Eric P. 2007. "Low-Salinity Waterflooding to Improve Oil Recovery - Historical Field Evidence." *Proceedings - SPE Annual Technical Conference and Exhibition* 3: 1612–20. <https://doi.org/10.2523/109965-ms>.
- Roth, Charles A. 1972. "Silylation of Organic Chemicals." *Industrial and Engineering Chemistry Product Research and Development* 11 (2): 134–39. <https://doi.org/10.1021/i360042a003>.
- Rovetta, M. R., and J. D. Blacic. 1989. "An Experimental Study of Hydroxyl in Quartz Using Infrared Spectroscopy and Ion Microprobe Techniques." *Journal of Geophysical Research* 94 (B5): 5840–50. <https://doi.org/10.1029/JB094iB05p05840>.
- Rudnick, R.L. & Gao, S. 2003. "Composition of the Continental Crust." *Treatise on Geochemistry* 3: 1–64.

- Saeedi, Ali. 2005. *Experimental Study of Multiphase Flow in Porous Media during CO₂ Geo-Sequestration Processes*. Springer. <https://doi.org/10.1007/978-3-642-25041-5>.
- Saeedi, Ali, Claudio Delle Piane, Lionel Esteban, and Quan Xie. 2016. "Flood Characteristic and Fluid Rock Interactions of a Supercritical CO₂, Brine, Rock System: South West Hub, Western Australia." *International Journal of Greenhouse Gas Control* 54: 309–21. <https://doi.org/10.1016/j.ijggc.2016.09.017>.
- Salathiel, R. A. 1973. "Oil Recovery By Surface Film Drainage in Mixed-Wettability Rocks." *JPT, Journal of Petroleum Technology* 25: 1216–24. <https://doi.org/10.2118/4104-PA>.
- Sánchez-Vicente, Yolanda, Concepción Pando, Manuel Cortijo, and Albertina Cabañas. 2014. "Chemical Surface Modification of Mesoporous Silica SBA-15 with a Tertiary Aminosilane Using Supercritical Carbon Dioxide." *Microporous and Mesoporous Materials* 193: 145–53. <https://doi.org/10.1016/j.micromeso.2014.03.021>.
- Sanli, D, and C Erkey. 2013. "Monolithic Composites of Silica Aerogels by Reactive Supercritical Deposition of Hydroxy-Terminated Poly(Dimethylsiloxane)." *Applied Materials & Interfaces* 5: 11708–17. <https://doi.org/10.1021/am403200d>.
- Sanli, Deniz, and Can Erkey. 2015. "Silylation from Supercritical Carbon Dioxide: A Powerful Technique for Modification of Surfaces." *Journal of Materials Science* 50 (22): 7159–81.
- Sanz, R., G. Calleja, A. Arencibia, and E. S. Sanz-Pérez. 2010. "CO₂ Adsorption on Branched Polyethyleneimine-Impregnated Mesoporous Silica SBA-15." *Applied Surface Science* 256 (17): 5323–28. <https://doi.org/10.1016/j.apsusc.2009.12.070>.
- Saraji, Soheil, Lamia Goual, Mohammad Piri, and Henry Plancher. 2013. "Wettability of Supercritical Carbon Dioxide/Water/Quartz Systems: Simultaneous Measurement of Contact Angle and Interfacial Tension at Reservoir Conditions." *Langmuir* 29 (23): 6856–66. <https://doi.org/10.1021/la3050863>.
- Sari, Ahmad, Yongqiang Chen, Quan Xie, and Ali Saeedi. 2019. "Low Salinity Water Flooding in High Acidic Oil Reservoirs: Impact of PH on Wettability of Carbonate Reservoirs." *Journal of Molecular Liquids* 281: 444–50. <https://doi.org/10.1016/j.molliq.2019.02.081>.
- Sari, Ahmad, Quan Xie, Yongqiang Chen, A. Saeedi, and Ehsan Pooryousefy. 2017. "Drivers of Low Salinity Effect in Carbonate Reservoirs." *Energy and Fuels* 31 (9): 8951–58. <https://doi.org/10.1021/acs.energyfuels.7b00966>.
- Schramm, Laurier L. 2000. *Surfactants: Fundamentals and Applications in the Petroleum Industry. Surfactants*. United Kingdom: Cambridge University Press.
- Sharma, Mukul M., and Teh Fu Yen. 1984. "Interfacial Electrochemistry of Oxide Surfaces in Oil-Bearing Sands and Sandstones." *Journal of Colloid And Interface Science* 98 (1): 39–54. [https://doi.org/10.1016/0021-9797\(84\)90476-4](https://doi.org/10.1016/0021-9797(84)90476-4).
- Shojai Kaveh, N., E. S.J. Rudolph, P. Van Hemert, W. R. Rossen, and K. H. Wolf. 2014. "Wettability Evaluation of a CO₂/Water/Bentheimer Sandstone System: Contact Angle, Dissolution, and Bubble

- Size.” *Energy and Fuels* 28 (6): 4002–20. <https://doi.org/10.1021/ef500034j>.
- Sigmund, P M, and F G McCaffery. 1979. “An Improved Unsteady-State Procedure for Determining the Relative-Permeability Characteristics of Heterogeneous Porous Media.” *Soc. Petrol. Eng. J.* 19 (1): 15–28.
- Soliveri, Guido, Daniela Meroni, Giuseppe Cappelletti, Rita Annunziata, Valentina Aina, Giuseppina Cerrato, and Silvia Ardizzone. 2014. “Engineered Organic/Inorganic Hybrids for Superhydrophobic Coatings by Wet and Vapour Procedures.” *Journal of Materials Science* 49 (7): 2734–44. <https://doi.org/10.1007/s10853-013-7976-3>.
- Speight, James G. 2017. *Rules of Thumb for Petroleum Engineers*. 1st ed. John Wiley & Sons.
- Stahl, Thorsten, Daniela Mattern, and Hubertus Brunn. 2011. “Toxicology of Perfluorinated Compounds.” *Environmental Sciences Europe* 23 (1): 1–52. <https://doi.org/10.1186/2190-4715-23-38>.
- Standnes, Dag C, and Tor Austad. 2000. “Wettability Alteration in Chalk: 2. Mechanism for Wettability Alteration from Oil-Wet to Water-Wet Using Surfactants.” *Journal of Petroleum Science and Engineering* 28 (3): 123–43. [https://doi.org/10.1016/s0920-4105\(00\)00084-x](https://doi.org/10.1016/s0920-4105(00)00084-x).
- Stiles, L. H., and J. B. Magruder. 1998. “Reservoir Management in the Means San Andres Unit.” *SPE Reprint Series*, no. 48: 186–92. <https://doi.org/10.2118/20751-pa>.
- Strand, Skule, Dag C. Standnes, and Tor Austad. 2003. “Spontaneous Imbibition of Aqueous Surfactant Solutions into Neutral to Oil-Wet Carbonate Cores: Effects of Brine Salinity and Composition.” *Energy and Fuels*. <https://doi.org/10.1021/ef030051s>.
- Suijkerbuijk, B.M.J.M., T.G. Sorop, A.R. Parker, S.K. Masalmeh, I.V. Chmuzh, V.M. Karpan, Y.E. Volokitin, and A.G. Skripin. 2014. “Low Salinity Waterflooding at West Salym : Laboratory Experiments and Field Forecasts.” In *SPE EOR Conference at Oil and Gas West Asia Held in Muscat, Oman*.
- Tan, Bien, Christopher L. Bray, and Andrew I. Cooper. 2009. “Fractionation of Polyvinyl Acetate and the Phase Behavior of End-Group Modified Oligo(Vinyl Acetate)s in CO₂.” *Macromolecules* 42 (20): 7945–52. <https://doi.org/10.1021/ma901458a>.
- Täuber, Daniela, Ines Trenkmann, and Christian Von Borczyskowski. 2013. “Influence of van Der Waals Interactions on Morphology and Dynamics in Ultrathin Liquid Films at Silicon Oxide Interfaces.” *Langmuir* 29 (11): 3583–93. <https://doi.org/10.1021/la3043796>.
- Tenorio, M. J., J. Morère, C. Carnerero, M. J. Torralvo, C. Pando, and A. Cabañas. 2018. “Thiol Group Functionalization of Mesoporous SiO₂ SBA-15 Using Supercritical CO₂.” *Microporous and Mesoporous Materials* 256: 147–54. <https://doi.org/10.1016/j.micromeso.2017.07.056>.
- The Prasino Group. 2012. “Joffre Viking CO₂ Injection Project Offset Project Report.”
- Tiab, Djebbar, and Erle C. Donaldson. 2012. *Petrophysics - Theory and Practice of Measuring Reservoir Rock and Fluid Transport Properties*. 3rd ed. Elsevier.
- Tokunaga, Tetsu K. 2012. “DLVO-Based Estimates of Adsorbed Water Film Thicknesses in Geologic CO₂ Reservoirs.” *Langmuir* 28: 8001–8009. <https://doi.org/10.1021/la2044587>.

- Tripp, C. P., and M. L. Hair. 1993. "Chemical Attachment of Chlorosilanes to Silica: A Two-Step Amine-Promoted Reaction." *Journal of Physical Chemistry* 97 (21): 5693–98. <https://doi.org/10.1021/j100123a038>.
- Tripp, C P., and M L Hair. 1992a. "An Infrared Study of the Reaction of Octadecyltrichlorosilane with Silica." *Langmuir* 8 (4): 1120–26. <https://doi.org/10.1021/la00040a018>.
- Tripp, C P, and M L Hair. 1992b. "Reaction of Alkylchlorosilanes with Silica at the Solid/Gas and Solid/Liquid Interface." *Langmuir* 8 (8): 1961–67. <https://doi.org/10.1021/la00044a014>.
- Ulman, a. 1996. "Formation and Structure of Self-Assembled Monolayers." *Chemical Reviews* 96 (4): 1533–54. <https://doi.org/10.1021/cr9502357>.
- Voort, P. Van Der, and E. F. Vansant. 1996. *Silylation of the Silica Surface A Review. Journal of Liquid Chromatography & Related Technologies*. Vol. 19. <https://doi.org/10.1080/10826079608015107>.
- Vyhmeister, Eduardo, Héctor Valdés-González, Anthony J. Muscat, David Suleiman, and L. Antonio Estévez. 2013. "Surface Modification of Porous Silicon-Based Films Using Dichlorosilanes Dissolved in Supercritical Carbon Dioxide." *Industrial and Engineering Chemistry Research* 52 (13): 4762–71. <https://doi.org/10.1021/ie302686e>.
- Wang, Lu, Yongming He, Hao Chen, Zhan Meng, and Zhilin Wang. 2019. "Experimental Investigation of the Live Oil-Water Relative Permeability and Displacement Efficiency on Kingfisher Waxy Oil Reservoir." *Journal of Petroleum Science and Engineering* 178: 1029–43. <https://doi.org/10.1016/j.petrol.2019.04.027>.
- Wang, Yanling, Jiafeng Jin, Li Ma, Liang Li, and Xiao Zhao. 2015. "Influence of Wettability Alteration to Preferential Gas-Wetting on Displacement Efficiency at Elevated Temperatures." *Journal of Dispersion Science and Technology* 36 (9): 1274–81. <https://doi.org/10.1080/01932691.2014.972516>.
- Wang, Yuliang, and Marya Lieberman. 2003. "Growth of Ultrasooth Octadecyltrichlorosilane Self-Assembled Monolayers on SiO₂." *Langmuir* 19 (4): 1159–67. <https://doi.org/10.1021/la020697x>.
- Welge, Henry. J. 1951. "A Simplified Method for Computing Oil Recovery by Gas or Water Drive." *Petroleum Transactions AIME* 195: 91–98. <https://doi.org/10.2118/124-G>.
- Wolthers, Mariëtte, Laurent Charlet, and Philippe Van Cappellen. 2008. "The Surface Chemistry of Divalent Metal Carbonate Minerals: A Critical Assessment of Surface Charge and Potential Data Using the Charge Distribution Multi-Site Ion Complexation Model." *American Journal of Science* 308 (8): 905–41. <https://doi.org/10.2475/08.2008.02>.
- Xie, Bo, and Anthony J. Muscat. 2005. "The Restoration of Porous Methylsilsesquioxane (p-MSQ) Films Using Trimethylhalosilanes Dissolved in Supercritical Carbon Dioxide." *Microelectronic Engineering* 82 (3–4 SPEC. ISS.): 434–40. <https://doi.org/10.1016/j.mee.2005.07.027>.
- Xie, Xina, and Norman R. Morrow. 2001. "Oil Recovery by Spontaneous Imbibition from Weakly Water-Wet Rocks." *Petrophysics* 42 (4): 313–22.
- Xie, Xina, Norman R. Morrow, and Jill S. Buckley. 2002. "Contact Angle Hysteresis and the Stability of

- Wetting Changes Induced by Adsorption from Crude Oil.” *Journal of Petroleum Science and Engineering* 33 (1–3): 147–59. [https://doi.org/10.1016/S0920-4105\(01\)00182-6](https://doi.org/10.1016/S0920-4105(01)00182-6).
- Yadav, Amrita R., Rashmi Sriram, Jared A. Carter, and Benjamin L. Miller. 2014. “Comparative Study of Solution-Phase and Vapor-Phase Deposition of Aminosilanes on Silicon Dioxide Surfaces.” *Materials Science and Engineering C* 35 (1): 283–90. <https://doi.org/10.1016/j.msec.2013.11.017>.
- Yang, Daoyong, Yongan Gu, and Paitoon Tontiwachwuthikul. 2008. “Wettability Determination of the Reservoir Brine - Reservoir Rock System with Dissolution of CO₂ at High Pressures and Elevated Temperatures.” *Energy & Fuels* 22 (10): 504–9.
- Yang, Jianjun, Sheng Meng, Lifang Xu, and E. G. Wang. 2005. “Water Adsorption on Hydroxylated Silica Surfaces Studied Using the Density Functional Theory.” *Physical Review B - Condensed Matter and Materials Physics* 71 (3): 1–12. <https://doi.org/10.1103/PhysRevB.71.035413>.
- Yarita, Takashi, Akira Nomura, and Yoshiyuki Horimoto. 1996. “In Situ Silylation of Silica-Based Packings Using Supercritical Fluid as Reaction Medium.” *Journal of Chromatography A* 724 (1–2): 373–77. [https://doi.org/10.1016/0021-9673\(95\)01145-5](https://doi.org/10.1016/0021-9673(95)01145-5).
- Yoshida, Wayne, Robert P. Castro, Jeng Dung Jou, and Yoram Cohen. 2001. “Multilayer Alkoxysilane Silylation of Oxide Surfaces.” *Langmuir* 17 (19): 5882–88. <https://doi.org/10.1021/la001780s>.
- Yousef, Ali A., Salah Al-Saleh, and Mohammad Al-Jawfi. 2012. “The Impact of the Injection Water Chemistry on Oil Recovery from Carbonate Reservoirs.” In *SPE EOR Conference o a t Oil and Gas West Asia Held in Muscat. Oman*.
- Zdziennicka, Anna., Katarzyna Szymczyk, and Bronisław Jańczuk. 2009a. “Correlation between Surface Free Energy of Quartz and Its Wettability by Aqueous Solutions of Nonionic, Anionic and Cationic Surfactants.” *Journal of Colloid and Interface Science* 340 (2): 243–48. <https://doi.org/10.1016/j.jcis.2009.08.040>.
- Zdziennicka, Anna, Katarzyna Szymczyk, and Bronisław Jańczuk. 2009b. “Correlation between Surface Free Energy of Quartz and Its Wettability by Aqueous Solutions of Nonionic, Anionic and Cationic Surfactants.” *Journal of Colloid and Interface Science* 340 (2): 243–48. <https://doi.org/10.1016/j.jcis.2009.08.040>.
- Zemanian, Thomas S., Glen E. Fryxell, Jun Liu, Shas Mattigod, James A. Franz, and Zimin Nie. 2001. “Deposition of Self-Assembled Monolayers in Mesoporous Silica from Supercritical Fluids.” *Langmuir* 17 (26): 8172–77. <https://doi.org/10.1021/la0107401>.
- Zhang, Feng, Ken Sautter, Adam M. Larsen, Daniel A. Findley, Robert C. Davis, Hussein Samha, and Matthew R. Linford. 2010. “Chemical Vapor Deposition of Three Aminosilanes on Silicon Dioxide: Surface Characterization, Stability, Effects of Silane Concentration, and Cyanine Dye Adsorption.” *Langmuir* 26 (18): 14648–54. <https://doi.org/10.1021/la102447y>.
- Zhang, Hua, T. S. Ramakrishnan, Alex Nikolov, and Darsh Wasan. 2016. “Enhanced Oil Recovery Driven by Nanofilm Structural Disjoining Pressure: Flooding Experiments and Microvisualization.” *Energy and Fuels* 30 (4): 2771–79. <https://doi.org/10.1021/acs.energyfuels.6b00035>.

- Zhang, Peimao, Medad T. Tweheyo, and Tor Austad. 2007. "Wettability Alteration and Improved Oil Recovery by Spontaneous Imbibition of Seawater into Chalk: Impact of the Potential Determining Ions Ca^{2+} , Mg^{2+} , and SO_4^{2-} ." *Colloids and Surfaces A: Physicochemical and Engineering Aspects*. <https://doi.org/10.1016/j.colsurfa.2006.12.058>.
- Zhang, Shiyang, Yuehui She, and Yongan Gu. 2011. "Evaluation of Polymers as Direct Thickeners for CO_2 Enhanced Oil Recovery." *Journal of Chemical and Engineering Data* 56 (4): 1069–79. <https://doi.org/10.1021/je1010449>.
- Zhang, Shuo, Guan Cheng Jiang, Le Wang, Wang Qing, Hai Tao Guo, Xin guo Tang, and Dian Gang Bai. 2014. "Wettability Alteration to Intermediate Gas-Wetting in Low-Permeability Gas-Condensate Reservoirs." *Journal of Petroleum Exploration and Production Technology* 4 (3): 301–8. <https://doi.org/10.1007/s13202-014-0119-9>.
- Zhang, Tiantian, Michael J. Murphy, Haiyang Yu, Hitesh G. Bagaria, Ki Youl Yoon, Bethany M. Neilson, Christopher W. Bielawski, Keith P. Johnston, Chun Huh, and Steven L. Bryant. 2015. "Investigation of Nanoparticle Adsorption during Transport in Porous Media." *SPE Journal* 20 (4): 667–77. <https://doi.org/10.2118/166346-PA>.
- Zhu, Mojun, Maria Z. Lerum, and Wei Chen. 2012. "How to Prepare Reproducible, Homogeneous, and Hydrolytically Stable Aminosilane-Derived Layers on Silica." *Langmuir* 28 (1): 416–23. <https://doi.org/10.1021/la203638g>.
- Zhuravlev, L. T. 1986. "Concentration of Hydroxyl Groups on the Surface of Amorphous Silicas." *Langmuir* 3 (3): 316–18. <https://doi.org/10.1021/la00075a004>.
- Zhuravlev, L T. 2000. "The Surface Chemistry of Amorphous Silica. Zhuravlev Model." *Colloids and Surfaces A: Physicochemical and Engineering Aspects* 173 (1–3): 1–38. [https://doi.org/10.1016/S0927-7757\(00\)00556-2](https://doi.org/10.1016/S0927-7757(00)00556-2).

Every reasonable effort has been made to acknowledge the owners of copyright material. I would be pleased to hear from any copyright owner who has been omitted or incorrectly acknowledged.

APPENDIX A Supporting Information

Table A. 1. Elemental Quantification for Gray Berea derived from XPS survey spectra. Listed are the mean values based on 2 analysis points.

Gray Berea								
Sample:	Control Sample	CPTS-CO ₂	DD_TS-CO ₂	CPhe_TS-CO ₂	BHEA_TS-CO ₂	BHEA_TS-Conventional	GPTS-CO ₂	GPTS-Conventional
Atomic%	Mean	Mean	Mean	Mean	Mean	Mean	Mean	Mean
O 1s	59.06	56.31	43.81	53.17	53.87	57.73	55.04	56.77
Si 2p	17.25	16.95	15.53	16.59	15.54	16.84	15.63	17.43
C 1s	9.99	12.79	30.39	16.99	16.34	12.04	19.15	13.80
Al 2p	9.04	8.16	6.35	7.67	7.52	8.22	6.80	7.25
Fe 2p	1.67	1.60	0.97	1.34	1.07	1.34	1.21	1.18
Cl 2p	0.27	1.04	0.00	1.09	0.18	0.00	0.07	0.27
K 2p	2.10	1.29	1.21	1.61	2.11	1.65	0.60	1.67
Na 1s	0.57	0.35	0.20	0.26	0.34	0.41	0.29	0.32
Mg KLL	0.75	0.50	0.43	0.49	0.63	0.60	0.45	0.51
Ca 2s	0.45	0.52	0.34	0.36	0.38	0.42	0.80	0.44
F 1s	0.00	0.15	0.00	0.12	0.41	0.00	0.00	0.00
Mn 2p	0.00	0.00	0.00	0.00	0.00	0.00	0.00	0.00
N 1s	0.38	0.38	0.33	0.34	1.44	0.77	0.42	0.38

Table A. 2. Elemental Quantification for Upper Gray Berea derived from XPS survey spectra. Listed are the mean values based on 2 analysis points.

Upper Gray Berea								
Sample:	Control Sample	CPTS-CO ₂	DD_TS-CO ₂	CPhe_TS-CO ₂	BHEA_TS-CO ₂	BHEA_TS-Conventional	GPTS-CO ₂	GPTS-Conventional
Atomic%	Mean	Mean	Mean	Mean	Mean	Mean	Mean	Mean
O 1s	63.57	57.69	44.84	51.04	53.99	57.53	55.41	58.01
Si 2p	17.32	21.61	18.19	19.92	17.66	19.22	20.43	20.60
C 1s	7.25	10.92	29.14	18.96	15.50	12.06	14.86	12.76
Al 2p	7.32	5.93	5.53	5.91	6.93	7.10	5.87	6.10
Fe 2p	1.81	0.74	0.54	0.59	0.76	0.79	1.16	0.74
Cl 2p	0.20	0.98	0.00	1.25	0.12	0.00	0.10	0.20
K 2p	1.78	1.32	1.23	1.57	2.04	1.69	0.95	1.32
Na 1s	0.39	0.14	0.00	0.11	0.19	0.17	0.15	0.00
Mg KLL	0.64	0.21	0.22	0.20	0.24	0.28	0.35	0.22
Ca 2s	0.50	0.12	0.00	0.08	0.12	0.07	0.37	0.11
F 1s	0.00	0.00	0.00	0.00	0.80	0.19	0.24	0.00
Mn 2p	0.00	0.00	0.00	0.00	0.00	0.00	0.02	0.00
N 1s	0.00	0.38	0.33	0.41	1.40	0.93	0.04	0.33

Table A. 3. Elemental Quantification for Bandera Brown derived from XPS survey spectra. Listed are the mean values based on 2 analysis points.

Bandera Brown								
Sample:	Control Sample	CPTS-CO ₂	DD_TS-CO ₂	CPhe_TS-CO ₂	BHEA_TS-CO ₂	BHEA_TS-Conventional	GPTS-CO ₂	GPTS-Conventional
Atomic%	Mean	Mean	Mean	Mean	Mean	Mean	<i>Mean</i>	Mean
O 1s	57.94	55.45	37.33	49.23	52.53	57.57	52.89	56.72
Si 2p	14.98	16.79	13.47	16.07	14.47	17.56	16.13	15.97
C 1s	12.86	14.74	41.99	22.49	19.99	13.51	21.04	15.46
Al 2p	7.08	6.44	4.61	5.83	6.18	6.58	5.34	6.38
Fe 2p	3.17	2.01	0.87	1.63	1.85	2.17	1.56	2.03
Cl 2p	0.27	1.61	0.10	1.56	0.20	0.00	0.16	0.41
K 2p	1.03	0.85	0.41	0.96	0.84	0.76	0.25	0.92
Na 1s	0.54	0.31	0.26	0.31	0.27	0.47	0.35	0.26
Mg KLL	0.53	0.39	0.31	0.38	0.40	0.41	0.36	0.36
Ca 2s	1.10	0.61	0.41	0.73	0.36	0.62	1.03	0.92
F 1s	0.09	0.14	0.00	0.17	0.30	0.00	0.11	0.00
Mn 2p	0.44	0.38	0.15	0.39	0.66	0.44	0.21	0.36
N 1s	0.43	0.30	0.13	0.28	1.75	0.59	0.29	0.24

Table A. 4. Elemental Quantification for Bentheimer derived from XPS survey spectra. Listed are the mean values based on 2 analysis points.

Bentheimer								
Sample:	Control Sample	CPTS-CO ₂	DD_TS-CO ₂	CPhe_TS-CO ₂	BHEA_TS-CO ₂	BHEA_TS-Conventional	GPTS-CO ₂	GPTS-Conventional
Atomic%	Mean	Mean	Mean	Mean	Mean	Mean	Mean	Mean
O 1s	59.13	57.67	43.40	52.57	52.46	57.20	54.36	57.75
Si 2p	23.20	24.80	19.80	23.71	21.76	22.98	23.03	23.77
C 1s	10.90	11.88	32.21	18.26	17.78	13.47	18.48	14.00
Al 2p	4.06	3.11	3.48	3.50	3.37	3.77	2.93	3.21
Fe 2p	0.60	0.58	0.47	0.41	0.41	0.38	0.20	0.48
Cl 2p	0.35	1.06	0.00	0.80	0.26	0.00	0.23	0.21
K 2p	1.08	0.47	0.39	0.50	0.60	0.91	0.14	0.39
Na 1s	0.57	0.29	0.05	0.07	0.32	0.24	0.14	0.31
Mg KLL	0.00	0.00	0.00	0.00	0.00	0.00	0.06	0.00
Ca 2s	0.13	0.00	0.08	0.04	0.07	0.00	0.14	0.14
F 1s	0.00	0.00	0.00	0.00	1.15	0.16	0.00	0.00
Mn 2p	0.00	0.00	0.00	0.00	0.00	0.00	0.09	0.00
N 1s	0.24	0.18	0.16	0.17	1.53	0.90	0.16	0.19

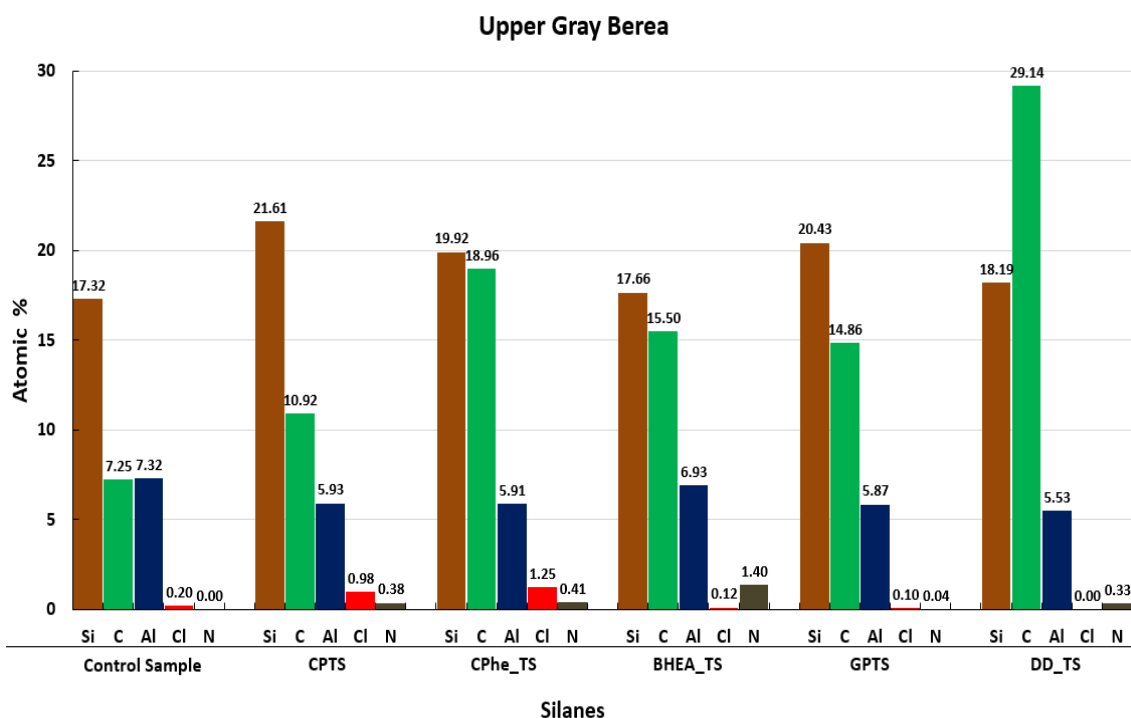


Figure A. 1. XPS elemental quantification expressed as atomic % of Upper Gray Berea substrate and modified samples. (Graph contains data for Control Sample and aged through scCO₂ method with CPTS, CPhe_TS, BHEA_TS, GPTS and DD_TS). Note: Not all the elements present in the substrates are included in the graphs.

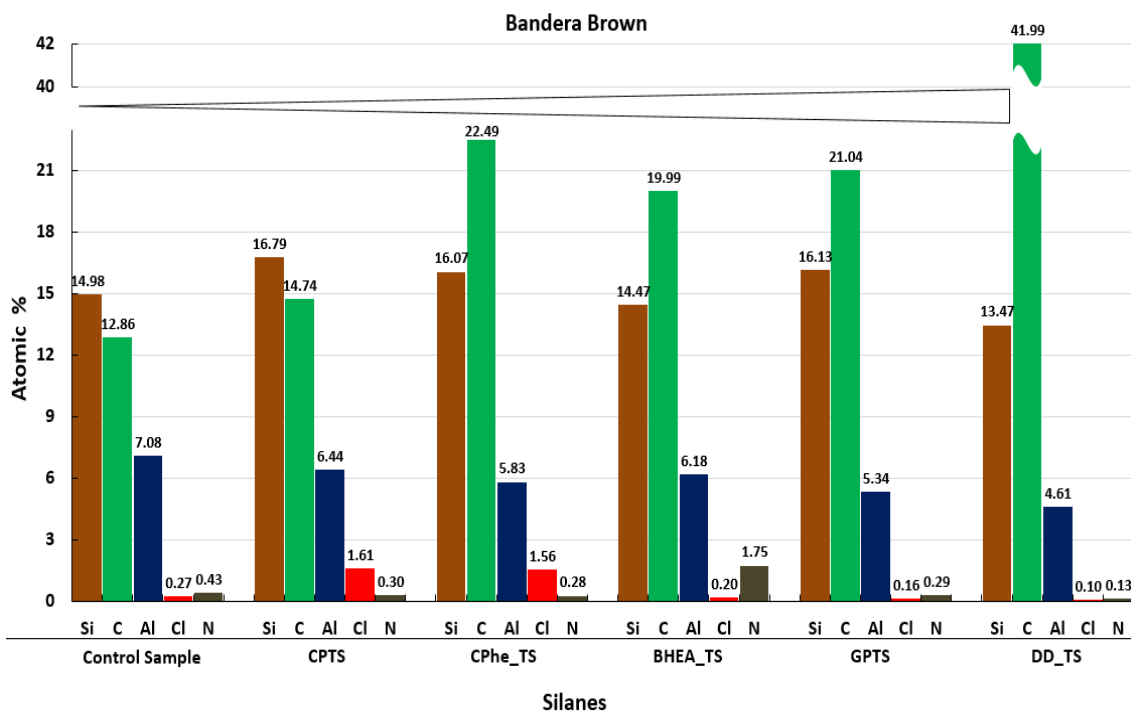


Figure A. 2. XPS elemental quantification expressed as atomic % of Bandera Brown substrate and modified samples. (Graph contains data for Control Sample and aged through scCO₂ method with CPTS, CPhe_TS, BHEA_TS, GPTS and DD_TS). Note: Not all the elements present in the substrates are included in the graphs.

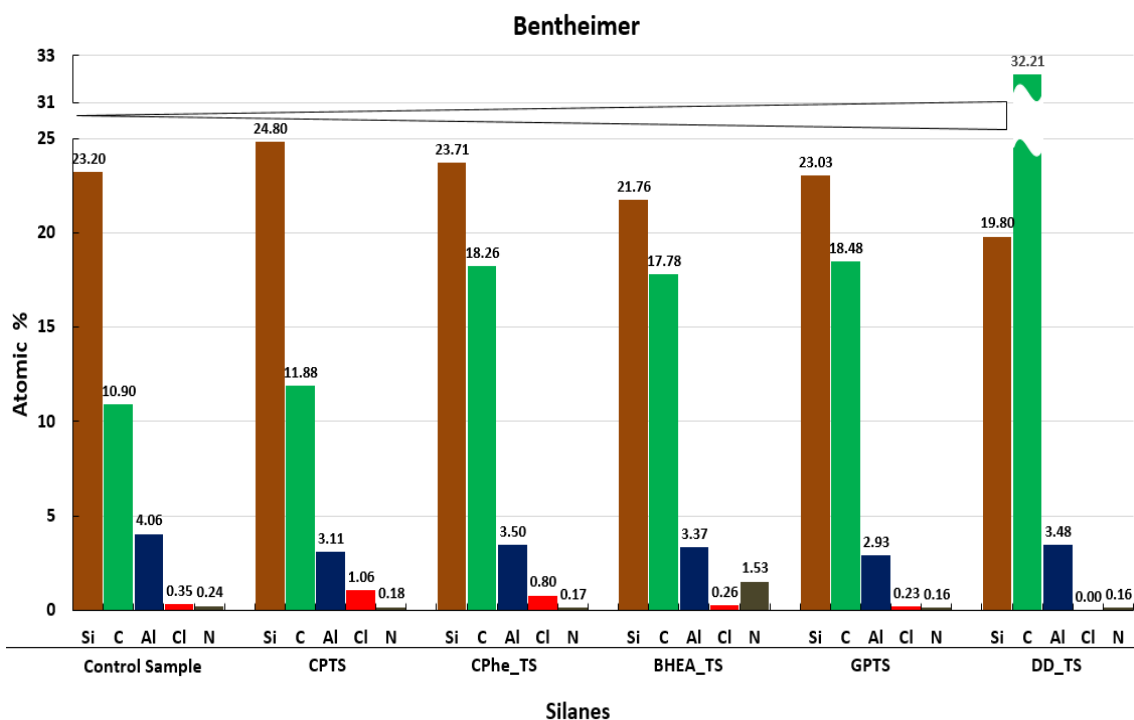


Figure A. 3. XPS elemental quantification expressed as atomic % of Bentheimer substrate and modified samples. (Graph contains data for Control Sample and aged through $scCO_2$ method with CPTS, CPhe_TS, BHEA_TS, GPTS and DD_TS). Note: Not all the elements present in the substrates are included in the graphs.

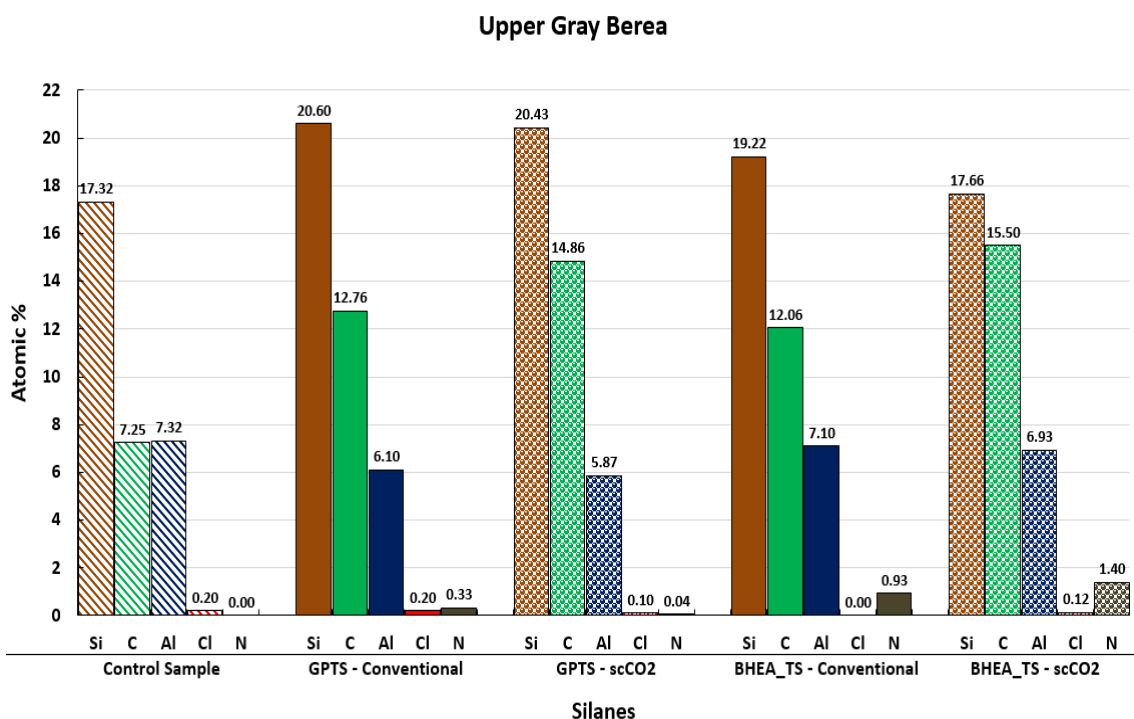


Figure A. 4. XPS elemental quantification expressed as atomic % of Upper Gray Berea substrate and modified samples. (Graph contains data for Control Sample (hashed bars) and aged through Conventional method (solid bars) and $scCO_2$ method (dotted bars) with BHEA_TS and GPTS). Note: Not all the elements present in the substrates are included in the graphs.

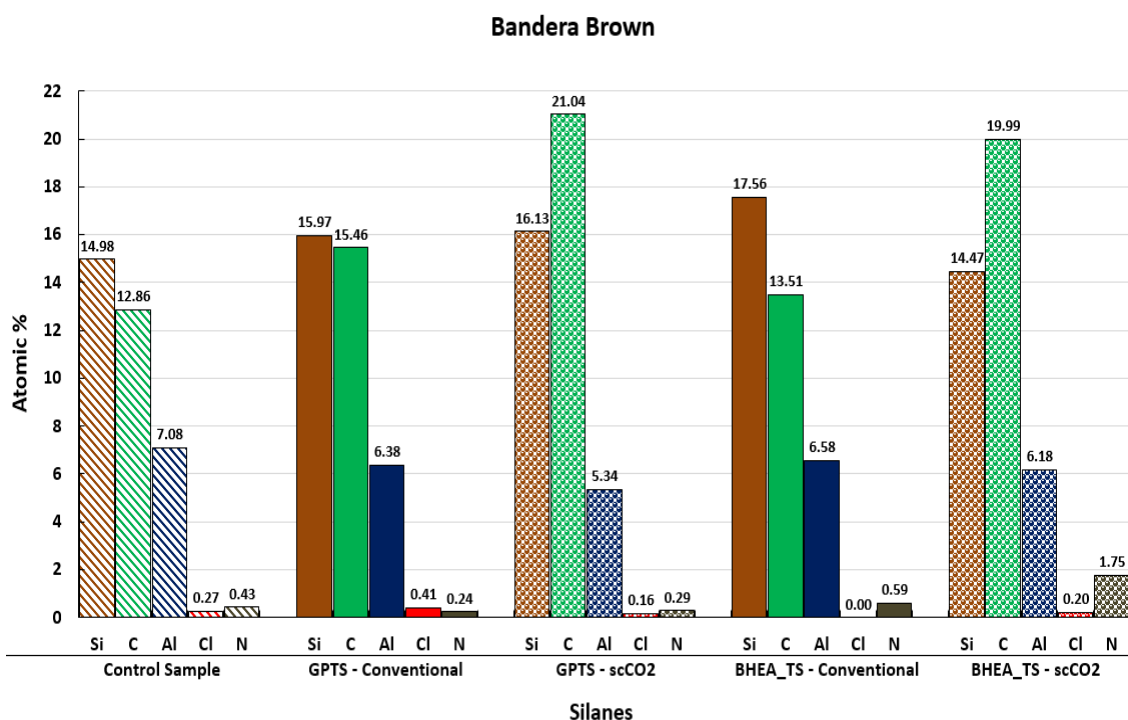


Figure A. 5. XPS elemental quantification expressed as atomic % of Bandera Brown substrate and modified samples. (Graph contains data for Control Sample (hashed bars) and aged through Conventional method (solid bars) and scCO₂ method (dotted bars) with BHEA_TS and GPTS). Note: Not all the elements present in the substrates are included in the graphs.

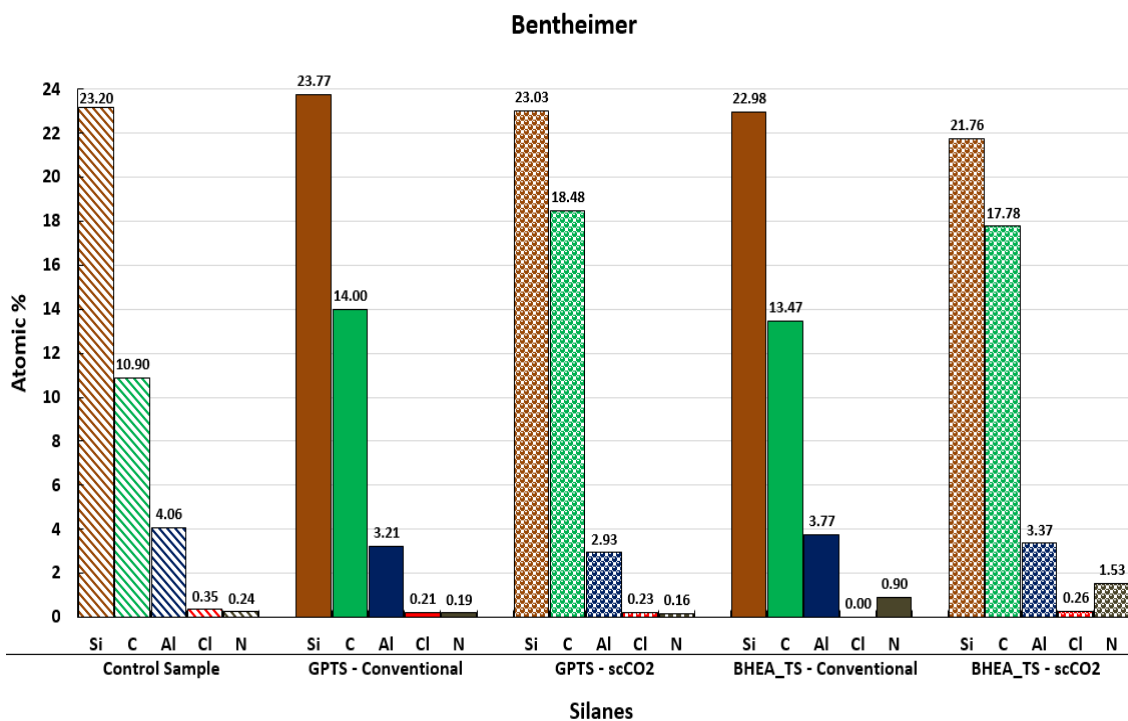


Figure A. 6. XPS elemental quantification expressed as atomic % of Bentheimer substrate and modified samples. (Graph contains data for Control Sample (hashed bars) and aged through conventional method (solid bars) and scCO₂ method (dotted bars) with BHEA_TS and GPTS). Note: Not all the elements present in the substrates are included in the graphs.

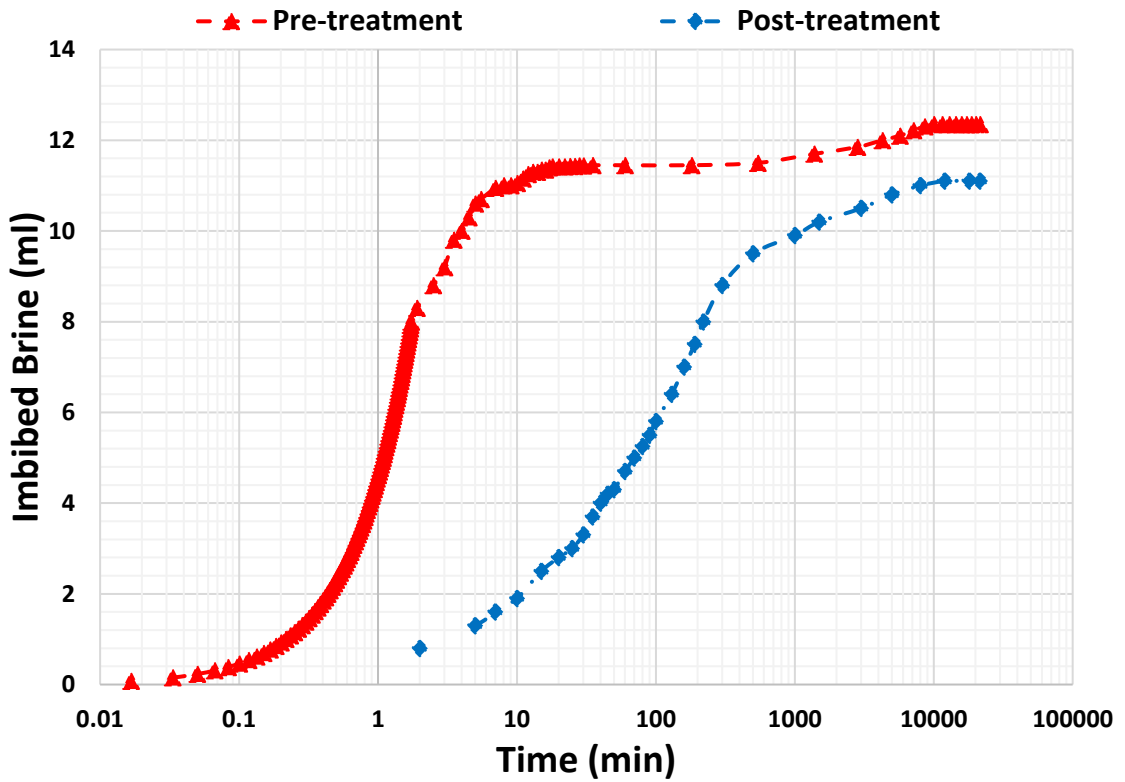


Figure A. 7. Spontaneous brine imbibition vs. time in GB.1, pre-treatment (red triangle) and post-treatment (blue diamond).

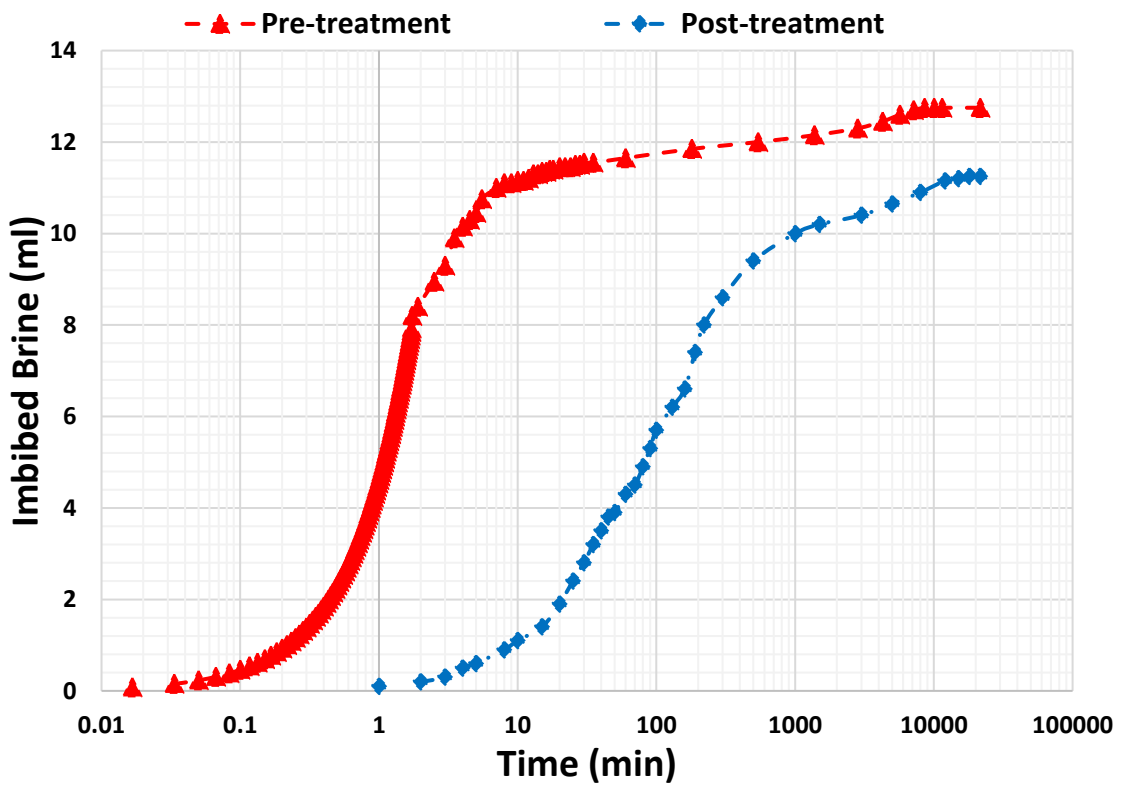


Figure A. 8. Spontaneous brine imbibition vs. time in GB.3, pre-treatment (red triangle) and post-treatment (blue diamond).

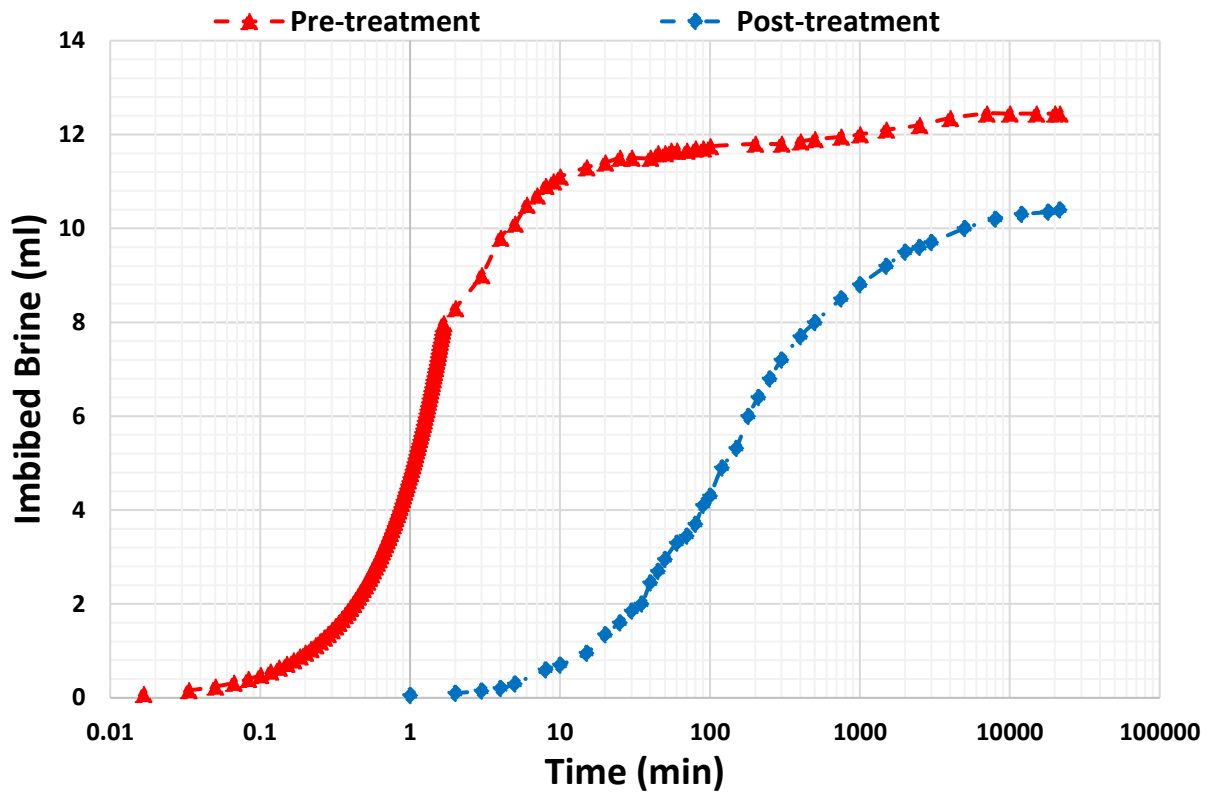


Figure A. 9. Spontaneous brine imbibition vs. time in GB.4, pre-treatment (red triangle) and post-treatment (blue diamond).

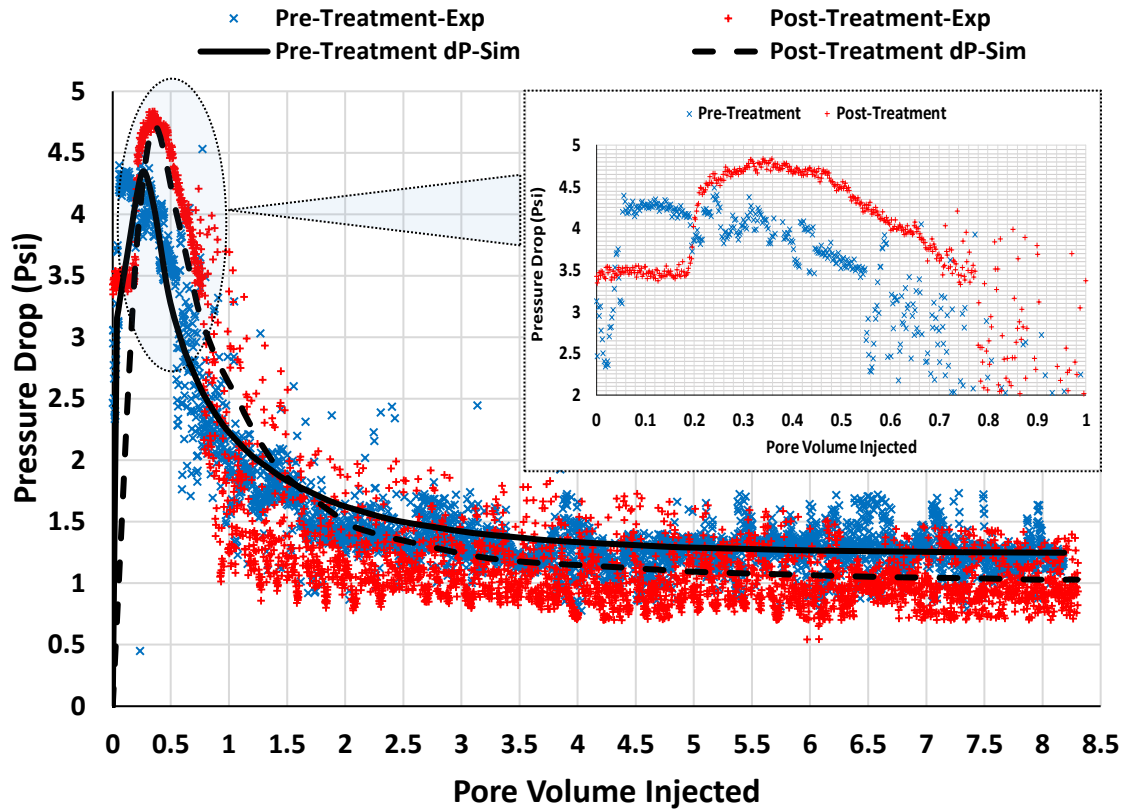


Figure A. 10. Experimental differential pressure (denoted by Exp) vs. pore volumes of CO₂ injected through the GB.1 sandstone sample pre- (blue cross symbol) and post-silylation (red plus symbol) with 2 wt. % of CPTS (inset compares the breakthrough points) Solid and dashed black lines represent the numerical simulation history matched differential pressure for pre- and post-silylation, respectively (denoted by Sim).

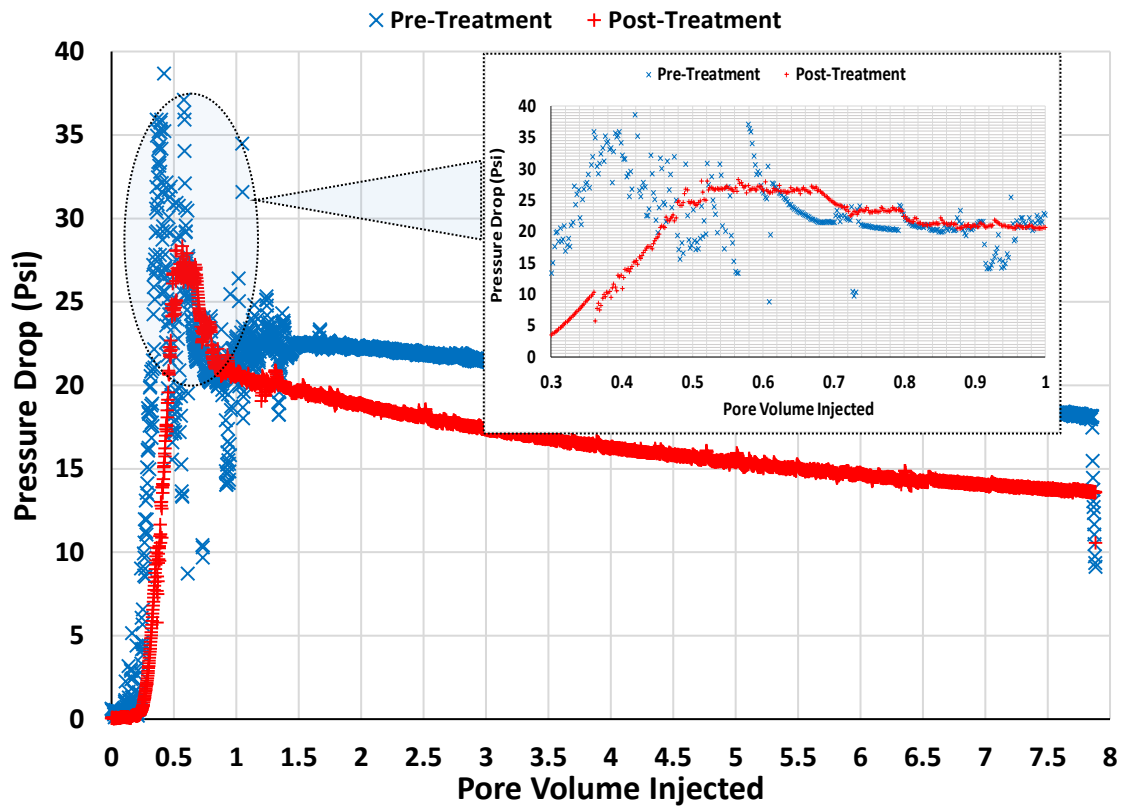


Figure A. 11. Differential pressure vs. pore volumes of brine injected through the GB.1 sandstone sample pre- (blue cross symbol) and post-silylation (red plus symbol) with 2 wt. % of CPTS (inset compares the breakthrough points).

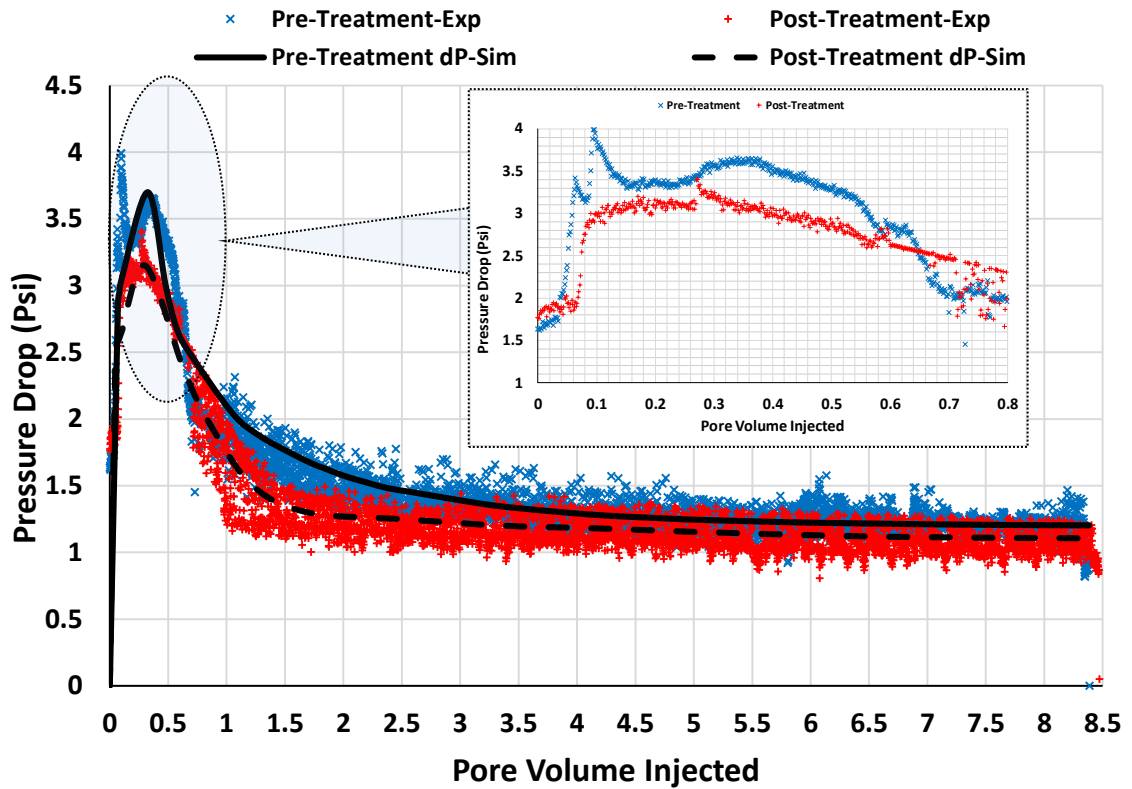


Figure A. 12. Experimental differential pressure (denoted by Exp) vs. pore volumes of CO₂ injected through the GB.3 sandstone sample pre- (blue cross symbol) and post-silylation (red plus symbol) with 2 wt. % of CPTS (inset compares the breakthrough points). Solid and dashed black lines represent the numerical simulation history matched differential pressure for pre- and post-silylation, respectively (denoted by Sim).

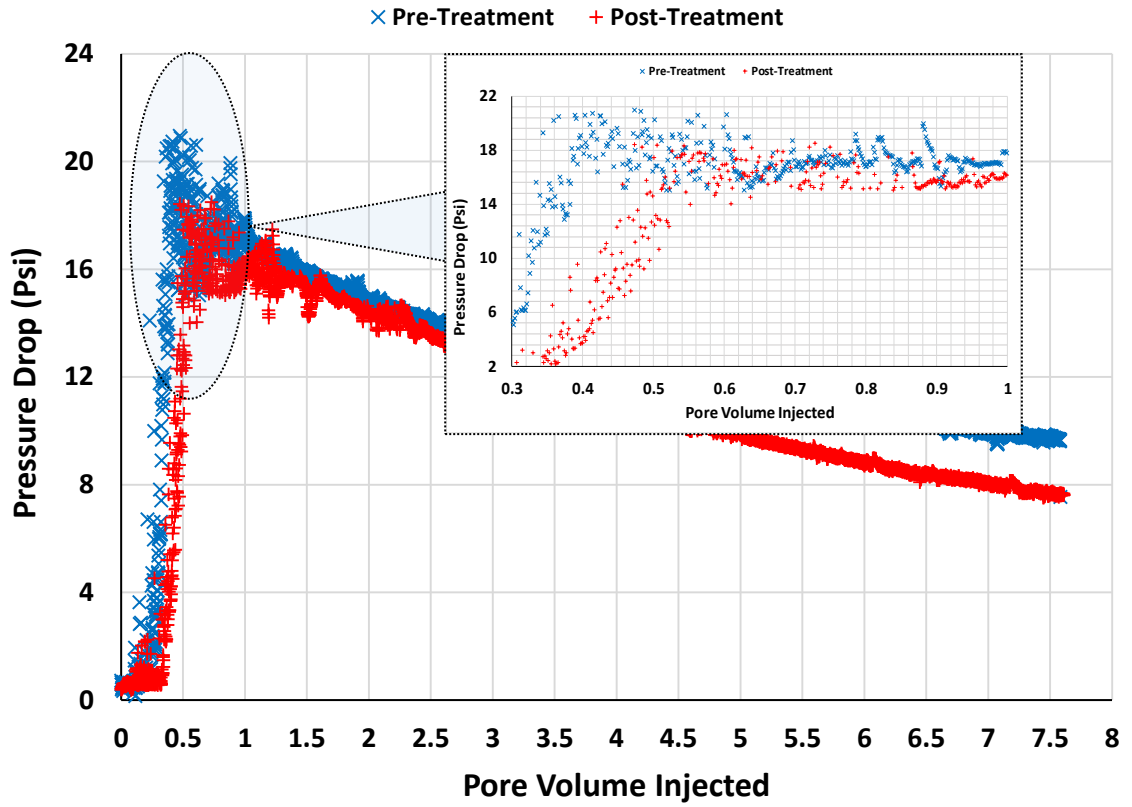


Figure A. 13. Differential pressure vs. pore volumes of brine injected through the GB.3 sandstone sample pre- (blue cross symbol) and post-silylation (red plus symbol) with 2 wt. % of CPTS (inset compares the breakthrough points).

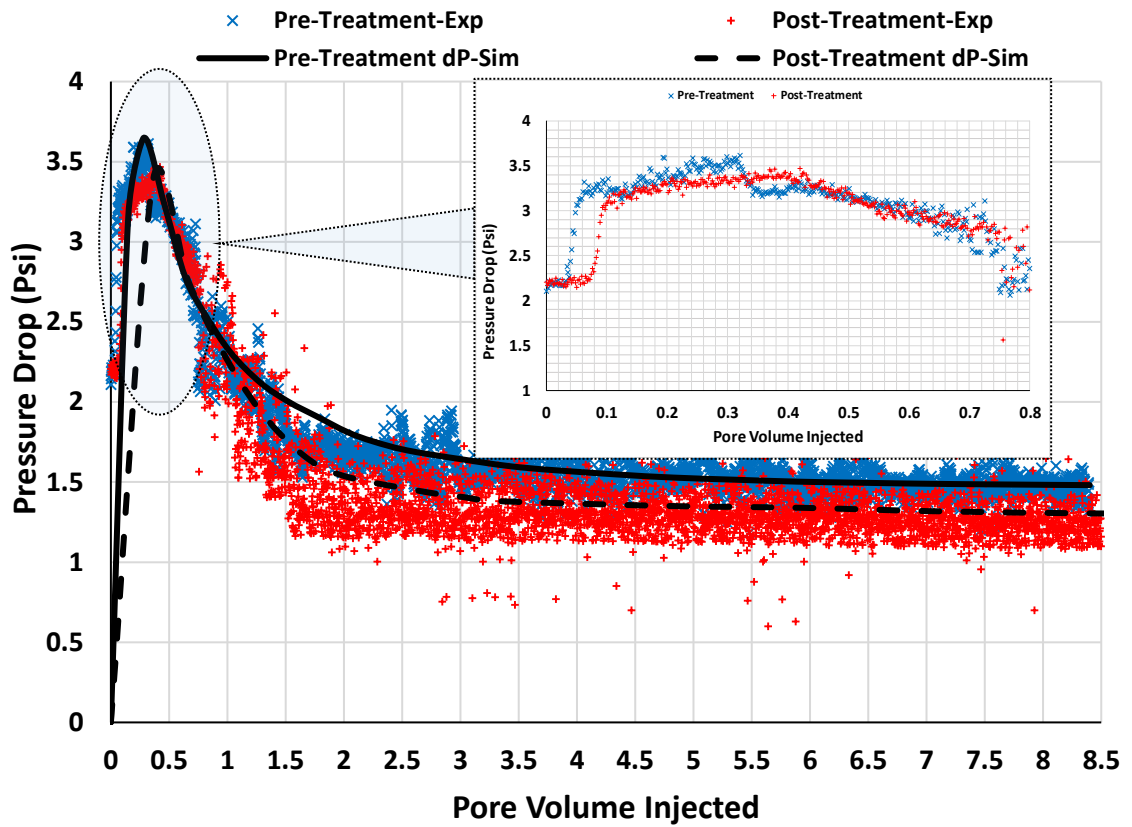


Figure A. 14. Experimental differential pressure (denoted by Exp) vs. pore volumes of CO₂ injected through the GB.4 sandstone sample pre- (blue cross symbol) and post-silylation (red plus symbol) with 2 wt. % of CPTS (inset compares the breakthrough points). Solid and dashed black lines represent the numerical simulation history matched differential pressure for pre- and post-silylation, respectively (denoted by Sim).

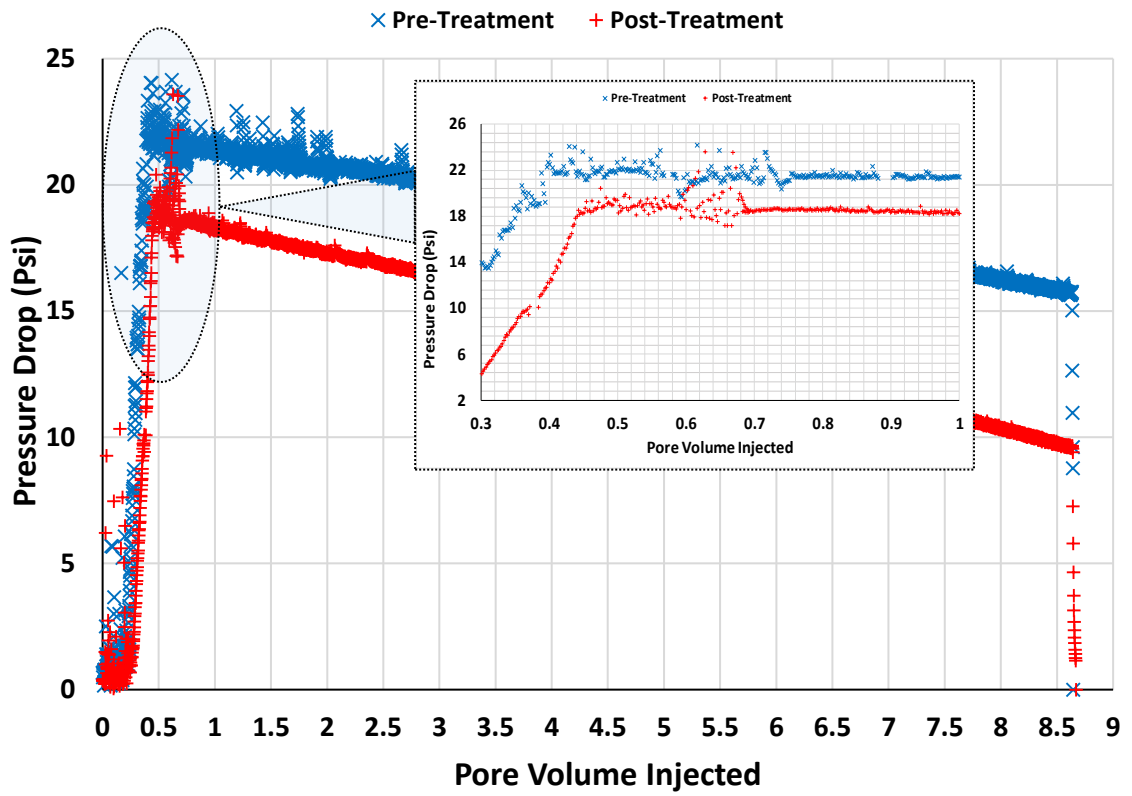


Figure A. 15. Differential pressure vs. pore volumes of brine injected through the GB.4 sandstone sample pre- (blue cross symbol) and post-silylation (red plus symbol) with 2 wt. % of CPTS (inset compares the breakthrough points).

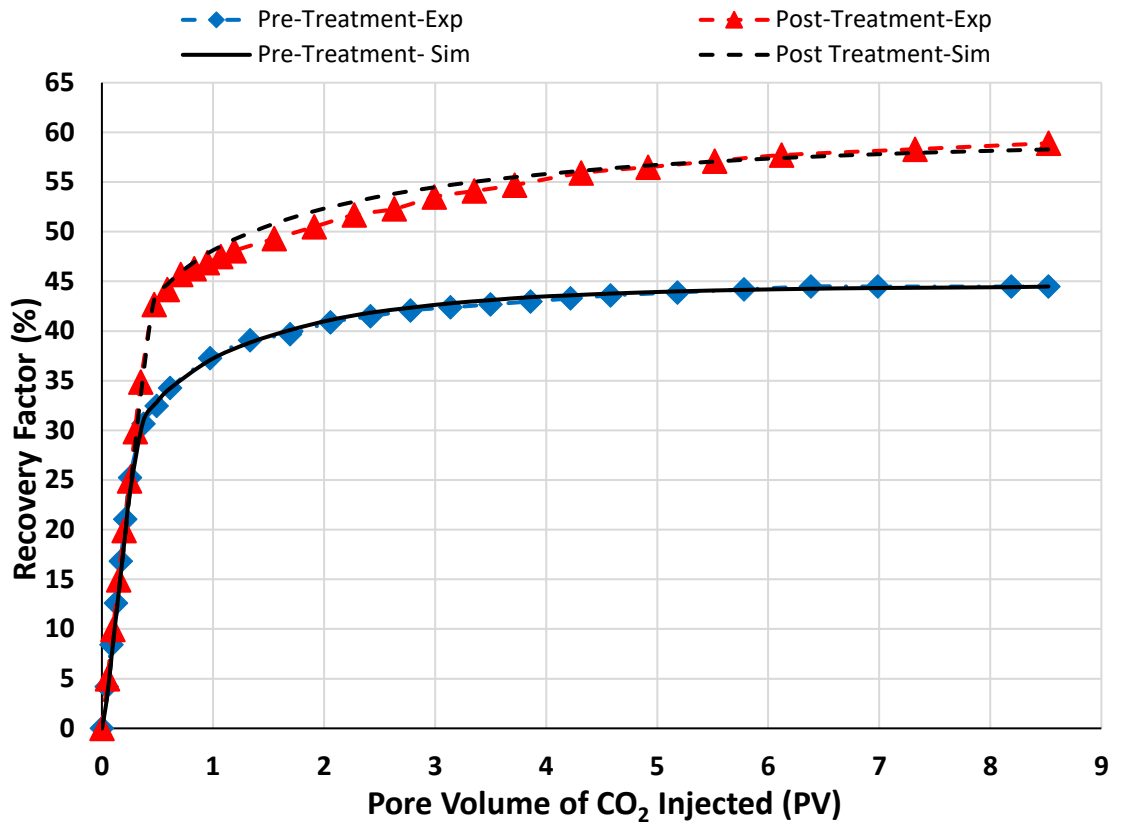


Figure A. 16. Experimental brine recovery factor during scCO₂ injection for pre-treatment (blue diamond symbol) and post-treatment (red triangle symbol) for GB.1 (denoted by Exp). Solid and dashed black lines represent the numerical simulated brine recovery for pre- and post-treatment, respectively (denoted by Sim).

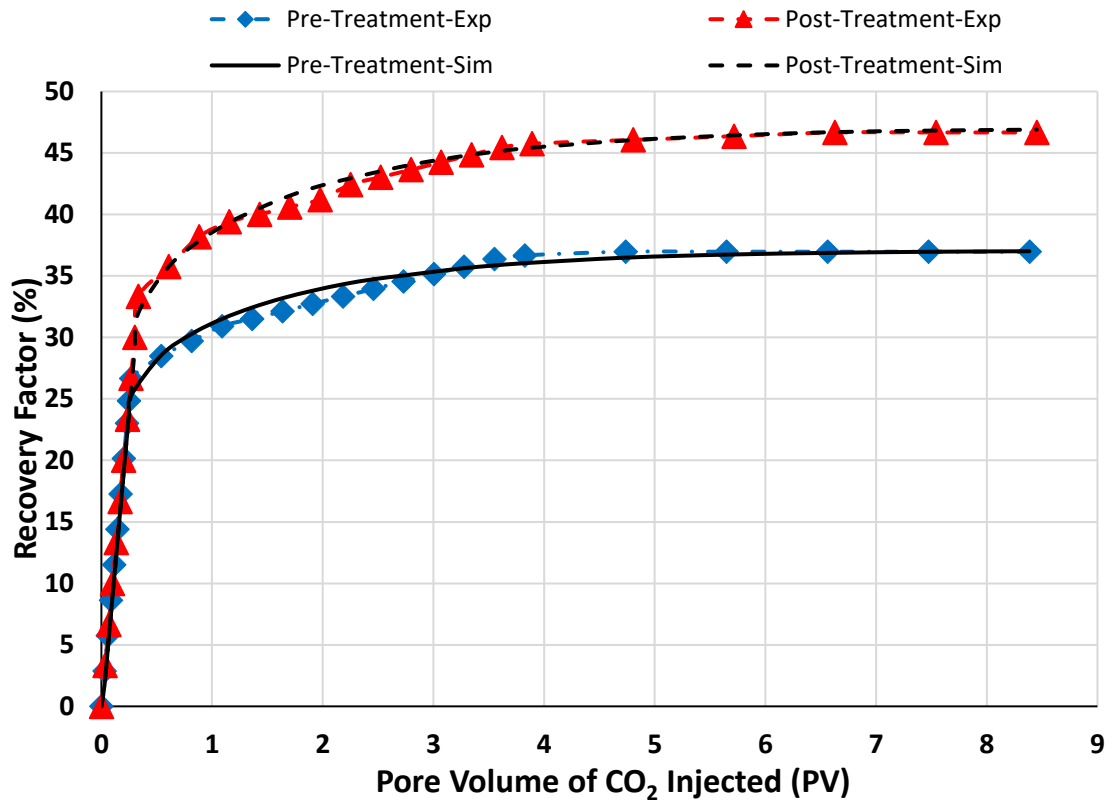


Figure A. 17. Experimental brine recovery factor during scCO₂ injection for pre-treatment (blue diamond symbol) and post-treatment (red triangle symbol) for GB.3 (denoted by Exp). Solid and dashed black lines represent the numerical simulated brine recovery for pre- and post-treatment, respectively (denoted by Sim).

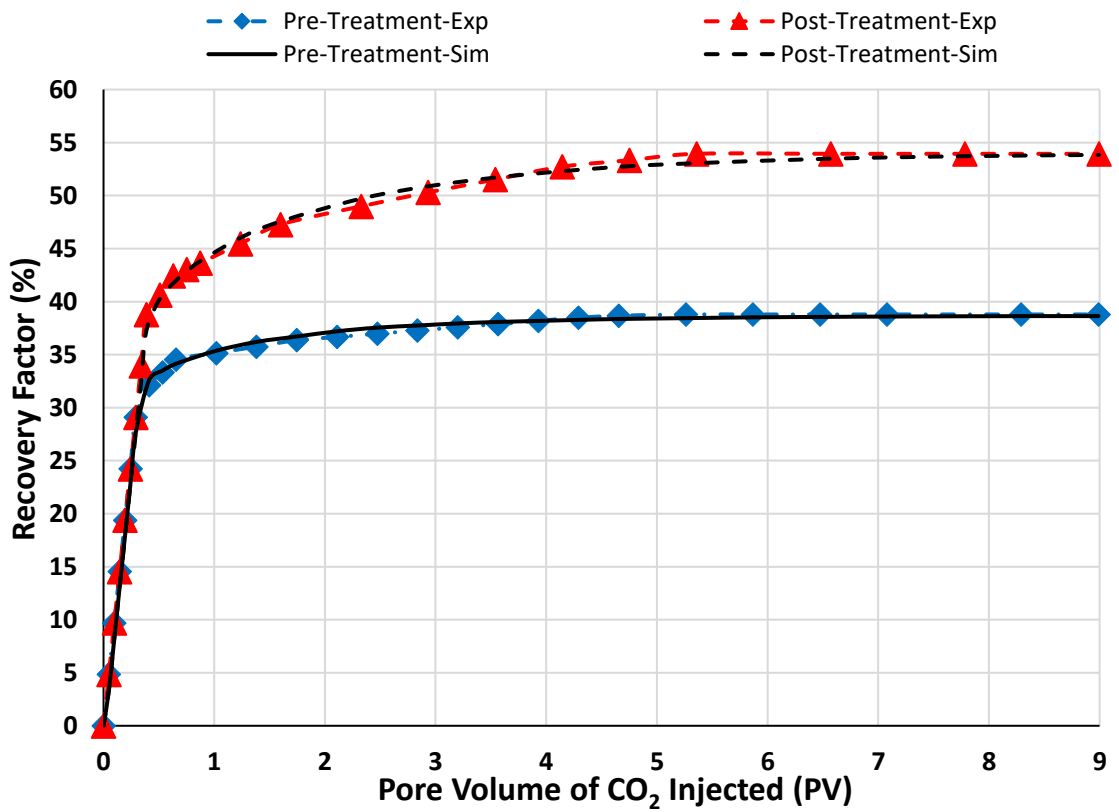


Figure A. 18. Experimental brine recovery factor during scCO₂ injection for pre-treatment (blue diamond symbol) and post-treatment (red triangle symbol) for GB.4 (denoted by Exp). Solid and dashed black lines represent the numerical simulated brine recovery for pre- and post-treatment, respectively (denoted by Sim).

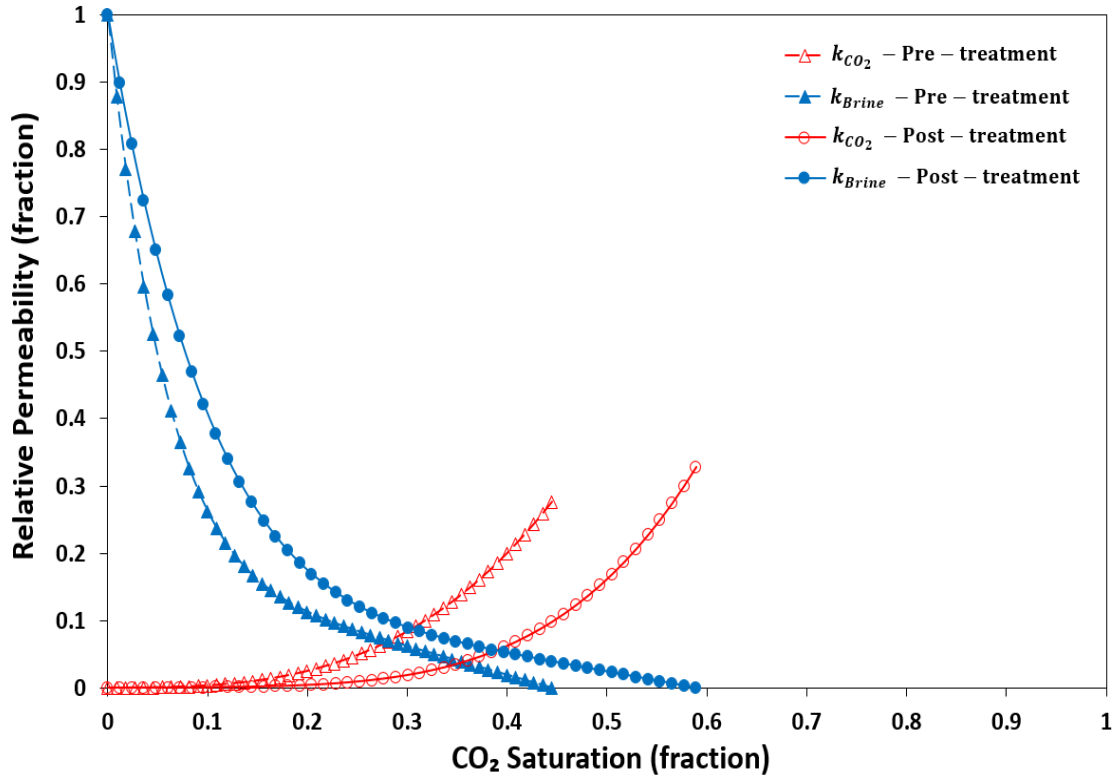


Figure A. 19. Relative permeability curves for the primary drainage conducted on pre-treated (triangle symbol) and post-treated (circle symbol) for GB.1 sample.

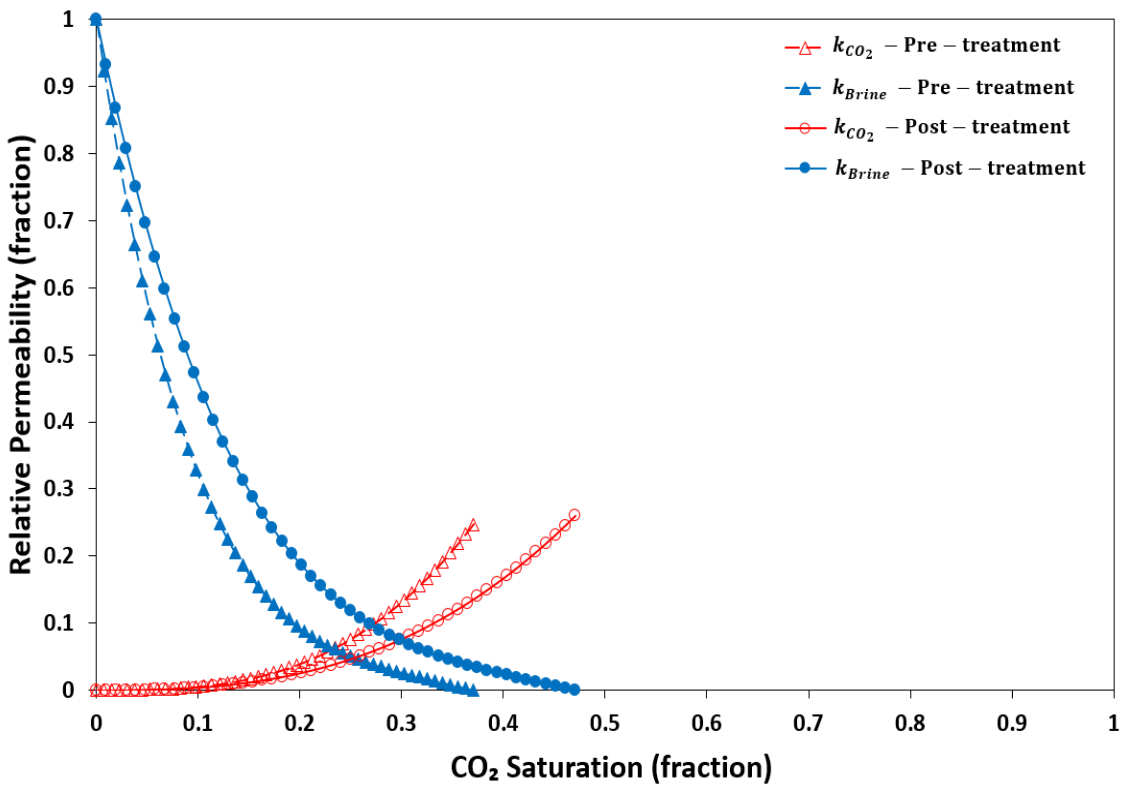


Figure A. 20. Relative permeability curves for the primary drainage conducted on pre-treated (triangle symbol) and post-treated (circle symbol) for GB.3 sample.

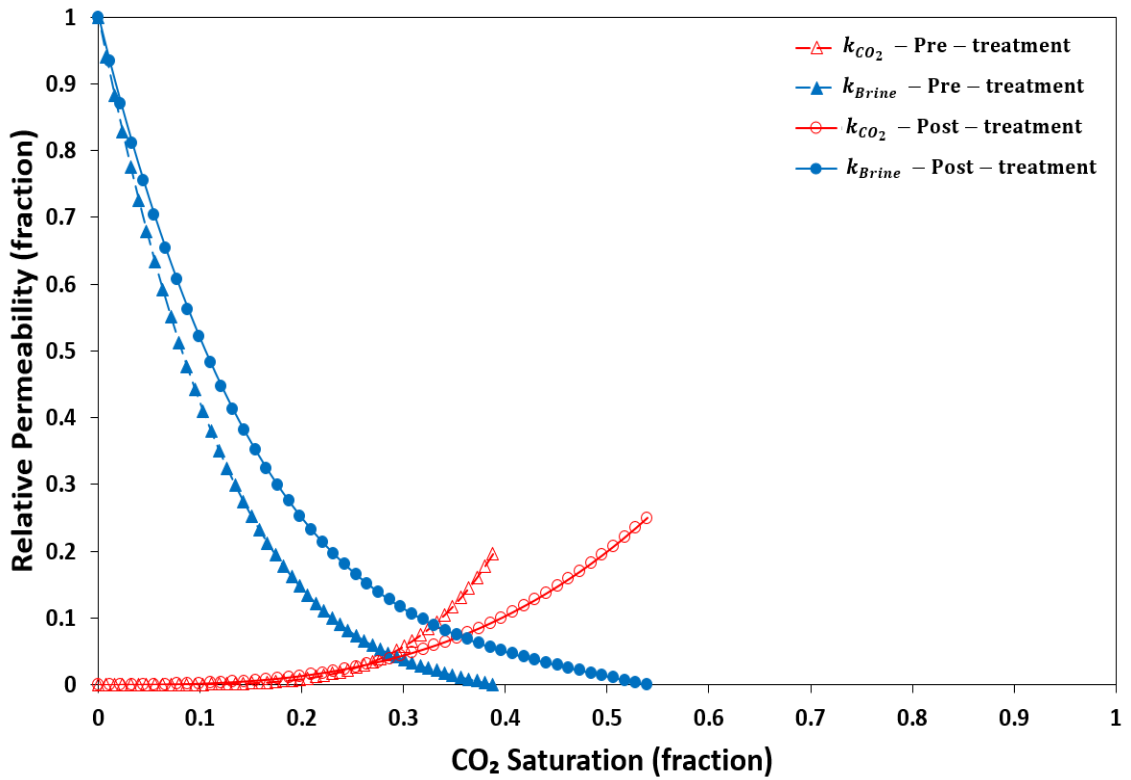


Figure A. 21. Relative permeability curves for the primary drainage conducted on pre-treated (triangle symbol) and post-treated (circle symbol) for GB.4 sample.

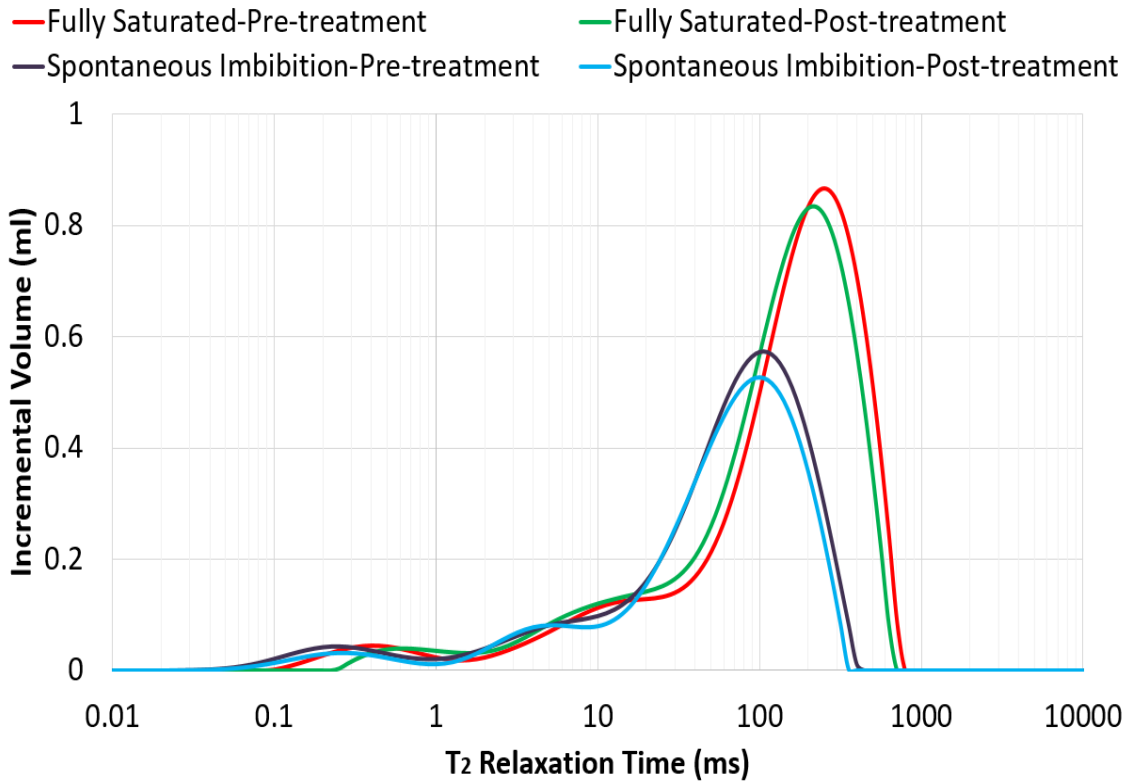


Figure A. 22. NMR derived incremental brine volume for pre- and post-treated GB.1.

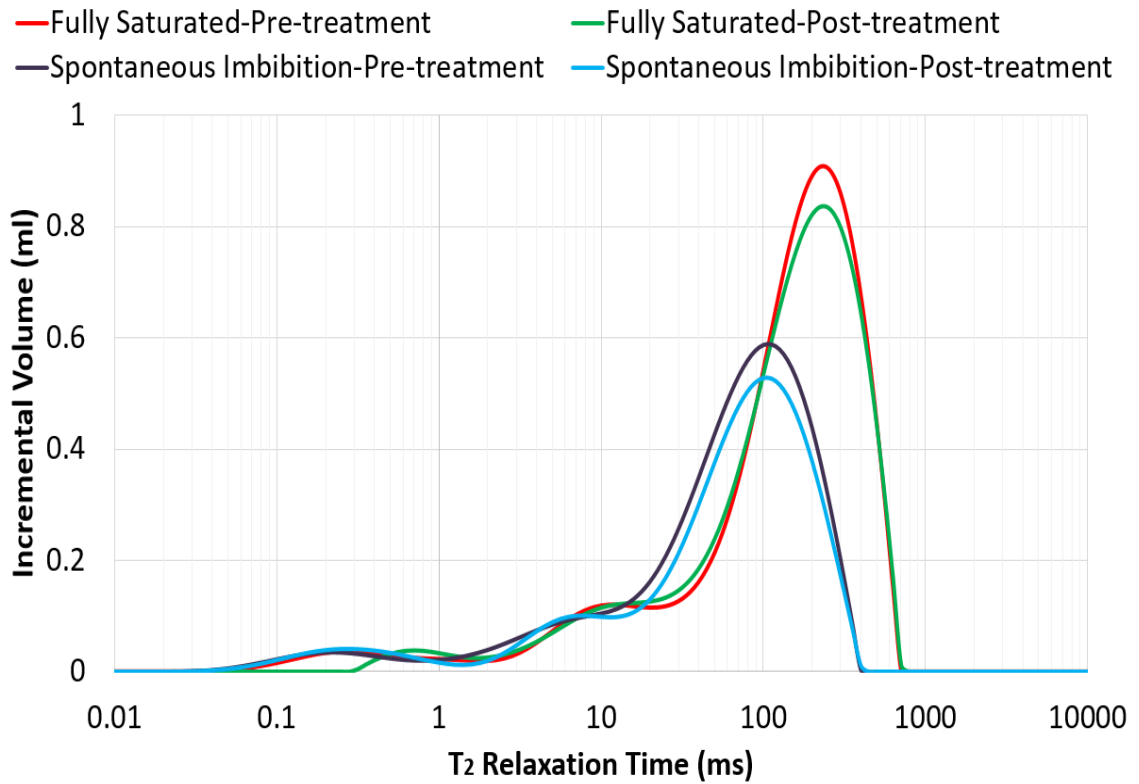


Figure A. 23. NMR driven incremental brine volume for pre- and post-treated GB.3.

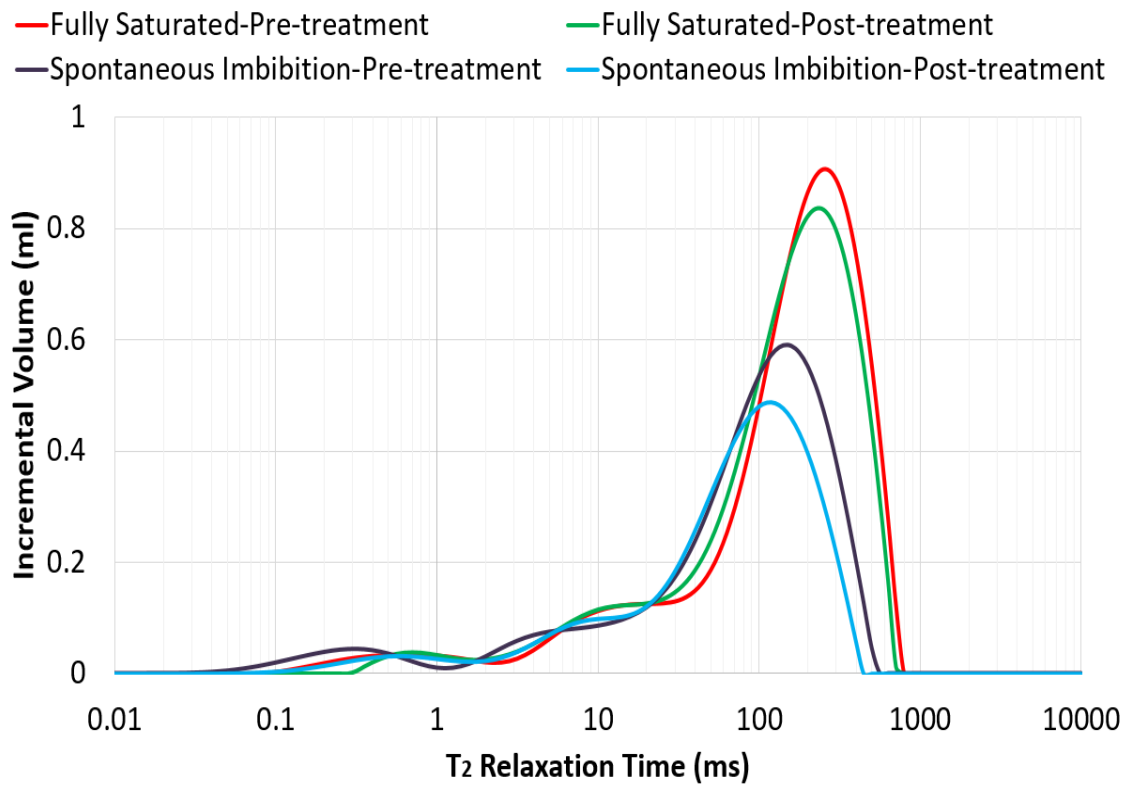


Figure A. 24. NMR derived incremental brine volume for pre- and post-treated GB.4.

APPENDIX B Official Permissions and Copyrights



RightsLink®



Home



Help



Email Support



Eghan Arjomand ▾

Changing Sandstone Rock Wettability with Supercritical CO₂-Based Silylation



Author: Eghan Arjomand, Christopher D. Easton, Matthew Myers, et al

Publication: Energy & Fuels

Publisher: American Chemical Society

Date: Jan 1, 2020

Copyright © 2020, American Chemical Society

PERMISSION/LICENSE IS GRANTED FOR YOUR ORDER AT NO CHARGE

This type of permission/license, instead of the standard Terms & Conditions, is sent to you because no fee is being charged for your order. Please note the following:

- Permission is granted for your request in both print and electronic formats, and translations.
- If figures and/or tables were requested, they may be adapted or used in part.
- Please print this page for your records and send a copy of it to your publisher/graduate school.
- Appropriate credit for the requested material should be given as follows: "Reprinted (adapted) with permission from (COMPLETE REFERENCE CITATION). Copyright (YEAR) American Chemical Society." Insert appropriate information in place of the capitalized words.
- One-time permission is granted only for the use specified in your request. No additional uses are granted (such as derivative works or other editions). For any other uses, please submit a new request.

[BACK](#)

[CLOSE WINDOW](#)

Modifying the Wettability of Sandstones Using Nonfluorinated Silylation: To Minimize the Water Blockage Effect



Author: Eghan Arjomand, Matthew Myers, Nasser Mohammed Al Hinaï, et al

Publication: Energy & Fuels

Publisher: American Chemical Society

Date: Jan 1, 2020

Copyright © 2020, American Chemical Society

PERMISSION/LICENSE IS GRANTED FOR YOUR ORDER AT NO CHARGE

This type of permission/license, instead of the standard Terms & Conditions, is sent to you because no fee is being charged for your order. Please note the following:

- Permission is granted for your request in both print and electronic formats, and translations.
- If figures and/or tables were requested, they may be adapted or used in part.
- Please print this page for your records and send a copy of it to your publisher/graduate school.
- Appropriate credit for the requested material should be given as follows: "Reprinted (adapted) with permission from (COMPLETE REFERENCE CITATION). Copyright (YEAR) American Chemical Society." Insert appropriate information in place of the capitalized words.
- One-time permission is granted only for the use specified in your request. No additional uses are granted (such as derivative works or other editions). For any other uses, please submit a new request.

[BACK](#)[CLOSE WINDOW](#)

APPENDIX C Attributions of Co-authors

Paper title: “Modifying the Wettability of Sandstones Using Nonfluorinated Silylation: To Minimize the Water Blockage Effect”, *Energy Fuels* 2020, 34, (1), 709-719

Eghan Arjomand, ^{†,‡} *Matthew Myers*, [‡] *Nasser Mohammed Al Hinai*, [†] *Colin D. Wood*, ^{*,†,‡} and *Ali Saeedi*, ^{*,†}

[†]Curtin University, Kensington, WA 6151, Australia

[‡]CSIRO Australian Resources Research Centre, Kensington, WA 6151, Australia

Author Name	Concept & Design	Data Acquisition	Data Analysis	Interpretation & Discussion	Manuscript Proof Reading & Approval
Matthew Myers (Co-author-1)			✓	✓	✓
I acknowledge that these present my contributions to the above research output. Signature: 					
Nasser Mohammed Al Hinai (Co-author-2)		X			
I acknowledge that these present my contributions to the above research output. Signature: 					
Colin D. Wood (Co-author-3)	X			X	X
I acknowledge that these present my contributions to the above research output. Signature: 					
Ali Saeedi (Co-author-4)	X			X	X
I acknowledge that these present my contributions to the above research output. Signature: 					

Paper title: "Changing Sandstone Rock Wettability with Supercritical CO₂-Based Silylation", *Energy Fuels* 2020, 34, (2), 2015-2027

Eghan Arjomand,^{†,‡} Christopher D. Easton,[§] Matthew Myers,[‡] Wendy Tian,[§] Ali Saeedi,^{*,†}
and Colin D. Wood,^{*,†,‡}

[†]Curtin University of Technology, Kensington, WA 6152, Australia

[‡]CSIRO Australian Resources Research Centre, Kensington, WA 6152, Australia

[§]CSIRO Manufacturing, Clayton, VIC 3168, Australia

Author Name	Concept & Design	Data Acquisition	Data Analysis	Interpretation & Discussion	Manuscript Proof Reading & Approval
Christopher D. Easton (Co-author-1)		✓	✓	✓	✓
I acknowledge that these present my contributions to the above research output.					
Signature: 					
Matthew Myers (Co-author-2)			✓	✓	✓
I acknowledge that these present my contributions to the above research output.					
Signature: 					
Wendy Tian (Co-author-3)		X	X		
I acknowledge that these present my contributions to the above research output.					
Signature: 					
Ali Saeedi (Co-author-4)				X	X
I acknowledge that these present my contributions to the above research output.					
Signature: 					
Colin D. Wood (Co-author-5)	X			X	X
I acknowledge that these present my contributions to the above research output.					
Signature: 					